ISAS - INTERNATIONAL SCHOOL
FOR ADVANCED STUDIES

Scaling Properties of the Large–Scale Structure of the Universe

Thesis submitted for the degree of
"Doctor Philosophiae"

Astrophysics Sector

Candidate:

Stefano Borgani

Supervisor:

Professor
George F. R. Ellis

Academic Year 1991/92

TRIESTE

SISSA - SCUOLA
INTERNAZIONALE
SUPERIORE
DI STUDI AVANZATI
TRIESTE
Strada Costiera 11

Scaling Properties of the Large–Scale Structure of the Universe

Thesis presented by

Stefano Borgani

for the degree of Doctor Philosophiae

Supervisor: Professor George F. R. Ellis

S.I.S.S.A. – I.S.A.S.

Astrophysics Sector

Academic Year 1991 - 92

To my girl, Valeria, and to my parents, Emore and Liliana.

Acknowledgements

It is very difficult for me to remember and adequately acknowledge all the people who contributed in different ways to the realization of this Thesis.

First of all, I would like to mention all my collaborators, who made possible the presentation of the original material contained in this work. In alphabetic order, they are: Prof. S.A.Bonometto, Dr. Y.P.Jing, Dr. G.Murante, Dr. M.Persic, Dr. M.Plionis, Dr. A.Provenzale, Dr. P.Salucci and Dr. R.Valdarnini.

I wish to thank Manolis Plionis for our long, stimulating discussions on social and political subjects, my "chaotic" friend Antonello Provenzale for the enthusiasm he devoted to our fractal collaborations, and Riccardo Valdarnini for his patience in sharing the room with me in the last two years. I thank Paul Haines for a careful reading of a provisional version of this Thesis and for his efforts to improve my English. Massimo Persic and Paolo Salucci are deeply acknowledged for several useful comments and suggestions.

A special thought is devoted to my friend Manolis, who is now serving in the Greek Air Force, with the hope that he will be back in research as soon as possible.

Many thanks are due to Prof. S.A. Bonometto, for introducing me to the study of the Large-Scale Structure of the Universe, to my supervisor Prof. G.F.R.Ellis and to Prof. D.W.Sciama for their continuous advice, encouragement and support during the course of my graduate study at SISSA.

I acknowledge Dr. P.Coles, Prof. F.Lucchin, Dr. V.Martinez, Prof. S.Matarrese, Dr. L.Moscardini and Dr. Sathyaprakash for stimulating discussions, which also opened the possibility for further developments of the results presented here.

Besides the scientific aspects, these four years that I spent in SISSA have also represented for me the opportunity to meet a lot of new good friends. It would take too long mentioning all them here. However, remembering all the time we spent together must not be interpreted as the final exchange of greetings. Instead, I sincerely hope to stay strictly in touch with all of them even after the completion of our PhD program.

Finally, I would also to acknowledge the INFN (Istituto Nazionale di Fisica Nucleare) of Perugia, where I got a permanent position one year ago. Other than the people of the Theoretical Group, who gave me a quick "acclimatization" course during my first period of work, I would mention the system-manager, F.Gentile, for his kindness in tolerating my continuous requests of implementation of new software products.

Contents

Introduction

I.1 Large Scale Structure and Cosmology

The study of the large-scale structure of the Universe represents one of the most exciting research fields in cosmology. In the last twenty years or so the collection of a huge body of observational data has greatly contributed to improve our knowledge of "cosmography", so as to adequately test theoretical models about the origin and evolution of the Universe. The currently accepted view is that the structures observed today represent the result of gravitational evolution, starting from very homogeneous initial conditions, with fluctuations of the energy density of the order $\delta \sim 10^{-5}$, which have subsequently grown by gravitational instability. This picture is considered extremely plausible for a number of reasons, and recently received further support from the first detection of temperature anisotropies in the Cosmic Microwave Background (CMB), as provided by COBE [393].

The idea that the Universe should be uniform led to the formulation of the *Cosmological Principle*, on which most of the current cosmogonic pictures are based. In one of its versions, the Cosmological Principle states that the Universe is homogeneous and isotropic in its spatial part. Under this assumption about the symmetry of the space-like hypersurfaces, it is possible to show (see, *e.g.*, ref.[388]) that a system of coordinates can always be found in which the line element is written as

$$ds^2 \;=\; c^2\,dt^2 - a^2(t)\,\left[\frac{dr^2}{1-kr^2} + r^2\,(d\vartheta^2 + \sin^2\vartheta\,d\varphi^2)\right]\,. \qquad (I.1)$$

With a suitable definition of the units of r, in the above expression the curvature constant k can be considered to have only three possible values; $k = 0$ for a spatially flat Universe, $k = +1$ for a closed (positive curvature) Universe and $k = -1$ for an open (negative curvature) Universe. The quantity $a(t)$ represents the cosmic expansion factor. It gives the rate at which two points of fixed comoving coordinates $(r_1, \vartheta_1, \varphi_1)$ and $(r_2, \vartheta_2, \varphi_2)$ increase their mutual physical distance as $a(t)$ increases. Its time dependence can be worked out by solving Einstein's equations for the Friedmann-Lemaitre-Robertson-Walker (FLRW) metric of eq.(I.1). If the matter content of the Universe is that of a perfect fluid, such equations reduce to the system of two equations

$$\left(\frac{\dot{a}}{a}\right)^2 \equiv H^2 = \frac{8\pi G}{3}\rho + \frac{\Lambda}{3} - \frac{k}{a^2} \qquad (I.2a)$$

$$-\frac{\ddot{a}}{a} = \frac{4\pi G}{3}(\rho + 3p)\,, \qquad (I.2b)$$

which are usually called Friedmann's equations. In eq.($I.2a$) we have also included the cosmological constant term Λ, which is assumed to be negligible in most cases. From a heuristic point of view, such equations can be seen as the equivalent of the energy conservation principle and of the second law of dynamics in classical (non relativistic) mechanics. Following the expression of the FLRW metric, two points at distance $d = a(t)r$ (r is the fixed comoving distance) will move apart with a velocity $v = \dot{a}r = Hd$, so as to reproduce the Hubble law for the recession velocities of galaxies. Determinations of the Hubble constant H by using redshift-independent methods to measure galaxy distances give us

$$H = 100\,h\,\mathrm{km\,s^{-1}\,Mpc^{-1}} \quad , \quad 0.4 \lesssim h \lesssim 1\,.$$

Note that this large uncertainty is not due to measurement errors, instead it comes from discrepancies between different distance estimators.

Based on eq.($I.2a$), we define the *critical* density $\rho_c = 3H^2/8\pi G = 1.9\times10^{-29}\,h^{-2}\,\mathrm{g\,cm^{-3}}$, such that density values ρ above, below or equal to ρ_c refer to closed, open or flat universes, respectively. Measurements of the cosmic mean density are usually expressed through the density parameter $\Omega \equiv \rho/\rho_c$. Current limits on its present value, Ω_o, are

$$0.2 < \Omega_o \lesssim 1\,,$$

the "closure" value $\Omega_o = 1$ being usually preferred on the ground of aesthetic, but also of theoretical motivations (*i.e.*, standard inflation).

Once we specify the equation of state, which gives the relation between the density ρ and the pressure p, the system of equations ($I.2$) can be solved for $a(t)$. In the following we recall some particular solutions:

$$\begin{array}{l} \Omega = 1,\ p = 0 \text{ (matter dominated)} \quad \Rightarrow \quad a(t) \propto t^{2/3} \\ \Omega = 1,\ p = \rho/3 \text{ (radiation dominated)} \quad \Rightarrow \quad a(t) \propto t^{1/2} \\ \Omega = 0 \text{ (free expansion)} \quad \Rightarrow \quad a(t) \propto t \\ p = -\rho \text{ (vacuum dominated)} \quad \Rightarrow \quad a(t) \propto \exp(Ht)\,. \end{array} \qquad (0.1)$$

Note that the $\Omega = 1$ cases approximate the expansion in non-flat geometries at sufficiently early times, when the curvature term in eq.($I.2a$) becomes negligible. Viceversa, the $\Omega = 0$ case represents the asymptotic expansion of an open Universe, when a very large value of $a(t)$ makes the density term so small that it gives negligible deceleration ($\ddot{a} \simeq 0$).

One of the fundamental consequences of the Cosmological Principle is the prediction that the Universe has undergone in the past a hot phase, during which the cosmic temperature took a much higher value than that, $T_o \simeq 2.7\,K$, which is today observed for the cosmic microwave background. The resulting cosmological framework of the hot Big Bang in a spatially homogeneous and isotropic Universe is so widely accepted that it received the denomination of Standard Model (not to be confused with the Standard Model for electroweak interactions !). Indications point in favour of this model and the most striking and direct supports can be summarized as follows.

i) The observed proportionality between the recession velocity of galaxies and their distance (Hubble law), which is a natural consequence of assuming the FLRW metric of eq.(I.1).

ii) The detection and the high degree of isotropy of the cosmic microwave background radiation, which is the evidence of a primordial hot stage of the Universe, characterized by a high degree of isotropy.

iii) The observed light element abundances, which match remarkably well the predictions of primordial nucleosynthesis, which is an unavoidable step in the evolution of the hot Universe.

Although the assumption of a homogeneous and isotropic Universe is correct at an early stage of the Universe or today at sufficiently large scales, nevertheless it is manifestly violated at scales below the typical correlation length of density fluctuations, where the structure of the Universe is much more complex. However, this does not represent a problem for the Cosmological Principle, which, instead, would be in trouble if we were observing non negligible anisotropies at scales comparable to the horizon size.

Observations of the Universe on scales similar to the typical galaxy dimension, $\sim$ 10 kpc, reveal large inhomogeneities and the current view is that below such scales non-gravitational forces are dynamically dominant. On the other hand, scales $R \gg 10$ kpc are considered relevant to the Large Scale Structure. The main difference between small (galaxy) and the large scale lies essentially in the dynamics giving rise to structure formation. Indeed, the galaxy mass is determined by the capacity of the baryonic content to cool down during gravitational collapse, as the density increases. A quantitative analysis shows that, for masses $M \gtrsim 10^{12} M_\odot$, the heat produced during the initial collapse prevents a further compression [317]. Apart from the details of the heat production and dissipation, it is clear that, while the efficiency of the dissipation in a proto-object of dimension R is proportional to R^2 (*i.e.*, to the extension of its surface), the heat production is proportional to R^3 (*i.e.*, to the mass of the object). Then, it is easy to understand that a characteristic scale R^* must exist, such that above R^* the rate of heat production is greater than the dissipation rate, which prevents the gravitational collapse from proceeding. The precise value of R^* depends on the geometry of the collapse process, on environmental effects, and on the dissipation characteristics of the collapsing material. Detailed analysis give R^* values that are very similar to the typical scale of normal galaxies. The study of dissipative processes, which determine the internal structure and dynamics of galaxies, are then essential in understanding the origin of galaxies. However, such analysis can be very difficult and the details of the *genesis* and evolution of structures below the galaxy scales are widely debated.

On the contrary, on scales much larger than the galaxy ones, it is possible to study the formation and evolution of cosmic structure only on the basis of the gravitational interaction. This evolution follows initially a linear pattern, while later, when the fluctuation amplitude increases sufficiently, it undergoes non-linear phases. For this reason, the large scale dynamics are not so easy to understand. However, on such scales the problem is much better determined and ones hope is to solve adequately the dynamical picture.

On such scales the essential observation is that galaxies have a spatial distribution with highly non-random characteristics. They show a strong tendency to group together forming clusters, while clusters themselves are clumped into "superclusters" on even larger scales. The resulting hierarchical appearance of the galaxy distribution suggests the presence of a sort of scale-invariance, which is also supported by several quantitative statistical analyses. The classical example is represented by the 2-point correlation function, which is observed to decline with a power-law shape, having the same slope for both galaxies and clusters, although at different scales and with different amplitudes. Such scaling properties for the object distribution is one of the most relevant characteristics that must be accounted for by any galaxy formation model. The hierarchical arrangement of the clustering is even more remarkable if we consider that it extends from the small scales, where gravitational dynamics are in the non-linear regime, up to large scales where linearity still holds. Therefore, a detailed statistical representation of the clustering displayed by the distribution of galaxies and galaxy systems is fundamental in order to compare the present Universe with the predictions of theoretical models for structure formation.

Instead of using positions of luminous objects, an investigation of the large scale matter distribution in the Universe can be efficiently realized also by observing the effects of the background gravitational field on galaxy peculiar motions. A direct estimate of the radial peculiar velocity of a galaxy at distance d is obtained by subtracting the Hubble velocity, $H_o d$, from the observed recessional velocity, once a redshift-independent estimate of d is available. This kind of distance measurement is usually based on intrinsic relations between intrinsic structural parameters of galaxies, such as the famous Tully-Fisher relation for spirals [369] (which relates the absolute luminosity and the observed rotation velocities), the Faber-Jackson relation for ellipticals [134] (which relates the absolute luminosity and the internal velocity dispersion) and the D_n-σ relation for ellipticals [245] (which relates a suitably defined apparent diameter D_n to the line-of-sight velocity dispersion σ). An exciting development in this field has been the recent completion of large galaxy redshift surveys and the availability of a considerable amount of redshift-independent distance estimates (see ref.[67] for a recent review). As a consequence, a lot of theoretical work has been devoted to find methods for extracting the large-scale three-dimensional velocity and mass density fields from measurements of radial peculiar velocities. At large scales peculiar motions are related to the gravitational potential field by linear dynamical equations. In this regime, it makes sense to address the problem of reconstructing the matter distribution from the observed galaxy motions. Since the linearity of the gravitational clustering at large scales should have preserved the initial shape of the primordial fluctuation spectrum, the reconstruction procedure could furnish precise indications about the initial conditions. Several attempts in this direction have been already pursued (see, *e.g.*, refs.[37, 38]), with quite promising results, despite the rather limited and sparse amount of available data. A decisive step forward in this direction should be however possible in the next years, with the availability of a more complete sampling of the velocity field traced by galaxy motions.

A further very efficient way to probe the nature of primordial fluctuations is represented by the investigation of the temperature fluctuations in the CMB. Such fluctuations are expected to be originated at the recombination time (corresponding to a redshift $z_{rec} \sim 1000$), when matter and radiation decouple. After that epoch, the Universe became transparent to the electromagnetic radiation. For this reason, inhomogeneities in the CMB should reflect the matter fluctuations just before decoupling. In past years, many efforts have been devoted to detect such anisotropies, with the result of continuously pushing down the lower limits for their amplitude. Only very recently, the COBE satellite succeeded in detecting a significant signal for CMB temperature fluctuations at the angular scale $\vartheta = 7°$. Although a detection at such a large angle (corresponding to a physical scale largely exceeding the horizon size at recombination) does not definitely fix the nature of the primordial fluctuations, nevertheless it provides fundamental support to the idea that the presently observed structures have grown from very small initial perturbations in the Friedmann background. Hopefully, in few years more refined measurements at smaller angular scales should be able to further restrict the number of allowed initial condition models.

I.2 Overview

In this Thesis we will mainly concentrate on the statistical analysis of the distribution of galaxies and galaxy systems, also comparing observational data to both numerical and analytical approaches to gravitational clustering. Although information coming from the study of peculiar motions and CBM temperature anisotropies are mentioned in order to constrain theoretical models for the initial perturbation spectrum, we will essentially deal with the study of the large-scale structure in the "configuration space".

Our work has been essentially motivated by the need to explain the nature and the origin of the hierarchical arrangement of the observed galaxy distribution. Particularly surprising is the coexistence of the observed complexity of the large-scale texture with the regularity of its statistical properties. The scaling displayed by the detected clustering, from the small scales ($\sim 10\,h^{-1}$ kpc) of galaxy halos, to those ($0.1\lesssim r\lesssim 10h^{-1}$ Mpc) of galaxy clustering, up to the large scales ($10\lesssim r\lesssim 100h^{-1}$ Mpc) for the clustering of rich galaxy systems, calls for a dynamical mechanism, which should be able to generate them over such a wide scale range. In order to make a close investigation of such scaling properties and of their possible dynamical origin, we extensively apply both correlation and fractal analysis to observational data and N-body simulations of non-linear gravitational clustering.

More in detail, this Thesis is organized as follows.

In Chapter 1 we give a "by eye" description of the large-scale galaxy distribution, as obtainable from the available data sets. The presentation of a series of plots of galaxy and cluster samples will contribute to give a more precise idea about the great variety of the large-scale structure. We will also briefly discuss the essential characteristics of currently employed catalogues.

After this qualitative presentation of the large-scale clustering, we introduce in Chapter 2 the more important statistical methods, which are employed to quantify the properties of the galaxy distribution. We also review the results of the application of these methods to the analysis of extended data sets. Other than the classical approach based on correlation functions, we also present the power-spectrum analysis, the topological description of galaxy clustering based on the *genus characteristics*, and the study of mass and luminosity functions for cosmic structures. Technical descriptions about the implementation of such methods are beyond the scope of this Thesis, while emphasis will be given to the discussion of the statistical information provided by the clustering analysis.

Chapter 3 is devoted to a detailed presentation of the concept of fractal structure and to a discussion of its relevance in the general framework of statistical mechanics and, more in particular, to the study of the galaxy distribution. Starting from the observed power-law shape of correlation functions, it has been argued that the galaxy distribution possesses well defined scale-invariant properties. It is clear that using fractal concepts to characterize the large-scale clustering does not imply that it is represented by a self-similar structure extending up to arbitrarily large scales, as some authors have suggested (see, *e.g.*, ref.[87]). Viceversa, methods of fractal analysis are probably best suited to characterizing the presence of scaling and the width of the scale-range where it takes place. After the introduction of the concept of fractal (self-similar) structure, we show that it is characterized by the so-called *fractal dimension.* We present several definitions of fractal dimension, as introduced in the study of non-linear systems and deterministic chaos. The *multifractal* spectrum extends the concept of fractal dimension by providing a hierarchy of scaling indices, which give a complete description of the scaling properties of a self-similar structure. In order to evaluate the fractal dimension for a point distribution, we introduce a list of algorithms, which are based on different definitions of dimension and rely on different approximations to its "true" value.

These methods have already been proved to be quite reliable when applied to very rich self-similar point distributions. However, the rather limited amount of data provided by galaxy samples and the presence of characteristic scales in the large-scale clustering could seriously affect their answers. Therefore, in view of the application of these methods to the study of galaxy clustering, we make a close check of their reliability. We apply them to the analysis of point distributions with *a priori* known scaling properties and verify their robustness as a function of the sample richness and of the clustering strength. This represents a necessary step in order to assess the reliability of any fractal measure of the galaxy distribution. Finally, we review the results obtained up to now from the fractal interpretation of the large-scale structure.

Chapter 4 is devoted to the discussion of the dynamics of structure formation in the framework of the gravitational instability picture. After writing the equations for the evolution of density inhomogeneities, we give their solution in the simple linear regime and also describe some approximations used to treat the non-linear stage of the gravitational clustering. We also discuss the origin of primordial fluctuations, in relation with the matter content of the Universe. Both baryonic and the two popular non-baryonic models, based on hot and cold dark matter, are described, while the effect of taking non-Gaussian initial conditions is also considered. In the framework of *biassed* models of galaxy formation, we discuss the motivations which support the idea that galaxies and galaxy systems are more clustered than the underlying dark matter. After describing suitable physical mechanisms which are able to provide a segregation between dark and luminous matter, we give some prescriptions to relate the statistics of the galaxy distribution to that of the density field.

In order to provide a comprehensive treatment of gravitational clustering in the strongly non-liner regime, we resort in Chapter 5 to the analysis of numerical N-body simulations. The purpose of this analysis is to verify the existing connections between scale-invariant clustering and non-linear gravitational dynamics. After an introductory description of cosmological N-body codes, we apply both the classical correlation analysis and the fractal approach, starting from different initial fluctuation spectra. As for correlation functions, they are analyzed up to the fourth order. We find that the hierarchical expression for higher-order functions are naturally produced by non-linear clustering. In terms of fractal analysis, it turns out that self-similarity is always associated with non-linear gravitational dynamics. The application of several fractal dimension estimators points toward a multifractality of the small-scale clustering, with a dimension $D \simeq 1$ which always characterizes the distribution inside the overdense, virialized structures. This represents a robust outcome of our analysis, quite independent of the initial conditions and supports the idea that a $D \simeq 1$ fractal dimension is a sort of attracting solution of the non-linear gravitational dynamics.

In order to check whether such scaling behaviours can be extended to larger scales, we analyze in Chapter 6 the Plionis *et al.* [300] angular samples of galaxy clusters, which have been selected as those peaks of the galaxy density field of the Lick map which exceed fixed threshold values. This objective cluster identification algorithm allows us to compare the clustering properties for galaxy aggregates of different richness. We analyze the 2- and 3-point correlation functions for these samples by applying different methods of analysis and error estimators. We find that there is a well defined trend for the clustering amplitude to increase with the cluster richness. The 2-point function turns out to depend on the density threshold consistently with the predictions of biassing. Higher signals for the 3-point functions are detected for richer systems, as the effect of non-Gaussian statistics introduced by the cluster selection criteria. The application of the fractal analysis to these samples shows that a remarkable scale-invariance characterizes the non-linear clustering of the highest selected peaks of the galaxy density field. Also in this case, the resulting multifractal spectrum has a characteristic dimension $D \simeq 1$ corresponding to the more dense parts of the distribution. A breaking of the scale-invariance occurs around a physical scale $\sim 20h^{-1}$ Mpc, which is remarkably similar to the cluster correlation length (*i.e*, the scale at which the cluster correlation function attains unity value). We also make simulations of projection effects on a three-dimensional fractal structure and find that the presence of a characteristic scale should be inherent also to the three-dimensional cluster distribution.

In order to unify the statistical descriptions provided by correlation functions and fractal dimensions, we analytically investigate in Chapter 7 the small-scale fractal properties implied by a list of non-Gaussian hierarchical random fields, which have been introduced in the literature to account for the small-scale galaxy clustering. We show that monofractality inside the overclustered structures is implied in a straightforward way by assuming hierarchical correlation functions, independently of the model details. A much better discriminant is the dimensionality for the distribution inside the underdense regions. A comparison with the multifractal behaviour displayed by N-body simulations shows that all the hierarchical models are excellent in accounting for the statistics inside virialized structures. Although some models are ruled out, nevertheless incompleteness in the sampling of the underdensities makes it difficult to discriminate the best suited model to describe non-linear gravitational clustering. This shows how crucial a proper investigation of the devoid regions of the galaxy distribution could be.

At the end of this Thesis we summarize and discuss the more relevant results and indicate some possible research lines for future investigations.

Chapter 1

Observations of large scale structure

In this Chapter we describe the visual appearance of the large-scale structure of the Universe, as emerging from the available data sets. First of all, we give a qualitative description of the global texture of the galaxy distribution, showing how recent improvements of data sets enlarged our view of the large-scale clustering. After that, we describe the more important catalogues of galaxies and galaxy clusters, that are used to trace the large-scale structure of the Universe. The non-trivial emerging picture of the galaxy clustering can not be satisfactorily accounted for just by a crude photograph of the galaxy distribution, but requires a quantitative statistical analysis, that will be described in much more detail in following chapters.

1.1 An "eye ball " description of galaxy clustering

Starting from the first investigation of the galaxy distribution in the sky, it has been recognized that galaxies in our neighborhood are distributed in a very inhomogeneous way, while only considering sufficiently large patches of the Universe the homogeneity expected on the ground of the Cosmological Principle seems to be attained. A first pioneering attempt to realize a systematic survey of galaxies was realized by Shapley & Ames already in 1932 [351]. They included in their catalogue the galaxies brighter than the 13th photographic magnitude. The first visual impression, which this catalogue provided, was that of a Universe in which galaxies are not randomly distributed on the sky, but tend to be clumped to form large structures. After that, more deep and detailed surveys confirmed and strengthened this kind of picture. The Zwicky catalogue [402], that reach the apparent magnitude $m = 15.5$, showed the presence of cluster of galaxies containing up to 1000 objects and more, superclusters and filaments, with characteristic sizes of several tens of Mpc. We show in Figure 1.1a, b the distribution of galaxies on portions of the sky surveyed by the Zwicky sample. Some

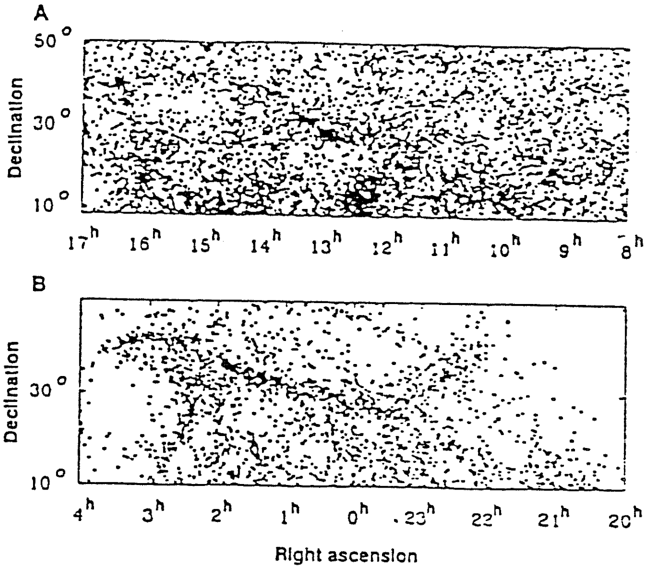

Figure 1.1: *Position of galaxies in the Zwicky catalogue, with* $m \leq 15.5$ *in the northern galactic cap (panel a) and in the southern galactic cap (panel b). The coordinates are cartesian.*

known structures clearly emerge; the Coma cluster is the dense concentration at $\alpha = 13^h$ and $\delta = 28°$, while the Virgo cluster is centered at $\alpha = 12.5^h$ and $\delta = 12^\circ\!.5$. A decrease in the galaxy density west of 9^h and east of 16^h is due to galaxy obscuration. In the southern hemisphere the most relevant structure is the Pisces-Perseus chain which runs across the sky in the declination interval 30°-40°. Again, the apparent absence of galaxies at 21^h and 3^h is due to galactic absorption.

A great step forward in the description of the large-scale distribution of galaxies has been subsequently realized with the compilation of the Lick map by Shane & Wirtanen [348]. This sample, that goes even deeper than the Zwicky compilation, is complete down the magnitude $m = 18$ and includes roughly one million galaxies, for which the count in cells of 10×10 arcmin are given, instead of the position of each object. Despite the great depth reached by the Lick map, that would be expected to wash out many details of the galaxy clustering, a great variety of structures still appears. Although the Lick map surely provided for a long time a fundamental basis for many studies of large-scale structure, in recent years our knowledge of the galaxy distribution on the sky has reached a much greater depth, thanks to recently compiled angular samples, such as the APM sample [246] (see Figure 1.2) and the Edinburgh/Durham Southern Galaxy Catalogue [192].

Although such enormous angular samples provide a great amount of information about the large-scale distribution of galaxies, nevertheless the availability of complete redshift surveys led to a dramatic change in our view of the geometry of the galaxy clustering pattern. It is however clear that measuring redshifts and, thus, distances of galaxies, is a much harder task than only measuring angular positions on the sky. For this reason, three-dimensional galaxy samples include nowadays only a small fraction of all the galaxies listed in the angular

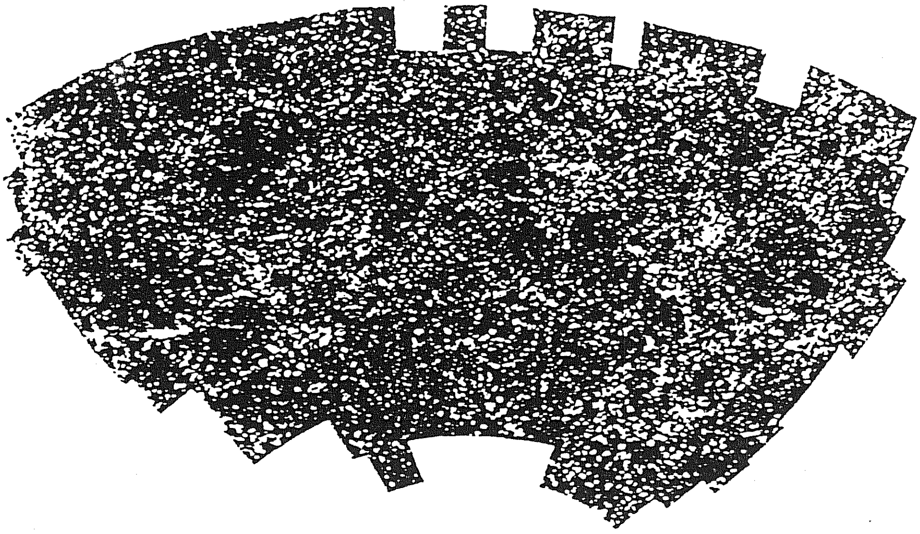

Figure 1.2: *Equal-area projection of the APM galaxy distribution, centred on the southern galactic pole. Nearly two million galaxies are reported, with apparent magnitude in J-band* $-17 \leq m \leq -20.5$ *(after [246]).*

surveys, although continuous efforts are devoted to enlarge and improve our three-dimensional view of the Universe. Because of the intrinsic difficulty of having redshift samples with the same depth and sky coverage as angular ones, three-dimensional surveys are usually realized by restricting the attention on particularly interesting regions of the sky.

Kirshner *et al.* [221], in their redshift survey of the Bōotes region, revealed the presence of a big underdense structure, where the density of bright galaxies is $\lesssim 20\%$ of the mean, and which has a diameter of $\sim 60\,h^{-1}$ Mpc (Figure 1.3). Another example of a redshift survey devoted to the investigation of a single structure is that realized by Haynes and Giovanelli [188], in order to properly study the spatial structure of the Perseus-Pisces region. In this redshift survey, the authors have shown that many of the galaxies in the region lie in a narrow redshift range around $\sim 50\,h^{-1}$ Mpc. Then, as well as in the angular projection, the Perseus-Pisces filaments turns out to be a thin structure in the redshift direction too.

More extended surveys reveal an even greater variety of structure in the three-dimensional pictures of the Universe. In Figure 1.4, surfaces of constant densities from the first Center for Astrophysics (CfA) catalog are shown [140]. The contours correspond to 4 times the mean density. This picture indicates that 90% of all galaxies are in clusters or strings, while the volume occupied by these structures is 10% of the total sampled volume. Then, 90% of the Universe seems to be empty, in the sense that these regions do not contain appreciable quantities of luminous matter. Instead of investigating the details of the galaxy distribution in a specific region, the CfA survey [108, 199] is an attempt to map the general galaxy distribution, rather than to explore a particular feature on the sky. When this survey will be completed, it will represent the three-dimensional version of the Zwicky map. Partial results of such an investigation are shown in Figures 1.5b, c, d, where the wedge diagrams of

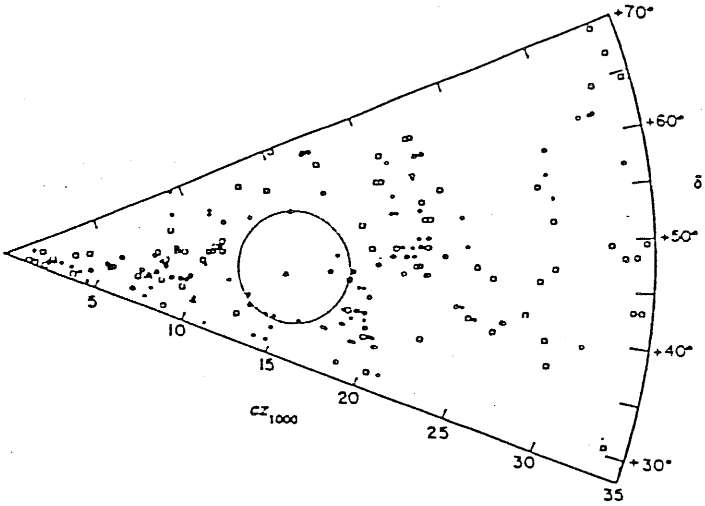

Figure 1.3: *Cone diagram for the Boötes survey. The circle shows the location of the void; the galaxies within the circle are outside the right ascension range of the void (after [221]).*

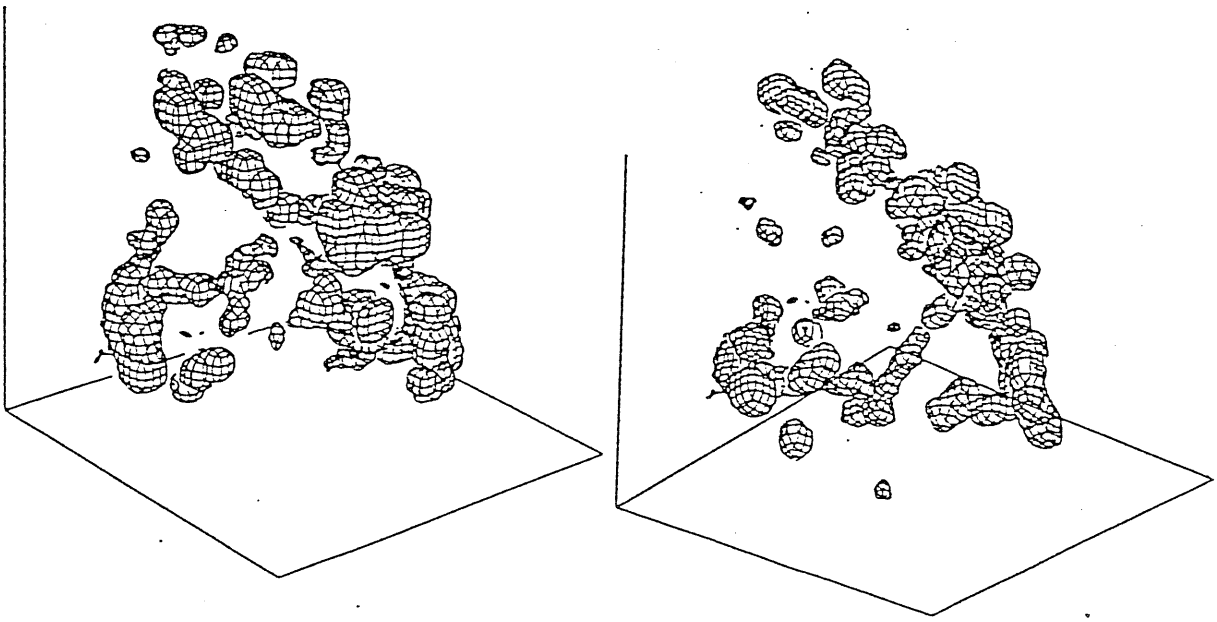

Figure 1.4: *Surfaces of constant density from the CfA catalogue. The northern hemisphere map contains 1130 galaxies (after [140]).*

declination slices of the sky are plotted. One of the most relevant features is the presence of several large regions that appear to be almost devoid of galaxies, while galaxies seem to be distributed in elongated structures. De Lapparent *et al.* [108] suggested that "the apparent filament is a cut through boundaries of several bubble-like structures". The pronounced radial "finger" along the line of sight in Figures 1.5*b*, c is the Coma cluster. If we could map the actual position of galaxies rather than their redshifts, this feature would be approximately spherically symmetric, with a radius $\sim 1\,h^{-1}$ Mpc. The elongation in redshift space occurs because of peculiar velocities of galaxies inside the cluster, that affect the determination of the distance, if simply based on the Hubble relation. Although gravitationally bound systems produce local peculiar motions on scales of few Mpc, the removal of such effects is not expected to change the global picture very much on scales of tens of Mpcs. The slice of Figure 1.5*b* could suggest that filamentary structures in this region are cuts through two-dimensional sheets, not one dimensional filaments. Indeed in contrast to Figure 1.5*a*, that samples the apparent filaments of Figure 1.1*a*, there are no detected filaments on the sky in the region covered by Figure 1.5*b*. Thus, being difficult to expect that the intersection of a slice with a three-dimensional network of filaments give rise in turn to a network of filaments, a sheet-like distribution of galaxies around the voids could better account for the data.

Despite the great number of observations devoted to enlarging the sampled volume by means of three-dimensional surveys, there is up to now no striking evidence for an upper limit to the scale of structure discernible in the redshift analysis. Indeed, the existence of coherent structures involving scales comparable with the size of the sample itself is apparent. The most relevant of such structures is the so-called *Great Wall* revealed by the slices of the extended CfA sample [155]. The apparent extension of the *Great Wall* in both right ascension and declination is only limited by the extension of the survey. The detected spatial extent in these two dimensions is $\sim 60\,h^{-1}$ Mpc $\times$ $170\,h^{-1}$ Mpc. The typical thickness, approximately along the redshift direction, is $\lesssim 5\,h^{-1}$ Mpc. The density contrast between the wall and the mean of the survey is $\Delta\rho/\rho \simeq 5$. The 360° view of Figure 1.6 indicates the geometrical relation between the Perseus-Pisces chain and the Great Wall.

Quite differently from the optical samples, the recent availability of galaxy catalogues selected in the infrared band by IRAS (Infrared Astronomical Satellite) opens the possibility of having extended nearly all-sky redshift surveys, due to the limited absorbtion of the Galactic plane in the infrared. One of these, the QDOT (Queen Mary and Westfield-Durham-Oxford-Toronto) redshift survey [336] has been realized by measuring the redshifts of 1-on-6 randomly selected IRAS galaxies, thus containing 2163 objects and reaching a depth of $\sim 140h^{-1}$ Mpc (see Figure 1.7). Although infrared selected galaxies are found to avoid rich clusters with respect to optical ones, so that they are more uniformly distributed, nevertheless the availability of such a redshift sample permits one to identify low-density, but very large, structures [336].

Due to the already mentioned problems in measuring a large number of redshifts,

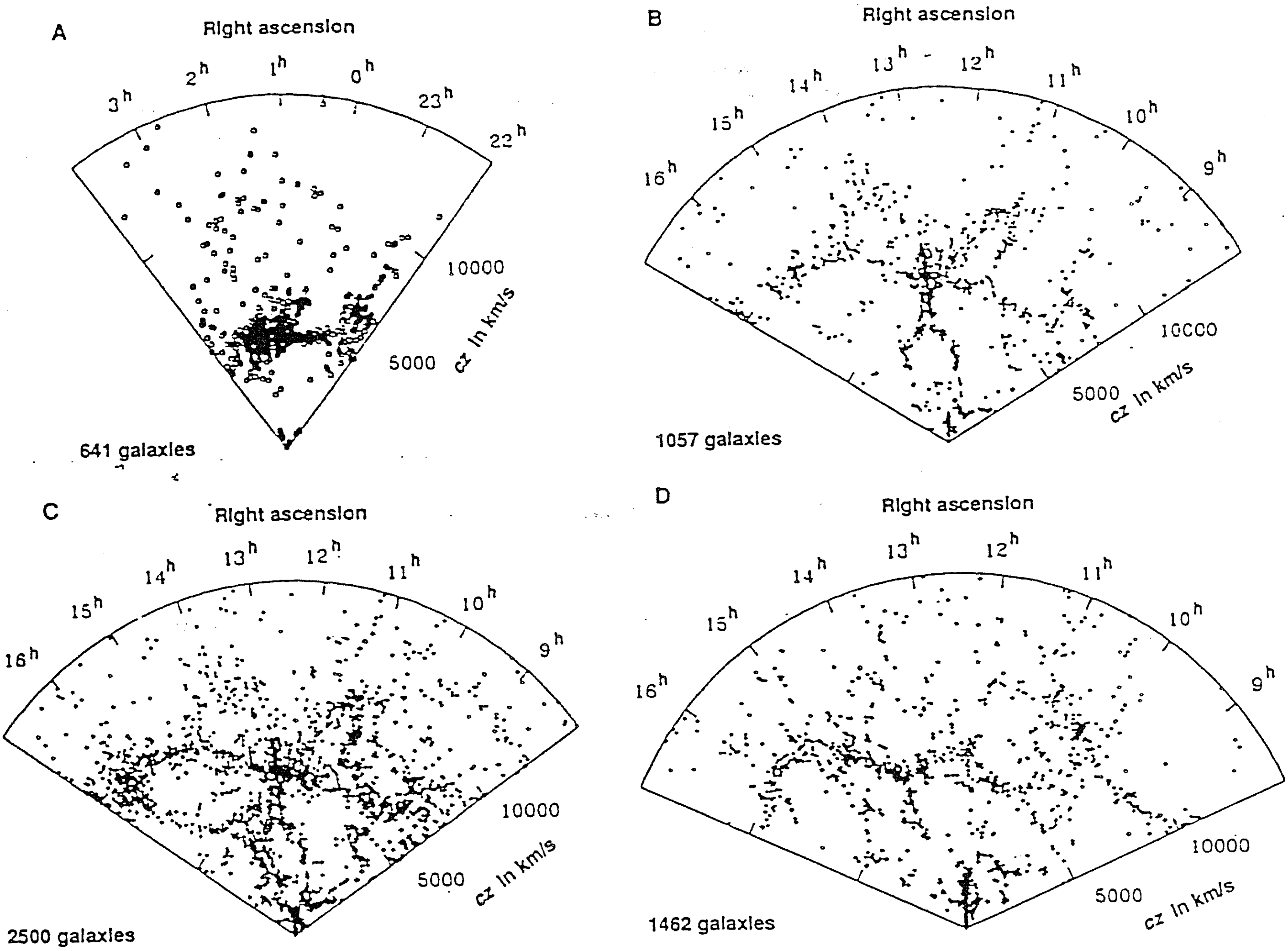

Figure 1.5: *(a) Cone diagram for galaxies in the region of the Perseus-Pisces chain. (b) Cone diagram for a complete sample of galaxies with* $m \leq 15.5$ *in the declination range* $26^\circ\!.5 \leq \delta \leq 32^\circ\!.5$. *(c) Cone diagram for a complete sample covering the declination range* $26^\circ\!.5 \leq \delta \leq 44^\circ\!.5$. *Note the "Great Wall" that runs across the survey. (d) Cone diagram for a nearly complete sample covering the declination range* $8^\circ\!.5 \leq \delta \leq 14^\circ\!.5$ *(after [155]).*

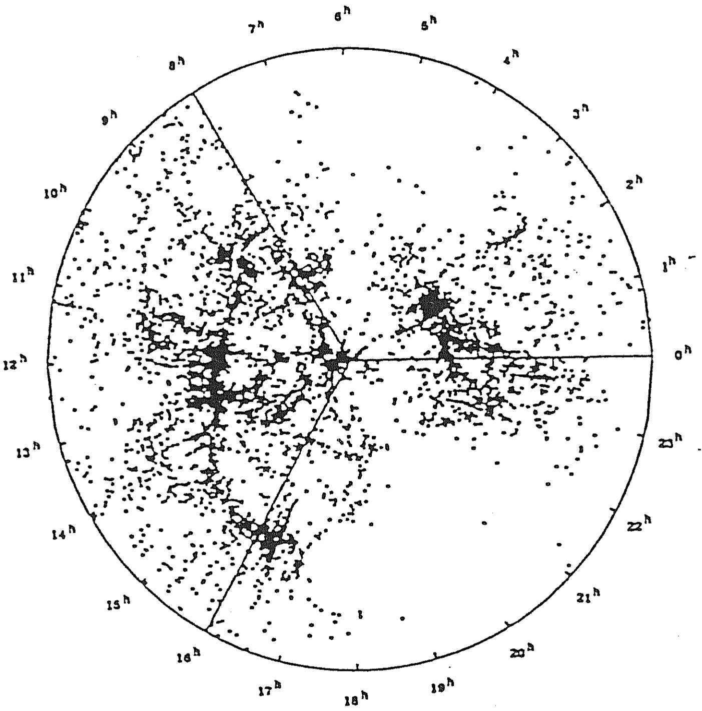

Figure 1.6: *A 360° view that shows a relation between the "Great Wall" and the Perseus–Pisces chain. The slice covers the declination region $20^\circ \leq \delta < 40^\circ$ and contains all the 6112 galaxies with detected redshift $cz \leq 15,000\, km\, s^{-1}$. The regions that appear to be almost devoid of galaxies are obscured by the galactic plane (after [155]).*

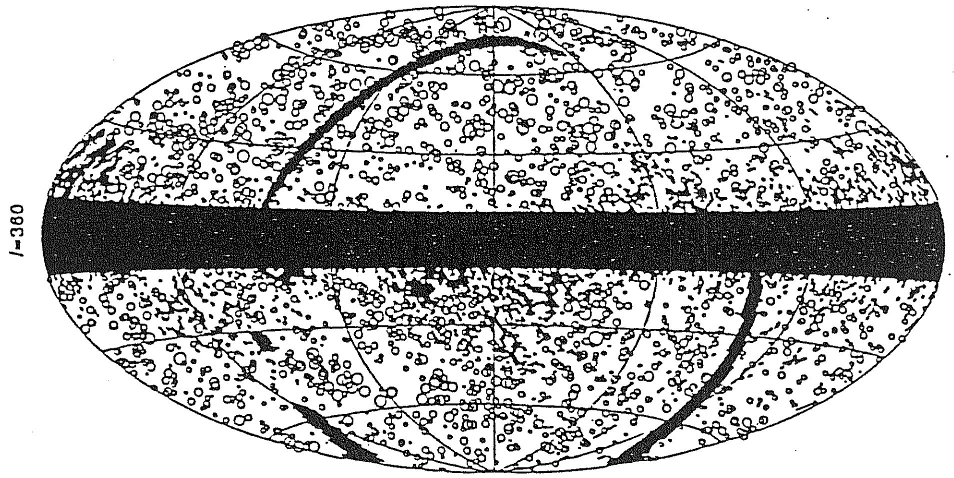

Figure 1.7: *Sky distribution of galaxies of the QDOT survey. Also shown are the areas not included in the survey owing to incomplete satellite coverage, source confusion or redshift incompleteness (after [336]).*

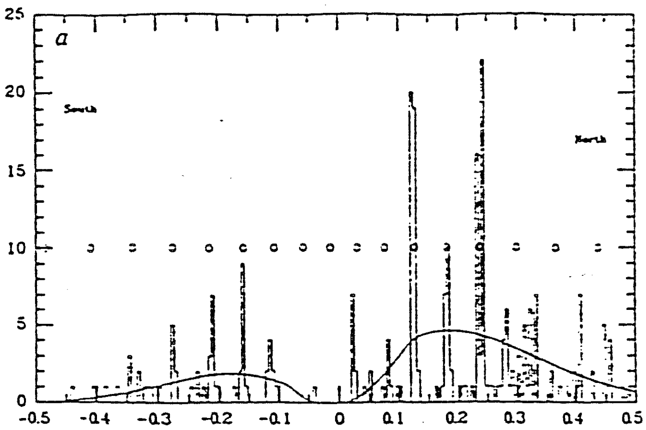

Figure 1.8: *Redshift distribution for the four pencil-beam surveys at the galactic poles. Circles indicate a best-fit constant comoving separation of* $128\,h^{-1}$ Mpc *(after [62]).*

an alternative way to have hints about the spatial distribution of galaxies is to realize the so-called pencil-beam survey: instead of considering a quite large patch of the sky, with a rather limited depth, a different strategy is to realize very deep, but very narrow, surveys so to include a not exceedingly large number of galaxies. Adopting this kind of approach, significant results about the galaxy redshift distribution have been obtained by Broadhurst *et al.* [62], that combined data coming from four distinct surveys at the north and south Galactic poles to produce a well sampled distribution of galaxies by redshift on a linear scale extending to $2{,}000h^{-1}$ Mpc. By analysing their pencil-beam survey, they found a remarkably regular redshift distribution with most galaxies lying in discrete peaks, having a well defined periodicity over a scale of $\sim 128\,h^{-1}$ Mpc (Figure 1.8). A comparison with the CfA galaxy distribution shows that the first peak occurs just in correspondence of the Great Wall, while a recent analysis of the spatial distribution of southern clusters selected from the Edinburgh-Durham Galaxy Catalogue [180] indicates a correspondence between the maxima of cluster density and the first peaks detected by Broadhurst *at al.*. The detection of such peaks in the galaxy distribution, at least in one direction, lead some authors to model the large scale structure of the Universe by means of suitable cellular structures, such as provided by the Voronoi tessellation [83, 201, 376]. In this picture, the cross section of a pencil-beam with the three-dimensional cellular pattern could generate one-dimensional redshift distributions which strongly depend on the direction of the beam itself. By studying the power-spectrum of a three-dimensional Gaussian random field, Kaiser & Peakock [217] claimed that the periodicity at the scale of $128h^{-1}$ Mpc does not necessarily imply the presence of an excess of power at this scale in the three-dimensional structure.

Although galaxies can safely be used to trace the large-scale structure of the Universe, the statistics of their distribution becomes nearly Poissonian above 30-40h^{-1} Mpc, so that it becomes rather difficult to reveal the details of the clustering. At greater scales it has been observed that galaxy clusters can be much more efficient structure tracers (see, *e.g.*, the review by Bahcall [16]). In fact, the enhanced clustering of rich galaxy systems with respect

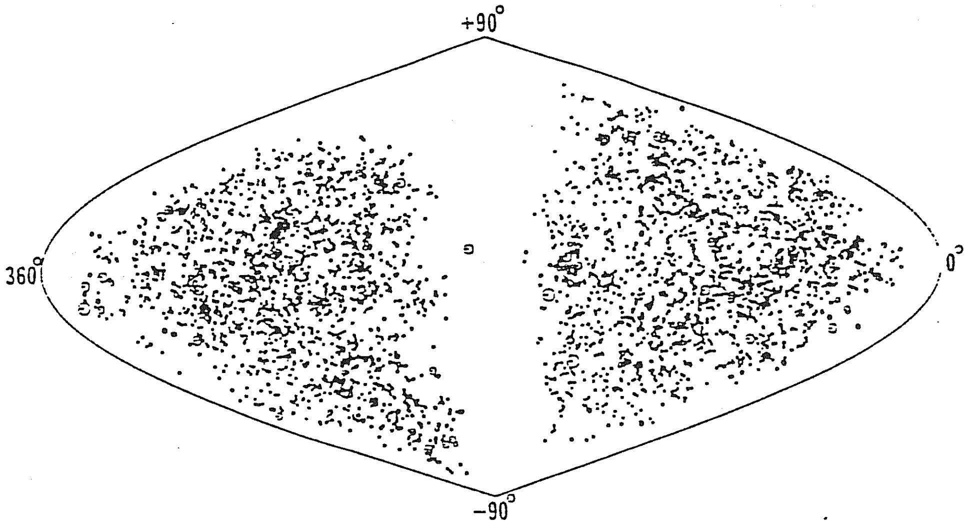

Figure 1.9: *All-sky distribution in supergalactic coordinates of the 4073 Abell clusters contained in the Abell and ACO samples. The symbol size has been scaled by distance class: the $D = 0$ clusters are represented by large open circles, while $D = 7$ clusters corresponds to small dots (after [5]).*

to the clustering of galaxies [18] makes it possible to reveal structures, which are otherwise only detectable on the ground of the observed galaxy distribution. To this purpose, many attempts have been devoted to compile homogeneous samples of galaxy clusters. The most famous of these samples is probably the Abell catalogue [3], selected already in 1958 from the Palomar Survey Plates, that includes visually selected clusters lying north of declination $\delta = -27°$. More recently, the extension of this sample to the southern sky led to the compilation of the ACO cluster sample [5], that used the same selection criteria as Abell's, so to give a consistent whole sky coverage of the cluster distribution (see Figure 1.9). Based on the these samples, many features have been observed in the distribution of rich galaxy clusters, indicating the presence of relevant structures up to scales of $\sim 300h^{-1}$ Mpc. For instance, Tully [372] detected the presence of structures of this size lying in the plane of the Local Supercluster. Another relevant structure is the Shapley concentration [350], that is a remarkable overdensity in the cluster distribution lying $\sim 20°$ away from the direction of the cosmic microwave background (CMB) dipole ($l \simeq 256°$, $b \simeq 48°$; see ref. [357]) and at a distance of $\sim 140h^{-1}$ Mpc.

Several investigations have shown the great dynamical relevance of this cluster concentration to determine the motion inferred from the CMB dipole [337, 312] and the optical dipole of the cluster distribution [302, 338]. Thanks to the recent availability of sufficiently large redshift data for galaxy clusters [308], more and more efforts are nowadays produced to give a detailed description of the clustering and the geometry of the cluster distribution [370, 304, 69].

From the above description of the large-scale texture of the Universe the great complexity and the variety of observed structures is apparent. Galaxies, instead of being uniformly distributed, are arranged to form filaments of some tens of Mpcs and rich clusters, while leaving nearly devoid regions of sizes up to $\sim 50h^{-1}$ Mpc. In turn, clusters are themselves non-trivially clustered, but give rise to huge concentrations and, thus, to structures of even higher hierarchy, such as superclusters. The appearance of this complexity makes it clear that any comparison with dynamical models should pass through two fundamental steps. Firstly, compiling homogeneous samples of galaxies and galaxy clusters as extended as possible, both in two- and, even better, in three-dimensions. Secondly, realizing detailed statistical analyses of observational data, that were able to quantify both the global geometrical properties and the details of the clustering of the distribution of cosmic structures. In the following of this Chapter we will describe in some details the more important data sets, while the next Chapter will be devoted to a review of several statistical analyses of the large-scale distribution of galaxies and galaxy clusters.

1.2 Galaxy samples

The statistical investigation of the distribution of galaxies has been initially realized by means of bidimensional homogeneous samples, in which angular positions of the objects on the sky are reported. An angular sample contains all the galaxies that satisfy a given selection criterion. Since galaxy distances are not known a priori, selection criteria are based on "apparent" properties of these objects.

A first criterion is based on the apparent luminosity. Samples, whose compilation is based on it, include all the galaxies in a given region of the sky, which have observed luminosities exceeding a fixed value. For historical reasons, apparent luminosities are expressed in logarithmic units, by means of the apparent magnitude

$$m \;=\; \mathrm{M} + 5\log d + 25\,. \tag{1.1}$$

Here d represents the distance, expressed in Mpc, of the object from the observer, while M is the *absolute* magnitude (*i.e.*, the apparent magnitude of the same object, if placed at the fixed distance $d = 10\,pc$).

Once a limiting apparent magnitude is chosen, an important related quantity that characterizes a galaxy sample is the *depth* of the survey. Galaxies selected by apparent magnitude are found to have fairly definite absolute magnitudes, M^*, with a standard deviation around this value of about one magnitude. Thus, according to eq. (1.1), M^* and m define a characteristic distance

$$D \;=\; 10^{0.2(m-\mathrm{M}^*)-5}\,\mathrm{Mpc}\,, \tag{1.2}$$

that defines the depth of the sample.

With the recent availability of satellites to realize complete surveys of the galaxy distribution, the possibility to select object in bands that are different from the optical one has also been opened, as traditionally done by ground-based telescopes. However, since galaxies of different morphology are characterized by having largely different luminosity at different frequencies, it turns out that catalogues compiled in different bands do not sample in the same way galaxy populations having different morphology. The classical example is represented by the IRAS survey (see below), which select objects according to their observed flux in the infrared band. Since early-type galaxies have on average a greater infrared emissivity, this sample preferentially selects spirals instead of ellipticals.

A further problem arising in the comparison of different samples is due to the fact that galaxies are selected not always according to their apparent magnitude, but also according to other intrinsic properties, such as the angular diameter (diameter limited samples). Accordingly, a different definition of depth of the sample is given, reflecting the relation between distance and apparent size. Note that using angular sizes instead of apparent magnitudes causes some bias in the completeness of the sample. For instance, spiral and irregular galaxies are known to have a lower surface brightness, with respect to ellipticals and spheroidals [159, 94]. This causes them to be more preferentially included in diameter-limited samples than in magnitude-limited samples.

For the above reasons, particular care must be payed when one is comparing the results of statistical analyses made from galaxy catalogues, compiled by using different selection criteria. In the following, we give a list of the most important angular galaxy samples, that are used to trace the large-scale structure of the Universe.

i) **The Zwicky sample** [402], that is based on the Palomar Observatory Sky Survey (POSS). This sample contains the angular positions of 3753 galaxies, having apparent magnitudes $m \leq 15.5$ and coordinates with *declination* $\delta \geq 0$ and *galactic latitude* $b \geq +40^\circ$ (see Figure 1.1).

ii) **The Lick sample** [348], that includes galaxies with apparent magnitudes $m \leq 18$, each belonging to an elementary cell of $10' \times 10'$. In turn, these cells are grouped in sets of 36×36 to form maps, that have an extension of $6^\circ \times 6^\circ$. The centers of each map are separated one from each other by 5° in declination, from $\delta = -20^\circ$ up to $\delta = +90^\circ$. In addition, the separation in right ascension is such that each map is overlapped to adjacent one at most for 1°.

iii) **The Uppsala General Catalogue (UGC)** [269], that is based on the POSS plates and contains all the galaxies in the northern hemisphere ($\delta \geq -2^\circ 20'$), having apparent diameter $\geq 1\overset{'}{.}0$. In addition, it also includes all the galaxies of the Zwicky sample brighter than $m = 14.5$, even if their diameter is smaller than $1\overset{'}{.}0$. Informations are also listed about major and minor photometric axes, morphology, colour index and radial velocity, when available.

iv) **The Jagellonian field** [325], that includes more than 10,000 galaxies comprised in a small angular region of $6^\circ \times 6^\circ$. This sample turns out to be almost 8 times deeper than the Zwicky sample in such a way that, even though the angular extension of the latter is ~ 10 times larger, the *spatial* dimension of the two sampled regions are almost the same.

v) **The ESO/Uppsala Catalogue** [230], which is based on the *ESO Quick Blue Atlas.* This sample is considered complete for those galaxies of the southern hemisphere having declination $\delta < -17\overset{\circ}{.}5$ and major diameters greater than $1'$. As for the UGC, it also contains additional informations, such as photometric axes, position angles, morphological types, other than colour indices and radial velocities, when available.

vi) **The APM Galaxy Survey** [246], that has been realized by using the Automate Plate Measuring (APM) machine for an automatic scan of $5\overset{\circ}{.}8 \times 5\overset{\circ}{.}8$ for each of the 185 plates of the UK Schmidt J Survey. The plates cover an area of 4,300 square degrees in the region $\delta < -20°$ and $b \lesssim 40°$. It includes around 2 millions galaxies brighter than $m = 20.5$ and is considered 95% complete in the range $17 < m < 20.5$. Adjacent plate centers are separated by 5°, so that the resulting overlap can be used to check for the presence of systematic errors (see Figure 1.2).

vii) **The Edinburgh/Durham Southern Galaxy Catalogue** [192], that has been realized by scanning with the Edinburgh plate measuring machine (COSMOS) 60 plates of the UK Schmidt J Survey. The plates are located around the south galactic pole. The sample reaches a limiting magnitude $m \simeq 20$ and contains some 10^6 galaxies. The scanning of $5\overset{\circ}{.}3 \times 5\overset{\circ}{.}3$ ensures some overlapping between adjacent plates to correct for systematics. The sample is considered to be a 95 per cent complete, with $< 10\%$ stellar contamination.

Other than the above angular samples, there exist also some *redshift* samples, that, in addition to the angular coordinates, give also the redshift for each object . Although the redshift data can be translated into distance data according to the Hubble law, nevertheless galaxy peculiar motions can affect to some extent the three-dimensional picture of the galaxy clustering, producing elongation of the clustering along the line-of-sight (see,*e.g.*, ref.[375]). As discussed in the previous section, the effect is expected to be more important at small scales, where a weakening of the clustering is produced, while it is less important at large scales. In general, redshift samples use angular catalogues as reference databases from which to select galaxies, while some objective criteria is applied to extract those galaxies for which the redshift measure is realized. In the following we will describe the most relevant galaxy redshift samples.

i) **The CfA1 (Center for Astrophysics) survey** [197], that select galaxies from the Zwicky and UGC samples. This survey includes all the 2400 galaxies having magnitudes $m \leq 14.5$ and angular positions characterized by ($\delta > 0°$, $b > +40°$) and by ($\delta \geq$

$-2^{\circ}.5$, $b < -30^{\circ}$). For each galaxy, equatorial coordinates, heliocentric velocity and apparent magnitude are given.

ii) **The Southern Sky Redshift Survey (SSRS)** [94], that includes galaxies selected from the ESO/Uppsala catalogue. The survey lists 1657 galaxies, selected from the ESO Catalogue [230], in an area of 1.75 steradians, with declination south of $-17^{\circ}.5$ and galactic latitude below -30°. The sample diameter is limited with all galaxies having $\log D > 0.1$, where D is a "face-on" diameter, in arcminutes, that is related to the galaxy morphological type and to the angular dimension. According to the angular sample, which is used as the source, SSRS also provides morphological types and diameters. The depth of the sample is estimated to be $120h^{-1}$ Mpc.

iii) **The Perseus-Pisces survey** [154], that has been realized with the aim of studying the spatial galaxy distribution inside the Perseus-Pisces supercluster. It includes about 4700 galaxies with equatorial coordinates ($22^h \leq \alpha \leq 4^h$, $0^{\circ} \leq \delta \leq 45^{\circ}$). The completeness magnitude is $m = 15.5$ and diameter $1'.0$. Morphology and diameter information is also provided.

iv) **The CfA2 survey** that is slowly emerging and that, when completed, should represent the extension of the CfA1 survey to the apparent magnitude $m = 15.5$. The already published data are organized in declination slices, that are 6° thick. A first slice, that contains 1057 objects in the declination range $26^{\circ}.5 \leq \delta \leq 32^{\circ}.5$ (Figure 1.5*b*), was completed in 1986 [108], while the data have been subsequently published [199]. Two other complete slices [155] contain 1443 galaxies in the declination range $32^{\circ}.5 \leq \delta \leq 44^{\circ}.5$ (Figure 1.5*c*). Nowadays, the survey should be complete in eleven slices, six in the north and 5 in the south. The CfA2 North covers the portion of the sky $8^h < \alpha < 17^h$, $20^{\circ}.5 < \delta < 44^{\circ}.5$ and $8^{\circ}.5 < \delta < 14^{\circ}.5$, and includes 5248 galaxies. The CfA South covers $20^h < \alpha < 4^h$, $6^{\circ} < \delta < 42^{\circ}$ and includes 3045 galaxies [384].

v) **The QDOT IRAS redshift survey** [336], which contains 2163 randomly selected IRAS galaxies with measured redshifts, with a 1-to-6 sampling rate. All the included objects have a flux greater than 0. 6 Jy and the sample covers nearly all the sky at galactic latitudes $|b| > 10^{\circ}$. The overall completeness after excluding galactic sources is estimated to be 98%.

vi) **The Strauss et al. IRAS redshift survey** [358], which also selects galaxies from the IRAS Point Source Catalogue. The sample includes 2649 galaxies flux limited at 60 μm and covers 11 steradians of the sky, thus providing excellent coverage. The sampling rate is here 1-to-1, but at the expenses of reduced depth.

vii) **The Stromlo-APM redshift survey** [238], that is presented to be essentially complete to the limiting magnitude $m = 17.15$ and contains 1769 galaxies randomly selected at a rate of 1 in 20 from the APM catalogue. The extension of this survey is ~ 30 times that of the CfA1 survey, so that it is particularly suitable to the determination of the mean galaxy density.

1.3 Cluster samples

As already shown in the previous Section, galaxies do not represent the only class of cosmic structures that can be used to investigate the large scale structure of the Universe. In fact, galaxies themselves tend to group together to form structures on larger scales, such as groups or clusters. In turn, such structures can be considered as single objects and, then, the statistics of their distribution can be analysed in full analogy with the case of galaxies. The advantage of using clusters mainly resides in the fact that they trace the structures at very large scales, where the galaxy distribution becomes essentially indistinguishable from a Poissonian process.

In order to use galaxy clusters and groups as tracers of the large-scale structure in the Universe, complete samples, that describe their distribution over wide volumes, are required. In general, different samples use different selection criteria for identifying clusters, so that different it can be also their respective distributions. In general, cluster samples can be divided in two main categories: those in which clusters are selected by the visual inspection of the galaxy distribution and those in which they are identified by means of an objective computer algorithm. It is clear that samples of the first type are likely to suffer by human biases, which are quite difficult to account for. On the other hand, even in the case of automatically selected cluster catalogues, some biases could be in any case be present. As an example, if they are selected from an angular galaxy distribution, serious contaminations due to projection effects can be present in any case. It is clear that the best one can hope to do is by using three-dimensional galaxy samples from which to select galaxy systems. However, as we have seen in the previous section, at the present time only relatively small redshift samples are available, so that the cluster catalogues selected from these are also far from being extended and complete samples.

The most important *angular* samples of clusters are described as follows.

i) **The Abell Catalogue** [3] includes a total of 2712 clusters that are the richest, densest clusters selected by visual inspection from the POSS plates (see Figure 1.9). Out of these rich clusters, 1682 constitute Abell's complete statistical sample and are distributed over 4.26 steradians. The Abell selection criteria can be summarized as follows: (*a*) a cluster must contain at least 50 members in the magnitude range m_3 to $m_3 + 2$, where m_3 is the magnitude of the third brightest galaxy; (*b*) all these members should be contained within a circle of radius $1.5h^{-1}$ Mpc around the center of the cluster; (*c*) the cluster redshift z should be in the range $0.02 \lesssim z \lesssim 0.20$; and (*d*) the cluster should lie north of declination $-27°$. The 1682 clusters in the sample are divided in 6 distance classes, D. Each distance class contains clusters lying in a magnitude interval of width $\Delta m = 0.7$, starting from $m = 13.3$; 104 clusters belong to the first 4 distance classes (nearest clusters), while the remaining belong to the subsample $D = 5 + 6$. Also a richness class is assigned to each cluster, with $R = 0$ through 5, that is related to the number of members belonging to each cluster. The corresponding ranges of member counts are 30-49, 50-79, 80-129, 130-199, 200-299, and above 300.

ii) **The Zwicky Catalogue** [402] contains 9700 clusters of galaxies visible to the limit of the Palomar plates ($m \simeq 20$). The criteria for including clusters in the sample are less restrictive than Abell's; (a) The cluster must contain at least 50 galaxies in the magnitude range m_1 to $m_1 + 3$, where m_1 is the magnitude of the brightest galaxy; (b) these galaxies must lie within the isopleth, where the projected density of galaxies is about twice that of the neighboring field; (c) no limits on the redshift are specified, but structures such as the Virgo cluster (which cover very large areas) are not included; and (d) the clusters must lie north of declination $-3°$ and within well specified areas. Cluster richness is defined as the number of galaxies, corrected for the mean field count, that are located within the isopleth of twice the field density. In general, Zwicky clusters differ in size from Abell's, the former being mostly larger, lower density systems. These differences mainly arise because of the different criteria used in the identification process.

iii) **The Schectman Catalogue** [340] identifies 646 clusters of galaxies, based on the Lick counts and using an automated procedure. The clusters are located at galactic latitudes $|b| \geq 40°$ and declinations $\delta > -22\overset{\circ}{.}5$. The selection was based on local density maxima of the galaxy distribution above a given threshold value. A selected threshold of five galaxies per 10×10 arcmin cell was used; this threshold is considerably higher than the tail of the background distribution of galaxy counts, which has a median of 1.3 galaxies per bin. Such a threshold of five galaxies succeeds in detecting 70% of Abell's $D \leq 4$ clusters and 10% of the $D = 5$ clusters. Moreover, the Schectman procedure selects clusters that are considerably poorer than the Abell $R \geq 1$ clusters.

iv) **The ACO Catalogue** [5] is the extension to the southern hemisphere of the Abell sample. It contains 1635 clusters of richness class $R \geq 0$ and includes clusters in the $-27° < \delta < -17°$ overlap region with the Abell clusters. Together with the Abell Catalogue, it constitutes an all-sky sample of 4073 rich Abell clusters (see Figure 1.9), nominally complete to a redshift $z = 2$ for clusters with populations of 30 or more galaxies in the magnitude range m_3 to $m_3 + 2.0$.

iv) **The Edinburgh/Durham Southern Cluster Catalogue (EDSCG)** [244], which select clusters with an overdensity criterion from the Edinburgh/Durham galaxy catalogue. The sample contains 737 clusters and covers an area of $80° \times 20°$, centered at the south galactic pole. The EDSCG is constructed using an automated peak-finding algorithm and is complete to $m_{10} = 18.75$. Cluster selection criteria have been suitably chosen so to reduce projection contamination effects.

As in the case of the galaxy samples, the detection of redshifts for clusters included in angular catalogues permits the compilation of three-dimensional surveys. We describe in the following the most relevant spatial samples of clusters and groups.

i) **The Hoessel, Gunn & Thuan (HGT) sample** [194] includes the redshifts of all the Abell clusters with distance class $D \leq 4$ and richness class $R \geq 1$, which are located at galactic latitude $|b| \geq 30°$. A total amount of 104 clusters belong to this sample.

ii) **The Bahcall & Soneira (BS) sample of superclusters** [19], that is complete to a redshift of $z \leq 0.08$ and defines superclusters as density enhancements of the cluster distribution, as deduced from the HGT sample. The selection process was repeated for different overdensity values f, from $f = 10$ to $f = 400$. In particular, a total of 16 superclusters are listed for $f = 20$, 12 superclusters for $f = 40$ and 11 superclusters for $f = 100$.

iii) **The Struble & Rood (SR) catalogue** [359], that contains all the 588 Abell clusters (including richness class $R = 0$) with measured redshifts.

iv) **Geller & Huchra (GH) deep redshift survey** [154], that consists of the 145 Abell clusters with $R \geq 0$, $D \leq 6$ and with redshift $z \lesssim 0.2$, in the area $10^h < \alpha < 15^h$, $58° < \delta < 78°$.

v) **The Ramella, Geller & Huchra (RGH) group sample** [313], that identifies groups of galaxies in the first two complete strips of the CfA redshift survey [199]. The group catalogue is produced by applying an algorithm which searches for "friends of friends" in redshift space [198]. Galaxies in groups are separated by limiting values of the line-of-sight velocity and of the projected separation. The catalogue contains 128 groups with at least three members and 56 with at least five members.

vi) **The Southern Hemisphere Group (SEG) sample** [95] contains 87 groups with 3 or more members and with a surrounding density contrast greater than 20, identified from the SSRS galaxy catalogue. The groups are located southwards of declination $-17.^\circ5$, below galactic latitude $-30°$ and have mean radial velocities less than 800 km s^{-1}.

vii) **The Postman et al. (PGH) Cluster sample** [308], which is a complete sample of 351 Abell clusters with tenth-ranked galaxy magnitude $m_{10} \leq 16.5$. The survey includes all the clusters lying north of $\delta = -27°30'$, being 15 objects selected from the ACO sample. Today, it represents the largest available complete redshift survey of rich clusters.

viii) **The APM Cluster survey** [96], that contains about 200 clusters with measured redshift $z \lesssim 0.1$, that have been selected from the APM galaxy sample, using an overdensity criterion. The survey covers an area of ~ 4300 square degrees of the southern sky. The resulting spatial density is $2.4 \times 10^{-5}\, h^3 \mathrm{Mpc}^{-3}$, four times that of $R \geq 1$ Abell clusters and twice than that of $R \geq 0$ clusters, thus indicating their lower richness.

ix) **The Edinburgh/Milano Cluster Redshift survey** [268], which contains clusters selected from EDCG. Selection criteria require: at least 22 member galaxies inside a radius $r = 1h^{-1}$ Mpc with magnitude between m_3 and $m_3 + 2$, tenth-ranked galaxy magnitude $m_{10} \leq 18.75$, and equatorial coordinates in the range ($\alpha \geq 21^h 53^m$, $\alpha \leq 3^h 35^m$; $-42°12' \leq \delta \leq -22°53'$). The resulting number of selected clusters is 97.

In the following of this Thesis we will use some angular cluster samples that have been selected by Plionis *et al.* [300] from the Lick map by using several overdensity criteria and that represent an extension of the Schectman catalogue. Also the complete Lick map will be investigated. A detailed presentation of these samples is given in Chapter 6.

Chapter 2

Statistical measures of the Universe

In this Chapter we review the more important statistical measures, that have been used to quantitatively investigate the large-scale distribution of cosmic structures. Other than introducing the basic statistical formalism, we will also describe the results provided by such methods. Firstly, we introduce the approach based on the analysis of correlation functions, that from an "historical" point of view represents the first serious attempt to quantitatively investigate the statistics of the galaxy distribution. Based on the path-integral approach, as developed in the framework of statistical mechanics and quantum field theory, we formally describe the correlation properties for a generic density field. A review of the main results of correlation analysis in clustering studies will be finally given. After that, we discuss the power-spectrum analysis that, although strictly related to correlation functions, recently provided extremely significant results and represents a sort of complementary approach to the correlation one. As a further characterization of the galaxy distribution, we describe some measures of the topology of the density field traced by cosmic structures and show how efficient they are to characterize the geometry of the clustering pattern. A further statistical measure concerns the distribution of the luminosities of galaxies and galaxy systems. Its relevance in connection with the mass spectrum of density fluctuations is outlined and observational results about luminosity and mass functions are discussed.

Further statistical measures of large-scale clustering, such as the fractal analysis and the count-in-cell statistics represent an important part of this Thesis and will be discussed in details in the following chapters. Also more technical and applicative aspects of the correlation analysis are given in the following.

2.1 Correlation functions

The classical correlation analysis of the galaxy distribution, as pioneered by Totsuji & Kihara [367] and extended during the seventies by Peebles and coworkers [291, 285, 173], was based on the determination of the angular 2-point correlation function, $w(\vartheta)$, from projected galaxy samples. Its definition is related to the joint probability

$$\delta^{(2)}P = n^2\,\delta\Omega_1\,\delta\Omega_2\,[1+w(\vartheta_{12})] \tag{2.1}$$

of finding two objects in the solid angles $\delta\Omega_1$ and $\delta\Omega_2$, respectively, at angular separation ϑ_{12}. In eq.(2.1) the factorization of the n^2 term (n being the angular mean galaxy density) makes $w(\vartheta)$ an dimensionless quantity, while the total probability turns out to be normalized to the square of the total number of object in the distribution. According to its definition, the value of the correlation function is a measure of the non-randomness of the distribution. In particular, object positions are said to be correlated if $w(\vartheta) > 0$, anticorrelated if $-1 \leq w(\vartheta) \lesssim 0$, while a Poissonian distribution is characterized by $w(\vartheta) = 0$ at any angular separation. In general, for greater and greater values of $|w(\vartheta)|$, the distribution of galaxies turns out to be less and less random.

In a similar way, the availability of redshift samples make it possible to describe the clustering pattern in terms of the spatial 2-point function, that, in analogy with eq.(2.1), is defined through the joint probability

$$\delta^{(2)}P = n^2\,\delta V_1\,\delta V_2\,[1+\xi(r_{12})] \tag{2.2}$$

of finding an object in the small volume δV_1 and another one in δV_2, at separation r_{12}. In this case too, the spatial 2-point function $\xi(r_{12})$ is a measure of the departure from a Poissonian statistics of the spatial galaxy distribution and, for an isotropic clustering, depends only on the modulus of the separation vector $\mathbf{r}_{12}$.

It is clear that the concept of correlation functions can be extended to higher orders, by considering the joint probabilities between more than two points. In this Section, we will formally introduce the concept of correlations for a generic density field. After that, we will show how the correlation analysis is usually applied to the study of galaxy and cluster distributions and which are the main results it has provided in the last twenty years.

2.1.1 Density field and correlation functions

Let us consider a generic density field that can either represent the matter density field or the galaxy distribution. In the latter case, instead of a continuous distribution, this field is described by a point-like process,

$$\rho(\mathbf{x}) = \sum_i \delta_{\mathrm{D}}^{(3)}(\mathbf{x}-\mathbf{x}_i)\,, \tag{2.3}$$

where $\delta_D^{(3)}$ is the Dirac delta-function in three-dimensions, and the typical galaxy dimension (few tens of kpc) is considered negligible with respect to their mean separation ($\simeq 5h^{-1}$ Mpc). Relative fluctuation amplitudes are then described by means of the field

$$\delta(\mathrm{x}) = \frac{\rho(\mathrm{x}) - \bar{\rho}}{\bar{\rho}}, \tag{2.4}$$

being $\bar{\rho}$ the average density value. From the above definition of the fluctuation field $\delta(\mathrm{x})$, it immediately follows that it must have vanishing mean value, $\langle \delta(\mathrm{x}) \rangle = 0$. The requirement of a positively defined $\rho(\mathrm{x})$ leads to $\delta(\mathrm{x}) > -1$. In the following, we will assume that $\delta(\mathrm{x})$ is described by a random function, so that the Universe can be considered as a particular realization of an ensemble (functional space) $\mathcal{F}$ containing all the $\delta(\mathrm{x})$ fields satisfying the above two requirements.

In order to describe the statistics of the $\delta(\mathrm{x})$ field, let $\mathcal{P}[\delta(\mathrm{x})]$ be the probability that the density fluctuations are described by a given $\delta(\mathrm{x}) \in \mathcal{F}$. With the assumption of statistical homogeneity, the probability functional $\mathcal{P}[\delta(\mathrm{x})]$ turns out to be independent of the position x, while, due to the requirement of isotropic clustering, the joint distribution of $\delta(\mathrm{x}_1)$ and $\delta(\mathrm{x}_2)$ depends only on the the separation $r_{12} = |\mathrm{x}_1 - \mathrm{x}_2|$. By definition, the probability distribution in the functional space must be be normalized so that the total probability is unity, that is

$$\int_{\mathcal{F}} \mathcal{D}[\delta(\mathrm{x})]\, \mathcal{P}[\delta(\mathrm{x})] = 1\,. \tag{2.5}$$

In the above expression $\mathcal{D}[\delta(\mathrm{x})]$ represents a suitable measure introduced in $\mathcal{F}$ in order to define the functional integral.

A complete characterization of the statistics of the density distribution can be given in terms of the n-point correlation functions

$$\mu_n(\mathrm{x}_1, \ldots, \mathrm{x}_n) = \langle \delta(\mathrm{x}_1) \ldots \delta(\mathrm{x}_n) \rangle\,. \tag{2.6}$$

In the above expression, the notation $\langle \cdot \rangle$ indicates the average over the $\mathcal{F}$ space. Under the assumption of *ergodicity* of our system, the averages taken over the (physical) configuration space are completely equivalent to the expectations taken over an ensemble of universes, *i.e.* over the functional space $\mathcal{F}$. From now on we will indifferently use the symbol $\langle \cdot \rangle$ to indicate both kind of average.

The great relevance of correlation functions in statistical mechanics lies in the fact that their knowledge is required in order to uniquely specify the statistics of the distribution. In fact, let us consider the *partition functional*

$$\mathcal{Z}[J(\mathrm{x})] \equiv \int \mathcal{D}[\delta(\mathrm{x})]\, \mathcal{P}[\delta(\mathrm{x})]\, e^{i\int d\mathrm{x}\, \delta(\mathrm{x}) J(\mathrm{x})} = \langle e^{i\int d\mathrm{x}\, \delta(\mathrm{x}) J(\mathrm{x})} \rangle, \tag{2.7}$$

where $J(\mathrm{x})$ is a generic function, that plays the role of an external source perturbing the underlying statistics. According to the definitions (2.7) of $Z[J(\mathrm{x})]$ and (2.2) of n-point correlation function, it turns out that

$$\mu_n(\mathrm{x}_1,\ldots,\mathrm{x}_n) \;=\; i^{-n}\,\frac{\delta^n \mathcal{Z}[J]}{\delta J(\mathrm{x}_1)\ldots\delta J(\mathrm{x}_n)}\bigg|_{J=0}, \tag{2.8}$$

and the McLaurin functional series of the partition function reads

$$\begin{aligned}\mathcal{Z}[J] &= 1+\sum_{n=2}^{\infty}\frac{1}{n!}\int d\mathrm{x}_1\ldots\int d\mathrm{x}_n\,\frac{\delta^n\mathcal{Z}}{\delta J(\mathrm{x}_1)\ldots\delta J(\mathrm{x}_n)}\bigg|_{J=0}J(\mathrm{x}_1)\ldots J(\mathrm{x}_n) = \\ &= 1+\sum_{n=2}^{\infty}\frac{i^n}{n!}\int d\mathrm{x}_1\ldots\int d\mathrm{x}_n\,\mu_n(\mathrm{x}_1,\ldots,\mathrm{x}_n)J(\mathrm{x}_1)\ldots J(\mathrm{x}_n)\,. \end{aligned}\tag{2.9}$$

Thus, $\mathcal{Z}[J]$ is defined as the generating functional of the correlation functions, in the sense that such functions can be defined as the coefficients of the McLaurin expansion of $\mathcal{Z}[J]$ itself [note that in eq. (2.9) the sum runs from $n=2$ because of the vanishing of $\langle\,\delta(\mathrm{x})\,\rangle$].

It is also convenient to introduce the so-called *connected* or *irreducible* correlation functions, $\kappa_n(\mathrm{x}_1,\ldots,\mathrm{x}_n)$, through their generating functional

$$\mathcal{W}[J(\mathrm{x})] \;\equiv\; \ln\mathcal{Z}[J(\mathrm{x})]\,, \tag{2.10}$$

so that

$$\kappa_n(\mathrm{x}_1,\ldots,\mathrm{x}_n) \;=\; i^{-n}\frac{\delta^n\mathcal{W}[J]}{\delta J(\mathrm{x}_1)\ldots\delta J(\mathrm{x}_n)}\bigg|_{J=0}. \tag{2.11}$$

Such definitions of correlation functions have been originally introduced in the statistical study of liquids [319] and are completely analogous to the Green's functions usually considered in quantum field theory [315, 305]. It is apparent that a unique characterization of the statistics, *i.e.* the knowledge of the partition functions, requires that correlation functions of any order are known.

It is easy to show that the definition (2.6) of correlation functions is completely equivalent to that provided by eq. (2.2). In fact, in the simple case of the 2-point joint probability of having the density values $\rho(\mathrm{x}_1)$ in the position x_1 and $\rho(\mathrm{x}_2)$ in x_2, it turns out that

$$\langle\,\rho(\mathrm{x}_1)\,\rho(\mathrm{x}_2)\,\rangle \;=\; \bar{\rho}^2[1+\mu_{2,12}]\,, \tag{2.12}$$

which is analogous to eq.(2.2), once we take $\xi(r_{12})=\mu_2(r_{12})$. If the positions of the objects are correlated (*i.e.*, the presence of one of them influences positively the presence of the other), it follows that $\xi>0$, while $-1\le\xi<0$ if the two positions are anticorrelated. According to its definition, it is also easy to show that the 2-point correlation function must satisfy the integral constraint

$$\int_0^{\infty} dr\,\xi(r) \;=\; 0\,.$$

In order to study the structure of the 3-point correlation function, let us suppose that the point x_3 is sufficiently far away from x_1 and x_2, so that the event probability in x_3 does not depend on that in the other two points. If this is the case, the 3-point joint probability is

$$\langle\,\rho_1\,\rho_2\,\rho_3\,\rangle \;=\; \langle\,\rho_1\,\rho_2\,\rangle\times\bar{\rho}\,, \tag{2.13}$$

where the meaning of the indices is obvious. Hence, requiring symmetry for the exchange of x_3 with x_1 and with x_2, the 3-point probability can be cast in the form

$$\langle \rho_1 \rho_2 \rho_3 \rangle = \bar{\rho}^3 [1 + \xi_{12} + \xi_{23} + \xi_{13} + \zeta_{123}] \quad . \tag{2.14}$$

Here, $\zeta \equiv \kappa_3$ is the term that correlates the three points all together and must vanish when one of these points is removed:

$$\zeta(x_i, x_j, x_l \to \infty) = 0 \qquad i \neq j \neq l \quad ; \quad i, j, l = 1, 2, 3 \, . \tag{2.15}$$

A graphic representation of eq. (2.14) is

$\langle \rho_1 \rho_2 \rho_3 \rangle = \bar{\rho}^3$

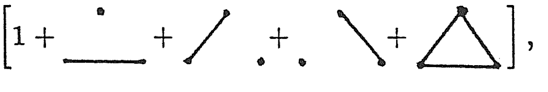

(2.16)

where each leg represents a ξ term, while the triangle corresponds to the ζ contribution.

On the basis of the same considerations that led us to eq. (2.14), we can write the 4-point joint probability in the form

$$\begin{aligned} \langle \rho_1 \rho_2 \rho_3 \rho_4 \rangle &= \bar{\rho}^4 \{1 + [\xi_{12} + ... + 6 \; terms] \\ &+ [\zeta_{123} + ... + 4 \text{ terms}] + \mu_{4,1234}\} \, . \end{aligned} \tag{2.17}$$

Here the 4-point correlation function

$$\mu_{4,1234} = \xi_{12}\xi_{34} + \xi_{23}\xi_{14} + \xi_{13}\xi_{24} + \eta_{1234} \tag{2.18}$$

represents the term connecting the four points and gives a vanishing contribution when at least one point is moved to infinite separation from the others. In more details, the μ_4 term contains three terms connecting two pairs separately, while $\eta \equiv \kappa_4$ is the usual notation to indicate the connected 4-point function, which accounts for the amount of correlation due to the simultaneous presence of the four points. Graphically, eq. (2.18) takes the form

$\mu_{4,1234} =$

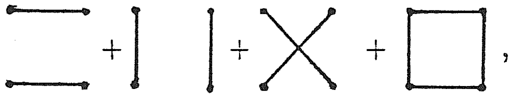

(2.19)

where the square represents the η term.

More generally, correlations of generic order n can be introduced through the n-point joint probability,

$$\langle \rho(x_1) \dots \rho(x_n) \rangle = \bar{\rho}^n \left[1 + (\text{terms of order} < n) + \mu_n(x_1, ..., x_n)\right], \tag{2.20}$$

and are such that they give null contribution when any subset of $\{x_1, \dots, x_n\}$ is removed to infinity. In turn, an important theorem of combinatorial analysis (*e.g.*, ref.[305]) shows that, removing from the μ_n function all the disconnected contributions, the remaining connected part is just the κ_n function defined by eq.(2.11). The general proof of this theorem is rather tricky and will not be reported here. It is however not difficult to see that, expressing the derivatives of the $\mathcal{W}[J]$ partition function in terms of that of $\mathcal{Z}[J]$, we get at the first correlation orders

$$\mu_2 = \kappa_2\,, \qquad \mu_3 = \kappa_3\,, \qquad \mu_4 = 3\kappa_2^2 + \kappa_4\,, \qquad \mu_5 = 10\kappa_2\kappa_3 + \kappa_5\,,$$

$$\mu_6 = 15\kappa_2^3 + 10\kappa_3^2 + 15\kappa_2\kappa_4 + \kappa_6\,. \tag{2.21}$$

From eq.(2.20), it follows that the n-point functions measure by how much the distribution differs from a completely random (Poissonian) process. In fact, for a Poissonian distribution the probability of some events in any subset of $\{x_1, ..., x_n\}$ does not affect the probability in the other points. Accordingly,

$$\langle \rho(x_1) ... \rho(x_n) \rangle \;=\; \bar{\rho}^n\,. \tag{2.22}$$

and correlations of any order vanish.

As already observed, the key relevance of correlation functions lies in the fact that their expressions, deducible from observational data at least at the lowest order, completely determine the statistics of the large-scale texture of the galaxy distribution. Viceversa, once a theoretical model is assumed for the probability distribution, the explicit form of μ_n and κ_n are uniquely fixed.

As a first example, a suitable expression for the n-point probability is provided by the so-called Kirkwood model [220]

$$\langle \rho_1 \cdots \rho_n \rangle \;=\; \bar{\rho}^n \prod_{i \neq j}^{\binom{N}{2}} [1 + \xi_{ij}]\,, \tag{2.23}$$

that has been originally introduced in the study of rarefied gases.

Another popular expression in the cosmological context is the hierarchical pattern for the connected functions [146],

$$\kappa_n(x_1, \ldots, x_n) \;=\; \sum_{n-trees\ a}^{t_n} Q_{n,a} \sum_{labelings} \prod_{edges}^{(n-1)} \kappa_{2,ij}\,, \tag{2.24}$$

which expresses the n-point connected function in terms of products of $(n-1)$ 2-point functions. In eq.(2.24), distinct "trees" designated by a have in general different coefficients Q_a, while the complete sequence of these coefficients uniquely specify the details of the hierarchical model. Configurations that differ only in interchange of labels 1,...,n all have the same amplitude coefficients, and ij is a single index which identifies links (see Figure 2.1). The number of trees t_n with n vertices is a result of combinatorial analysis [320], while the total number of labeled trees is $T_n = n^{n-2}$. Thus, eq. (2.24) has t_n amplitude coefficients $(a = 1, ..., t_n)$ and T_n total terms.

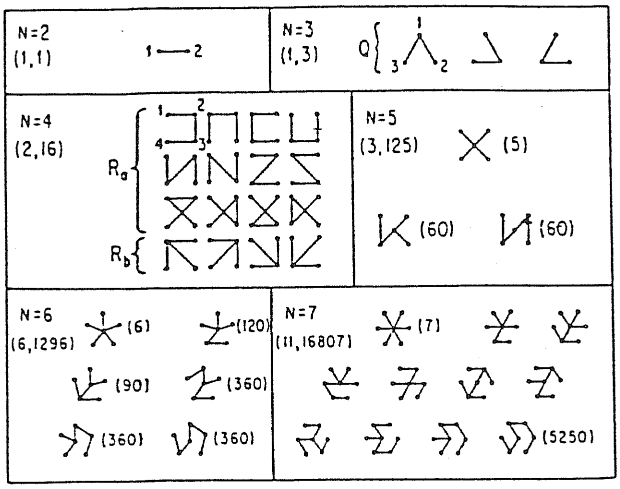

Figure 2.1: *Tree graphs contributing to the hierarchical expression (2.24) for $N = 2$ to 7. The pair of numbers below each N indicates the number of free trees and the number of labeled trees; a number in parentheses next to a graph indicates the number of distinct labelings (after [146]).*

It is worth observing that the hierarchical pattern does not represents a purely phenomenological description of the galaxy clustering, instead it is also justified on several theoretical grounds. In fact, it is predicted by dynamical models of gravitational clustering, such as the solution of the BBGKY equations in the strongly non-linear, fully relaxed regime [101, 287, 144, 145, 183], or perturbative analysis of non-linear fluctuation evolution [146], and is also supported by the thermodynamical approach to gravitational evolution proposed by Saslaw and coworkers [335, 333]. As we will show in the following of this Section, the hierarchical model also represents a quite satisfactory description for the (low-order) correlation properties of cosmic structures.

The predictions of the hierarchical model will be compared in following chapters to the results of our correlation analysis for N-body simulations and cluster samples. In Chapter 7 we explicitly work out the scale-invariant (fractal) structure implied by eq.(2.24) for different choices of hierarchical behaviour (*i.e.*, of the Q_n coefficients).

2.1.2 Correlations of a Gaussian field

A particularly interesting and simple case is that in which the density fluctuations are approximated by a random Gaussian process. This means that the density fluctuations for the matter contained inside a sphere of fixed radius and centered on a randomly chosen point has a frequency distribution of Gaussian type. The very important role of Gaussian perturbations in cosmological context lies in the fact that, according to the classical inflationary scenario, they are expected to be originated from quantum fluctuations of a free scalar field at the outset of the inflationary expansion (see, *e.g.*, ref.[25] and references therein). Even without resorting to inflation, the Central Limit Theorem guarantees that Gaussianity is the consequence of a large variety of random processes, which makes it a sort of natural choice to describe the initial conditions for the evolution of density fluctuations.

In the Gaussian case, the probability distribution in the functional space $\mathcal{F}$ takes the form

$$\mathcal{P}[\delta(\mathrm{x})] = (\det K)^{1/2} \exp\left\{-\frac{1}{2}\int d\mathrm{x} \int d\mathrm{x}'\, \delta(\mathrm{x})K(\mathrm{x},\mathrm{x}')\delta(\mathrm{x}')\right\}. \qquad (2.25)$$

Here $K(\mathrm{x},\mathrm{x}')$ in an invertible operator acting on $\mathcal{F}$ and symmetric with respect to the variables x,x'. From eq. (2.25), it follows that such an operator determines the variance of the distribution and, more generally, the correlation properties of the fluctuation field. Note that the above expression of the probability distribution is such as to satisfy the normalization requirement (2.5).

Expressing the 2-point correlation function as the second derivative of the partition functional $\mathcal{Z}[J]$, evaluated for $J(x) = 0$, it is straightforward to see that the operator K determines the 2-point function according to

$$\xi(x_{12}) = \int \frac{d^3k}{(2\pi)^3} \frac{e^{i\mathrm{k}\cdot(\mathrm{x}_1-\mathrm{x}_2)}}{\hat{K}(k)}. \qquad (2.26)$$

Here $\hat{K}(k)$ is the representation of the operator K in momentum space, where it acts as a multiplicative operator. In order to prove eq. (2.26), let us observe that the partition functional $\mathcal{Z}[J]$ relative to the Gaussian distribution functional (2.25) is

$$\begin{aligned}\mathcal{Z}[J] &= (\det K)^{1/2} e^{-\frac{1}{2}\int d\mathrm{x} \int d\mathrm{x}'\, J(\mathrm{x})K^{-1}J(\mathrm{x}')} \int \mathcal{D}[\delta(\mathrm{x})]\, e^{-\frac{1}{2}\int d\mathrm{x} \int d\mathrm{x}'\, \delta(\mathrm{x})K\delta(\mathrm{x}')} \\ &= e^{-\frac{1}{2}\int d\mathrm{x} \int d\mathrm{x}'\, J(\mathrm{x})K^{-1}J(\mathrm{x}')}. \qquad (2.27)\end{aligned}$$

Twice differentiating the above expression with respect to $J(\mathrm{x})$, the 2-point function reads

$$\begin{aligned}\xi(x_{12}) &= \left[K^{-1}\delta_{\mathrm{D}}(\mathrm{x}_1-\mathrm{x}_2) - K^{-2}J(\mathrm{x}_1)J(\mathrm{x}_2)\right] e^{-\frac{1}{2}\int d\mathrm{x} \int d\mathrm{x}'\, J(\mathrm{x})K^{-1}J(\mathrm{x}')}\Big|_{J=0} \\ &= K^{-1}\delta_{\mathrm{D}}(\mathrm{x}_1-\mathrm{x}_2). \qquad (2.28)\end{aligned}$$

Thus, eq.(2.26) follows after Fourier transforming $\xi(x_{12})$.

A fundamental property of Gaussian random fields follows from expression (2.27) for the $\mathcal{Z}$ partition functional. In fact, according to the definition (2.10) of $\mathcal{W}[J]$, the generator of the connected correlation functions reads

$$\mathcal{W}[J] = -\frac{1}{2}\int d\mathrm{x} \int d\mathrm{x}'\, J(\mathrm{x})K^{-1}J(\mathrm{x}'), \qquad (2.29)$$

so that the corresponding connected correlation functions are

$$\kappa_n(x_1,\ldots,x_n) = 0 \qquad \text{if} \quad n \neq 2. \qquad (2.30)$$

Thus, if the density fluctuation field is characterized by a Gaussian distribution, its statistics is completely determined by 2-point correlations.

Although Gaussianity of density fluctuations seems to be the natural outcome of the primeval evolution of the Universe, nevertheless the observed distribution of cosmic structures displays clear non-Gaussian behaviour, as the detection of non-vanishing higher-order correlations shows (see below). However, even starting with an initial Gaussian density field, there are at least two valid motivations to understand the development of subsequent non-Gaussianity in the galaxy distribution. Firstly, gravitational clustering is known to generate higher-order correlation even in the mildly non-linear regime [287, 146], while the strongly non-linear evolution as described by numerical N-body simulations shows a remarkable spatial intermittency of small-scale structures, which represents the signature of non-Gaussian statistics. Secondly, non-Gaussianity is also expected in the framework of "biassed" models of galaxy formation [213, 24], in which the observed cosmic structures are identified with those peaks of the underlying Gaussian matter field, that exceeds a critical density value. In this case, analytical argument [306, 205] shows that non-Gaussianity arises as a threshold effect superimposed on a Gaussian background.

2.1.3 Galaxy correlations

Starting from the first attempts of Totsuji & Kihara [367], the correlation analysis of the galaxy distribution became a widely employed approach to investigate clustering and is nowadays considered as the "classical" study of the large-scale structure of the Universe. During the 70's, the availability of extended angular galaxy samples made possible the realization of many correlation analyses, mainly pursued by Peebles and his collaborators. Although based on different angular samples, such as the Zwicky catalogue [402], the Jagellonian field [325] and the Lick map [348], all these analyses converge to indicate that the angular 2-point function is well represented by the power law

$$w_g(\vartheta) \;=\; A_g\,\vartheta^{1-\gamma}\,, \tag{2.31}$$

with $\gamma = 1.77 \pm 0.04$ and amplitude $A_g \propto \mathrm{D}^{-1}$ decreasing with the depth D of the sample, with a break from the power-law behaviour at large angular separations.

In more recent years, from the analysis of the APM sample Maddox *et al.* [246] found an angular 2-point correlation function having the same slope as eq.(2.31), in the range of validity of the power-law. The break they found from the power law occurs roughly at the same physical separation as found by Groth & Peebles [173] from the analysis of the Lick map, but with a much more gently decline from a power law on larger scales, thus implying an excess of power at scales $\gtrsim 20h^{-1}$ Mpc (see Figure 2.2). The authors argued that this discrepancy with respect to the results of Groth & Peebles is probably due to the removal of clustering from the sample they used, when correcting for the presence of large-scale gradients. A similar result has also been found by Collins *et al.* [91] from the analysis of the Edinburgh/Durham galaxy catalogue.

In order to extract information about the *spatial* properties of the galaxy distribution from eq. (2.31), we need a method for deprojecting angular data, so to obtain the *spatial* 2-point correlation function, $\xi(r)$. A suitable deprojection method, that allows us to derive the expression of $\xi(r)$ from that of the angular function, is provided by the Limber equation [233]. This method, that holds under the hypothesis of absence of any correlation between position and luminosity of objects, permits us to express the angular function $w(\vartheta)$ in terms of the spatial function $\xi(r)$, according to the formula

$$w(\vartheta) \;=\; \frac{\int r^4\,\phi^2(r/\mathcal{D})\,dr \int d\rho\,\xi(\sqrt{\rho^2+r^2\vartheta^2})}{\left[\int r^2\,\phi(r/\mathcal{D})\,dr\right]^2}\,. \tag{2.32}$$

Here, $\phi(r/\mathcal{D})$ is the radial selection function and gives the probability for an object at distance r to be included in a sample of depth $\mathcal{D}$. Its detailed shape depends also on the luminosity distribution of galaxies. The inversion of the Limber equation, in which we are interested, is also possible in several cases [135]. For instance, taking the power-law model (2.31) for $w(\vartheta)$, the spatial 2-point function turns out to be

$$\xi_g(r) \;=\; \left(\frac{r_{o,g}}{r}\right)^{\gamma}, \tag{2.33}$$

with the same value of γ as in eq.(2.31) and clustering length, $r_{o,g}$, depending on the amplitude A_g of the angular function and on the depth $\mathcal{D}$ according to the scaling relation

$$A_g \;\propto\; \left(\frac{r_{o,g}}{\mathcal{D}}\right)^{\gamma}. \tag{2.34}$$

All the investigations of the spatial correlations by means of angular data indicate $r_{o,g} \simeq 5h^{-1}$ Mpc, with some scatter around this value, in the range of separations $0.1 < r < 10h^{-1}$ Mpc [291, 285, 173], but with a break of the power-law at larger separations. Viceversa, no deviations from a pure power-law have been found down to the smallest scales sampled by the galaxy distribution. In fact, there is evidence [166, 228] that support the validity of eq.(2.33) down to $r \sim 3\,h^{-1}$ kpc.

A direct test of the reliability of eq.(2.33) has been realized with the availability of sufficiently large and complete redshift surveys. By using the CfA1 sample, Davis & Huchra [100] deduced the galaxy spatial number density, while Davis & Peebles [102] obtained the expression (2.33), for the 2-point function, with $r_{o,g} = 5.4 \pm 0.3\,h^{-1}$ Mpc, in fairly good agreement with angular results in the same range of physical separations (see Figure 2.2). An analysis of the CfA1 sample for the region centered on the Virgo cluster led Einasto *et al.* [129] to find a shoulder in the 2-point function at $r = 4-5h^{-1}$ Mpc. This discrepancy with respect to the Davis & Peebles' result indicates that, in some cases, the galaxy distribution could have local features, which affect a safe determination of the clustering parameters and disappear when a larger (fair) sample is considered. In a further analysis of the CfA1 survey and dividing the full sample into subsamples of different volumes, Einasto *et al.* [130] found that the value of the galaxy clustering length turns out to vary with the volume of the subsample itself.

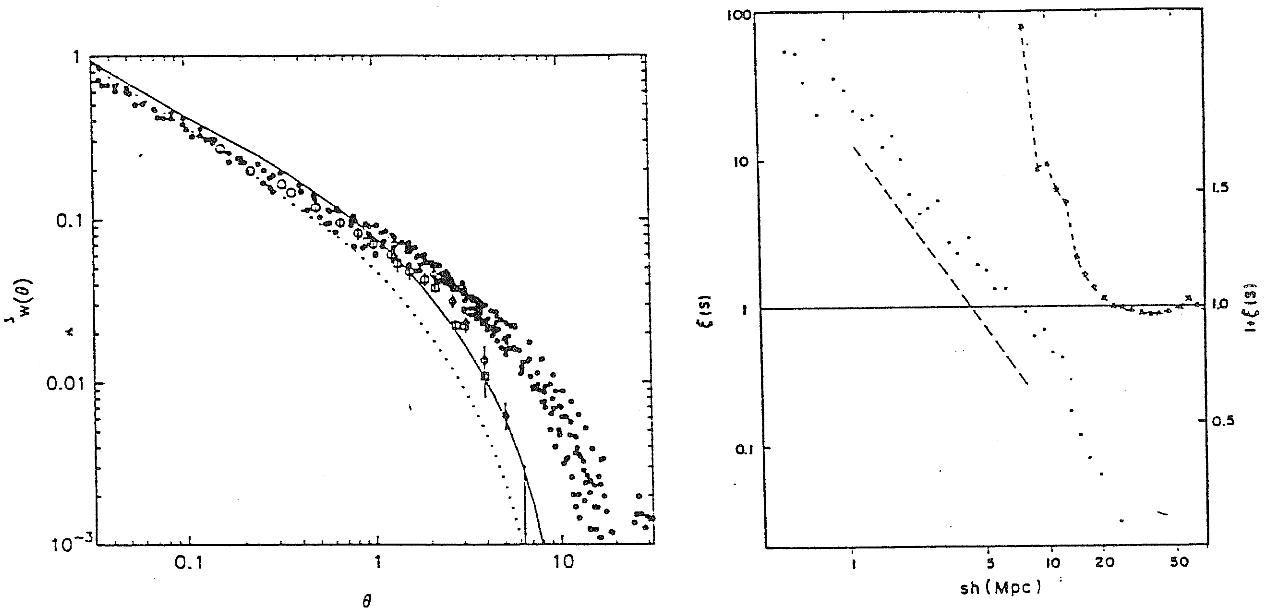

Figure 2.2: *Left panel: estimate of the galaxy 2-point* angular *correlation function from the APM galaxy survey (after [246]). Closed circles are for the APM data, while open ones are for the Lick map, scaled to the APM depth. The dotted and solid lines correspond to the* $w(\vartheta)$ *predicted by CDM models with* $h = 0.5$ *and* $h = 0.4$*. Right panel: estimate of the galaxy 2-point* spatial *correlation function from the CfA1 redshift survey; crosses on the right represent the quantity* $1 + \xi(r)$, *while the dashed line is a power-law with exponent* $\gamma = 1.8$ *(after [102]).*

In particular, the conventional value $r_{o,g} = 5h^{-1}$ Mpc is obtained for a sampling volume containing not more than one supercluster, while the estimated correlation length for a fair sample of the Universe is $r_{o,g} = 10h^{-1}$ Mpc. The authors argued that such an effect could be related to differences in relative volumes occupied by large voids; samples chosen from larger volumes have usually larger relative volumes of voids. A statistical investigation of the CfA2 sample led to quite large uncertainties in the determination of galaxy number density and 2-point correlation function. De Lapparent *et al.* [109] found an indetermination of $\sim 25\%$ in the galaxy number density. In this analysis the galaxy 2-point function was found to have a slope $\gamma \simeq 1.6$ and a correlation length $r_{o,g} \simeq 7.5\,h^{-1}$ Mpc, in the $3-14\,h^{-1}$ Mpc scale range. Because of the large uncertainty in the mean density, the ranges in the slope and amplitude are respectively $1.3-1.9$ and $5-12\,h^{-1}$ Mpc. On scales larger than $20\,h^{-1}$ Mpc, the correlation function is not well determined. Although consistent within the errors with the more stable indications coming from angular data, such results show how crucial it is to deal with a *fair* galaxy redshift sample. In fact, according to the definition (2.2) of 2-point function, it is clear that its unambiguous estimate relies on the possibility of uniquely define an average object number density. Although this can be done for angular samples, whose great depth by far encompasses the homogeneity scale, it could be more difficult when using redshift data. In fact, as shown by Figure 1.4, spatial samples trace structures having characteristic sizes of the same order of the sample size, so that it is not clear whether the galaxy distribution is statistically homogeneous within the sample boundaries. This problem can be even more important when single slices, such as those of the CfA2 survey are considered, in which case the sampled scales are widely different in different directions.

Instead of considering the galaxy distribution as a whole, several attempts have been also devoted to the investigation of the clustering properties of galaxies having different morphology. The relevance of this kind of analysis lies in the fact that a dependence of the clustering properties on galaxy morphology should be related to the physical processes that gave rise to galaxy formation. As we will mention in Chapter 4, many models of galaxy formation predict substantial differences between the clustering properties of different morphology galaxy distributions. It has been recognized for a long time that small compact groups tend to contain more elliptical galaxies than do looser groups [137]. The central regions of rich clusters appear to be dominated by elliptical and lenticular galaxies and contain few normal spirals; irregular, less dense clusters, which have a composition similar to that of the field, contain many spirals [271]. By analysing the Uppsala Catalogue, Davis & Geller [99] determined the angular 2-point correlation function for the distribution of galaxies of various morphological types. They found that elliptical galaxy clustering is characterized by a power law with a slope ($\gamma_{\rm E} \simeq 2.1$) steeper than that for spiral clustering ($\gamma_{\rm S} \simeq 1.69$), while the lenticular slope has an intermediate value ($\gamma_{\rm L} \simeq 1.71$). Dressler [115] studied the galaxy populations in 55 rich clusters. He found that a well defined relationship exists between local galaxy density and galaxy type, which confirms an increasing elliptical and S0 population and a corresponding decrease in spirals with increasing density inside the cluster. Still by using the Uppsala Catalogue, Giovanelli *et al.* [159] revealed evidence for a continuous morphological segregation in a wide range of galaxian densities in the Pisces-Perseus supercluster. Furthermore, significant differences in the slope of the angular 2-point function for different morphological types are found, in agreement with previous results. From the analysis of the three-dimensional CfA survey, Börner & Mo [57] obtained a correlation length for elliptical and lenticulars that they estimated to be ~ 1.7 times that of spiral and irregulars. In a detailed study of the correlation properties of different morphological types and using both angular and spatial galaxy samples, Jing *at al.* [207] and Mo [262] confirmed that elliptical galaxies tend to be more clustered and to have a steeper correlation function than spirals.

Although the analysis of the 2-point function surely provides remarkable hints about the large-scale galaxy distribution, nevertheless it does not represents a full statistical description. Further pieces of information are obtainable from the investigation of higher-order correlations. At the third order, the joint probability

$$\delta^{(3)}P \;=\; n^3\,\delta\Omega_1\,\delta\Omega_2\,\delta\Omega_3\,[1+w_{12}+w_{13}+w_{23}+z_{123}] \qquad (2.35)$$

defines the angular 3-point correlation function z_{123} (with obvious meaning of the indices), which depends on the shape of the triangle defined by the three points. It is clear that, as the correlation order increases, the statistical analysis becomes more and more complicated. In fact, while the estimate of the 2-point function requires the knowledge of the number of galaxy pairs at a given separation, computing the 3-point function amounts to counting the triplets of a given shape, with a subsequent increase of the noise, as well as of the required computational time. In Chapter 5 and 6 we will address the problem of the higher-order correlation analysis, by using different methods and different error estimates.

In past years, the analysis of the 3-point function in the Zwicky, Lick and Jagellonian samples has been discussed in a series of papers by Peebles and coworkers [292, 173, 285]. They concluded that data on the 3-point function can be well fitted by assuming the hierarchical model

$$z_{123} \;=\; Q\,[w_{12}w_{23}+w_{12}w_{13}+w_{13}w_{23}] \qquad (2.36)$$

with $Q = 1.29 \pm 0.21$ (see, however, Bonometto *et al.* [46] for a reanalysis of the Zwicky sample).

Going to even higher correlation orders causes a significant increase in the sampling noise. Some attempts in this direction have been however pursued by several authors. In their estimate of the 4-point function for the Lick map, Fry & Peebles [150] have shown that, even within the uncertainties, its expression is consistent with the hierarchical model of eq.(2.24). In order to avoid the high computational cost required by counting multiplets in the analysis of high-order functions, Sharp *at al.* [353] devised an alternative approach, that is based on the evaluation of the moments for the neighbour counts. By applying this method to the Zwicky catalogue, they found a marginal signal for the 4-point function, while an attempt to estimate the 5-point function gave results that are completely lost in the noise. More recently, the moment method has been extensively applied by Szapudi *et al.* [365] to the analysis of the Lick map, and by Szalay *et al.* [255] to the distribution of IRAS galaxies. Accordingly, these authors claim that signals of correlation are detected up to the eighth order, and are consistent with the hierarchical model. However, it is not clear how correlations of such a high order could provide statistical information that were both simple-to-handle and easy to compare with theoretical models.

2.1.4 Cluster correlations

Many attempts have been devoted in recent years in order to trace the large-scale structure of the Universe on the basis of the observed statistical properties for the cluster distribution [16]. Indications that the cluster distribution on the sky is not random was already found several years ago by Abell [3, 4]. A further evidence of super-clustering in the Abell survey was also detected by Bogart & Wagoner [42], Hauser & Peebles [187], and Rood [321] by means of nearest-neighbor distributions and angular correlation functions. Already from these preliminary investigations, it clearly appeared that rich galaxy systems display a clustering that is remarkably stronger than that of galaxies and developing on much larger scales. Thanks to this characteristic, it has been immediately recognized that the cluster distribution can be extremely important to test the structure of the Universe at very large scales, where gravitational interaction is still in the linear regime and preserves memory of initial conditions.

Bahcall & Soneira [18] and, independently, Klypin & Kopylov [222] determined the rich ($R \geq 1$) Abell cluster 2-point correlation function from the HGT redshift sample. They found strong correlations in both the $D \leq 4$ redshift sample and in the larger and deeper $D = 5 + 6$ sample. Moreover, the spatial correlation function was found to fit a power-law relation of the form

$$\xi_c(r) = \left(\frac{r_{o,c}}{r}\right)^{\gamma}, \tag{2.37}$$

with $r_{o,c} \simeq 25h^{-1}$ Mpc and $\gamma \simeq 1.8$, in the distance range $5 \lesssim r \lesssim 150h^{-1}$ Mpc. Thus, the rich-cluster autocorrelation function exhibits the same slope as the galaxy function, but with a greater value of the correlation length. They also noted that, due to peculiar motions that affect the redshift-distance relation, cluster correlations are elongated along the line-of-sight direction. Accounting for these effects, an estimate of peculiar velocities between clusters gives ~ 2000 km s^{-1}. A similar conclusion was also reached by Postman *et al.* [307] and by Batuski *et al.* [30] from the analysis of the Zwicky sample and of the ACO catalog, respectively.

A completely different conclusion has been however reached by Sutherland [361], who argued that random peculiar motions cannot explain the line-of-sight correlations at separations $\gtrsim 50h^{-1}$ Mpc. On the contrary, he claimed that such anisotropies in the redshift space correlation function are to be ascribed to spurious line-of-sight clustering; if the richness of Abell clusters is apparently enhanced by a significant amount because of foreground and background galaxies, spurious line-of-sight correlation is produced in a richness-limited sample. By analysing the SR spatial sample of Abell clusters and after correcting for the anisotropies in the redshift space correlations, Sutherland found that the power-law (2.37) for the rich cluster 2-point function is still satisfied, but with a reduced correlation length, $r_{o,c} \simeq 14h^{-1}$ Mpc. A numerical simulation of richness contamination [105] allowed the construction of a "decontaminated" sample of $D \leq 4$, $R \geq 1$ clusters, with the result that the correlation amplitude is reduced by a factor ~ 2 (in agreement with the Sutherland's claim). A similar conclusion has been also reached by Sutherland & Efstathiou [362]. In their analysis of the deep GH survey, they found further evidence of line-of-sight contamination and a resulting value of the clustering length $r_{o,c} \simeq 13h^{-1}$ Mpc. In addition, effects of projection contamination on the angular cluster correlation function has also been found by Olivier *et al.* [272] in the analysis of the Abell and ACO catalogs. After removing these effects by means of a suitable model for the galaxy distribution around clusters, the correlation strength at small angular separation is reduced by a factor 2-3, in agreement with the results obtained from spatial samples.

The crucial relevance of correctly measuring the amplitude of the rich-cluster correlation function as a test of several models for structure formation is still at the present time a matter of debate. By using an ensemble of simulated cluster catalogues, Jing *et al.* [208] checked whether the redshift correlation claimed by Sutherland is an effect of richness contamination or of real clustering. They found that the redshift correlation is a quite common feature in free-of-contamination simulated samples and concluded that the original Bahcall & Soneira estimate is not seriously affected by such effects. A similar conclusion has been also reached by Postman *et al.* [308] and Cappi & Maurogordato [69] from the analysis of the PGH cluster redshift survey. They found that the power-law shape of the 2-point function is consistent with a clustering length $r_{o,c} \simeq 20h^{-1}$ Mpc. Based on the recently compiled samples of clusters selected from the APM and Edinburgh/Durham galaxy surveys, several authors concluded in favour of a lower correlation length, in the range $r_{o,c} \simeq$ 13-16h^{-1} Mpc [96, 20, 244]. Despite the agreement of the results, completely opposite conclusions have been however reached by these authors. Dalton *et al.* [96] claim for a better reliability of these cluster samples and take the result as a probe of a smaller clustering amplitude. Efstathiou *et al.* [119] found an anisotropy in the clustering of the PGH sample, which they interpreted as due to artificial clustering. After correcting for this effect, they found consistence with the smaller correlation amplitude found for the APM cluster sample. Viceversa, Bahcall & West [20] ascribe the smaller correlation length as due to the richness-clustering dependence and conclude that the result is perfectly consistent with the Bahcall & Soneira result for the richer Abell clusters. Further support for a higher value of the cluster correlation length comes also from the analyses of the distribution of cD [389] and X-ray selected clusters [227], which should be unaffected by projection contamination, and point toward $r_{o,c} \simeq 21h^{-1}$ Mpc.

Differently from rich clusters, the analysis of samples of loose galaxy groups reveal that

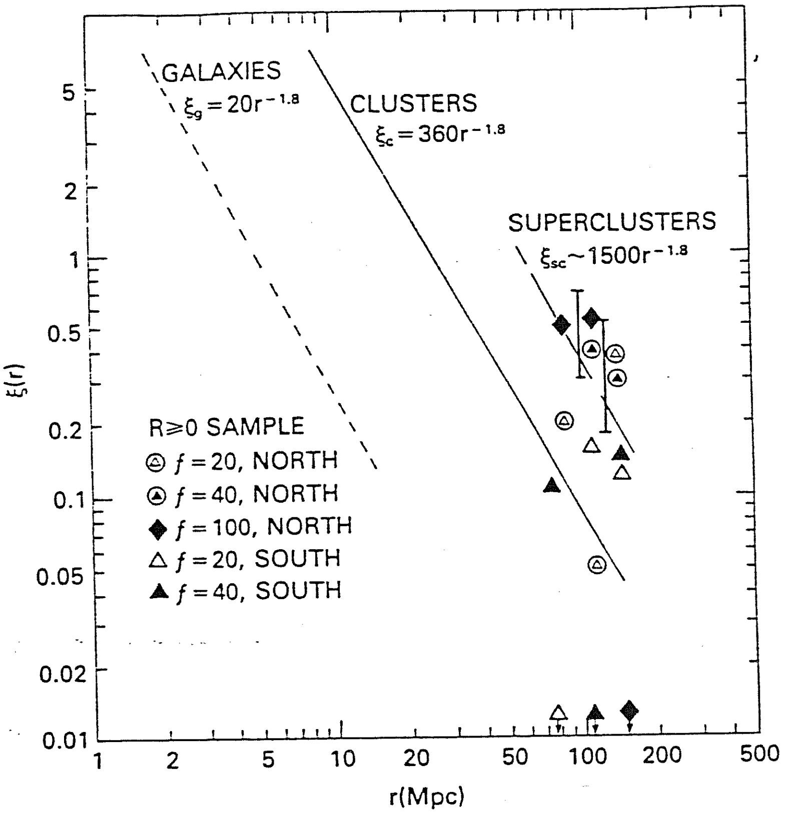

Figure 2.3: *Spatial correlation of superclusters. Different symbols indicate samples of different overdensity. The dashed line indicates the supercluster correlation function* if *it follows the power-law* $r^{-1.8}$. *The solid line represents the* $R \geq 1$ *cluster correlation function of Bahcall & Soneira, while the short–dashed line is the galaxy correlation function of Peebles and coworkers (after [17]).*

such structures are less clustered than galaxies. Indeed, from the investigation of the SEG sample, Maia & da Costa [247] showed that groups are characterized by a 2-point function with the same slope $\gamma \simeq 1.8$ in the range of separations 2-10h^{-1} Mpc, but with amplitude 2.5 times smaller than that of galaxies. In a similar analysis of the correlation function for groups defined in the RGH sample, Ramella *et al.* [314] found $\gamma \simeq -1$ and $r_{o,c} \simeq 6h^{-1}$ Mpc, over the range 3-10h^{-1} Mpc, but with very large uncertainties.

A further extension in the study of the large-scale structure of the galaxy distribution is possible by investigating the spatial correlations between superclusters of galaxies (*i.e.*, groups of rich clusters). Bahcall & Burgett [17] analysed the BS sample of superclusters. They found a correlation on scales $\sim 100h^{-1}$ Mpc, that is significant at about 95%-99% confidence level. The correlation appears to be stronger than that of galaxy and galaxy clusters (see Figure 2.3).

All these determinations of the 2-point correlation function for galaxy systems seem to suggest a dependence of the clustering strength on the richness, that is quite similar to the discrepancies found in the investigation of the clustering for galaxies with different morphology. In particular, an increase in the clustering is observed for richer systems. In their analysis

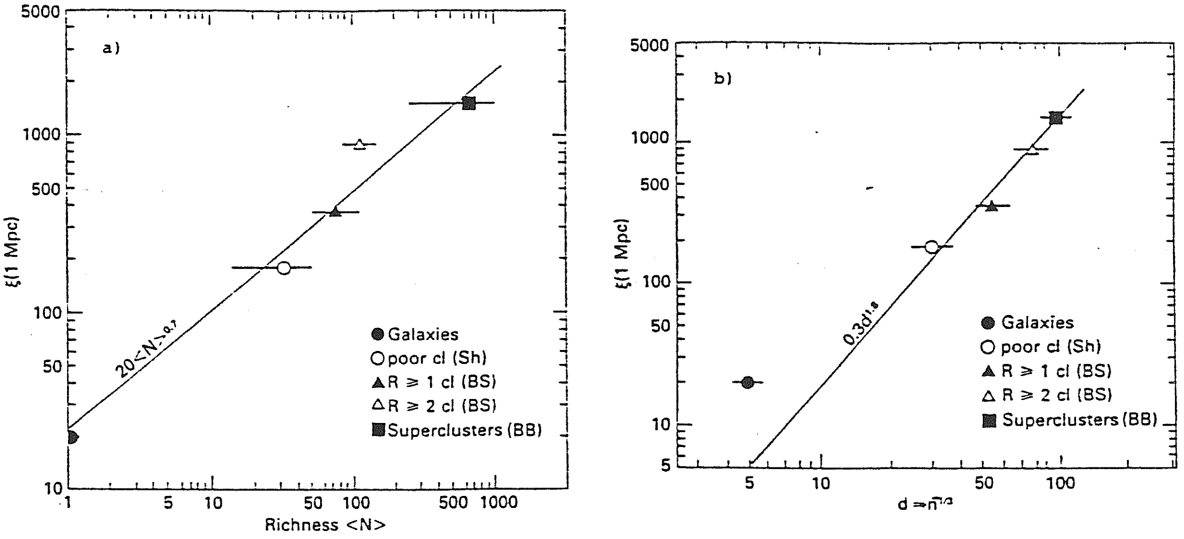

Figure 2.4: (*a*) *The dependence of the correlation function on the richness of the system. A range of the mean richness is shown for each cluster point. The solid line indicate an approximate dependence on richness.* (*b*) *The dependence of the correlation function on the mean separation of objects. The solid line represents the* $d^{1.8}$ *dependence (after [17]).*

of the spatial correlation function for Abell clusters, Bahcall & Soneira [18] discussed the decrease of the correlation amplitude with cluster richness. They classified individual galaxies as $N = 1$ systems (where N is Abell's criterion for richness classification) and suggested that galaxies have a correlation function amplitude that follows the richness-clustering relation holding for clusters. From a physical perspective, it would however be misleading to treat individual galaxies in the same way as galaxy systems, the processes governing galaxy formation probably being different from those relevant for groups and clusters. Indeed, Szalay & Schramm [364] pointed out that galaxy clustering may be intrinsically different from cluster clustering. They discussed a possible *universal* correlation function characterized by a slope $\gamma = 1.8$ and by a dimensionless amplitude

$$\beta(L) \;=\; \xi(L) \;=\; \left(\frac{r_o}{L}\right)^{\gamma}. \tag{2.38}$$

Here $L = n^{-1/3}$ (n is the mean spatial density of objects) represents the average value of the separation. They derive $\beta \simeq 0.35$ for Shechtman clusters and for Abell $R \geq 1$ and $R \geq 2$ clusters, while $\beta \simeq 1.1$ for galaxies. This result suggests that galaxies are relatively more strongly correlated than clusters (see Figure 2.4*b*). Bahcall & Burgett [17] extended such analysis to include also the correlation function of superclusters. They argued that the increasing of the clustering amplitude with the richness of the system is valid for supercluster clustering too (see Figure 2.4). Moreover, by using the dimensionless correlation amplitude (2.38), they found that superclusters have $\beta \simeq 0.3$, in agreement with the value for clusters (see Figure 2.4*a*).

As in the case of the galaxy distribution, some attempts have also been devoted to the investigation of higher order correlations for galaxy clusters. It is however clear that, since cluster samples contain a much smaller number of objects than galaxy samples, the analysis of higher-order functions becomes particularly difficult and care must be taken about the statistical significance of any result.

Jing & Zhang [211] analyzed the Abell catalogue and found that the hierarchical expression of eq.(2.36) reproduces quite well the cluster 3-point function, with a value $Q \simeq 0.7 \pm 0.2$ for the hierarchical coefficient. This result has been confirmed by Toth *et al.* [366], who considered the northern Abell, the southern ACO and the Shechtman angular samples or rich clusters. They found that the angular 3-point correlation function is still consistent with the hierarchical expression, as in the galaxy case, with $Q \simeq 1.0 \pm 0.1$ for Abell clusters and a systematically lower value $Q = 0.64 \pm 0.04$ for the Shechtman groups. This smaller value could well be interpreted on the light of the lower average richness, which characterizes Shechtman groups with respect to Abell clusters. An investigation of the spatial 3-point function has been recently performed by Jing & Valdarnini [209], that considered a sample of 227 Abell clusters with known distances. They found that a hierarchical expression with $Q \simeq 0.7$ give a reasonable fit to the data, without, however, completely ruling out the Kirkwood model (2.23) within the quite large uncertainties. A similar analysis based on the spatial distribution of Abell clusters, as well as on a synthetic cluster catalog extracted from large N-body simulations, led Gott *et al.* [161] to conclude that the 3-point function of rich clusters agrees with the hierarchical expression.

In Chapter 6 we will discuss our analysis of the 2- and 3-point functions for angular samples of galaxy clusters having different richness.

2.1.5 Galaxy-cluster crosscorrelations

Other than analyze the correlation properties of galaxies and clusters separately, it is also possible to investigate the cross-correlations between the relative positions of galaxies and clusters. This kind of investigation is relevant in order to study the galaxy distribution inside cluster halos. In order to introduce the angular *cross-correlation* function $w_{cg}(\vartheta)$, let us consider the joint probability

$$\delta^{(2)}P \;=\; n_c n_g \delta\Omega_1 \delta\Omega_2 [1 + w_{cg}(\vartheta_{12})] \qquad (2.39)$$

of having a cluster in the solid angle element $\delta\Omega_1$ and a galaxy in $\delta\Omega_2$. High values of w_{cg} indicate a strong concentration of galaxies around cluster centers, while its shape is determined by the variation with the distance of the galaxy density out of the cluster.

The first joint statistical investigation of the distribution of galaxies and clusters was performed by Seldner & Peebles [346]. In this analysis, the distribution of galaxies is that of the Lick Catalog, while the Abell Catalog is used for the cluster positions. A good fit to the data was found by using for the cross-correlation function the expression

$$w_{cg}(\vartheta) = A\vartheta^{-\rho} + B\vartheta^{-\sigma}, \tag{2.40}$$

with $\rho \simeq 1.4$ and $\sigma \simeq 0.2$. In the above relation, the first term, which is dominant at small scales, is essentially due to the galaxy density around each cluster, while the second term, that dominates for larger angular separations, takes into account the contribution of the clustering between clusters.

A further investigation of the cross-correlation properties for the distributions of galaxies and clusters has been realized by Lilje & Efstathiou [232], which used the same catalogs for both galaxies and clusters. They used redshifts for Abell clusters to compute a cross-correlation function $w_{cg}(\sigma)$, where $\sigma \equiv v\vartheta/H_o$ is the projected separation between a cluster with recession speed v and a galaxy at angular distance ϑ from the cluster center. Their results show that on scales $r < 20h^{-1}$ Mpc the shape of the spatial cross-correlation function is well described by a unique power-law,

$$\xi_{cg}(r) \simeq \left(\frac{8.8h^{-1}\ \mathrm{Mpc}}{r}\right)^{2.2}, \tag{2.41}$$

so that galaxies are distributed around rich clusters with a density profile slightly steeper than for an isothermal profile. It is worth observing that the above shape of the galaxy-cluster cross-correlation is consistent with the cluster density profile as reconstructed from X-ray data about the temperature profile of the intracluster gas (see, *e.g.*, ref.[133]). This analysis indicates that, at least for the few considered clusters, the average density inside the radius r scales as $\rho(r) \propto r^{-\gamma}$, with γ slightly exceeding two, thus indicating that at scales $\lesssim 1h^{-1}$ Mpc from the cluster centre galaxies are fairly good tracers of the dark matter distribution.

2.1.6 Dark matter correlations in galaxy halos

Here we describe a method we devised [45, 53, 49] to explore matter correlation properties at galaxy scales, by probing the distribution of halo matter surrounding galaxies. To this purpose, we base our analysis on the dynamical information provided by rotation curves of spiral galaxies. In this way, we are able to probe the extension down to very small scales ($\lesssim 10\, h^{-1}$ kpc) of the clustering pattern traced at larger scales by the galaxy distribution.

If the Universe is dominated by dark matter on the larger scales, then, on the scale of galaxies, continuity arguments invite us to consider only their dark mass components rather than their overall mass distribution in order to meaningfully compare the clustering properties of matter at small and large scales. To this purpose, we resort to a suitable mass-decomposition method, which has been originally devised by Persic & Salucci [294, 295], in order to separate the dynamical contributions of dark (halo) and luminous (disk) matter to the overall rotation curve.

In spiral galaxies, the optical disk radius, R_{opt}, is both the only observable lengthscale of their internal structure (R_{opt} is $\sim$ 3 times the scale of the exponential light distribution [139, 375]) and the innermost radius where DM affects strongly and systematically the observed dynamics [323, 294]. For this reason, R_{opt} is the appropriate reference radius suitable for studying the statistical properties of DM at one same radius (in galaxy-normalized units) for all galaxies. Let $V_{opt} = V(R_{opt})$ be the value of the observed velocity at R_{opt}, and $V_{h,opt}$ the halo component of V_{opt}; also let M_{disk} and M_{halo} be the disk and halo masses evaluated at R_{opt}. Then, from the relation

$$V^2_{h,opt} = V^2_{opt} \, \frac{M_{halo}}{M_{disk} + M_{halo}} , \qquad (2.42)$$

$V_{h,opt}$ can be obtained as soon as the mass ratio at the right hand side of eq. (2.42) is known. According to Persic & Salucci [294, 295] the disk-to-total mass ratio in spiral galaxies at the optical disk radius is directly obtainable from the profiles of optical rotation curves. They used a two–component mass model including a spherical dark halo and a luminous thin disk with exponential surface brightness distribution $I(R) = I_o \; e^{-R/R_D}$, while no halo matter density profile is assumed. According to this mass–decomposition technique for ordinary spirals, the disk-to-total mass ratio at the optical radius is

$$\frac{M_{disk}}{M_{disk} + M_{halo}} = \frac{0.8 - \frac{d \; logV}{d \; logR}|_{R_{opt}}}{0.1 \, \frac{d \; logV}{d \; logR}|_{R_{opt}} + 1.1} . \qquad (2.43)$$

Therefore $V_{h,opt}$ is obtainable from the observable quantities V_{opt} and its logarithmic derivative $\frac{d \; logV}{d \; logR}|_{R_{opt}}$. (Here, velocities V and distances R are expressed in km s^{-1} and kpc respectively, unless otherwise stated.)

Let us now consider the condition of centrifugal equilibrium for the halo at R_{opt}, *i.e.* $M_{halo} = G^{-1} V^2_{opt} R_{opt}$. It implies that the volume-averaged density in the spherical halo is

$$\frac{\bar{\rho}_{h,opt}}{\mathrm{g \; cm^{-3}}} = 4 \times 10^{-27} \left[\frac{(V_{h,opt}/\mathrm{km \; s^{-1}})}{(R_{opt}/\mathrm{kpc})} \right]^2 \qquad (2.44)$$

Owing to eqs.(2.42) and (2.43), $\bar{\rho}_{h,opt}$ is therefore directly obtainable from velocity data. In doing such analysis, we took a sample of 58 spiral galaxies [295, 296]. These are all non-local galaxies for which both good (blue) photometry (*rms* errors < 0.05 mag) and high-quality, extended (out to $R \geq 0.8 \; R_{opt}$) rotation curves were available in the literature by the end of 1988. They span the (absolute blue) magnitude range from -17.5 up to -23.2. Disk radii range between about 2 and 27 kpc. Peripheral velocities range between about 120 and 400 km s^{-1}. They are of morphological types Sb through Sc, apart from two Sa and one Sab cases. In Figure 2.5 we plot the mean halo matter density at the optical disk radius as a function of R_{opt} for the spiral sample, which exhibits a power-law dependence.

Let us now investigate the correlation properties of the halo DM, that can be obtained from this kind of analysis. Let $M_{\mathrm{R}} = V_{\mathrm{R}} \, \bar{\rho}_{h,opt}$ be the matter contained inside the spherical

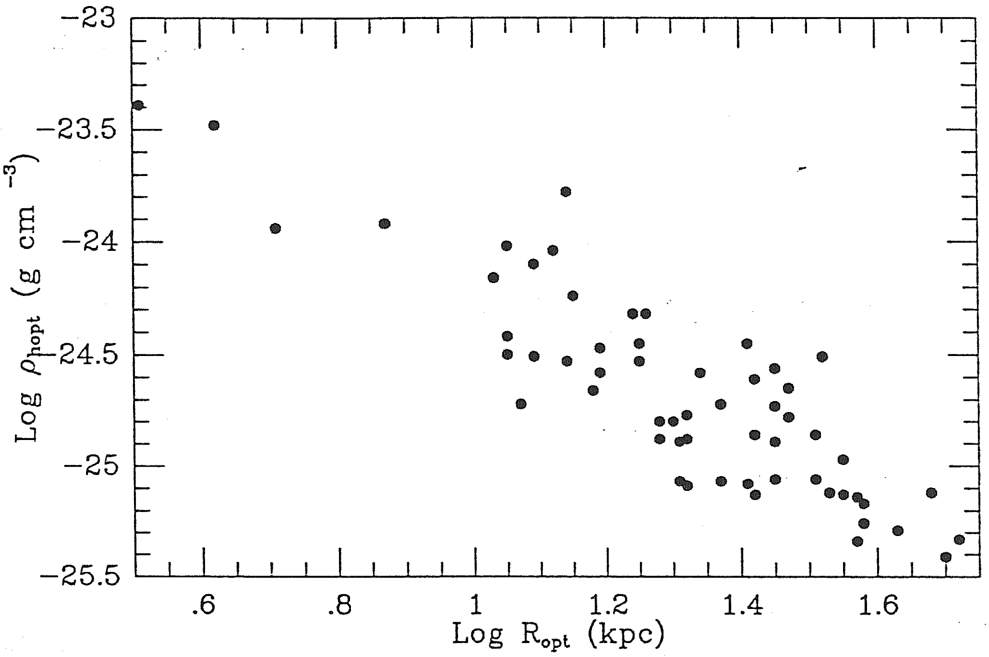

Figure 2.5: *The mean halo matter density at the optical disk radius, $\bar{\rho}_{h,opt}$ as a function of the optical disk radius, R_{opt}, for the PS90 sample of 58 Sb–Sc spiral galaxies with extended rotation curves.*

volume $V_R = 4\pi R^3/3$ encompassed by the optical radius of a given galaxy. According to the definition (2.2) of the 2-point correlation function, its first-order moment evaluated in a statistical sample reads

$$\langle M \rangle_R = \bar{M}_R + \bar{\rho}\, 4\pi \int_0^R r^2 dr\; \xi_{gb}(r)\,. \tag{2.45}$$

In the above expression, $\bar{\rho} = 1.9 \times 10^{-29} h^{-2}\, \Omega_o$ g cm^{-3} is the mean matter density and $\bar{M}_R = \bar{\rho}\, V_R$ is the expected mass contained in a randomly places sphere of radius R. Moreover, $\xi_{gb}(r)$ is the *galaxy-background* cross-correlation function, that arises since we are measuring the mass contained around the galaxy center, instead of around a randomly selected point. Taking $\xi_{gb}(r) = (r_o/r)^\gamma$, according to what is suggested by Figure 2.5, and for $R \ll r_o$, from eq. (2.45) we obtain

$$\frac{\langle M \rangle_R}{\bar{M}_R} = \xi_{gb}(R) K_1\,, \tag{2.46}$$

with and $K_1 = 3/(3-\gamma)$. The estimate of the parameter of $\xi_{gb}(R)$ from our spiral sample gives $r_o = (3.2 \pm 0.3)\Omega_o^{-1/\gamma} h^{-1}$ Mpc and $\gamma = 1.71 \pm 0.05$. This result is extremely significant since the resulting correlation function for the distribution of DM inside galaxy halos follows at small scales of a few tens of kpc the same power-law shape as that of galaxies at the scales of some Mpcs. The amplitude of the clustering turns out to depend on the value of the density parameter Ω_o.

By comparing the detected $r_{o,gb}$ with that, $r_{o,gg} \simeq 5h^{-1}$ Mpc, coming from the analysis of the galaxy distribution at scales ($\sim 10\, h^{-1}$ kpc, see refs.[173, 166, 228]) comparable to that sampled by rotation curves, and requiring continuity of the clustering between the DM and the galaxy distributions, we get for the density parameter

$$\Omega_o \; = \; 0.3 \pm 0.1 \tag{2.47}$$

(see ref.[329]). Note that this result agrees with estimates of the density parameter based on the virial analysis of galaxy pair velocity dispersions realized by Davis & Peebles [102], Bean *et al.* [33] and Hale-Sutton *et al.* [182]. Viceversa, if we allow the galaxies to be more strongly clustered than the underlying matter distribution, according to the prescription of biassing (see Chapter 4 and ref.[106] for a review), then matter fluctuations and object number count fluctuations are related by $\delta N/N = b\,(\delta M/M)$, $b > 1$ being the biassing parameter. In this case, assuming a flat Universe ($\Omega_o = 1$) amounts to requiring that galaxies are more strongly clustered than matter by an amount $b \simeq 2$.

As a concluding remark of our review about the correlation analysis of the large-scale structure of the Universe, we would like to stress the relevance of the detected scaling properties in the distribution of cosmic structures, as revealed by the power-law shape of the correlation functions. This fact is even more remarkable considering that, although their amplitudes turn out to increase when passing from the halo dark matter, to galaxies, and to galaxy aggregates of increasing richness, their slopes are remarkably similar. This suggests a sort of self-similarity for the large-scale structure of the Universe, extending from few kpc scales, traced by spiral rotation curves, to scales of some tens of Mpc, where rich galaxy clusters still display a non-negligible clustering.

2.2 The power-spectrum

It is often very useful to analyze the statistics of the galaxy distribution in Fourier space, instead of in configuration space, as done by correlation functions. To this purpose, let us introduce the Fourier transform of the fluctuation field $\delta(\mathrm{x})$

$$\tilde\delta(\mathrm{k}) \; = \; \frac{\bar\rho a^3}{M}\int d^3\mathrm{x}\,\delta(\mathrm{x})\,e^{i\mathrm{k}\cdot\mathrm{x}}\,, \tag{2.48}$$

where $M = \bar\rho a^3 \int d^3x$ is the total mass of the system and $a(t)$ the cosmic expansion factor. The modulus of the wavevector $\mathbf{k}$ is related to the comoving wavelength of the fluctuation mode according to $k = 2\pi a(t)/\lambda$. By inverting eq.(2.48), we have

$$\delta(\mathrm{x}) \; = \; \frac{M}{\bar\rho a^3}\int \frac{d^3\mathrm{k}}{(2\pi)^3}\,\tilde\delta(\mathrm{k})\,e^{-i\mathrm{k}\cdot\mathrm{x}}\,, \tag{2.49}$$

so that the two representations $\delta(\mathrm{x})$ and $\tilde\delta(\mathrm{k})$ of the fluctuation field contain the same amount of information. Accordingly, the correlation in Fourier space is related to that in x-space by means of the relation

$$\begin{aligned}\langle \tilde{\delta}(\mathbf{k}_1)\,\tilde{\delta}(\mathbf{k}_2)\rangle &= \left(\frac{\bar{\rho}a^3}{M}\right)^2 \int \mathcal{D}[\delta]\,\mathcal{P}[\delta] \int d^3k_1\, d^3k_2\, \delta(\mathbf{x}_1)\,\delta(\mathbf{x}_1+\mathbf{x}_{12})\, e^{i[\mathbf{k}_1\cdot\mathbf{x}_1+\mathbf{k}_2\cdot(\mathbf{x}_1+\mathbf{x}_{12})]} \\ &= (2\pi)^3\,\delta_{\rm D}(\mathbf{k}_1+\mathbf{k}_2) \left(\frac{\bar{\rho}a^3}{M}\right)^2 \int d^3x_{12}\,\xi(x_{12})\, e^{i\mathbf{k}_2\cdot\mathbf{x}_{12}}\,. \qquad (2.50)\end{aligned}$$

In the above expression the presence of the Dirac delta function $\delta_{\rm D}(\mathbf{k}_1+\mathbf{k}_2)$ is analogous to the momentum-conserving term appearing in the Fourier representation of the Green's function in quantum field theory. Since $(2\pi)^3\delta_{\rm D}(0) = \int d^3x$ and factoring out this term, we get the expression of the power-spectrum

$$P(k) \;\equiv\; \langle|\tilde{\delta}(\mathbf{k})|^2\rangle \;=\; \frac{\bar{\rho}a^3}{M}\int d^3x_{12}\,\xi(x_{12})\,e^{i\mathbf{k}_2\cdot\mathbf{x}_{12}}\,. \qquad (2.51)$$

The relevance of the power-spectrum in characterizing the large-scale clustering lies in the fact that the fluctuation spectrum is the fundamental observational quantity provided by any theoretical model about the origin of primordial fluctuations. In Chapter 4 we will discuss in more detail how the primordial power-spectrum originates at the outset of the recombination epoch (*i.e.*, the epoch at which hydrogen recombines and the Universe becomes essentially transparent to the electromagnetic radiation), and how it depends on the matter content of the Universe. In the simple case of a Gaussian fluctuation field, the power-spectrum is the only quantity that is needed to describe the statistics. If this is the case, the Central Limit Theorem ensures that the Fourier transform of the fluctuation field can be written as $\tilde{\delta}(\mathbf{k}) = \sqrt{P(k)}\,\exp i\varphi_{\mathbf{k}}$, with phases $\varphi_{\mathbf{k}}$ randomly distributed in the interval $(0,2\pi]$.

A particularly simple model for the power spectrum is given by the power-law shape

$$P(k) \;=\; Ak^n e^{-\lambda_o k}\,, \qquad (2.52)$$

with A the amplitude of the spectrum and $n > -3$ in order to allow for the convergence of the integral of $P(k)$ at large wavelength. The presence of the small-scale exponential cutoff in eq.(2.52) is required for $n \geq 0$ in order to allow for the inversion of eq.(2.51). The value $n = 1$ for the spectral index corresponds to the scale-free Harrison-Zel'dovich spectrum [186, 400], that describes the fluctuations generated in the framework of the canonical inflationary scenario [179, 234, 235].

The power law (2.52) for the spectrum gives in turn a power law for the 2-point correlation function. Indeed, inverting eq. (2.51) for $R \gg \lambda_o$, we get

$$\begin{aligned}\xi(r) &= \frac{M}{\bar{\rho}a^3}\,\frac{A}{(2\pi)^3}\int d^3k\, k^n e^{i\mathbf{k}\cdot\mathbf{r}} \\ &= \frac{M}{\bar{\rho}a^3}\,\frac{A}{2\pi^2}\,\frac{\Gamma(n+3)}{n+2}\,\sin\!\left[\frac{(n+2)\pi}{2}\right] r^{-(n+3)}\,. \qquad (2.53)\end{aligned}$$

Thus, the detected power-law shape for the 2-point function, $\xi(r) \propto r^{-1.8}$, turns into a constant logarithmic slope of the power spectrum, with spectral index $n = -1.2$, at least at scales $r \lesssim 10\,h^{-1}$ Mpc. Although this value of the spectral index is decidedly far from that, $n = 1$, predicted by the inflationary paradigm, we should bear in mind that it refers to a scale-range where the primordial inflationary spectrum is likely to be distorted not only by the fluctuation evolution through the equivalence and recombination epoch, but also by the departure of gravitational clustering from the linearity regime.

As far as the amplitude A is concerned, one's hope is that it should be fixed by a theoretical model predicting the primordial fluctuation spectrum. However, there are at present no compelling theory about that, and is common to consider A as a free parameter to be fixed on the ground of observational data. A first normalization, that is often used, refers to the variance of the galaxy number counts inside volumes of a given size. The variance $\sigma^2_{\rm R}$ of the fluctuation field $\delta(\mathrm{x})$ at a given scale R is defined as

$$\sigma^2_{\rm R} \;=\; \frac{M}{\bar{\rho}a^3}\,\frac{A}{(2\pi)^3}\int d^3k\,P(k)\,W^2_{\rm R}(k)\,. \tag{2.54}$$

In the above equation, the scale R enters through the *window* function $W_{\rm R}(k)$, which provides an ultraviolet cut-off and has the effect of suppressing the modes with wavelength $\lambda \lesssim R$. Its detailed shape defines the profile of the sampling volume. For a window given by a "sharp" sphere of radius R, it is

$$W_{\rm R}(k) \;=\; \frac{3\,(\sin kR - kR\,\cos kR)}{(kR)^3}\,, \tag{2.55}$$

while a sphere with Gaussian profile has

$$W_{\rm R}(k) \;=\; \exp\left(-\frac{k^2R^2}{2}\right). \tag{2.56}$$

Observational results indicates a unity variance for the galaxy counts inside a sphere having radius $R = 8\,h^{-1}$ Mpc [102]. Thus, if matter density fluctuations, $\delta\rho/\bar{\rho}$ are related to galaxy count fluctuations $\delta n/\bar{n}$ according to

$$\frac{\delta n}{\bar{n}} \;=\; b_g\,\frac{\delta\rho}{\bar{\rho}}\,, \tag{2.57}$$

then the normalization condition $\sigma(R = 8\,h^{-1}\mathrm{Mpc}) = b_g^{-1}$ determines the power-spectrum amplitude A. In eq.(2.57), the parameter b_g is the so-called galaxy *biassing* factor, that accounts for a possible difference in the clustering of galaxies with respect to the underlying matter distribution and, in the linear-bias approximation, is independent of the scale. Usually, values $b_g > 1$ are considered, according to the suggestion of the *biassed* model (*e.g.*, see refs. [24, 106]) that galaxies are preferentially located in correspondence to density peaks, with a subsequent amplification of their clustering (see §4.3 below, for a more detailed discussion about biassed galaxy formation).

An alternative way to normalize the spectrum is provided by the J_3 integral that is defined as

$$J_3(R) \;=\; \int_0^R dr\,r^2\,\xi(r)$$

$$= \frac{M}{\bar{\rho}a^3}\,\frac{1}{2\pi^2}\,R^3 \int_0^\infty dk\,k^2\,P(k)\left[\frac{\sin(kR)}{(kR)^3} - \frac{\cos(kR)}{(kR)^2}\right] . \qquad (2.58)$$

Thus, the knowledge of $J_3(R)$ at a given scale from observational data [102] provides a further normalization of the power-spectrum. This procedure is particularly useful since, as observed by Groth & Peebles [172], the J_3 integral evolves according to linear theory if R is chosen so that $\xi(R) \ll 1$, even if at $x \ll R$ the clustering is strongly non-linear. This enable us to linearly evaluate J_3 from the primordial power-spectrum and compare it with estimates from galaxy redshift surveys. From the correlation analysis of the CfA1 sample, Davis & Peebles [102] found $J_3(10h^{-1}\,\mathrm{Mpc}) \simeq 270\,h^{-3}\,\mathrm{Mpc}^3$. Since $\xi(r) = 1$ at $r \simeq 5h^{-1}$ Mpc, one would like to push the estimate of J_3 to even larger scales, where no departure from linear evolution is expected. It is however an unfortunate fact of live that correlation analysis of available redshift samples does not provide reliable answers at scales $\gtrsim 10h^{-1}$ Mpc. A final warning that we should bear in mind concerns the fact that any estimate of σ_{R} or $J_3(R)$ is realized in redshift space, while local peculiar velocities are expected to distort the line-of-sight clustering in the real space (see ref.[375] for a discussion about this point).

Although it seems at first sight that the amount of information provided by the analysis of the 2-point function is completely equivalent to that provided by the power-spectrum analysis, nevertheless these two approaches are to be considered as complementary. In fact, while the usual correlation analysis is more sensitive in detecting the clustering at small scales, where the 2-point function exceeds unity, the power-spectrum approach is more suitable for investigating the low wavenumber, *i.e.* the large-scale, regime, where memory of initial conditions is still preserved, thanks to linear evolution. Thus, the power-spectrum analysis could well represent an useful tool to get precise hints about the large-wavelength shape of the primordial fluctuation spectrum.

Due to such advantages, several efforts have been recently devoted to tracing the power-spectrum implied by the observed object distribution. Baumgart & Fry [32], using the observed distribution of CfA and Perseus-Pisces surveys, detected the power-spectrum up to scales $\sim 100h^{-1}$ Mpc. Efstathiou *et al.* [125] and Saunders *et al.* [336] analysed the power-spectrum of the QDOT galaxies in terms of the variance of the counting inside cubical cells and Gaussian spheres, respectively. Testing scales of some tens of Mpcs, they found that such data are at variance with respect to the predictions of the standard Cold Dark Matter scenario. Peacock & Nicholson [283] analysed the distribution of radio galaxies, thus reaching very large scales. Peacock [282] found an expression for $P(k)$ to fit the data on the angular 2-point function of APM galaxies. Extrapolating this power-spectrum to larger scales, he observed that the same $P(k)$ provides a quite good fit also to IRAS, CfA and radio-galaxies, apart from suitable rescalings in the amplitude (see Figure 2.6). The resulting fluctuation spectrum exhibits a break toward large-scale homogeneity at wavelength $\lambda \gtrsim 200h^{-1}$ Mpc. On these scales, where the memory of the initial conditions is surely preserved, the effective spectral index is $n \simeq 1$, thus in agreement with the scale-invariant one predicted by inflation.

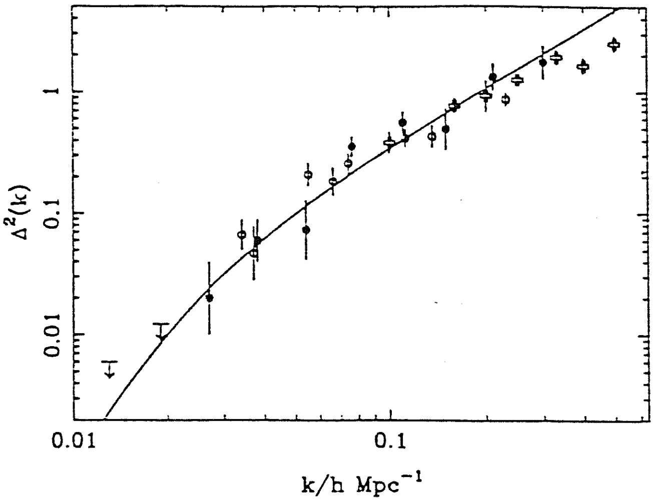

Figure 2.6: *The power-spectrum in dimensionless form, as the variance per* $\ln k$*:* $\Delta^2 = d\sigma^2/d\ln k$*. The solid line is the best-fit power-spectrum to APM data. Filled Points are for radio galaxies [283], with* $P(k)$ *reduced by a factor 3; open circles are are for IRAS [125, 336] and crosses are for CfA [32]. After [282].*

If one tries to account for these data by means of a CDM model, the amplitude of $P(k)$ requires a high normalization at large scales, whose linear extrapolation at small scales generates an excess of clustering. A similar result has also been found by Jing & Valdarnini [210] from the analysis of the Strauss *et al.* [358] redshift survey of IRAS galaxies, combined with the Postman *et al.* [308] cluster sample. They also evaluated the quadrupole in the CMB temperature fluctuations predicted by the resulting power-spectrum. By extrapolating their result to the much larger scales sampled by COBE [357], they found a remarkable agreement with the detected quadrupole for temperature fluctuations, once a biassing parameter $b \simeq 1.5$ for IRAS galaxies is taken. With the availability of extended galaxy redshift survey, namely the SSRS and CfA2 catalogues, Park *at al.* [278] and Vogeley *at al.* [384], analysed the resulting power-spectrum from $\sim 10h^{-1}$ Mpc scales, where the effective spectral index $n \simeq -1$ agrees with the results of correlation analysis, up to $\sim 100h^{-1}$ Mpc, where the amplitude of $P(k)$ makes the standard CDM model inconsistent with the data.

It is clear that the measurement of the power-spectrum traced by cosmic structures at large (50–$100h^{-1}$ Mpc) scales could become of crucial relevance, in the light of the possibility of detecting in the next few years anisotropies of the CMB temperature at small or intermediate angular scales ($\vartheta \lesssim 1°$). In fact, a comparison of the $P(k)$ profile for galaxy or cluster distributions with that of the primordial fluctuations could furnish precise hints about the formation and the evolution of observable structures.

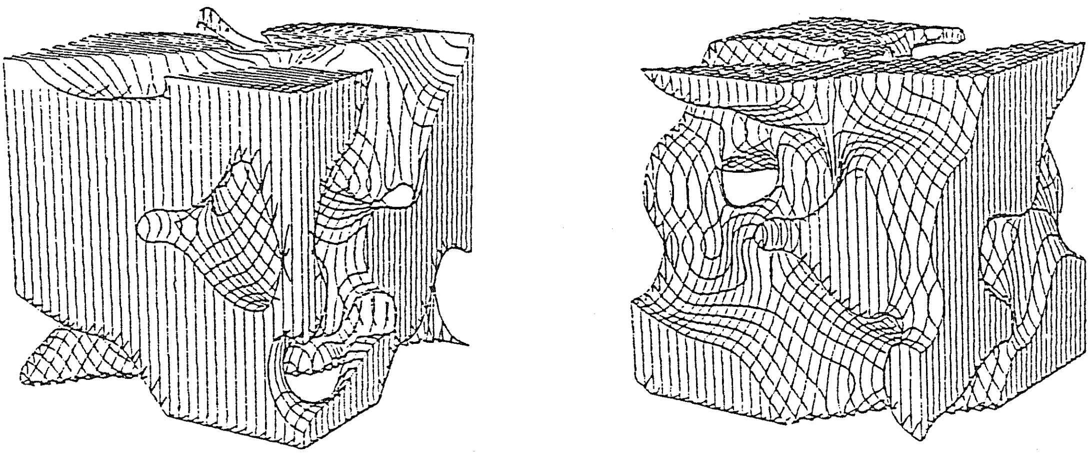

Figure 2.7: *Isodensity contours about the mean value in a Gaussian random field (from [163]). Left panel: regions above the mean density. Right panel: regions below the median density. It is apparent how the two regions are one the complement of the other.*

2.3 Topology of the large-scale structure

The description of the great variety of structures in the galaxy distribution, like filaments, voids, clusters, extending over a large range of scales, requires a global description of the geometry of the large-scale texture. Although correlation analysis provides rather useful information about clustering strength and scaling properties, nevertheless is says only a little about the shape of the emerging structures. In this respect, the approach based on the analysis of the topology of the large-scale clustering has been proved to be a useful tool in characterizing its geometry and "connectivity".

A detailed description of topological concepts in a formal mathematical language is out of our scope. Here we only briefly introduce the measures of topology introduced in cosmological context and what we learn from their application. In this context, the concept of "genus" has been introduced to describe the topology of isodensity surfaces, drawn from a density field. As an example, we show in Figure 2.7 the isodensity contour for a Gaussian density field, for both the regions above and below the mean density. The genus G can be introduced as

$$G = (\text{number of holes}) - (\text{number of isolated regions}) + 1\,. \tag{2.59}$$

In this way, we note that a single sphere has genus $G = 0$, a distribution made of N disjoint spheres has $G = -(N-1)$, while $G = 1$ for a torus. Roughly speaking, we can also say that the genus of a surface corresponds to the number of "handles" it has, or, equivalently, to the number of cuts that can be realized on that surface without disconnecting it into separate parts. A more formal definition of genus can be given by means of the Gauss-Bonnet theorem (see, *e.g.*, ref. [267]), which relates the curvature of the surface to the number of holes. According to this theorem, for any compact two-dimensional surface, the genus G is related to the curvature C according to

$$C = \int K\, dA = 4\pi(1-G). \tag{2.60}$$

Here, K represents the local Gaussian curvature of the surface that, at each point, is defined as the reciprocal of the product of the two principal curvature radii, $K = (a_1 a_2)^{-1}$. Since K has the dimension of length^{-2}, the curvature C and, thus, the genus are dimensionless quantities. For a sphere of radius r it is $K = r^{-2}$, so that $C = 4\pi$ and $G = 0$, as previously argued. Strictly speaking, while the genus of a surface gives the number of its "handles", eq.(2.59) defines a related quantity, that is the Euler-Poincaré (EP) characteristic [267]. In a sense, we can say that, while the genus deals with the properties of a surface, the EP characteristics describe the properties of the excursion set, *i.e.* of the part of the density field exceeding a density threshold value. Based on the Gauss-Bonnet theorem, it can be proved that genus and EP characteristics are completely equivalent in the three-dimensional case.

In topology analysis it is very useful to study the dependence of the genus of isodensity surfaces on the value of the density thresholds. If a high density value is selected, only a few very dense and isolated regions will be above the threshold and the genus is negative. For a very low threshold, only few isolated voids are identified and, again, the corresponding genus is negative. For thresholds around the median density value we expect in general that the isodensity surfaces have a multiply connected structure, with a resulting positive genus. These general considerations can be verified on a more quantitative ground for models having an analytically evaluable genus. The simplest case occurs for a Gaussian random field [7, 24, 184], which, in three dimensions, has a threshold dependent genus per unit volume

$$g(\nu) = \frac{1}{(2\pi)^2} \left(\frac{\langle k^2 \rangle}{3} \right)^{3/2} (1-\nu^2)\, e^{-\nu^2/2}. \tag{2.61}$$

In this expression, the density threshold is set so as to select only fluctuations exceeding ν times the *rms* value σ. Therefore, $g(\nu)$ describes the topology of the isodensity surfaces, where the fluctuations take the value $\delta = \nu\sigma$. Moreover,

$$\langle k^2 \rangle = \frac{\int P(k)\, k^2\, d^3k}{\int P(k)\, d^3k} \tag{2.62}$$

is the second order spectral moment, whose definition implies that $g(\nu)$ depends on the shape of the power spectrum, but not on its amplitude. Following eq.(2.61), several interesting features of the $g(\nu)$ curve appear. First of all, as expected for a Gaussian field which has the same structure in the overdense and underdense regions, $g(\nu)$ is an even function of ν, with its maximum at $\nu = 0$. This is characteristic of the so-called "sponge-like" topology. For $|\nu| < 1$ it is $g(\nu) > 0$, due to the multiple connectivity of the isodensity surfaces, while $g(\nu) < 0$ for $|\nu| > 1$, due to the predominance of isolated clusters or voids.

Different topologies are however expected when non-Gaussian fields are considered. Coles [81] proposed analytical expressions of the genus characteristic for a series of non-Gaussian fields, obtainable as local transformations of a Gaussian process. In the case of a distribution realized by superimposing dense clusters on a smooth background, isolated structures start dominating also at rather low density values and the $g(\nu)$ curve peaks at negative ν's. Viceversa, at large and positive ν values the distribution is that of isolated regions and $g(\nu)$ becomes more negative than expected for a Gaussian field. Quite significantly, this case is usually referred to as "meatball" topology. The opposite case occurs when the distribution is dominated by large voids, with objects arranged in sheets surrounding the voids. The resulting topology is usually called "cellular" or "Swiss-cheese" and the corresponding $g(\nu)$ curve peaks at positive ν's.

It is clear that topological measures can also be usefully employed when dealing with two-dimensional density fields. However, in this case some ambiguities arise, for example in distinguishing whether an underdense area is due to a tunnel or to a spherical void in three-dimensions. In addition, the interpretation of the genus in terms of the number of handles of an isodensity surface can not be applied in two dimensions. In this case, the topology measure can be given in terms of the EP characteristics, which is now defined as the difference between the number of isolated high-density regions and the number of isolated low-density regions. In this case, the EP characteristics per unit area at the overdensity level ν for a Gaussian random field is

$$g(\nu) \;=\; \frac{1}{(2\pi)^{3/2}}\,\frac{\langle k^2\rangle}{2}\,\nu\, e^{-\nu^2/2}\,, \tag{2.63}$$

so that $g(\nu)$ is an odd function of ν and $g(0)=0$.

In order to quantify the genus of the observed large-scale clustering, the first step is to extract a continuous density field starting from the discrete object distribution. This can be easily done by collecting the points in cells and then by smoothing the resulting cell count with a suitable window function. It is clear that in order to keep Poissonian shot noise from dominating the geometry of the smoothed field, the smoothing radius should be chosen not to be much smaller than the typical correlation length. Since the amplitude of the genus curve turns out to depend on the profile of the power spectrum through the second-order spectral moment, repeating genus measures for different smoothing radii gives information about the shape of $P(k)$. Moreover, since different profiles of $g(\nu)$ are expected for Gaussian and non-Gaussian fluctuations, topology analysis could be also suited to properly test the random-phase prediction of the inflationary paradigm, at least at the large scales, where no phase correlation is introduced by gravitational evolution.

Application of the genus statistics to the study of large scale structure has been employed in recent years (see ref.[257] for a review), both analysing the evolution of N-body simulations and observational data sets. Gott *et al.* [167] realized a detailed genus analysis for galaxy and cluster redshift samples. They found that, at scales much larger than the

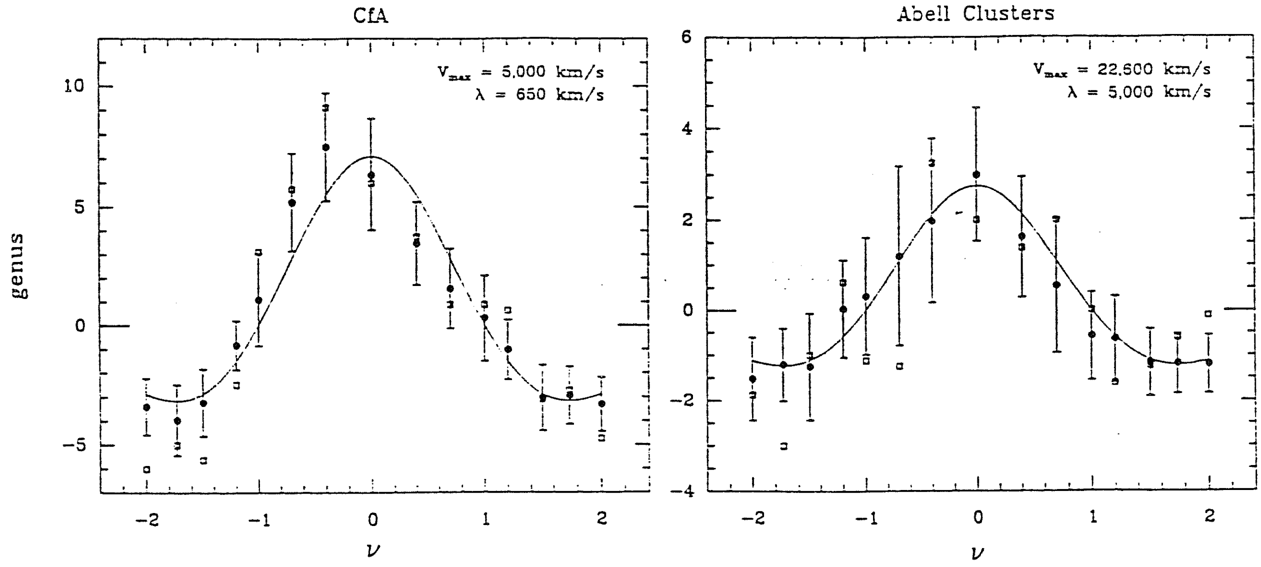

Figure 2.8: *The genus curves for* (a) *Abell clusters and* (b) *CfA galaxies, plotted together with the best fit random-phase approximation of eq.(2.61). Filled circles are the mean values between bootstrap resamplings and errorbars are the bootstrap one. Open squares are from raw data. It is apparent the shift toward meatball topology for the CfA sample (after [167]).*

correlation length, no departure from a sponge-like topology is detected, thus supporting the random-phase hypothesis. Viceversa, at higher resolutions, evidences of some meatball shift appear in the $g(\nu)$ curve, due to the effect of non-linear gravitational evolution acting at small scales (see Figure 2.8). A comparison with N-body results shows that a CDM model with Gaussian initial conditions [259] provides an overall quite good fit, apart from a slightly smaller meatball shift. Viceversa, hot dark matter (HDM) models, which develop a cellular topology, seem to be in trouble.

Although the analysis of contour genus in two dimensions was originally proposed to characterize the geometry of the CMB temperature fluctuations [81, 164], it has been recently applied to characterize the large-scale clustering of cosmic structures. Coles & Plionis [86] evaluated $g(\nu)$ for the galaxy distribution of the Lick map at different angular resolutions. They confirmed the meatball shift at small scales, while Gaussianity is rapidly recovered at larger angles. It is however clear that, at the depth of the Lick map, projection effects are likely to "gaussianize" the clustering geometry. A comparison of these results with simulated Lick maps, as obtained from CDM N-body simulations with non-Gaussian initial conditions, have been recently realized [85]. Although all the models produces some meatball shift, the positive-skewness ones do not reproduce Lick data. The Gaussian model is quite good, although it requires more large-scale power than that provided by CDM, while this problem is overcome by taking negative skewness models. Gott *et al.* [162] and Park *et al.* [311] analysed the two-dimensional genus for slices of three-dimensional galaxy surveys, further confirming the presence of meatball shift at small angular scales. Quite differently, Moore *et al.* [264] analysed the QDOT IRAS redshift survey and concluded that the galaxy distribution is consistent with a Gaussian random field, with sponge-like topology, up to scales $\sim 200h^{-1}$ Mpc. Using the genus amplitude to test the power-spectrum shape in the range (10-50)h^{-1} Mpc, they found a roughly constant spectral index $n \simeq -1$ thus consistent with the results of correlation analysis. Plionis *et al.* [303] analysed projected distributions of Abell and ACO clusters and compared them with synthetic catalogues. They found that the genus for the Abell distribution is consistent with that of high peaks of a Gaussian random field, while ACO clusters show a slight excess of meatball shift with respect to this model.

At the end of this section, it is worth recalling that the statistical information provided by the topology analysis mostly concerns the geometry of the large scale structure, rather than the clustering strength, like correlation functions do. In fact, once a given threshold ν is fixed, the genus measure is sensitive neither to the excess of "matter" in overdense regions nor to the *deficit* in the underdense regions. This is the reason for the independence of $g(\nu)$ of the amplitude of the power spectrum $P(k)$ and, thus, of the clustering strength. Thus, measuring topology represents a useful and complementary approach to the correlation analysis.

2.4 Mass and luminosity of cosmic structures

Other than studying the spatial distribution of galaxies and galaxy systems, a further important test for any theory of evolution and formation of these structures is provided by their luminosity distribution. If we were able to determine the existing relation between mass and luminosity for a given class of objects, we could in principle deduce their mass spectrum, in order to have hints about that statistics of the density fluctuations. In this Section we review the main observational data about mass and luminosity distribution of galaxies and galaxy systems. Then, we introduce the concept of mass-function for cosmic structures and discuss how it is related to global statistical properties of the matter distribution. The connection between mass and luminosity distribution, although not straightforward, is extremely important since it provides a very useful test for models describing formation and evolution of cosmic structures.

2.4.1 The galaxy luminosity function

An essential statistical tool for the investigation of the luminosity distributions of galaxies is the *luminosity function.* This is defined as the comoving number density of galaxies with luminosity between L and $L + \delta L$. Accordingly, we introduce the luminosity function by means of the probability,

$$\delta P \;=\; \Phi(L)\,\delta L\,\delta V\,, \tag{2.64}$$

of finding an object with luminosity between L and $L + \delta L$ in the volume element δV. Following the definition of luminosity function $\Phi(L)$, the number density of galaxies is expressed as

$$n_g = \int_0^\infty \Phi(L)\, dL\,. \tag{2.65}$$

In order to extract the galaxy luminosity function from observational data, it is useful to introduce the *luminosity distribution* $n_S(L)$. This is defined so that $n_S(L)\,\Delta L$ gives the number of galaxies contained in the sample S, in the luminosity interval of width ΔL centered on L [339]. Let $V_S(L)$ be the characteristic volume of the sample S at luminosity L. Then, the luminosity function $\Phi_S(L)$ of a galaxy sample can be expressed as

$$\Phi_S(L)\,\Delta(L) = \frac{n_S(L)\,\Delta L}{V_S(L)}\,. \tag{2.66}$$

Assuming large–scale homogeneity for the Universe, in the limit of large, randomly chosen sample volumes, all luminosity functions approach a universal limit defined by

$$\Phi(L) = \lim_{V_S(L)\to\infty} \Phi_S(L)\,. \tag{2.67}$$

We shall henceforth refer to this limit as the luminosity function for galaxies. In practice, one can only determine the luminosity function for finite samples. Sample luminosity functions will show deviations from the universal luminosity function that decrease as sample volumes increase. The size of these deviations depends on the nature of the processes that give rise to the distribution of galaxies in space and luminosity. For a randomly chosen sample volume, the luminosity function yields an *expected* luminosity distribution

$$n_e(L) = \Phi(L)\, V_S(L)\,. \tag{2.68}$$

Luminosity functions (and distributions) may be obtained for each subclass of galaxies which can be identified with criteria other than luminosity. Typical examples are represented by the UGC and the ESO/Uppsala catalogues, that are limited by galaxy apparent size. In this case, the relevant quantity is the diameter function, defined as the number density of objects, having angular size in a given interval.

A first attempt to find an analytical fitting expression to the observed galaxy luminosity function is due to Schechter [339]. He used the galaxy sample by de Vaucoleurs & de Vaucoleurs [378]. This sample includes galaxies with magnitude $m \leq 11.75$ and $b \geq 30°$, without including all the galaxies having angular distance $\leq 6°$ from the center of the *Virgo cluster* (in fact, the high velocity dispersion in this region is such that redshifts are not good distance indicators). In this analysis, he determined both the general luminosity function and the luminosity function only for galaxies contained inside clusters and found that the latter differs from the former only by a multiplicative factor. A good fit to the data was obtained with a luminosity function of the type

$$n_e(L)\, dL = \Phi^* V^* \left(\frac{L}{L^*}\right)^\alpha e^{-L/L^*}\, d\left(\frac{L}{L^*}\right), \tag{2.69}$$

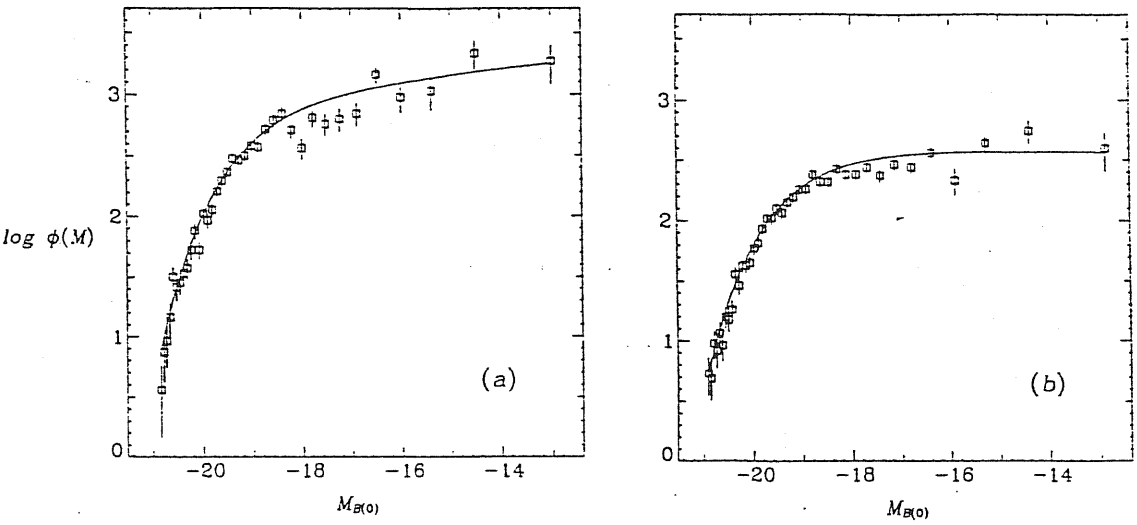

Figure 2.9: *Luminosity function* Φ(M) *for (a) two slices of the CfA2 sample, and (b) the CfA1 sample. Vertical lines are the* $\pm 1\sigma$ *error bars, and the smoothed curves are the fitted Schechter functions. The values of* M^* *and* α *for the fitted functions are (a)* −19.18 *and* −1.12; *(b)* −19.30 *and* −0.98. *Amplitudes are arbitrary (after [110]).*

with $\alpha = -5/4$ and L^* corresponding to an absolute magnitude $M^* = -21.4$ (taking for the Hubble parameter $h = 1/2$), and with $\Phi^* V^* = 216 \pm 6$ for the general luminosity function, while $\Phi^* V^* = 910 \pm 120$ for the cluster galaxies.

After Schechter's investigation of the galaxy luminosity function, many attempts have been devoted to provide fits to galaxy data using Schechter-like expressions. All such investigations converge to indicate that the power-law plus exponential tail always provides a good fit, although with some differences in the deduced values of the parameters (see ref.[136] for a review about observational aspects of the galaxy luminosity function). By analysing several magnitude-limited redshift surveys, Efstathiou *et al.* [122] found that the field galaxy luminosity function is well described by a Schechter function, with $\alpha = -1.07 \pm 0.05$, $M^* = -19.68 \pm 0.10$ and $\Phi^* = (1.56 \pm 0.34) \times 10^{-2}\ \mathrm{Mpc}^{-3}$ for $H_o = 100\,\mathrm{km\,s^{-1}\,Mpc^{-1}}$. Recently, de Lapparent *et al.* [110] calculated the luminosity function for two complete slices of the extension of the CfA redshift survey. They found that the shape of the luminosity function can still be approximated by a Schechter function with $M^* = -19.2 \pm 0.1$ and $\alpha = -1.1 \pm 0.2$. Large-scale inhomogeneities in the sample (comparable with the size of the sampled volume) introduce large fluctuations in the derived amplitude of the luminosity function; $\Phi^* = 0.020 \pm 0.005\, h^3\ \mathrm{Mpc}^{-3}$. A comparison with the luminosity function deduced from the first CfA survey [197] shows consistency at the $\sim 2\sigma$ level (see Figure 1.11).

The luminosity function of galaxies inside clusters has been analysed by Lugger [243], who considered nine Abell clusters. He found that in three clusters there appears to be a deficit of bright galaxies in the inner regions with respect to the outer regions, as expected on the ground of luminosity segregation effects. In the composite luminosity function of all nine clusters there is evidence for an excess of bright galaxies in the high–density regions relative to the low–density regions. Moreover, the faint end of the luminosity function is flatter in the high–density regions than in the low–density regions.

2.4.2 The multiplicity function of galaxy systems

The concept of luminosity function of galaxies can be generalized to describe the luminosity distribution of galaxy systems. A first attempt in this direction has been pursued by Gott & Turner [165], who introduced the *group multiplicity function*,$\Phi_g(L)$, defined as the luminosity function of groups in a group catalogue.

A first determination of the multiplicity function from a data sample has been performed by Gott & Turner [165], who selected groups from the Zwicky catalogue by using overdensity criteria. A further investigation of the multiplicity function has been carried out by Bahcall [15], that found a universal multiplicity function holding at the same time for rich Abell clusters and Turner & Gott's groups. In this analysis, the author firstly determined the expression for $\Phi(L)$ that represents the best fit to the data on rich Abell clusters,

$$\Phi(L) \; = \; \Phi^* \left(\frac{L}{L_o}\right)^{-2} e^{-L/L_o} (10^{12} L_\odot)^{-1} \, , \tag{2.70}$$

with $\Phi^* = 5.2 \times 10^{-7}\,\mathrm{Mpc}^{-3}$ and $L_o = 0.8 \times 10^{13} L_\odot$. This fit has been extended to include the groups of the Turner & Gott sample, with the same shape as in eq.(2.70), but with parameters $\Phi^* = 1.6 \times 10^{-7}\,\mathrm{Mpc}^{-3}$ and $L_o = 1.6 \times 10^{13} L_\odot$.

As a final comment, let us observe that the shape of the multiplicity function, as deducible from data samples, is very sensitive to the different techniques and definitions that are used for identifying galaxy systems on different scales. This show the necessity of obtaining homogeneous samples in which groups of galaxies are defined in an objective and scale-independent way.

2.4.3 The mass function

In order to describe the mass spectrum of cosmic structures, let us introduce the concept of *mass function*, $n(M)$, that is defined as the number density of objects having mass between M and $M + dM$. Although we expect that the shape of the mass function should depend on the statistics of the underlying matter distribution, a precise link with the shape of the primordial spectrum implies knowledge of the mechanisms of fluctuation evolution and structure formation. Due to the great relevance of a theoretical deduction of the mass function, many attempts have been devoted in this direction in order to account for the observed luminosity distribution of galaxies and galaxy systems. Despite the great variety of models that have been proposed in the literature, here we will mainly concentrate on the classical model originally proposed by Press & Schechter [309]. The reason for our choice is due to the fact that, although the major part of alternative approaches to the mass function represents just modifications of this model, it is remarkably good in keeping the main features displayed by observational data and cosmological N-body simulations.

In the framework of the Press & Schechter (PS) approach, let us assume the fluctuation field $\delta(\mathrm{x})$ to be Gaussian and introduce the smoothed field

$$\delta_{\rm R}(\mathrm{x}) \;=\; \int \delta(\mathrm{y})\, W_{\rm R}(|\mathrm{x}-\mathrm{y}|)\, d\mathrm{y}\,. \tag{2.71}$$

Here $W_{\rm R}(|\mathrm{x}|)$ represents a suitable window function that suppresses the fluctuation modes at wavelengths $\lesssim R$. Accordingly, the variance $\sigma_{\rm R}^2$ of $\delta_{\rm R}(\mathrm{x})$ is given by eq.(2.54). If $V_{\rm R}$ is the volume associated to a window of size R, then the mass scale associated to the smoothing radius R is $M = \bar\rho\, V_{\rm R}$, $\bar\rho$ being the mean matter density of the Universe. In the case of top-hat and Gaussian filters, it is

$$M \;=\; \frac{4}{3}\pi\,\bar\rho\, R^3 \qquad \text{and} \qquad M \;=\; (2\pi)^{3/2}\bar\rho\, R^3\,, \tag{2.72}$$

respectively. Accordingly, the mass variance scales as $\sigma_{\rm M}^2 = (M_o/M)^\beta$, with $\beta = 1 + n/3$ for a power-law spectrum $P(k) \propto k^n$. This indicates that for $n > -3$ the variance increases for small scale fluctuations, so that smaller structures go non-linear first and the clustering proceeds hierarchically. Press & Schechter's idea for deriving the mass-function was to identify today observable structures of mass M with overdensities of the primeval linear fluctuation field, that exceed a critical threshold δ_c, once smoothed at a scale R. They suggested that an overdensity above δ_c will turn into an object of mass M or greater, M being related to the smoothing radius R according to eq. (2.72). The critical density contrast δ_c is that required at the initial time, so as to give rise to an observable structure at the present epoch. If, for instance, we assume that structures become observable after recollapse, then linear theory for spherical collapse gives $\delta_c = 1.68$.

For a Gaussian field smoothed at the scale R, the probability of exceeding the threshold level, *i.e.* the mass fraction in objects with mass above M, reads

$$p(\delta_c, M) \;=\; \frac{1}{\sqrt{2\pi}\,\sigma_{\rm M}} \int_{\delta_c}^{\infty} \exp\left(-\frac{\delta^2}{2\sigma_{\rm M}^2}\right) d\delta \;=\; \frac{1}{2}\,\mathrm{erfc}\left(\frac{\delta_c}{\sqrt{2}\sigma_{\rm M}}\right)\,. \tag{2.73}$$

From the above expression, we can recognize a serious drawback of the PS approach. In fact, taking $dp(\delta_c, M) = -(\partial p(\delta_c, M)/\partial M) dM$ to be the fraction of the total mass in structures with mass between M and $M + dM$, its integral over the whole mass spectrum is $\int_0^\infty dp(\delta_c, M) = \frac{1}{2}$ and it fails to account for half the mass in the Universe. The origin of this problem lies in the fact that eq.(2.73) does not actually provide the fraction of mass in structures greater than M. For this to be the case, the mass in regions where $\delta < \delta_c$ should be assigned to structures of a greater mass, when smoothing the field on a larger scale. Press & Schechter overcame this problem simply by adding a factor 2 in front of eq.(2.73) and interpreting it as due to a secondary accretion of surrounding matter, according to the secondary infall paradigm (see, *e.g.*, ref.[175]).

Since eq.(2.73) can also be interpreted as the fraction of volume occupied by fluctuations that turn into structures of mass $> M$, the number density of objects with mass between M and $M + dM$ is

$$n(M)\,dM \;=\; -\frac{2}{V_{\rm R}}\,\frac{\partial p(\delta_c, M)}{\partial M}\,dM\,. \tag{2.74}$$

Taking the top-hat filter and the power-law shape for $P(k)$, eq.(2.74) gives

$$n(M)\,dM \;=\; \frac{\bar{\rho}}{\sqrt{\pi}}\left(1+\frac{n}{3}\right)\left(\frac{M}{M^*}\right)^{\frac{1}{2}+\frac{n}{6}}\exp\left[-\left(\frac{M}{M^*}\right)^{1+\frac{n}{3}}\right]\frac{dM}{M^2}\,. \tag{2.75}$$

The characteristic scale $M^* = (\delta_c/\sqrt{2})^{1/\beta}\,M_o$ corresponds to the scale above which the exponential tail starts to dominate the profile of the mass function. More complicated expressions for $n(M)$ will be expected for more "physical" power-spectra, like the CDM or HDM ones, which possess characteristic scales (see Chapter 4, below).

Other than the above mentioned problem, the PS approach also presents other conceptual difficulties, which make its qualitative agreement with observational data and N-body results even more surprising. For example, during gravitational collapse the profiles of the lumps probably do not maintain spherical symmetry, while asphericity is expected to be more important at small mass scales. In addition, other processes such as fragmentation or merging between perturbations at different scales could play a relevant role, but it is not clear how they can be accounted for in the framework of the crude PS approach. Several alternative approaches have been proposed in recent years to work out the mass function in the framework of more realistic models of structure formation (see, *e.g.*, refs.[239, 281] for comprehensive reviews on this subject). In Chapter 4, we will only briefly mention a modification of the classical PS approach, that we proposed in the framework of generalized biassed models of structure formation, in order to account for some aspects of non-spherical collapse [52].

Although the power-law plus exponential tail displayed by observed luminosity functions seems to be a quite natural outcome of many theoretical models of mass function, it is however not clear how mass and luminosity are related in a given class of cosmic structures. Thus, apart from the difficulty in properly accounting for the non-linear gravitational dynamics, which originates the "true" $n(M)$, a further crucial problem is to understand the non-gravitational (hydrodynamical) processes, which determine the scale-dependence of the M/L ratio to be used when passing from luminosity to mass spectrum.

In this context, it becomes very important to devise observational prescriptions to directly work out the mass of cosmic structures on the basis of their internal dynamics. Based on a sample of observed spiral rotation curves, Ashman *et al.* [12] determined the mass content of dark halos surrounding galaxies at the optical disk radius. The resulting mass-luminosity relation, $M \propto L^{0.6}$ implies a mass-function shape $n(M) \propto M^{-1.6}$ in the 10^{10}-$10^{12}\,M_\odot$ mass range. Thus, according to the PS prescription, an effective spectral index $n \sim -1$ is implied at such scales by the dark matter content of spiral galaxies.

Since galaxies surely represent virialized structures, it is quite easy to relate their dynamics to the respective mass content. The situation is however less clear when considering galaxy systems, that, at larger scales, have an uncertain degree of virialization. Some attempts to work out the mass function of galaxy groups have been recently realized by Pisani *et al.* [298]. They considered several group samples, based on different selection algorithms, and different mass estimators. They found that, although no significant differences arise when adopting different mass estimators, larger discrepancies are found by taking different group selection criteria. This shows how crucial it is to find an objective way to identify physical galaxy systems out of extended and complete galaxy samples.

The results of the analysis presented in §2.1.6 about the clustering of dark matter inside galaxy halos are discussed in details in two papers, that already appeared in *The Astrophysical Journal* (Bononmetto, Borgani, Persic & Salucci 1990, [45]; Borgani, Bonometto, Persic & Salucci 1991, [53]), and in a third paper, which is in press in *The Astrophysical Journal* (Salucci, Persic & Borgani 1992, [329]). More details can also be found in our *Magister Thesis* [49].

Chapter 3

Using fractals to measure the Universe

In this Chapter we introduce the concept of fractal structure and discuss its applications to the study of the large-scale galaxy clustering. After characterizing a scale-invariant structure through its fractal dimension, we show that different definitions of dimension can be given. In this context, the possibility of having scale-invariant structures with local scaling properties (multifractals) requires the introduction of an infinite set of dimensions, which corresponds to the infinite sequence of correlation functions. In order to measure this multifractal spectrum of dimensions, a list of algorithms has been introduced in the framework of the study of complex and chaotic systems. We introduce these methods and verify their reliability by applying them to fractal sets with *a priori* known dimensionality. We consider this a necessary step in order to assess the robustness of the results provided by the fractal analysis of galaxy and cluster distributions, where the limited amount of statistics and the presence of characteristic scales could affect the dimension estimates (see Chapters 5 and 6). We conclude the Chapter with a review of the more important results obtained up to now from the application of fractal analysis to the study of the large-scale structure.

3.1 Fractals and fractal dimensions

The concept of scale-invariance is of key importance in the characterization of many physical systems. For a long time, it has been recognized that scale-invariant behaviours are usually associated to the complexity displayed by a given structure, that renders completely inadequate the usual instruments based on differentiable geometry. A classical example is represented by the study of the Brownian motion, that led Perrin [293] at the beginning of the century to interpret it in terms of non-differentiable manifolds (curve and surfaces). Although the concept of non-differentiable geometry has been subsequently used in many physical and mathematical applications, the concept of "fractal object" has been explicitly introduced and formalized only quite recently by Mandelbrot [254]. He showed that a description in terms of fractals gives a good representation of a wide spectrum of phenomena, not only in physics, but also in biology, geology, economics, social sciences, and so on. Particularly fruitful it was the application of fractal techniques to the study of chaotic dynamical systems. Many of these systems display completely unpredictable trajectories in the configuration space, while their position in the corresponding phase space shows a tendency to be located around a structure that is neither fixed, nor periodic, and is usually called *strange attractor*. This kind of structure can not be represented by a means of a usual geometrical object; instead it is a fractal. As an example, Figure 3.1*a* shows the attractor generated by the phase space of the Henon map [190]. Another important phenomenological application of fractal concepts is in the study of turbulence. Despite the extreme difficulty in solving exactly the dynamics of turbulent flows in the regime of fully developed turbulence, their statistical characterization led to the discovery of relevant systematics. In particular, turbulent flows have been shown to be characterized by the presence of small-scale coherent structures, that are the signature of strongly non-Gaussian statistics, superimposed on a large-scale laminar (Gaussian) flow (see, *e.g.*, refs. [141, 226, 355]). This *intermittent* behaviour has been interpreted as due to the energy transfer from large scales and subsequent small-scale dissipation. Starting from the pioneering work by Kolmogorov [225], it has been recognized that modelling the dissipation in turbulent flows by means of cascading processes with fluctuations in the energy transfer leads to a fractal description of such intermittent structures [35, 36].

Despite the great difference existing between the dissipative dynamics of fully developed turbulence and the non-dissipative gravitational dynamics, nevertheless several common aspects can be identified. First of all, both the Navier-Stokes equation of fluidodynamics and the BBGKY equations which describe the gravitational dynamics (see Chapter 4, below), do not possess characteristic scales. Furthermore, numerical simulations of both non-linear gravity and turbulent flows are seen to generate small-scale coherent structures arising from a large-scale Gaussian background. On the ground of these similarities, we expect that the fractal description, so successful in characterizing the statistics of dissipative eddies in turbulent flows, can be usefully employed also to analyze the statistics of gravitational clustering.

Mandelbrot was also the first to apply fractals to describe the large-scale distribution of cosmic structures, while several other contributions have followed in recent years to better clarify the nature of the scaling properties associated with the gravitational clustering in terms of fractal language. In §3.4 we briefly mention the main results coming from the fractal analysis of the galaxy distribution. In this Section we introduce the concept of fractal structure and of fractal dimension, which will be of primary relevance for our study of the scaling properties of the large-scale structure of the Universe.

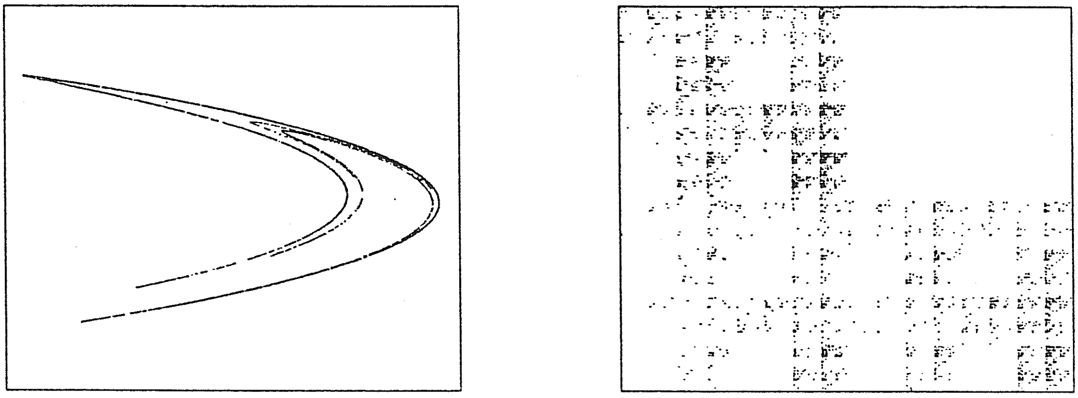

Figure 3.1: (*a*) *The phase space structure of the Henon attractor [190], which is generated by the iterative map* $x_1' = 1-1.4x_1^2+x_2$, $x_2' = 0.3x_1$; *15,000 point are plotted.* (*b*) *Two-dimensional projection of a three-dimensional multifractal structure generated by the random* β*-model discussed in* §*3.3. The rich variety of structures is apparent. Note also the presence of big voids, which also survive after projection. Also for the random* β*-model 15,000 points are plotted.*

3.1.1 What is a fractal ?

A rough definition of a fractal object can be given by referring to the scale-invariance displayed by these structures. In this sense, we say that a fractal is a geometrical structure which looks always the same (at least in a statistical sense), independently of the resolution at which it is observed. In Figure 3.1*b* we show an example of fractal point distribution, that is generated by means of a cascading process, according to the prescription of the β-model of turbulence [142] (see §3.3 below for a more complete description of this algorithm). From this picture, it is apparent that each part of the distribution is an exact replica of the whole.

A more formal and correct definition of a fractal set, as given by Mandelbrot [254], is "a mathematical object whose fractal (Hausdorff) dimension D_H is strictly larger than its topological dimension D_T". Thus, for a fractal point distribution in a d-dimensional ambient space it is $D_T = 0$ and $0 < D_H \leq d$. A fractal dimension $D_H = d$ characterizes a space-filling and homogeneous distribution. In order to rigorously define the Hausdorff dimension D_H for a given set $\mathcal{A}$ embedded in a d-dimensional ambient space, let us consider for any $r > 0$ the set of all the possible coverings of $\mathcal{A}$ ($\Gamma^r_{\mathcal{A}}$), having diameters $r_i \leq r$. Then, for any value of $\beta > 0$, we define the β-dimensional outer measure over $\mathcal{A}$ as

$$H^\beta(\mathcal{A}) = \lim_{r\to 0}\inf_{\Gamma^r_{\mathcal{A}}}\sum_i r_i^\beta \, . \tag{3.1}$$

The above expression defines the Hausdorff dimension D_H as the unique value of β that renders finite $H^\beta(\mathcal{A})$, with it vanishing for $\beta > D_H$ and diverging for $\beta < D_H$.

Another characterization of a fractal set can be given in terms of the *capacity dimen-*

sion. Let us consider the number $N(r)$ of d-dimensional hypercubes, all having the same side r, that are needed to cover $\mathcal{A}$. In the limit $r \to 0$, we expect for a fractal structure

$$N(r) \sim r^{-D_C}, \tag{3.2}$$

D_C being defined as the the capacity, or box-counting, dimension. It can be shown in general that $D_C \geq D_H$, while in most cases of practical interest the two definitions of dimension can be considered as equivalent. According to eq.(3.2), for a space-filling distribution we expect that $N(r)$ should decrease as r^{-3}, so that $D_C = 3$. In a similar way, for a filamentary structure it is $N(r) \sim r^{-1}$, while for a planar point distribution $N(r) \sim r^{-2}$, with resulting dimensions $D_C = 1$ and $D_C = 2$, respectively. In more general cases, non integer dimensions can be expected.

Note that the two above definitions of dimension deal with the number of required coverings, with no regard to the number of points contained inside each of them. In this sense, such dimensions depend on the "shape" of the distribution, and provide a purely geometrical description, while no information is given about the clumpiness, as correlation functions do. In order to extend the description in terms of fractal dimensions, so to include the clustering properties of a distribution, we need to introduce a probability measure $d\mu$. Then, the coarse grained probability

$$p_i(r) = \int_{\Lambda_i} d\mu(\mathrm{x}) \tag{3.3}$$

gives the "mass" contained inside the hypercube Λ_i of side r, with $i = 1, 2, \ldots, N(r)$. Accordingly, we take the set $P_r = \{p_i;\ i = 1, \ldots N(r)\}$ as the probability distribution over the $N(r)$ different states. The *information* content of the distribution [204] can be defined as

$$J(r, P_r) \equiv \log_2 N(r) + \sum_{i=1}^{N(r)} p_i \log_2 p_i\,. \tag{3.4}$$

For a homogenous distribution, all the boxes are equally populated, that is, all the states are equally probable. Correspondingly, the quantity $J(r, P_r)$ vanishes, thus indicating the absence of any information carried by unclustered structures. Viceversa, the maximum information content is obtained when one single state has unity probability, while it is vanishing for all the other states. In this case, $J(r, P_r) = N(r)$, while in general $0 \leq J(r, P_r) \leq N(r)$. We define the Shannon information (or entropy),

$$I(r, P_r) \equiv -\sum_{i=1}^{N(r)} p_i \log_2 p_i\,, \tag{3.5}$$

as the difference between the maximum information content and the actual information provided by the P_r distribution. Then, we introduce the *information dimension*

$$D_I = \lim_{r \to 0} \frac{I(r, P_r)}{\log_2(1/r)}, \tag{3.6}$$

which gives the rate of information loss as the resolution scale increases.

A further characterization of the scale-invariant properties of a fractal set is given in terms of the *correlation dimension*, originally introduced by Grassberger & Procaccia [169, 170]. For a given point $\mathbf{x}_i$ belonging to $\mathcal{A}$, let

$$C_i(r) = \frac{1}{N}\sum_{j=1}^{N}\Theta(r-|\mathbf{x}_i-\mathbf{x}_j|) = \frac{n_i(<r)}{N} \tag{3.7}$$

be the measure for the probability of finding $n_i(<r)$ out of the N points of the set within a distance r from $\mathbf{x}_i$. In eq.(3.7), Θ is the Heaviside step function. Then, we introduce the correlation integral

$$C(r) = \lim_{N\to\infty}\frac{1}{N}C_i(r) \tag{3.8}$$

whose scaling in the limit $r \to 0$ defines the correlation dimension, D_ν according to

$$C(r) \sim r^{D_\nu}. \tag{3.9}$$

Note that for a structure that behaves like a fractal at all scales it is not possible to define an average density, since it turns out to depend on the dimension of the fractal itself. In fact, if eq.(3.9) gives the scaling of the number of neighbors, the density around the i-th point will scale as r^{3-D_ν}, and, thus, unless $D_\nu = 3$, it decreases for increasing scales (note that this kind of behaviour is not expected for the distribution of cosmic structures, which, on grounds of the Cosmological Principle, should reach homogeneity at sufficiently large scales). However, we can define fractal dimensions in a finite scale range, while taking homogeneity at large scales, so as to define an average point density n, that does not depend on the extension of the distribution. In this case, following the definition of the 2-point correlation function given in §2.1, it is easy to see that it is related to the correlation integral of eq.(3.8) according to

$$C(r) = n\int_0^r d^3r'\,[1+\xi(r')] = \bar{N}\left[1+\left(\frac{r_c}{r}\right)^{\gamma}\right]. \tag{3.10}$$

Here, $\bar{N} = \frac{4}{3}\pi r^3 n$ is the number of neighbors within r expected for a homogeneous distribution, while the clustering scale r_c is related to the correlation length r_o as $r_c = [3/(3-\gamma)]^{1/\gamma}r_o$. Thus, according to the definition (3.9) of correlation dimension, the observed power-law shape of the 2-point correlation function implies that at $r \ll r_c$ the galaxy distribution behaves like a fractal with $D_\nu \simeq 1.2$, while assuming large scale homogeneity gives $D_\nu = 3$ at $r \gg r_c$.

However, a complete statistical description of a given distribution requires the knowledge of correlations or moments of any order. In a similar way, we expect that a complete characterization of the scaling properties of a fractal set should require the introduction of a hierarchy of scaling indices, that generalize those already introduced and that account for the scaling of correlation functions of different orders. This will be realized in the following by introducing the concept of the multifractal spectrum of generalized dimensions.

3.1.2 Generalized dimensions

The various definitions of fractal dimension that we have introduced represent only some particular cases of a continuous sequence of scaling indices, known as generalized spectrum of multifractal dimensions [191, 35, 276] (see ref.[277] for a comprehensive review of multifractals).

A first definition can be given in terms of the generalized Hausdorff dimensions, which represents the extension of the classical Hausdorff dimension introduced according to eq.(3.1). To this purpose, let p_i be the measure associated to a given set Λ_i, and having diameter r_i, as defined by eq.(3.3). Thus, we define the partition function

$$\Gamma(q,\tau) = \begin{cases} \lim_{r\to 0} \inf_{\Gamma^r_{\mathcal{A}}} \sum_i \frac{p_i^q}{r_i^\tau} & \tau \le 0 \ , \quad q \le 1, \\ \lim_{r\to 0} \sup_{\Gamma^r_{\mathcal{A}}} \sum_i \frac{p_i^q}{r_i^\tau} & \tau \ge 0 \ , \quad q \ge 1 . \end{cases} \tag{3.11}$$

For each value of q, the respective $\tau(q)$ is defined as the unique value such that $\Gamma(q,\tau)$ is a finite constant. Then, the generalized Hausdorff dimensions are defined as

$$D(q) = \frac{\tau(q)}{(q-1)} \quad , \quad D(1) = \lim_{q\to 1} D(q) \ . \tag{3.12}$$

From this definition, it is easy to recognize that $D_H = D(0) = -\tau(0)$.

A further set of scaling indices used to characterize fractal structures is given by the Renyi dimensions [318]. Let us consider a covering of $\mathcal{A}$ formed by $N(r)$ cells of the same size r. Then, if n_i is the number of points in the cell i, the occupancy probability $p_i = n_i(r)/\sum_j n_j$ is the measure associated to the i-th box. The Renyi dimensions are defined as

$$D_q = \lim_{r\to 0} \frac{1}{q-1} \frac{\log \sum_i p_i^q}{\log r} \tag{3.13}$$

In this case, the capacity dimension corresponds to the $q = 0$ case, while the information dimension is recovered in the limit $q \to 1$. In general, it can be proved that $D(q) \le D_q$, while in most cases of practical application the two definitions (3.12) and (3.13) of generalized dimensions can be considered as completely equivalent.

A slightly different definition is represented by the Minkowski-Bouligand dimensions. In this case, the covering of the fractal set is obtained by means of spheres of radius r, that are centered each at a point belonging to the fractal. If $n_i(< r)$ is the number of points within r from the i-th point, the Minkowski-Bouligand dimensions are defined as

$$D'_q = \lim_{M\to\infty} \frac{1}{N^2} \lim_{r\to 0} \frac{1}{q-1} \frac{\log \sum_i n_i^{q-1}}{\log r} \ . \tag{3.14}$$

This definition represents the generalization of the correlation dimension given by eq.(3.9), and it can be proved that the Renyi and Minkowski-Bouligand dimensions are completely equivalent [116].

An important class of fractals are self-similar mono-fractals. These fractal sets are characterized by the fact that every part of the set represents an exact replica of the whole set (in a statistical sense), so that the scaling properties are the same around each point. For these fractals $D_q = D_H$ for any q, so that a single dimension gives a complete characterization of the whole set. More complex fractal sets are represented by the so-called multifractals. In this case, the entire spectrum of generalized fractal dimensions D_q is required to describe the local character of the scaling properties. For a multifractal, it can be shown that the relation $D_q \leq D_{q'}$ when $q \geq q'$ is obeyed under general conditions.

According to the definitions (3.11) of the Γ partition function and (3.13) of Renyi dimensions, in the case $q \gg 0$ the summations are dominated by the densest regions in the set, while for $q \ll 0$ the least dense regions give the largest contribution. In this sense, for positive q's the generalized dimensions provide information about the scaling properties of the particle distribution in the regions of high density, as correlation functions do, and for $q \ll 0$ account for the scaling inside the underdense regions, thus providing a comprehensive statistical description of the entire point distribution.

3.1.3 The spectrum of singularities

A further characterization of a fractal set can be given in terms of the so-called spectrum of singularities. For a given fractal structure, we can define the "local dimension", or "crowding index", α through the scaling of the number of points $n_i(r)$ contained inside the i-th box. For a fractal structure, we expect that at small scales r it is

$$n_i(r) \sim r^{\alpha_i}, \tag{3.15}$$

where in general the scaling index α_i depends on the chosen box. Accordingly, we can group all the boxes that are characterized by a crowding index in the range $[\alpha, \alpha + d\alpha]$ into a subset $S(\alpha)$. Thus, in the scaling regime, the number of boxes $dN_\alpha(r)$ needed to cover $S(\alpha)$ behaves like

$$dN_\alpha(r) = d\rho(\alpha)\, r^{-f(\alpha)}, \tag{3.16}$$

$f(\alpha)$ being defined as the Hausdorff dimension of $S(\alpha)$. In the above expression, the measure $d\rho(\alpha)$ represents the density of scaling indices in the interval $[\alpha, \alpha + d\alpha]$. In this description, a generic fractal set is interpreted as formed by interwoven sets, each having dimension $f(\alpha)$ and formed by the distribution of those singularities, whose scaling index is α. Note, that in a d-dimensional ambient space, those boxes which have $\alpha > d$ are not singularities (peaks) of the density field, but minima of the distribution.

In order to relate the description given in terms of the singularity spectrum to that based on the D_q dimensions, we note that the moments of the box counts appearing in eq.(3.13) can be written as integrals over α, according to eq.(3.16):

$$\sum_{i=1}^{N(r)} p_i^q(r) \propto \int d\rho(\alpha)\, r^{\alpha q - f(\alpha)} . \tag{3.17}$$

In the $r \to 0$ limit, the above integral can be computed with the usual saddle point method, so that the definition (3.13) of Renyi dimensions gives

$$D_q = \frac{1}{q-1} \min_{\alpha}[\alpha q - f(\alpha)] . \tag{3.18}$$

Thus, the D_q dimensions are obtainable from $f(\alpha)$, while the inversion of eq.(3.18) gives the $f(\alpha)$ spectrum of singularities from the multifractal dimensions. It is worth noting that, in the case of a monofractal structure, it is $D_q = D_H$ for any q value, so that $f(\alpha)$ degenerates into a single point, whose coordinates are $(D_H, f(D_H) = D_H)$. In this sense, we can say that a monofractal structure has global scaling properties, since all the singularities have the same scaling index $\alpha = f(\alpha) = D_H$, while for a multifractal structure the scaling of the local density is different in different points.

According to eq.(3.18), for each q value, the corresponding D_q is determined by the crowding index $\alpha(q)$, that satisfies to the extremum conditions

$$q(\alpha) = \left. \frac{df(\alpha')}{d\alpha'} \right|_{\alpha'=\alpha} \quad ; \quad \tau_q = q\alpha - f(\alpha) . \tag{3.19}$$

This shows that the pairs of variables (q, τ_q) and $(\alpha, f(\alpha))$ give equivalent descriptions of the scaling properties of a fractal set and are related by the Legendre transform (3.19). Furthermore, the decreasing trend of D_q constrains $f(\alpha)$ to be convex function $(f''(\alpha) < 0)$. Since $S(\alpha)$ is a subset of the whole distribution, it follows that $N_\alpha(r) \leq N(r)$, so that $f(\alpha) \leq D_H$. The maximum allowed value of $f(\alpha)$ occurs in correspondence to $q = 0$, that is $f_{max} = D_H$, while the information dimension satisfies the relation $f(D_I) = D_I$. Inverting eq.(3.18), it is easy to see that the asymptotic values of D_q for $q \gg 0$ and $q \ll 0$ are given by the minimum and maximum allowed α values. That is,

$$\alpha_{min} = \lim_{q \to +\infty} D_q \quad ; \quad \alpha_{max} = \lim_{q \to -\infty} D_q . \tag{3.20}$$

This is a rather obvious consequence of the fact that, following the definition (3.15) of crowding index, its lowest and highest values dominate the scaling inside the overdense and underdense regions, respectively.

In Figure 3.2 we show the D_q spectrum of generalized dimensions for the random β-model plotted in Figure 3.1*b*, along with the corresponding $f(\alpha)$ spectrum. The multifractality of the structure is apparent from the D_q shape or, equivalently, from the spreading of the crowding index values over a quite large interval. The correspondence between f_{max} and D_o is clearly visible, while also the asymptotic relations (3.20) are rather well reproduced.

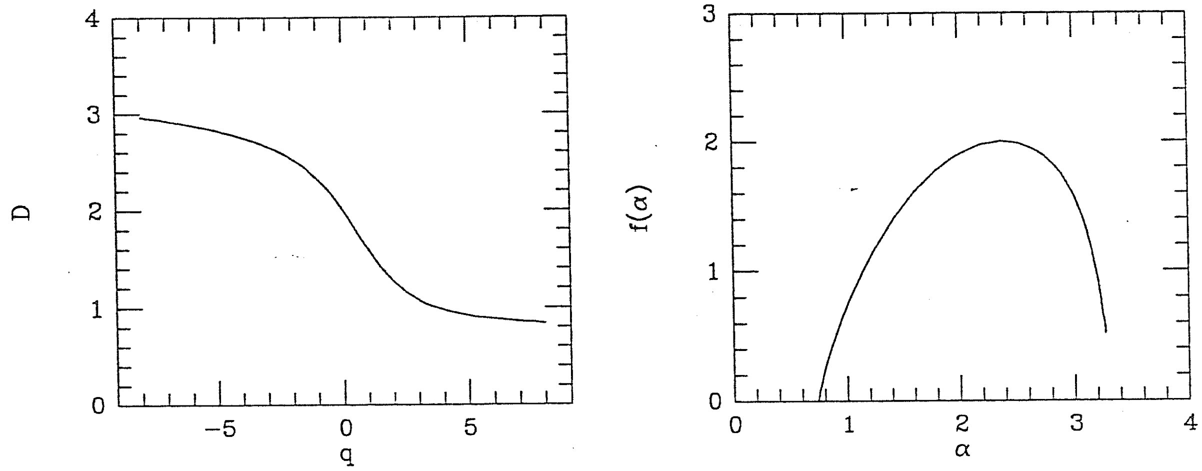

Figure 3.2: (*a*) *The multifractal dimension spectrum, D_q, for the random β-model of Figure 3.1b and* (*b*) *the corresponding $f(\alpha)$ spectrum of singularities, related to D_q according to eq.(3.19).*

3.2 Methods of fractal analysis

All the definitions of fractal dimensions, which we have introduced, are given in the limit $r \to 0$, that can be reached only when an arbitrarily large number of points is allowed. However, in practical estimates of the scaling properties of a point set, one is usually dealing with a finite number of points, so that the limit $r \to 0$ is never reached. The finite size of galaxies and galaxy clusters, as well as the presence of numerical smoothing in N-body simulations, put limits to the achievable small-scale resolution. In addition, small-scale noise can mask the fractal behavior, and a homogeneous distribution at the largest scales, as expected in the cosmological context for the galaxy distribution, also limits the scaling range. It is therefore necessary to resort to approximate methods that provide information on the scaling properties over a limited range of scales; these methods clearly have to converge to the rigorous definitions when the resolution in the sample increases. In some cases, different "characteristic" or "effective" fractal dimensions may be properly associated with different scale ranges if a sufficiently extended "local" scaling behavior is observed, in the spirit of "intermediate asymptotics" [26, 310]. In this sense, from a physical point of view a fractal behavior cannot be separated by intermediate scaling properties. In this Section we describe the algorithms of fractal analysis that will be applied in following chapters.

The **box-counting** (BC) algorithm is one practical method for computing the spectrum of generalized dimensions. This method uses the classic definition of Renyi dimensions (see eq.[3.13]). In this approach, we define the partition function

$$Z^B(q,r) = \sum_{i_b=1}^{N_b(r)} [p_{i_b}(r)]^q, \tag{3.21}$$

where $N_b(r)$ is the number of boxes with side r which are needed to completely cover the set and $p_i(r) = n_i(r)/N$, $n_i(r)$ being the number of points in the i-th box and N the total number of points. For a fractal set, at small values of r one has that

$$Z^B(q,r) \propto r^{\tau(q)}, \tag{3.22}$$

and $D_q = \tau(q)/(q-1)$ is an estimate of the generalized dimension of order q. The well-known box-counting dimension is found for $q = 0$. By plotting $\log Z^B(q,r)$ versus $\log r$ one immediately realizes whether the partition function possesses a power-law behavior. The generalized dimension D_q is then obtained by least-square fitting $\log Z^B(q,r)$ versus $\log r$ or by evaluating the average value of the local logarithmic slope of $Z^B(q,r)$ in the region of power-law behavior. As discussed above, positive values of q provide information on the overdense parts of the distribution, while negative q's are relevant to the particle distribution in the underdense regions.

A second method to compute the dimension spectrum is based on the **correlation integral** (CI) method proposed by Grassberger & Procaccia [169] and extended by Paladin & Vulpiani [276]. In this approach, which is based on the definition of Minkowski-Bouligand dimensions (see eq.[3.14]), one introduces the partition function

$$Z^C(q,r) = \frac{1}{N^2}\sum_{i=1}^{N}[n_i(<r)]^{q-1}, \tag{3.23}$$

In the above expression $n_i(<r)$ is the number of particles inside a sphere of radius r centered at the i-th object and N is the total number of points in the distribution. For a fractal distribution, at small r, the scaling relation

$$Z^C(q,r) \propto r^{\tau(q)}, \tag{3.24}$$

holds; the expression (3.24) gives another estimate of the q-th generalized dimension. The previously discussed correlation dimension is found for q=2.

A further method is based on the **density reconstruction** (DR) algorithm, that represents a sort of inversion of the CI method [168]; instead of measuring for each point the number of particles within a fixed distance, this method is based on the estimate of the minimum radius which includes a fixed number of points. The DR partition function is defined as

$$W(\tau,p) = \frac{1}{N}\sum_{i=1}^{N}[r_i(p)]^{-\tau}, \tag{3.25}$$

where $r_i(p)$ is the radius of the smallest sphere centered on i and containing Np points, with $\frac{2}{N} \leq p \leq 1$. In the scaling regime, the DR partition function depends upon the probability p according to

$$W(\tau,p) \propto p^{1-q}. \tag{3.26}$$

This gives a further evaluation of the set of D_q's. Note that in this case one obtains q (and consequently the dimension) as a function of τ.

Another useful algorithm is the so-called **nearest-neighbor** (NN) method [13]. For each point i of the set, let ${}_k\delta_i$ be the distance of the particle i to its $k-th$ neighbor. Then, the partition sum

$$
{}_k\bar{\delta} = \left[\frac{1}{n} \sum_{i=1}^{n} {}_k\delta_i{}^{\beta} \right]^{\frac{1}{\beta}} , \tag{3.27}
$$

can be shown to scale as ${}_k\bar{\delta}^{\beta} \propto n^{-\frac{\beta}{h(\beta)}}$, where n is the number of points in a randomly selected subsample of the whole distribution; the fixed point of $h(\beta)$, $h(D_C) = D_c$, is an estimate of the capacity dimension. Badii & Politi [14] have shown that eq.(3.27) can be used to estimate the Renyi generalized dimensions. To this end, let us consider the partition function

$$
G(k,n,\tau) = \frac{1}{n} \sum_{i=1}^{n} [{}_k\delta_i(n)]^{-\tau}. \tag{3.28}
$$

For a fractal distribution it is $G(k,n,\tau) \propto n^{q-1}$, independent of the neighbor order. Again, this methods furnishes q as a function of τ. Although the original formulation of the NN method was based on the identification of the nearest-neighbors, it is often very useful to consider higher-order neighbors, in order to eliminate small-scale noise [14]. Neighbor orders $k = 3,4$ are shown to be adequate in most cases, while taking even higher orders could miss the details of the small-scale statistics.

A final method to compute the spectrum of generalized dimensions has recently been proposed by Martinez *et al.* [250] and by Van de Weygaert, Jones & Martinez [377]. This method is based on the calculation of the minimal spanning tree (MST) [273, 397] connecting the points of a subsample which has been randomly selected from the distribution. For a sample of m points, the MST is defined as the unique graph connecting all the points, with no closed loops and having minimal length. From an operative point of view, the MST is constructed as follows. Starting from a randomly selected point of the subsample, we find its nearest neighbor. These two points have a distance λ_1 and form the tree T_1. At the k-th stage a point j not yet in the tree T_{k-1} has a distance $d_{jT_{k-1}}$ from the tree itself, defined as the minimal distance between j and all the points already included in the tree. The point having minimal distance from the tree is then added to T_{k-1}, which is now T_k. The MST of the sample is then given by T_{m-1} and contains the set of lengths $\{\lambda_i\}_{i=1}^{m-1}$. Statistical measures based on the construction of the MST have already been applied in studies of galaxy clustering [28, 304], and show that this structure gives an efficient characterization of the clustering pattern.

The MST method has been introduced with the goal of providing a close estimate of the generalized Hausdorff dimensions. In fact, the construction of the MST is based on the search for a tree with minimal length. This is somewhat similar to the search for a minimal covering required by the definition of the Hausdorff dimension. For this reason the MST tries to estimate the generalized Hausdorff dimension $D(q)$ rather than the Renyi dimensions D_q

[377]. In this approach, the basic quantity is the partition function

$$S(m,\tau) = \frac{1}{m-1}\sum_{i=1}^{m-1}[\lambda_i(m)]^{-\tau}. \tag{3.29}$$

For a fractal set it is $S(m,\tau) \propto m^{(q-1)}$. A fitting of this relation allows one to check the scaling properties of the sample and the dimensions D_q.

It is important to note that there is a crucial difference between the first two methods (BC and CI) and the remaining three (DR, NN and MST). In fact, the first two algorithms evaluate the partition function by a priori fixing the scale r. The "effective" dimension $D_q(r)$ (as given by the local logarithmic slope of the partition function) is thus a function of the physical scale r. This fact allows for disentangling the contributions of different scaling regimes at different scales, i.e. for detecting a scale-dependent fractal behavior (or, eventually, a non-scaling behavior). The other methods, however, evaluate the partition functions as functions of the probability p or of the number of points in random subsamples. All these quantities do not bear a one-to-one correspondence with the physical scale; for instance, in the DR method a given probability is associated with a broad distribution of scales, providing information on the distance scale only on average. As a consequence, the behavior of the partition function at a given value of p, n or m mixes several contributions from different scale ranges. This may cause troubles in situations where different scaling regimes are present at different scales. In addition, the shape of the scale distribution is a function of τ, being narrower for large values of τ and much broader for negative τ's. This dependence on τ leads to weighting the various scales in a different way at different values of τ; a monofractal distribution with two scaling regimes at different scales may thus be spuriously viewed as a multifractal distribution when analyzed with these methods. An example of this behavior is given in the next Section.

Before closing this Section, we stress the fact that the various generalized dimension estimators are based on different assumptions and they may be affected by different systematic errors. In addition, these methods may be sensitive in a different way to the scaling properties on different scale ranges, a fact which may be of relevance in the analysis of natural fractal sets, where the scaling behavior may be confined to a finite range of scales and where different types of fractal properties may be encountered at small and large scales. This aspect is extremely relevant in the cosmological context, where fractality of galaxy clustering is detected at small scales, while homogeneity is expected to hold at large enough scales. For the above reasons, some differences should a priori be expected among the results provided by the various multifractal analysis methods. The limited statistics normally encountered in the study of galaxy samples may be another source of problems. Analogously, the presence of boundary effects (related to the peculiar shapes of the galaxy surveys) may potentially affect the results.

3.3 Analysis of synthetic fractal structures

In order to assess the reliability of the results provided by the different multifractal estimators when dealing with a finite number of data points, in this Section we apply the different algorithms to fractal distributions with *a priori* known scaling properties. In particular, we consider a monofractal structure with dimension $D = 1$ and a multifractal structure. We also analyze a scale-dependent monofractal distribution to explore how the different methods are sensitive to scale changes in the fractal behavior. This is particularly interesting since it turns out that a scale-dependent monofractality may sometimes be seen as a spurious multifractality. In our opinion, these tests are a necessary step in order to obtain reliable estimates of multifractal properties from galaxy data. Clearly, the results discussed here should be of value for any fractal analysis of point distributions with a finite amount of data, independent of their physical origin.

3.3.1 The fractal-generating algorithm

The point distributions considered here have been generated by a modification of the β-model and random β-model of turbulence [142, 143], which have recently been proposed as simplified models of the large-scale distribution of galaxies [86, 310, 311, 212]. Such models provide fractal point distributions through a cascading process, that, in the context of turbulence, should represent the energy transfer from large to small scales, where dissipation occurs. To implement the cascading process, we start with a "parent" cube of side L, which breaks into 2^3 "son" subcubes, having side $L/2$. Let β be the fraction of the mass of the "parent" cube which is assigned to a given subcube. By repeating k times this cascade iteration, we end up with 2^{3k} small cubes with side $l_k = L/2^k$. Accordingly, the mass contained inside a cube is

$$M_k \sim \prod_{j=1}^{k} \beta_j \, , \tag{3.30}$$

and depends on its fragmentation history $\{\beta_1, ..., \beta_k\}$. Thus, the q-th order moment for the mass distribution inside the 2^{3k} cubes reads

$$\langle M_k^q \rangle \sim \int \left\{ \prod_{j=1}^{k} d\beta_j \, \beta_j^q \right\} P(\beta_1, ..., \beta_k) \, , \tag{3.31}$$

where $P(\beta_1, ..., \beta_k)$ is the probability distribution for the mass redistribution after k fragmentations. Assuming no correlation between different fragmentation iterations, then $P(\beta_1, ..., \beta_k) = \prod_{j=1}^{k} P(\beta_j)$. Since at each step the single cube is split into eight subcubes, $P(\beta)$ can be in general written as

$$P(\beta) = \sum_{i=1}^{8} c_i \, \delta(\beta - f_i) \, , \tag{3.32}$$

being $\sum_{i=1}^{8} c_i = 1$. In the above equation, each f_i represents the mass fraction assigned to a subcube and $\sum_{i=1}^{8} f_i = 1$ as required by mass conservation. Accordingly, the moment (3.31) evaluated at the scale $l_k = 2^{-3k}L$ is

$$\langle M_k^q \rangle \sim \left(\sum_{i=1}^{8} f_i^q \right)^k \propto l_k^{-\log_2(\sum_{i=1}^{8} f_i^q)} \qquad (3.33)$$

and the resulting spectrum of generalized dimensions reads

$$D_q = \frac{\log_2 \sum_{i=1}^{8} f_i^q}{1-q}. \qquad (3.34)$$

According to eq.(3.34), the number of non-vanishing f_i's determines the value of the Hausdorff dimension, while the asymptotic values $D_{-\infty}$ and $D_{+\infty}$ are fixed by the smallest and largest f_i, respectively. Once the final density field is obtained, its Monte Carlo sampling gives the required point distribution. A particularly simple case occurs when all the non-vanishing f_i's take the same value. In this case, eq.(3.34) gives a monofractal spectrum, with the dimension value uniquely fixed by the number of non-vanishing f_i's. A homogeneous space-filling distribution is obtained when the f_i's are all equal and different from zero, so that the mass is equally distributed between all the subcubes.

Another interesting case occurs when the f_i values change with the iteration step. The corresponding structure is not self-similar, but has different scaling properties on different scale-ranges, or a non-scaling behavior, depending upon the selected scale dependence of the f_i's. This case has been discussed in detail in refs.[310, 311], along with its applications to describe the large-scale galaxy clustering.

3.3.2 The monofractal distribution

We start our analysis by considering a monofractal point distribution with $D = 1$. According to eq.(3.34), this can be obtained from the above described cascading process by taking

$$P(\beta) = \frac{1}{4}\,\delta(\beta - 0.5) + \frac{3}{4}\,\delta(\beta) \qquad (3.35)$$

for the probability of the mass distribution.

Figure 3.3 reports the results of the multifractal analysis of the corresponding point distribution. To check the sensitivity of the various methods to changes in the statistics, we consider both a distribution with about 18,000 points, and a random subsample of 3,000 points. In Figure 3.3, the five different columns report the results of the methods introduced in the previous Section. The different panels in each column refer to different values of q or τ; they report the local logarithmic slopes of the partition functions, as obtained by a linear least-square-fit over three adjacent values (in log-log coordinates). Here and in other following plots, solid circles refer to the entire distribution, open triangles refer to the random subsample. A meaningful value of the "effective" generalized dimension is defined by the constancy

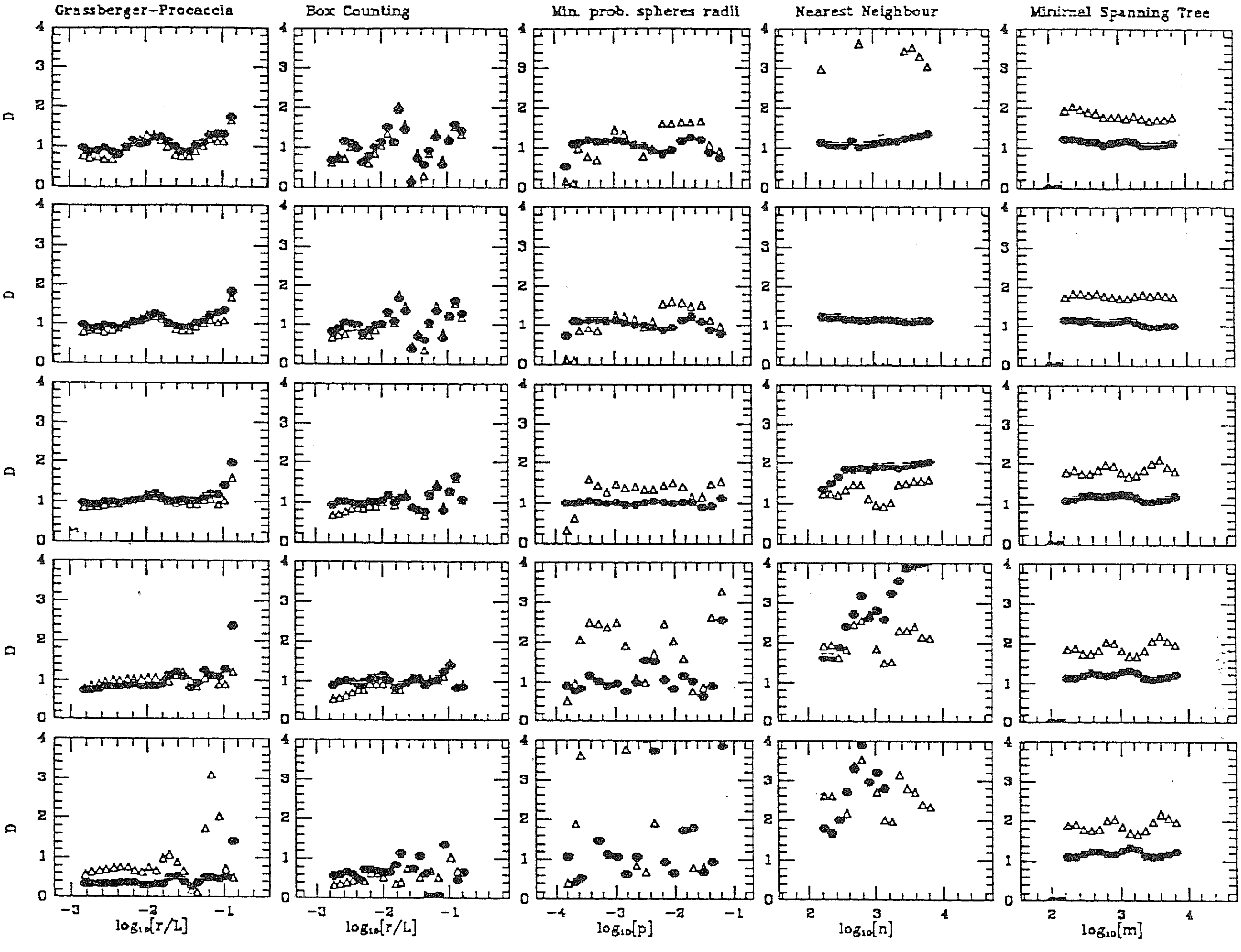

Figure 3.3: *The local dimension as estimated from the slope of the partition functions for a pure monofractal structure with* $D = 1$*; the local slopes have been obtained as a running least-square-fit over three adjacent values of the partition function. Filled circles refer to the complete distribution and open triangles refer to the 3000 points random subsample. Column 1 reports the results of the CI method, column 2 refers to the BC method, column 3 to the DR method, column 4 to the NN method and column 5 to the MST. In columns 1 and 2, the five panels refer to* $q = -2, 0, 2, 4$ *and* 6 *from bottom to top. In column 3, the five panels refer to* $\tau = -4, -2, 0.1, 4, 6$ *from bottom to top. In columns 4 and 5, the panels refer to* $\tau = -6, -4, -2, 0.1, 2$ *again from bottom to top.*

of the logarithmic slope over a sufficiently wide range of scales. A monofractal distribution is revealed by the equality of the generalized dimensions corresponding to different values of q or τ.

The first column indicates that the CI method works rather well for $q \geq 0$, both for the complete distribution and for the random subsample. Note also the oscillations presented by the local dimension around the correct value. This is not a spurious artifact of the dimension estimate, but is the consequence of the "lacunarity" (i.e., the presence of big voids with approximately periodic structure) generated by the cascading process [13]. For negative q's, this method does not provide the correct results. For example, for $q = -2$ the method indicates a well-defined scaling behavior with $D_{-2} = 0.4$ in the case of the complete distribution. This is due to lack of statistics and discreteness effects, that heavily affect the results at negative q's, when underdense regions with very few points are mostly weighted. Care should thus be taken in considering the results provided by this method for $q < 0$. A similar behaviour is evident in the results provided by the BC method (column two), although some larger scatter of the local dimension is observed. Reliable results are obtained for $0 \leq q \leq 4$; the scatter becomes rather strong for $q > 4$. This scatter is probably due to the difficulty of the BC algorithm in following the oscillations of the local dimension due to lacunarity effects. For negative q's, the method seems to work better than the CI approach, even though a dimension less than the correct value $D = 1$ is detected.

The results of the DR method (column 3) are particularly interesting. In fact, the correct dimension $D = 1$ is estimated for $\tau > 0$ in the case of the entire distribution; however, for the random subsample there is a tendency towards estimating a larger dimension; for example, the estimated dimension is $D \approx 1.4$ for $\tau = 0.1$ for the 3000 points sample. This trend becomes rather dramatic for the negative τ's. For $\tau < 0$ an average dimension $D \approx 1$ is correctly estimated from the entire distribution (even though with a noticeable scattering of the local slope). However, for the 3000 points sample the dimension estimates are much larger (*e.g.*, $D_\tau \approx 2$ for $\tau = -2$). However, the results in Figure 3.3 show that this method is very sensitive to the problem of limited statistics, especially for values of $\tau \leq 0$: the resulting variation of the dimension with τ simulates some spurious multifractality.

Column 4 reports the results for the NN method, when the fourth-order neighbor is considered for $\tau \geq 0$ and the first-order neighbor is used for $\tau < 0$. The analysis has been repeated for the first four orders of neighbors, for all values of τ. The results for all these neighbor orders are very similar; the above choice minimizes random scatter and fluctuations in the logarithmic slope of the partition function. In general, for the entire distribution this method provides the correct results for $\tau \geq 0$; the results for the random subsample are not reliable even for positive τ's. For negative values of τ, the NN method does not give the correct results, neither for the entire distribution nor for the random subsample. The discreteness problems present for $\tau < 0$ are sometimes translated by this algorithm into a wild scattering of the local slope of the partition function. On the other hand, note that the method provides a well-defined, but wrong, estimate $D \approx 2$ for $\tau = -2$ for the entire distribution. This behavior is rather critical since the flatness of the local dimension may lead to incorrect conclusions.

Column 5 shows the results for the MST method. This method provides the correct result $D = 1$ for all values of τ, in the case of the entire distribution. For the same values of τ, the results for the random subsample provide $D \approx 2$. Note that the local logarithmic slope of the partition function is apparently well-behaved also for the random subsample; however, the convergence is forced to a wrong value of the dimension. To optimize the performance of the MST method, it has been suggested to eliminate the very small (for $\tau > 0$) and the very long (for $\tau < 0$) edge links from the construction of the MST [377]. These edge links are in fact likely to introduce small- and large-scale noise, respectively. Progressively cutting the tails of the edge links distribution induces convergence to a well-defined local logarithmic slope of the partition function. For the case studied here, this procedure furnishes the correct results, since the partition function has either no scaling behavior (for the wrong edge links cuts) or a local logarithmic slope giving $D = 1$. As a conclusion, we observe that the MST method gives a correct answer for all values of τ, when a distribution with a sufficiently large statistics is analyzed. In general, this method should however be used with great care on distributions with limited statistics in order to avoid apparent convergence of the local slope and consequent spurious estimates of the dimensions.

3.3.3 The multifractal distribution

As a second step, we consider the analysis of a multifractal distribution. In order to fix the dimension spectrum, we choose

$$P(\beta) = \frac{1}{8}\,\delta(\beta - 0.6) + \frac{1}{4}\,\delta(\beta - 0.15) + \frac{1}{8}\,\delta(\beta - 0.1) + \frac{1}{2}\,\delta(\beta)\,. \tag{3.36}$$

The resulting spectrum has $D_\infty = 0.8$, $D_0 = 2$ and $D_{-\infty} = 3$. The field produced by the random β-model has been sampled with a total of 50,000 Monte Carlo points. Figure 3.4 reports the local dimensions estimated by the various partition functions.

Column 1 reports the results for the CI method. Note the growth of the local dimension at small scales, due to the presence of small-scale Gaussian noise generated by the Monte Carlo sampling. This is more evident at larger values of q; in fact, in the regions of high density there is a larger number of points, which are uniformly random distributed inside the same box. In this case, the average distance between points in high-density regions is less than the minimum scale generated by the random β-model; at very small scales the distribution has dimension three. At larger scales, the correct dimension is determined for values of $q > 0$, even though the local slope displays non-negligible fluctuations. For $q \leq 0$ the results provided by the CI method do not reproduce the correct dimension spectrum, as already noted in the study of the monofractal dust with $D = 1$. In the present case, the D_0 dimension is not correctly evaluated by the CI approach.

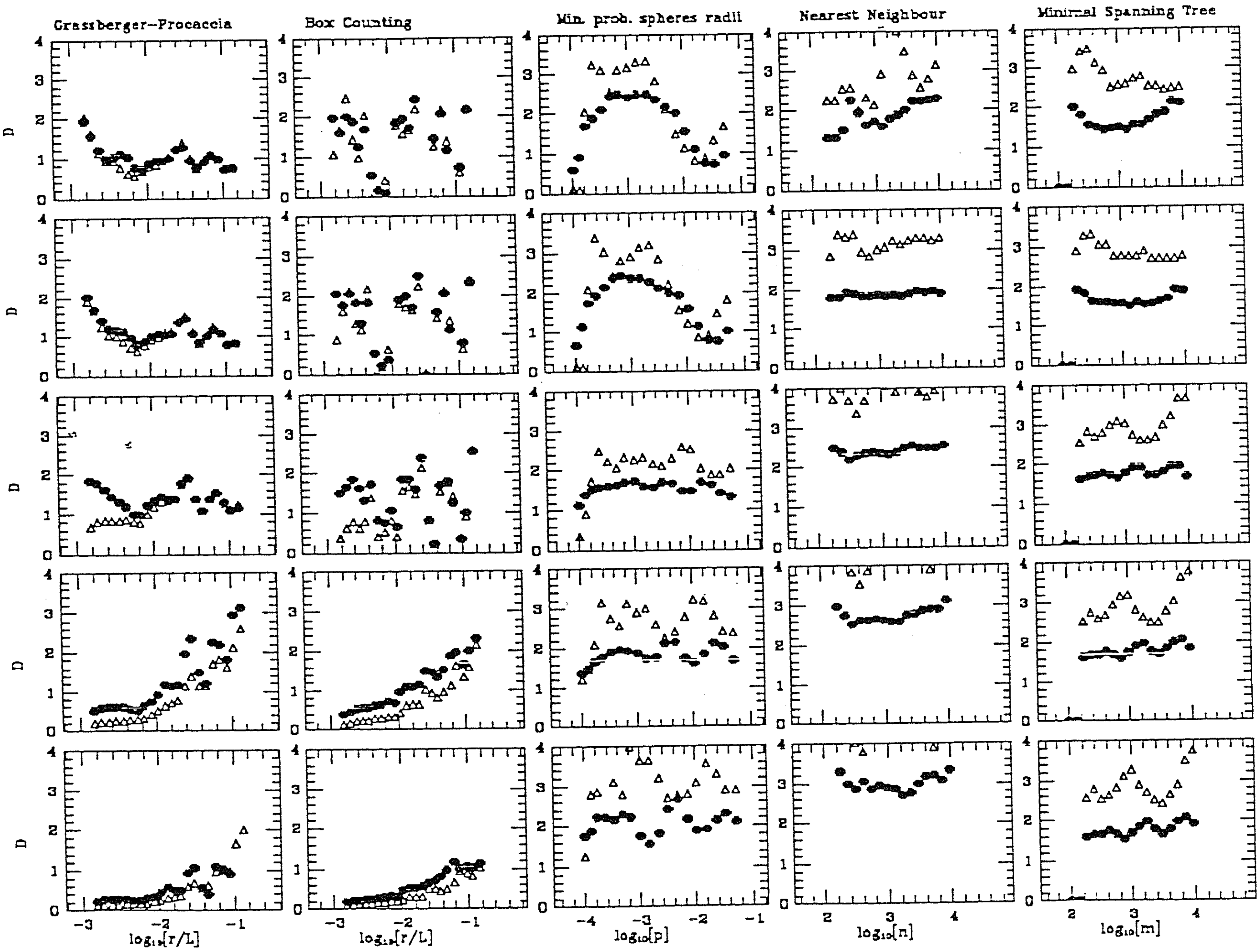

Figure 3.4: *The same as in Figure 3.3, but for the multifractal structure discussed in the text.*

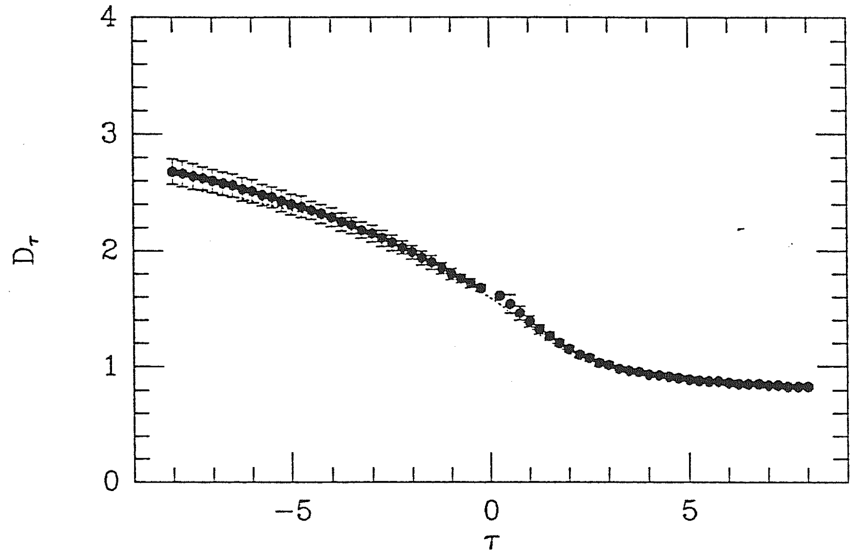

Figure 3.5: *Spectrum of generalized dimensions D_τ versus τ for the multifractal structure analyzed in Figure 3.4. The solid line indicates the theoretical values of the dimension while filled circles indicate the dimension estimates obtained by the DR method.*

The results of the BC method are reported in the second column. The local slope of the partition function is extremely scattered in this case, while discreteness effects do not allow the evaluation of the dimensions for $q \leq 0$. For positive q's, the average value of the logarithmic slope of the partition function provide an approximate estimate of the corresponding generalized dimension.

Column 3 reports the results for the DR method. For $\tau \gg 0$, this method is able to separate the (small) scales where random noise dominates, from the (larger) scales where the distribution is fractal. For example, in the case of the entire distribution, for $\tau = 6$ there is a large plateau with $D_\tau \approx 2.5$ for $p < 0.01$; the dimension estimates assume their correct value for $p > 0.01$. For the random subsample this effect is even more evident; the dimension estimate is $D_\tau \approx 3$ for large τ's and $p < 0.01$. For $\tau \leq 0$, the dimension estimates for the entire distribution are close to the theoretical values, even though they tend to remain below the correct values especially for $\tau \ll 0$ because of discreteness effects. For $\tau \leq 0$ the results for the random subsample provide dimension estimates which are larger than the correct ones. In general, the D_q estimates provided by the DR method are rather reliable once the local slope is evaluated over a p-range where small-scale noise is absent. This is clearly shown in Figure 3.5 which shows the dimension estimates obtained with this method together with the theoretical dimensions (as obtained by eq.[3.34]). A good agreement between the two spectra is obtained.

The NN method, shown in column 4, provides a correct evaluation of the multifractal spectrum for $\tau \leq 0$, if the large sample is considered. The analysis of the random subsample does not give any stable result. For positive values of τ, the analysis of the entire distribution reveals the small-scale random noise (corresponding in this case to large values of n), providing also an approximate estimate of the correct generalized dimension at small values of n.

The results of the MST approach are reported in the last column. This method provides a correct dimension estimate for $\tau = -2$, corresponding in this case to $q = 0$, for the entire distribution. The dimension estimates obtained for the other values of τ do not correctly reproduce the theoretical values of the generalized dimensions. For $\tau > -2$, the dimensions remain larger than the theoretical values, while for $\tau < -2$ the dimensions remain below the correct values. In general, this method displays some tendency towards providing dimension estimates about $D \simeq 2$ for this multifractal distribution. For the random subsample, the MST method does not provide reliable results. A dimension $D_\tau \approx 3$ is in fact detected for the random subsample; confirming the high sensitivity of the MST method to statistics.

For the MST, the choice of different cuts to the edge links distribution does not improve the evaluation of the multifractal spectrum. Figure 3.6 reports the local logarithmic slopes of the MST partition functions for different cuts in the edge link distribution. The various columns correspond to different edge link cuts, the values of τ are the same as already considered in Figure 3.4. As opposed to what happens in the analysis of a pure monofractal distribution, where either convergence to the correct value of the dimension or a huge scattering of the local slope is observed, for the multifractal dust the slopes appear to converge rather clearly to an approximately constant value for various choices of the edge link cuts. The spurious estimates provided by the MST are not an artifact of a particular choice of the cut on the distribution; rather they seem to be inherent in this method.

3.3.4 The scale-dependent distribution

In most natural systems, the fractal behavior does not extend over arbitrarily large scale ranges, instead it is observed only on a finite scaling regime. In the cosmological context, this is just the case for the large-scale distribution of galaxies. Observational evidences indicate that the multifractal properties of the galaxy distribution are confined to small scales, while $D_q \approx 3$ at scales larger than some appropriate homogeneity threshold. Such a behavior is consistent with the view that the fractal properties are built by the process of non-linear gravitational clustering (see Chapter 5 below and ref[374]). According to the results of N-body simulations of cosmological gravitational clustering, an initially homogeneous point distribution is transformed by the gravitational evolution into a fractal dust; since the gravitational clustering starts from the small scales, at every finite time there is the simultaneous presence of an evolved multifractal distribution at small scales and of an homogeneous distribution at large scales. In this case, it is important to verify the behavior of the various analysis methods, especially of those algorithms which mix different scale ranges in the evaluation of the partition function.

To approach this problem, here we consider a scale-dependent monofractal distribution

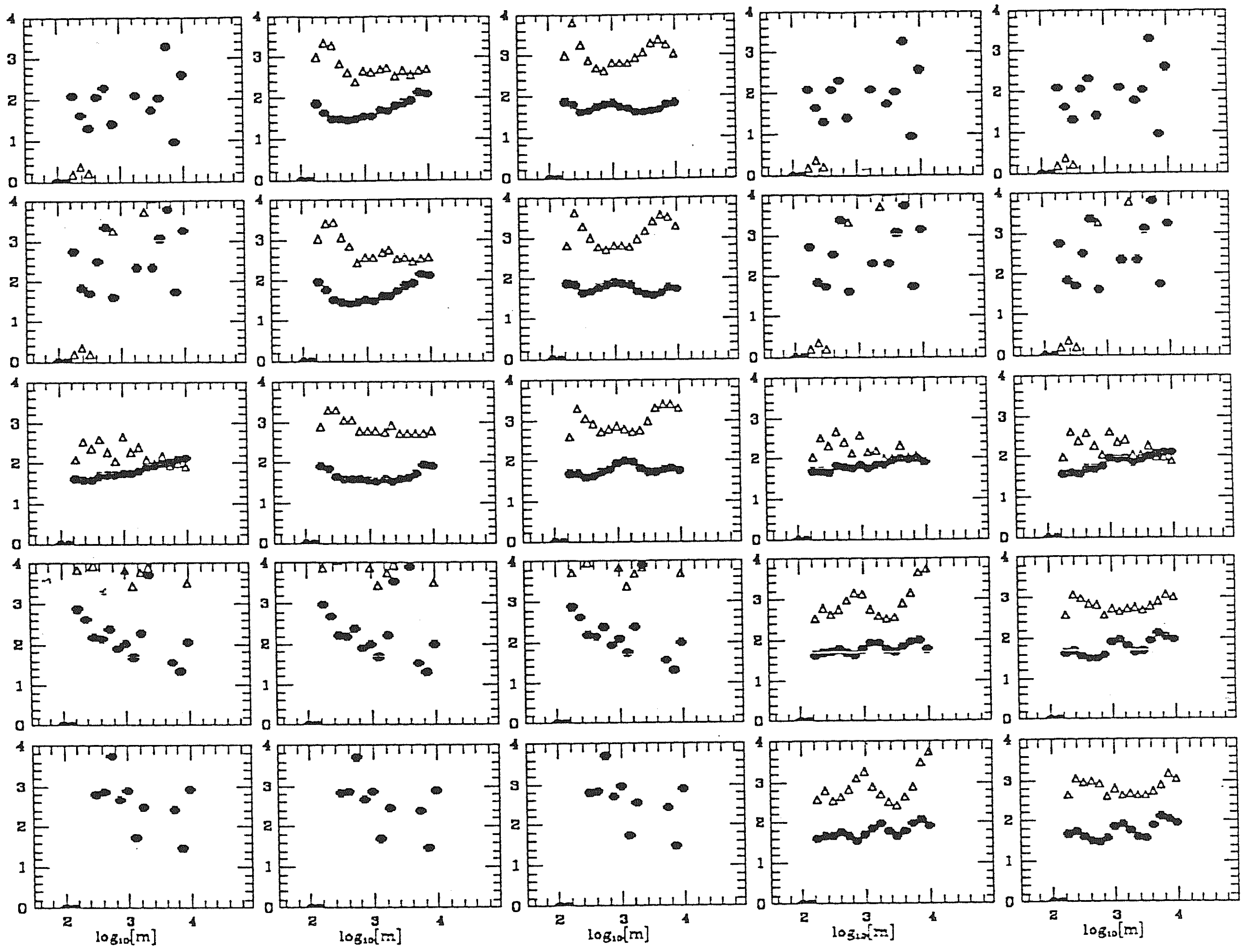

Figure 3.6: *The local dimension from the MST partition function for the multifractal structure and for different edge link cuts; the local slopes have been obtained as a running least-square-fit over three adjacent values of the partition function. Filled circles refer to the complete distribution and open triangles refer to the 3000 points random subsample. Column 1 reports the results when no edge links are cut. Columns 2 and 3 report the results obtained by cutting edge links shorter than* $0.1\langle L\rangle$ *and* $0.3\langle L\rangle$ *respectively; here* $\langle L\rangle$ *is the mean edge link length. Columns 4 and 5 report the results obtained by cutting edge links larger than* $2\langle L\rangle$ *and* $4\langle L\rangle$ *respectively.*

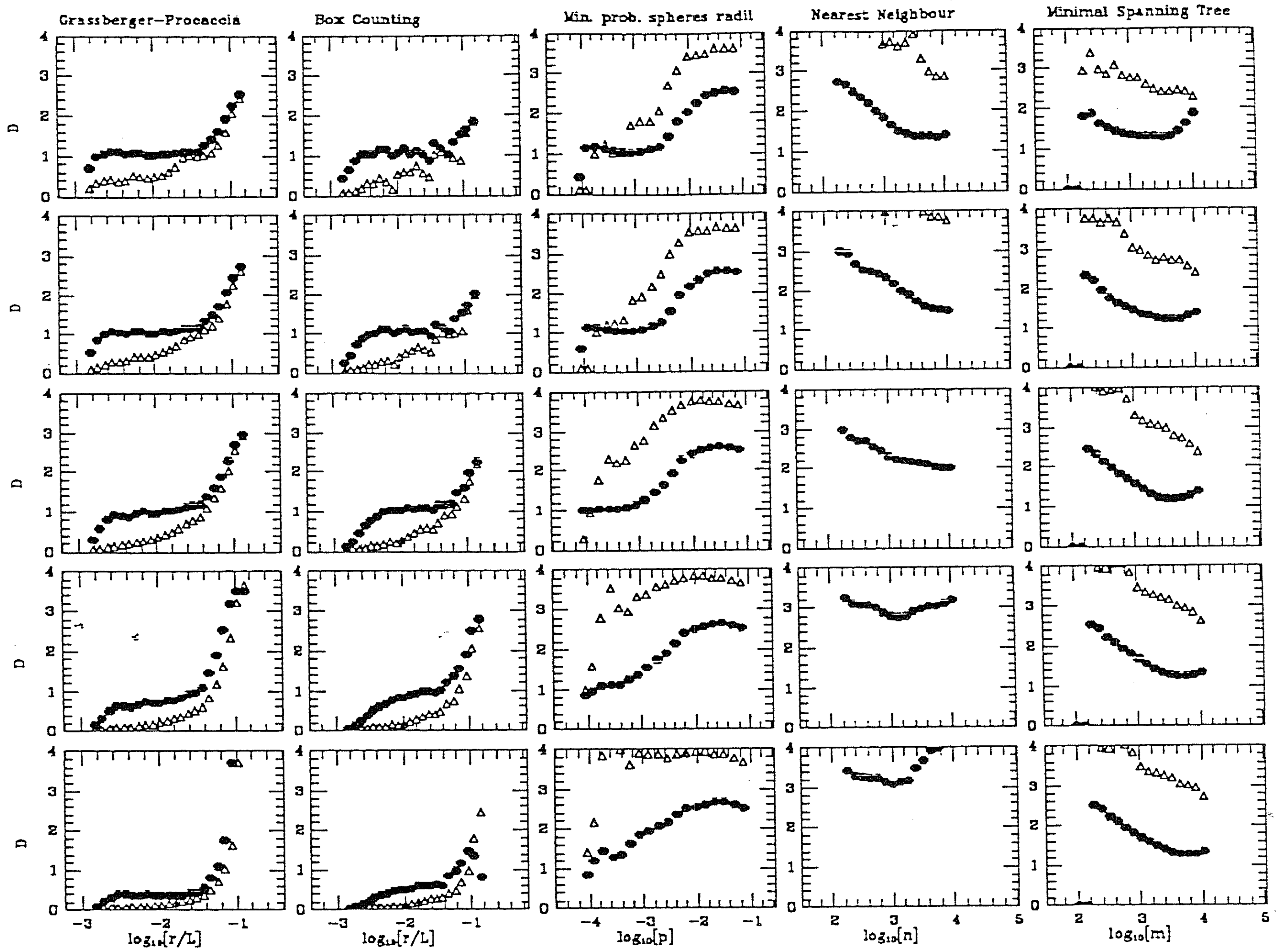

Figure 3.7: *The same as in Figure 3.3, but for the scale-dependent fractal structure discussed in the text.*

which is characterized by $D = 3$ for scales larger than an homogeneity scale L_h and by $D = 1$ for scales smaller than L_h. This distribution is obtained by the cascading process previously discussed, by an appropriate choice of the $P(\beta)$ distribution in the two different scaling ranges. The homogeneity scale is chosen to be 1/4 of the size L of the simulation box; there is a total of 30,000 points in the distribution. A comparison with the galaxy distribution is made possible by requiring the number density of the simulated distribution to be approximately equal to the average number density $< n >$ of bright galaxies, $\langle n \rangle = 0.01\ h^{-1}$ gal/Mpc^3. This density is consistent with the average galaxy density obtained in the CfA II redshift sample. The density indicated above gives $L = 140\ h^{-1}$ Mpc and $L_h = 35\ h^{-1}$ Mpc in physical units. As an example of undersampling, we also analyze a 3000-points random subsample of the complete distribution.

Figure 3.7 shows the results of the multifractal analysis of the entire scale-dependent monofractal distribution (solid circles) and of the random subsample (open triangles). For positive q's, both CI and BC provide extremely reliable results for the complete distribution, indicating both the correct value of the dimension at small scales ($D = 1$) and the transition to homogeneity above L_h. For $q = 0$, the BC method gives a correct estimate of the dimension, while CI provides a slight underestimate of the dimension. The improved reliability of the BC method with respect to the scale-free $D = 1$ structure is due to the fact that large-scale homogeneity fills the voids, thus suppressing the presence of lacunarity. This is also apparent from the remarkable stability of the local dimensions revealed by the CI method.

As usual, none of these methods is able to estimate at small scales the generalized dimensions for $q < 0$, due to discreteness effects, while detecting the large-scale homogeneity. Note that CI gives an apparently stable (but incorrect!) estimate $D_q \simeq 0.5$ for $q = -2$. For the random subsample, neither the CI nor BC provide reliable results at small scales. However, both methods still detect the transition to large-scale homogeneity. This behavior is generated by the fact that many points are now found at large mutual separations, due to the imposed large-scale homogeneity. In the case of the random subsample, the statistics are thus not sufficient to correctly sample the fractal behavior at scales smaller than L_h. Analogously, for the complete distribution this effect leads to the presence of discreteness effects at scales slightly larger than those detected for the pure $D = 1$ distribution, even though the total number of points in the scale-dependent distribution is larger.

The results of the DR method are reported in the third column. For $\tau \geq -2$, this method provides a reliable estimate of the fractal dimension and of the transition to homogeneity in the case of the complete distribution. For the random subsample, the results are not correct and they provide spurious estimates of the fractal behavior. As discussed in Section 2, an important characteristic of this method is that it mixes different scale ranges in the evaluation of the partition function at a given value of p. This mixing becomes more evident as the value of τ decreases; for $\tau \leq -4$ the results can hardly be interpreted, due to a strong mixing between the small scales (where $D = 1$) and the large scales (where $D = 3$). Care has thus to be taken when using this method for evaluating the negative τ dimensions on scale-dependent fractal sets.

Columns 4 and 5 of Figure 3.7 report the results of the NN approach and of the MST method, respectively. The random subsample provides extremely scattered and unstable results when analyzed with these two methods. For positive τ's, the NN method gives somewhat reliable results for the complete distribution, with the caveat that scale mixing tends to fuzzy the true scale dependence of the fractal dimension for moderate values of τ. The best scale separation is obtained here, as for the previous method, for large values of τ. For $\tau < 0$ scale-mixing becomes dramatic (even worse than for the DR method); for example, a small-scale (large n) dimension $D_\tau \approx 2$ is evaluated for $\tau = -2$, and $D_\tau \approx 3$ for $\tau = -4$, suggesting (erroneously) the presence of a multifractal distribution. The use of this method on scale-dependent fractal sets can thus spuriously transform the presence of two scaling regimes at different scales into an apparent multifractality, since the effects of the scale mixing are different for different values of τ. The results provided by the MST are quite stable along the whole sequence of τ values. For the complete distribution, it always detects the correct values, $D = 1$ and $D = 3$, holding at small and large scales, respectively. However, because of scale mixing, only a smooth transition between these two values is detected, without any evidence of scale invariance over a finite interval. Again, for the smaller sample the limited statistics heavily affects the dimension estimate.

3.3.5 Discussion of the results

The above described analysis has been motivated by the growing interest in the quantitative determination of the scaling properties of the galaxy distribution. It is clear, however, that the results discussed here are of more general interest, being relevant to any statistical analysis of experimental or numerical point distributions, in many different physical contexts.

The main conclusions about the reliability of the different multifractal dimension estimator, that we have introduced, can be summarized as follows.

a) The BC and the CI methods are in general quite reliable to estimate positive-order dimensions, while they suffer from discreteness effects for negative q's, where underdense regions are mostly weighted in the computation of the partition function. The stability of these methods, when the number of points in the sample is decreased, depends on the dimensionality of the structure; fractals having a lower dimension require a smaller number of points to be adequately sampled. A further advantage of these methods is also that they fix *a priori* the physical length scale where the dimension is estimated. This aspect is of particular relevance in the analysis of scale-dependent structures. In this case, the BC and CI methods allow one to safely detect the presence of a characteristic scale in the distribution, where the dimensionality sharply changes.

b) The DR method is rather good in estimating both positive- and negative-order dimensions. For this reason, it is particularly suited to follow the whole spectrum of dimensions in a multifractal structure. This is clearly seen in Figure 3.5, where the DR method measures D_q values, which are always remarkably similar to the true values expected on the ground of eq.(3.34). A possible drawback of this method lies in the fact that, differently from the BC and CI algorithms, each probability value does not correspond to a unique choice of the physical scale, instead scale mixing may occur. Clearly, this could represent a potential problem when dealing with scale-dependent structures. From Figure 3.7, one sees that the DR method is able to disentangle the different scaling regimes for positive τ's, where scale-mixing is less dramatic, while the results are much less reliable for negative τ's. Finally, this method severely suffers for lack of statistics. For poor samples, as shown in Figure 3.3, the DR method tends to overestimate the dimension.

c) As far as the MST and NN methods are concerned, they appear to give the least reliable answers. The only case in which they have been shown to be acceptable are for the $D = 1$ structure with 18,000 points. This suggests that such methods are efficient only when a very high sampling rate is allowed. In the analysis of the scale-dependent structure, these methods display a very strong scale mixing. As a consequence, the local dimension never flattens at an approximately constant value, although it ranges between the correct values, $D = 1$ and $D = 3$ at small and large scales, respectively. These results suggest that some care must be payed when using the MST and NN methods to analyse the multifractal spectrum of the galaxy distribution.

From such results, some general conclusions about the multifractal analysis of the galaxy distribution can be drawn. The scale-dependent structure considered here has a number of points and a homogeneity scale which are similar to those encountered in the analysis of real galaxy samples. The plots of Figure 3.7 show that an excessive sparse sampling (as in the case of the random subsample) does not allow one to trace adequately the scaling properties where the clustering is non-linear. However, the results obtained from the entire distribution indicate that the multifractal analysis methods discussed here should provide reliable results, when appropriately employed. Our conclusion is thus that complete and extended redshift samples, such as the emerging CfA II [111], have enough statistics to trace the fractal and scaling properties associated with gravitational dynamics. A crucial requisite, however, is the knowledge of the behavior and of the pitfalls of the various analysis methods; analogously, the simultaneous usage of several different analysis methods is an important ingredient for a reliable analysis.

3.4 Fractal analysis of the galaxy distribution

As emphasized in Chapter 2, the application of several clustering measures indicates the presence of well defined scaling properties for the galaxy distribution. In particular, the detection of the power-law shape for the 2-point correlation function, $\xi(r) \propto r^{-\gamma}$, for both galaxies and clusters, implies a small-scale fractality of the clustering pattern, with dimension $D = 3 - \gamma \simeq 1.2$ (see eq.[3.10]). The above picture is also supported by the hierarchical appearance of the large-scale galaxy distribution, where objects of small size are nested inside larger structures. The resulting texture of the galaxy distribution shows the presence of big voids, filaments and huge galaxy concentrations (superclusters), whose sizes are comparable to those of the largest available redshift samples. Such a complexity led several authors to interpret the observed large-scale clustering as a fractal process [123, 287, 254], having rigorously scale-invariant statistical properties. This conclusion is clearly at variance with respect to previously presented results based on the analysis of correlation functions. In fact, while at small scales non-linear clustering gives $\xi(r) \gg 1$, at scales much larger than the correlation length it is $\xi(r) \ll 1$ and the distribution becomes essentially homogeneous.

However, based on the increase of the galaxy correlation length with the volume of the sample, as already detected by Einasto *et al.* [130], serious criticisms in the use of the $\xi(r)$ correlation function have been raised by Pietronero and coworkers [305, 88, 87]. They claimed that the definition (2.2) for a dimensionless $\xi(r)$ includes a normalization with respect to the mean object density n. Thus, normalizing the observed galaxy distribution to a Poissonian distribution, as required by a consistent correlation analysis, forces the 2-point function to vanish at large scales. In this way, large-scale homogeneity is far from being verified, but it is only assumed. If the real distribution is such that the average density depends on the size of the sampled volume, as it should be for a fractal structure, the same distribution of objects appears to have different correlation lengths, as the volume of the sample changes. In fact, for a fractal structure, the number density of objects within r scales as

$$N(r) \;=\; B\,r^{D_\nu}, \tag{3.37}$$

where B is a constant, while D_ν is the usual correlation dimension. As a consequence, if R_S is the characteristic size of the sample, the average density inside a sphere of radius R_S,

$$n \;=\; \frac{N(R_S)}{V(R_S)} \;=\; \left(\frac{3}{4\pi}\right) B\, R_S^{3-D_\nu}, \tag{3.38}$$

turns out to be a decreasing function of R_S, and the 2-point function is

$$\xi(r) \;=\; \frac{D_\nu}{3}\left(\frac{r}{R_S}\right)^{-(3-D_\nu)} - 1\,. \tag{3.39}$$

Then, while the exponent of the power law, $\gamma = 3 - D_\nu$, is an intrinsic property of the distribution, the normalization of ξ depends explicitly on R_S. Accordingly, Pietronero and collaborators claimed that the large-scale structure of the Universe could be explained as a self-similar fractal extending at least up to scales $\sim 200h^{-1}$ Mpc, with no evidence of large-scale homogeneity. In this picture, they interpreted the increase of the galaxy correlation length with the sample size, while the amplification of the cluster 2-point function is just due to the fact that clusters sample much larger scales than galaxies, with a subsequent increase of the clustering amplitude (see Figure 3.8). Instead of $\xi(r)$, these authors proposed as an alternative clustering measure the quantity

$$\Gamma(r) \;=\; n\,[\xi(r)+1]\,, \tag{3.40}$$

that, by definition, is independent of the actual value of n and does not rely on the assumption of large-scale homogeneity. Making use of $\Gamma(r)$, Pietronero [305] analysed the CfA1 survey, dividing the whole sample into two volume-limited subsamples. He found that the galaxy distribution behaves like a simple fractal, which extends at least up to the sample size, without any evidence that homogeneity is attained within the sample boundaries. Apart from the obvious problem that this kind of picture has to account for other striking observational facts, such as the high degree of homogeneity of the cosmic microwave background, several further

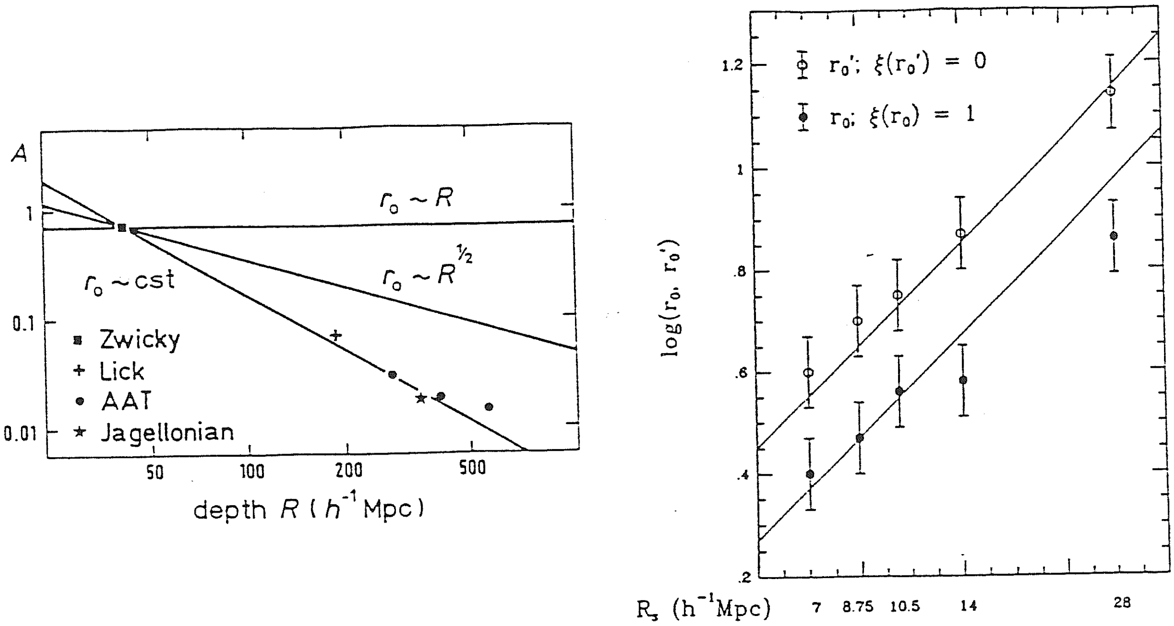

Figure 3.8: *Left panel: The characteristic scales for the galaxy and cluster distribution are plotted as a function of the sample size R_S. Open circles correspond to the smallest scale where $\xi(r)$ vanishes, while filled circles are the correlation length r_o defined as the scale at which $\xi(r)$ takes unity value (after [88]). Right panel: the amplitude of the angular 2-point function is plotted for different samples as a function of the sample depth. Straight lines correspond to a Universe with large-scale homogeneity and to a purely fractal Universe (after [23]).*

evidences appeared, that claim the scale-invariant properties of the galaxies distribution, if represented by means of a self-similar fractal, were overestimated.

The classical criticism to a purely fractal description of galaxy clustering arises from the results about the amplitude of the 2-point angular function, $w(\vartheta)$. In fact for an angular sample having a depth $\mathcal{D}$, the Limber equation (2.32) predicts that $w(\vartheta) \propto (r_o/\mathcal{D})^\gamma \vartheta^{1-\gamma}$. Thus, if homogeneity holds at large scales (that is, $r_o = const$), then $w(\vartheta) \propto \mathcal{D}^{-\gamma}$. Viceversa, if fractality extends at arbitrarily large scales, then $r_o \propto \mathcal{D}$ and the angular correlation amplitude does not depend on the sample depth. In Figure 3.8*b* we plot the amplitude of $w(\vartheta)$ as estimated for several angular samples, as a function of the depth. It is apparent that the data are by far much better represented by assuming large-scale homogeneity than by modelling the clustering with a self-similar fractal at arbitrarily large scales.

This argument has been however severely criticised by the supporters of a fractal Universe. Coleman & Pietronero [87] claimed that angular data are much less reliable than redshift data to establish the existence of large-scale homogeneity. Projection of a fractal structure onto a sphere could cause, differently from an orthogonal projection, a spurious homogeneization of the distribution at large angular scales. In Chapter 6 we will address in more detail the problem of preservation of scale-invariance after projection on a sphere.

Alternative interpretations of the observed scaling of $\xi(r)$ with the size of the sample volume have also been proposed, for example by invoking effects of luminosity segregation

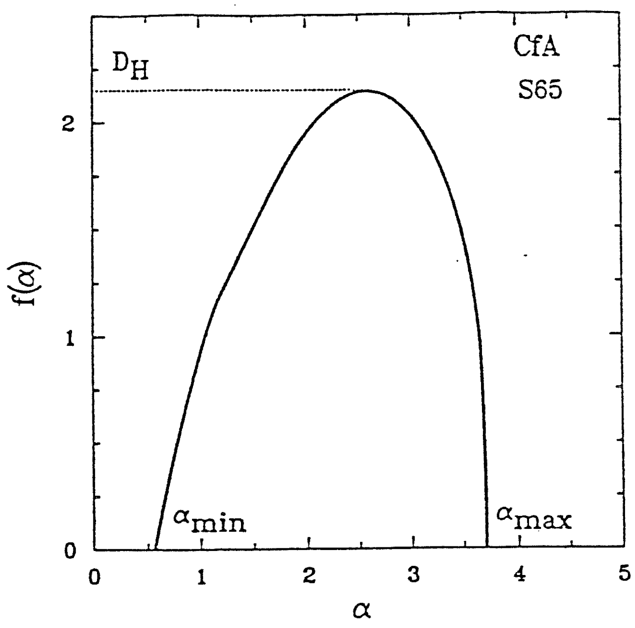

Figure 3.9: *The multifractal singularity spectrum for a volume-limited subsample of the CfA1 galaxy distribution (after [257]).*

[47, 58]. In fact, it is well known that the clustering strength is an increasing function of the absolute galaxy luminosity. Since galaxy samples are limited in apparent magnitude, enlarging the sampled volume one preferentially includes intrinsically more luminous objects, thus increasing the observed clustering as a spurious effect.

Martinez & Jones [249] divided the CfA1 sample into 10 volume limited subsamples, in order to carefully check the increase of the clustering length with the volume. They claimed that the observed increase of r_o for the CfA1 galaxies is most probably due to the luminosity dependence of the clustering pattern. Moreover, the resulting power-law shape of $\xi(r)$ implies self-similarity only at the small scales ($r \lesssim 5h^{-1}$ Mpc) of non-linear clustering, while homogeneity is attained at larger scales. More recently, Guzzo *et al.* [181] analysed the Perseus-Pisces redshift survey and detected two well defined scaling regimes for the galaxy distribution: at scales $r \lesssim 4h^{-1}$ Mpc it behaves like a fractal with correlation dimension $D_\nu \simeq 1$, while it takes $D_\nu \simeq 2$ up to $r \simeq 30h^{-1}$ Mpc. Homogeneity is definitely attained above this scale. While confirming previous indications by Dekel & Aarseth [104], the above result is also supported by further analyses by Einasto [128] and Calzetti *et al.* [68].

In order to investigate the whole spectrum of generalized dimensions, Martinez *at al.* [250] performed a multifractal analysis of the CfA1 sample. As a result, they found that the galaxy distribution is characterized by a non trivial scaling behaviour at the small scales of non-linear clustering, where self-similarity is detected. The resulting D_q curve shows a remarkable multifractality, with Hausdorff dimension $D_o \simeq 2.2$ and correlation dimension $D_\nu \simeq 1.3$. At negative q values it is $D_q \gtrsim 3$ thus indicating that points in the underdense regions are minima of the local density field, instead of singularities (see Figure 3.9).

Although these results strongly indicate that the galaxy clustering can not be described by a self-similar fractal extending to arbitrarily large scales, nevertheless fractal analysis has been proved to be an extremely powerful statistical instrument to properly study the scaling properties of the large-scale structure of the Universe. In this Thesis we will extensively apply fractal concepts to characterize both the development of non-linear gravitational clustering, as described by N-body simulations, and the observed distribution of cosmic structures.

The results of the analysis of synthetic structures presented in §3.3 are contained in a paper, that has been submitted to *Physical Review A* (Borgani, Murante, Provenzale & Valdarnini 1992, [64]).

Chapter 4

The dynamics of structure formation

In previous chapters we have described how the large-scale structure of the Universe appears and how its statistical properties can be characterized. The great cosmological relevance of providing an accurate clustering description resides in the fact that, in principle, we should be able to solve the dynamical evolution of the Universe back in time, in order to deduce the initial conditions on the basis of what is today observed. Other than referring to the large-scale distribution of galaxies and galaxy clusters, a very efficient way to get information about the primordial Universe is represented by the study of the cosmic microwave background (CMB) anisotropies, which contain the imprint of the initial density inhomogeneities at the outset of the recombination epoch. However, although the continuous refinements of measurements and the recent exciting results obtained by COBE [357, 393] have further restricted the set of possible initial conditions, no compelling evidences still exist in favour of one particular model. Data on the anisotropy of the CMB temperature indicate that the presently observed variety of structures should have evolved from extremely small fluctuations, with a characteristic amplitude $\delta \sim 10^{-5}$. If structure formation began after recombination, at a redshift $z \sim 1000$, a successful model for structure formation must be able to provide the observed global texture of the large-scale structure, starting from this high degree of isotropy.

Although reconstructing initial conditions from the observed galaxy distribution is likely to be possible at sufficiently large scales, where linear gravitational dynamics still preserves memory of the initial conditions, it becomes extremely difficult when considering the small scales, where both non-linear gravity and dissipative hydrodynamical effects are responsible for the structure formation processes. However, even considering sufficiently large scales, some problems arise due to incompleteness of galaxy samples, systematic errors in the estimate of the galaxy distances, or other observational biases. Going in the opposite direction, we can also choose the strategy of fixing initial conditions and let them dynamically evolve. A comparison of the results with the observed large-scale structure should indicate whether the chosen model is viable or not. Cosmological N-body simulations are based on this approach.

In this chapter we describe the dynamics which determines the evolution of density fluctuations in the framework of the gravitational instability picture. The non-gravitational mechanism based on cosmic explosions [275, 200] will be briefly described in §4.3. After writing the complete set of equations for the evolution of density perturbations in a Friedmann background, we show their solution in the linear regime. Although the fully non-linear dynamics can be adequately followed only by resorting to N-body simulations, we discuss some approximations introduced in order to account for the quasi-linear or mildly non-linear gravity. Also mentioned are analytical approaches to account for partial aspects of the non-linear clustering (a detailed treatment of non-linear clustering through N-body simulations is described in Chapter 5). Then, we discuss the more important models for the primordial fluctuation spectrum and show how they are uniquely related to the matter content of the Universe. Motivated by the problems displayed by the standard dark matter models, we also discuss alternative scenarios, which violate the random-phase prescription provided by the canonical inflationary model. Finally, the problem of the galaxy formation out of the initial density perturbations is treated. Particular attention is devoted to "biassed" models, in order to show how the history of formation of cosmic structures determines not only their morphology, but also their large-scale clustering properties.

4.1 The evolution of density perturbations

Let us assume that the matter content of the Universe is described by a pressureless and self-gravitating Newtonian fluid. Then, the fluidodynamical equations that describe its evolution (see, *e.g.*, refs.[229, 287]) are the equation of continuity for mass conservation, Euler's equation for the description of the motion, and Poisson's equation, that accounts for the Newtonian gravity. Let us choose a system in which $\mathbf{x}$ represents the comoving coordinates and $\mathbf{r} = a(t)\,\mathbf{x}$ the proper coordinates. If $\mathbf{v} = \dot{\mathbf{r}}$ is the physical velocity and $\mathbf{u} = a(t)\,\dot{\mathbf{x}}$ the peculiar velocity, then

$$\mathbf{v} \;=\; \dot{a}\mathbf{x} + \mathbf{u}\,, \qquad (4.1)$$

where the first term on the *rhs* accounts for the Hubble flow. With such conventions, the dynamical equations for the evolution of density inhomogeneities in a Friedmann background read

$$\begin{aligned} \frac{\partial\delta}{\partial t} + \nabla_x\cdot\mathbf{u} + \nabla_x\cdot(\delta\mathbf{u}) \;&=\; 0 \qquad \text{(continuity)} \\ \frac{\partial\mathbf{u}}{\partial t} + 2H\mathbf{u} + (\mathbf{u}\cdot\nabla_x)\mathbf{u} \;&=\; -\frac{\nabla_x\Phi}{a^2} \qquad \text{(Euler)} \qquad (4.2) \\ \nabla_x^2\Phi \;&=\; 4\pi G\bar{\rho}a^2\delta \qquad \text{(Poisson)}. \qquad (4.3) \end{aligned}$$

Here ∇_x is the comoving gradient, $\delta(\mathrm{x})$ indicates as usual the density perturbation field, Φ is the potential fluctuation, and $H = \dot{a}/a$ is the Hubble parameter. Newtonian theory is adequate to describe the evolution of density fluctuations on scales well inside the Hubble radius $\lambda_{\mathrm{H}} = ct$. However, on scales comparable or exceeding the horizon size, a general-relativistic treatment is required. In this regime, some ambiguities arise due to the fact that in general relativity ambiguities could arise when fixing the gauge, (*i.e.* the correspondence between background and physical space-time) in which fluctuation measurements are performed. In this case, a proper gauge-invariant description of fluctuation evolution is required and several prescriptions have been proposed by different authors (see ref.[266] for a recent review on this subject). At the present time, all the scales relevant for clustering studies are are well inside the horizon. However, since perturbation wavelengths scale with the redshift as $\lambda \propto (1+z)^{-1}$ and the horizon as $\lambda_{\mathrm{H}} \propto (1+z)^{-3/2}$, the typical scale of galaxy clustering, $\lambda \sim 10h^{-1}$ Mpc, crosses the horizon at $z \sim 10^5$, roughly corresponding to the epoch of matter-radiation equality. Thus, a gauge invariant treatment is required when studying the formation of density fluctuations relevant to the present observed clustering. In this Section we adopt a purely Newtonian treatment, which is adequate to follow the perturbation evolution after recombination, when structure formation starts.

Passing to the Fourier representation according to the prescriptions of §2.2, the system (4.3) becomes

$$\begin{aligned}
\frac{\partial \tilde{\delta}_{\mathrm{k}}}{\partial t} + i\mathrm{k} \cdot \tilde{\mathrm{u}}_{\mathrm{k}} + i \int d\mathrm{k}' \tilde{\delta}_{\mathrm{k}'} [\mathrm{k}' \cdot \tilde{\mathrm{u}}(\mathrm{k} - \mathrm{k}')]) &= 0 \\
\frac{\partial \tilde{\mathrm{u}}_{\mathrm{k}}}{\partial t} + 2H \tilde{\mathrm{u}}_{\mathrm{k}} + i \int d\mathrm{k}' [\tilde{\mathrm{u}}_{\mathrm{k}'} \cdot (\mathrm{k} - \mathrm{k}')]\, \mathrm{u}_{\mathrm{k}-\mathrm{k}'} &= i\, \frac{\mathrm{k} \tilde{\Phi}_{\mathrm{k}}}{a^2} \\
\tilde{\Phi}_{\mathrm{k}} &= -4\pi G \bar{\rho} \tilde{\delta}_{\mathrm{k}} \frac{a^2}{k^2} \,.
\end{aligned} \tag{4.4}$$

Eqs. (4.4) and (4.3) can be equivalently used as the non-linear systems describing the evolution of cosmic density fluctuations. In the remainder of this Section we will describe some approximations that have been proposed in order to get hints about the nature of gravitational clustering. In the next Chapter we will discuss the use of cosmological N-body simulations as a tool to follow in detail the non-linear dynamics implied by eqs.(4.4).

4.1.1 The linear approximation

A particularly simple case occurs when dealing with very small inhomogeneities. This is the case either at very early epochs or at the present time, when considering sufficiently large scales, so that the variance of the galaxy number counts is much less than unity. In this regime, $\delta \ll 1$ and $ut/d_c \ll 1$, $t \sim 1/\sqrt{G\bar{\rho}}$ being the expansion time-scale and d_c the characteristic coherence length of the fluctuation field. This enables us to neglect in eqs.(4.4) all the non-linear terms, to get

$$\frac{\partial^2 \delta}{\partial t^2} + 2H\frac{\partial \delta}{\partial t} = 4\pi G\bar{\rho}\delta . \tag{4.5}$$

Note that the linear approximation amounts to assuming no phase coupling, so that the initial randomicity of phases predicted by classical inflationary models is preserved at the linear stage.

In the case of a flat Universe with $\Omega_o = 1$, no cosmological constant, and matter dominated expansion, the Friedmann equations $(I.2)$ give $a(t) \propto t^{2/3}$, and eq.(4.5) has the general solution

$$\delta(\mathrm{x}) = A(\mathrm{x})t^{2/3} + B(\mathrm{x})t^{-1} . \tag{4.6}$$

The above expression essentially says that perturbation evolution is given by the superposition of a growing and a decaying mode, that becomes rapidly negligible as expansion goes on. It is interesting to note that $\delta(\mathrm{x})$ grows at the same rate as the scale factor $a(t)$. This is nothing but the consequence of the similarity between the gravitational collapse time-scale, $t_{dyn} \sim 1/\sqrt{G\rho}$, and the expansion time-scale, $t_{exp} \sim 1/\sqrt{G\bar{\rho}}$, that occurs in the $\delta \ll 1$ case. This result is valid both for a flat Universe and for an open Universe ($\Omega < 1$) at sufficiently early times, when $1 + z \gg |\Omega_o^{-1} - 1|$ and the spatial curvature can be neglected. However, in the last case, at later times the cosmic expansion rate increases, so that the fluctuation growing stops and their amplitudes are frozen. Thus, in order to allow observed structures to be formed , a not too low density parameter is required. Detailed calculations give the constraint $\Omega_o h^2 \gtrsim 0.006$, which is largely satisfied by all the estimates of the mean cosmic density, for any reasonable choice of the Hubble parameter.

As the typical fluctuation amplitude approaches unity at a given scale, phase coupling terms in eqs.(4.4) start playing a role and the linear approximation breaks down. In this case, a rigorous treatment for inhomogeneity evolution has not yet been derived, although different prescriptions have been developed to get hints about non-linear aspects of gravitational clustering.

As a direct approach, one can perturbatively expand eqs.(4.3) in terms of increasing order in δ and try to solve the system order by order. Attempts in this direction have been performed, at least at the lowest (second) perturbative order, and show some interesting features. While linear equations preserve initial Gaussianity, the inclusion of the lowest-order non-linear terms gives rise to a non vanishing skewness of the fluctuation probability distribution [287], that is the signature of non-Gaussian statistics. The corresponding connected correlation functions are shown to follow at this order the hierarchical expression of eq.(2.24) [146]. This approximation is expected to hold in the $\delta \lesssim 1$ regime, while in the $\delta \gg 1$ regime the convergence of the perturbative expansion series is no longer guaranteed. As a consequence, no clear indications exists about the width of the dynamical range of validity of the second-order perturbative approach. In Chapter 5 we will address this problem more in detail by comparing the prediction of the perturbative approach to the results of N-body simulations.

4.1.2 The Zeldovich approximation

A simple and elegant approximation to describe the non-linear stage of gravitational evolution has been developed by Zeldovich [399] (see the review by Shandarin & Zeldovich [349], for an exhaustive description of the Zeldovich approximation). In this approach, the initial matter distribution is considered to be homogeneous and collisionless. If the unperturbed (initial) Lagrangian coordinates of the particles are described by q, then the Eulerian coordinates of the particles at the time t are given by

$$\mathbf{r}(\mathbf{q},t) = a(t)\,[\mathbf{q}+b(t)\,\mathbf{s}(\mathbf{q})]\,. \tag{4.7}$$

Here $a(t)$ is the cosmic expansion factor and $b(t)$ the growing rate of linear fluctuations, as provided by eq.(4.5). Moreover, the velocity term $\mathbf{s}(\mathbf{q})$, which provides the particle displacement with respect to the initial (Laplacian) position, is related to the potential $\Phi_o(\mathbf{q})$ originated by the initially linear fluctuations, according to

$$\mathbf{s}(\mathbf{q}) = \nabla\Phi_o(\mathbf{q})\,. \tag{4.8}$$

In order to better visualize the meaning of eq.(4.7), let us consider a pressureless and viscosity-free, homogeneous medium without any gravitational interaction. For this system, the Eulerian positions x of the particles at time t are related to the Lagrangian positions q by the linear relation

$$\mathbf{x}(\mathbf{q},t) = \mathbf{q}+\mathbf{v}(\mathbf{q})t\,, \tag{4.9}$$

being $\mathbf{v}(\mathbf{q})$ the initial velocity. The above expression is essentially analogous to the Zeldovich approximation (4.7), apart from the presence of the $a(t)$ term, which accounts for the background cosmic expansion, and of the $b(t)$ term, which accounts for the presence of gravity, giving a deceleration of particles along the trajectories (actually, $b(t) \propto t^{2/3}$ in a $\Omega = 1$ matter dominated Universe).

Since at $t > 0$ density inhomogeneities are created, mass conservation requires that $\rho(\mathbf{r},t)\,d\mathbf{r} = \rho_o\,d\mathbf{q}$, so that the density field as a function of Lagrangian coordinates reads

$$\rho(\mathbf{q},t) = \rho_o\left|\frac{\partial\mathbf{r}}{\partial\mathbf{q}}\right| = \frac{\bar\rho}{\left|\delta_{ij}-b(t)\,\frac{\partial s_i}{\partial q_j}\right|}\,. \tag{4.10}$$

Here the *deformation tensor* $\partial r_i/\partial q_j$ accounts for the gravitational evolution of the fluid, while $\bar\rho = (a_o/a)^3\rho_o$ is the mean density at time t. At the linear stage, when $b(t)\,\mathbf{s}(\mathbf{q}) \ll 1$, eq.(4.10) can be approximated by

$$\rho(\mathbf{q},t) \simeq \bar\rho\,[1-b(t)\nabla_q\cdot\mathbf{s}(\mathbf{q})]\,, \tag{4.11}$$

so that $\bar{\rho}\delta(\mathbf{x}) \simeq -b(t)\,\nabla_q \cdot \mathbf{s}(\mathbf{q})$ and we recover (the growing mode of) the linear solution.

More in general, since the expression (4.8) for $\mathbf{s}(\mathbf{q})$ makes the deformation tensor a real symmetric matrix, its eigenvectors define a set of three principal (orthogonal) axes. After diagonalization, eq.(4.10) can be written in terms of its eigenvalues $-\alpha(\mathbf{q})$, $-\beta(\mathbf{q})$ and $-\gamma(\mathbf{q})$, which give the contraction or expansion along the three principal axes:

$$\rho(\mathbf{q},t) \;=\; \frac{\bar{\rho}}{[1-b(t)\,\alpha(\mathbf{q})]\,[1-b(t)\,\beta(\mathbf{q})]\,[1-b(t)\,\gamma(\mathbf{q})]}\,. \tag{4.12}$$

If the eigenvalues are ordered in such a way that $\alpha(\mathbf{q}) \geq \beta(\mathbf{q}) \geq \gamma(\mathbf{q})$, then, as evolution increases the $b(t)$ value, the first singularity in eq.(4.12) occurs in correspondence of the Lagrangian coordinate $\mathbf{q}_1$, where α attains its maximum positive value α_{max}, at the time t_1 such that $b(t_1) = \alpha_{max}^{-1}$. This corresponds to the formation of a pancake (sheet-like structure) by contraction along one of the principal axes. For this reason, Zeldovich [399] argued that pancakes are the first structures formed by gravitational clustering. Other structures like filaments and knots come from simultaneous contractions along two and three axes, respectively. Doroshkevich [113] evaluated the probability distribution for the three eigenvalues in the case of a Gaussian random field and concluded that simultaneous vanishing of more than one of them is quite unlikely. Thus, in this scenario, pancakes are the dominant features arising from the first stages of non-linear gravitational clustering.

The Zeldovich approximation predicts the first non-linear structure to arise in correspondence of the high peaks of the $\alpha(\mathbf{q})$ field and represents a significant step forward with respect to linear theory. For this reason, the Zeldovich approach is very well suited in many studies of gravitational clustering. In particular, it is widely employed in the realization of cosmological N-body simulations, where its ability to better follow non-linear clustering than the linear approximation permits one to fix initial conditions at a more evolved stage, thus significantly reducing the computational cost.

However, within the Zeldovich prescription, after a pancake forms in correspondence of crossing of particle orbits, such particles continue travelling along straight lines, according to eq.(4.7). Viceversa, in the framework of a realistic description of gravitational dynamics, we expect that the potential wells, that correspond to non-linear structures, should be able to retain particles and to accrete from surrounding regions. This is exactly what comes out by comparing N-body simulations purely based on the Zeldovich approximation to those obtained by exactly solving the dynamics of eq.(4.3) (see Figure 4.1). It is clear that the failure of this approximation is expected to be more pronounced for spectra having a large amount of power at small scales, where non-linear structures rapidly develop.

4.1.3 The adhesion approximation

In order to overcome the smearing of pancakes arising in the framework of the Zeldovich approach, an alternative approximation has been proposed, that is based on the idea of

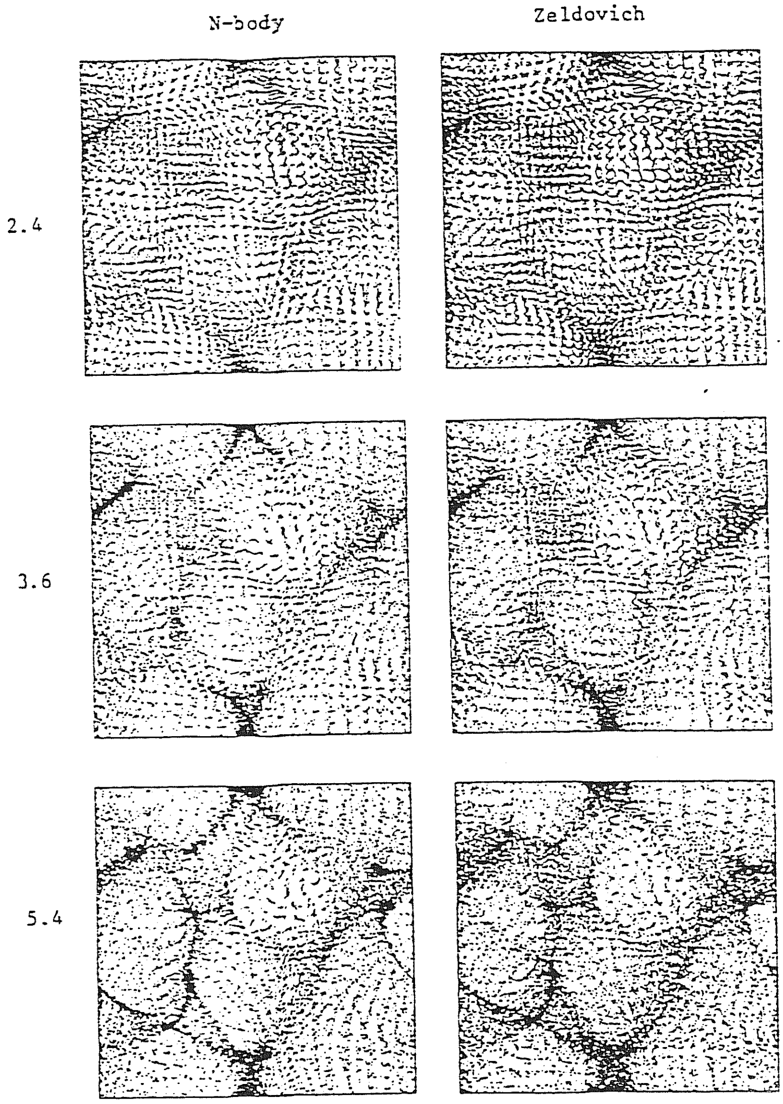

Figure 4.1: *Comparison between an exact N-body simulation and the Zeldovich approximation in a* $\Omega_o = 1$ *Universe. The scale factor* $a(t)$ *is normalized to be unity at the beginning of the simulation (after [118]).*

gravitational sticking of particles, occurring after their orbits cross. The idea of sticking in a collisionless medium has been originally introduced in the cosmological context by Gurbatov & Saichev [176] and Gurbatov *et al.* [177], with the aim of avoiding some undesirable features of the Zeldovich approximation. The fluctuation evolution with sticking is described by the Burgers equation [65, 66], that is well known in hydrodynamical studies of viscous fluids.

Starting from the approximate solution given by eq.(4.7), let us evaluate the velocity and the gravitational acceleration fields,

$$\mathbf{u} \;=\; \dot{\mathbf{x}} \;=\; a\dot{b}\mathbf{s}(\mathbf{q}) \qquad ; \qquad \dot{\mathbf{u}} \;=\; (\dot{a}\dot{b} + a\ddot{b})\,\mathbf{s}(\mathbf{q}) \;=\; \left(H + \frac{\ddot{b}}{\dot{b}}\right)\mathbf{u}\,. \tag{4.13}$$

Taking $b(t)$ as the new time variable and introducing the comoving density $\eta = a^3\rho$ (here we fix the scale factor to be unity at the present time), the first two of eqs.(4.3) becomes

$$\begin{aligned} \frac{\partial \eta}{\partial b} + \nabla_x \cdot (\eta \mathbf{s}) \;&=\; 0 \\ \frac{\partial \mathbf{s}}{\partial b} + (\mathbf{s} \cdot \nabla_x)\mathbf{s} \;&=\; 0\,. \end{aligned} \tag{4.14}$$

Consistently, the Zeldovich approximation $\mathbf{x} = \mathbf{q} + b\mathbf{s}(\mathbf{q})$ is the solution of the second of the above equations, with the first equation providing the continuity equation. A modification of the dynamics described by such equations is introduced in order to account for the effect of sticking and is obtained by introducing a viscosity term, so that

$$\frac{\partial \mathbf{s}}{\partial b} + \nabla_x \cdot (\eta \mathbf{s}) \;=\; \nu^2 \nabla_x^2 \mathbf{s}\,. \tag{4.15}$$

The above equation is very well known in studies in fluidodynamics as the Burgers equation [65, 66]. For any non-vanishing ν value, no matter how small it is, it prevents the penetration of one particle stream into another and avoids the orbit crossing occurring in the Zeldovich approximation. In the framework of Burgers dynamics, the forming structures are thin sheets, whose thickness depends on the viscosity parameter ν. Since viscosity is relevant on a scale-length $\nu^{1/2}$ (below which dissipation occurs and velocity gradients are erased), we expect that this should also be the typical thickness of arising non-linear structures. For this reason, the Burgers dynamics in the $\nu \rightarrow 0$ limit provides structures of vanishing thickness. The resulting clustering is different from that provided by the Zeldovich solution, which amounts to fixing $\nu = 0$ in eq.(4.15). While the Burgers dynamics gives rise to extremely thin pancakes, which correspond to the formation of shocks, the Zeldovich prescription generates more diffuse structures, since particles continue travelling after crossing of their orbits.

The application of the Burgers equation in gravitational clustering study is usually called the *adhesion* approximation. Many attempts have been devoted in recent years to investigating the dynamics of large-scale structure formation within this approach, by means of both analytical [178, 114] and numerical [387, 270] treatments. The relevance of the Burgers equation lies in the fact that, despite the fact that it is manifestly non-linear, it can be linearized in a straightforward way and its analytical solution can be explicitly evaluated. This permits one to characterize, at least partially, the statistics of the subsequent clustering [114]. In order to linearize eq.(4.15), let us consider the vectorial Hopf-Cole transformation for the velocity potential

$$s_i(\mathrm{q},t) \;=\; -2\nu \frac{\partial}{\partial x_i} \log U(\mathrm{x},b). \tag{4.16}$$

After substituting into the Burgers equation, we get

$$\frac{\partial U}{\partial b} \;=\; \nu \nabla_x^2 U\,, \tag{4.17}$$

which is the usual linear diffusion (heat) equation. Writing its solution for the velocity potential, we get

$$\mathrm{s}(\mathrm{x},b) \;=\; \frac{\int \frac{\mathrm{x}-\mathrm{q}}{b}\exp\left[-\frac{G(\mathrm{x},\mathrm{q},b)}{2\nu}\right] d\mathrm{q}}{\int \exp\left[-\frac{G(\mathrm{x},\mathrm{q},b)}{2\nu}\right] d\mathrm{q}}\,, \tag{4.18}$$

where

$$G(\mathrm{x},\mathrm{q},b) \;=\; \Phi_o(\mathrm{q}) + \frac{(\mathrm{x}-\mathrm{q})^2}{2b} \tag{4.19}$$

and $\Phi_o(\mathrm{q})$ is the potential of the initial field. Although a suitable geometrical method has been devised to study the structure of the potential velocity field given by eq.(4.18), a detailed characterization of the gravitational clustering described by Burgers dynamics has been made possible with the realization of N-body simulations based on the adhesion approximation (see *e.g.*, refs.[270, 387]). The reason for the great deal of attention to the adhesion approach lies essentially in the fact that the availability of the analytical solution for s(q) greatly reduces the computational costs with respect to usual N-body codes, while avoiding some of the limitations of the Zeldovich approach. The trick of putting in by hand the viscous term in the *rhs* of eq.(4.15) avoids the pancake smearing and simulates non-linear gravitational clustering as a sort of dissipative smoothing process. Although this could give a reasonable approximation at scales where not so much power is present in the fluctuation spectrum, it fails to describe the strong clustering regime, where "exact" N-body simulations show a greater variety of structures, that can not be generated only on the ground of a smoothing process.

Several other approximations have been proposed by several authors in order to overcome the drawbacks of the Zeldovich and adhesion approximations and better follow the development of non-linear clustering (see, *e.g.*, refs. [181, 394, 64, 253]). A quite common feature of these approximations resides in the fact that they seems rather inadequate to account for the essential features displayed by strongly non-linear gravitational dynamics. In the following, we discuss other approximations, that deal with the case of fully non-linear gravitational dynamics.

4.1.4 Self-similar clustering

The detection of the power-law shape for the correlation functions of cosmic structures (see Chapter 2) led to the suggestion that gravitational clustering should proceed in a self-similar way. Although eqs.(4.3), which describe the evolution of density inhomogeneities, do not introduce characteristic scales, nevertheless these can be present in the Friedmann background or in the initial fluctuation spectrum. For this reason, self-similar clustering is based on the assumption that *a)* the Universe is spatially flat, with $\Omega_o = 1$, in order to have no characteristic time- or length-scales, and *b)* the initial power-spectrum is scale-free,

$$P(k) \;=\; Ak^n \,. \tag{4.20}$$

In the above expression, the spectral index ranges in the interval $-1 < n < 1$, in order to allow for convergence of the peculiar velocity field at very small and very large scales. Actually, by introducing a small scale cutoff smaller n values are permitted, and self-similarity exists in a limited scale range. In any case, $n > -3$ is required in order to allow for gravitational clustering to proceed in a hierarchical way (see §2.2). Note, however, that cosmological spectra are expected to have characteristic scales (see §4.2, below). In this case, the argument of self-similar clustering still applies, at least if the effective spectral index takes a roughly constant value in a sufficiently large scale range.

In the linear regime, the variance at the comoving scale x (see eq.[2.54, for a matter-dominated expansion, reads

$$\sigma_x^2(t) \;=\; x^{-(n+3)}t^{4/3} \,. \tag{4.21}$$

If x represents the comoving scale at which unity variance is attained, then it scales with time as $x \propto t^{-3(n+3)/4}$, which shows that, as time increases, larger and larger scales go non-linear. Accordingly, the physical non-linearity scale is $r = a(t)\,x \propto x^{(5+n)/2}$. Moreover, the requirement for a non-linear lump of size r to be stable is that its characteristic dynamical time-scale, $t_{dyn} = (G\rho)^{-1/2}$, should be equal to t. Thus, the average density inside non-linear lumps scales as $\rho \propto t^{-2} \propto x^{-(9+3n)/2}$ and the density-radius relation, $\rho \propto r^{-\gamma}$, has the logarithmic slope

$$\gamma \;=\; \frac{9+3n}{5+n} \,. \tag{4.22}$$

The above result was derived for the first time by Peebles [284] and expresses the power-law shape of the 2-point function as a function of the primordial spectral index. According to this expression, it comes out that the value $\gamma = 1.8$, relevant to galaxy clustering, is produced by $n = 0$, which correspond to a white-noise initial spectrum. Starting from different scale-invariant initial conditions, Efstathiou *et al.* [124] tested the validity of the Peebles' scaling argument against evolved N-body simulations. They found that eq.(4.22) agrees quite well with their simulations only in the strongly non-linear, $\xi \gtrsim 100$, regime, while in the range $1 \lesssim \xi \lesssim 100$ the 2-point function declines more steeply than expected. This result leads to a quite paradoxical conclusion; since the observed $\xi(r)$ for galaxies is a unique power-law up to scales ($\sim 10h^{-1}$ Mpc) greater than the correlation length, the assumption of an initial self-similar spectrum gives rise to characteristic scales in the evolved $\xi(r)$. Viceversa, the observed scale-invariance of clustering forces one to conclude that the initial spectrum should have a scale dependence tuned in such a way that self-similarity is produced during dynamical evolution.

It is however to be observed that the above scaling argument is based on assumptions, whose validity is far from being proved. First of all, linear theory is used to establish the time dependence of the size of lumps that reach the non-linear phase. This amounts to assuming that the dynamical range in which the transition between linear and non-linear gravitational clustering is very narrow, so that linear theory can be safely applied to establish the initial conditions for non-linear evolution. Although this could be a reasonable approximation for $n \gtrsim 0$ spectra, which have strong small-scale power and rapidly decline at large scales, it is expected not to be true for less steep spectra. In this case, some aspects of gravitational evolution are present, which are not accounted for in the above simplified picture. As an example, if significant power is present at large scales, the forming clumps start to accrete material from surrounding regions, so as to steepen the density profile of the resulting structures. On the other hand, the secondary accretion will not be very important if the characteristic amplitude of large-scale fluctuations is very small. Hoffman & Shaham [195] evaluated the density profile of non-linear structures, by allowing initial clumps to accrete matter from the surrounding, according to the prescription of the secondary infall paradigm [160, 174]. In this way, they derived the logarithmic slope γ of the density-radius relation to be

$$\gamma = \begin{cases} \frac{9+3n}{4+n} & -3 < n \le -1\,, \\ 2 & -1 \le n < 1\,. \end{cases} \tag{4.23}$$

A comparison of this expression with eq.(4.22) shows that there is no remarkable difference between the two expressions for $0 \lesssim n \lesssim 1$, in accordance with the expectation that secondary accretion is not very important in the case of steep spectra. Vice-versa, for $n \lesssim 0$ eq.(4.23) systematically provides a larger slope for the density-radius relation, which significantly detaches from $\gamma \simeq 2$ only at $n \lesssim -1.5$. In this picture, the value $\gamma \simeq 2$ expected on the ground of galaxy clustering and flatness of spiral rotation curves is a much more natural outcome of non-linear gravitational clustering, than expected on the ground of the Peebles' scaling argument.

A similar conclusion has been also obtained by Saslaw [331], following a completely different approach to non-linear gravitational dynamics. In the framework of a thermodynamical approach, he suggested that $\gamma \sim 2$ is a sort of "attracting" solution for fully virialized structures, quite independently of initial conditions. It is remarkable to note how all these indications toward a unique density scaling relation produced by non-linear gravitational evolution confirm the earlier suggestion that Fournier d'Albe gave already in 1907 [138]. He observed that the requirement that the virial velocity $v = \sqrt{M/R}$ in a cluster of size R does not diverge, but converges to a finite constant value, leads to the density-scale relation

$\rho \propto R^{-\gamma}$ with $\gamma = 2$.

Although the above discussed descriptions of non-linear clustering evolution provide hints about the origin of the observed 2-point correlation function, nevertheless they say nothing about the scaling of higher-order correlations. A comprehensive treatment to include the whole hierarchy of n-point functions requires one to solve the non-linear dynamics for the probability distribution function, which generates correlations of any order.

A classical approach in this direction is represented by the BBGKY (Bogoliubov-Born-Green-Kirkwood-Yvon) equations for a collisionless and self-gravitating fluid. Since a complete description of the analysis of the BBGKY equations is rather long, here we will present only a brief sketch, while comprehensive treatments for applications in the cosmological context can be found in refs.[287, 145, 183]. In order to describe the statistics of the fluid particles, let $f(\mathbf{x},\mathbf{p},t)$ be the phase space distribution function, which depends on the comoving coordinate $\mathbf{x}$, on the moment $\mathbf{p} = ma^2\dot{\mathbf{x}}$ (m being the mass of the single particle) and on time t. Accordingly, the fluid density reads

$$\rho(\mathbf{x}) = \frac{m}{a^3}\int d\mathbf{p}\, f(\mathbf{x},\mathbf{p},t)\,, \tag{4.24}$$

while the statistics of the system is described by the phase-space correlation functions

$$C^{(n)}_{1,\dots,n} = \langle f_1 \dots f_n \rangle\,. \tag{4.25}$$

The evolution of the distribution function is described by Liouville's equation

$$\frac{\partial f}{\partial t} + \frac{p^\alpha}{ma^2}\frac{\partial f}{\partial x^\alpha} - m\frac{\partial \Phi}{\partial x_\alpha}\frac{\partial f}{\partial p^\alpha} = 0\,, \tag{4.26}$$

where Φ is the gravitational potential related to the density field according to

$$\Phi(\mathbf{x}) = -G\,a^2\int d\mathbf{x}\,\frac{\rho(\mathbf{x}) - \bar{\rho}}{|\mathbf{x}' - \mathbf{x}|}\,. \tag{4.27}$$

From eq.(4.26), an infinite sequence of equations can be obtained by evaluating its moments, that is, by solving the equation for the time-evolution of the phase-space correlation functions. The sequence of all such equations represents the hierarchy of BBGKY equations, which are obtained through a sort of moment expansion of the Liouville's equation (4.26). A characteristic of this hierarchy is represented by the fact that the solution of the equation of order n depends on the solution at the order $n+1$. This can be easily understood, by observing that the Φ term includes the integral of the distribution function, through eq.(4.25). Thus, at the order n, this term turns into the integral of the $(n+1)$-th order correlation. Because of this peculiarity, suitable assumptions are needed to close the hierarchy and provide a consistent solution.

Several attempts have been devoted to solving the BBGKY equations, although all such solutions rely on approximations, which are expected to hold only in the strongly non-linear regime. Davis & Peebles [101] observed that, in the case of a flat Universe with scale-free initial spectrum, the BBGKY equations admit a self-similar solution, with spatial n-point correlation functions of the type

$$\kappa_n \propto r^{(n-1)\gamma}, \tag{4.28}$$

As usual, γ is the slope of the 2-point function, so that eq. (4.28) is consistent with the hierarchical expression for the n-point function as provided by eq.(2.24). Both Fry [144, 145] and Hamilton [183] concluded that hierarchical correlations represent the solution of the BBGKY hierarchy in the strongly non-linear regime, although they found different sequences of hierarchical coefficients Q_n. The validity of these solutions to describe the non-linear clustering will be discussed in Chapter 5, where they will be compared to the correlation properties developed by N-body simulations.

4.2 The spectrum of primordial fluctuations

In the description of the evolution of density inhomogeneities, we often made the simplifying assumption that the initial power-spectrum has the simple power-law expression $P(k) \propto k^n$. Although the scale-free Zeldovich spectrum is expected on the grounds of the classical inflationary scenario, nevertheless distortions of its shape should arise during the subsequent phases of cosmic expansion, and characteristic scales are imprinted on the form of $P(k)$ at the onset of the structure formation. Since the amount of such distortions and the scales at which they occur are strictly related to the nature of the fluctuations and to the matter content of the Universe, their knowledge becomes of crucial relevance in order to fix the initial conditions for the galaxy formation process.

Theoretical models for the determination of the power-spectrum, which is responsible for structure formation, starts from the assumption of a primordial $P_{pr}(k)$ at a sufficiently high redshift, $z_{pr} \gg z_{eq}$ [$z_{eq} \simeq 4.2 \times 10^4\,(\Omega h^2)$ is the redshift of the epoch of matter-radiation equality]. The usual choice $P(k) = Ak$ corresponds to the Harrison-Zeldovich spectrum. Due to the evolution of density perturbations, the slope of the power-spectrum is left unchanged at wavelengths $\lambda \gg \lambda_{eq} \sim ct_{eq}$, that exceed the horizon size at t_{eq}. On the contrary, the shape of the spectrum at $\lambda \ll \lambda_{eq}$ crucially depends on the nature of the matter which dominates the expansion. In order to account for these effects, the post-recombination spectrum is usually written as

$$P(k) = T^2(k)\,P_{pr}(k), \tag{4.29}$$

where the *transmission factor* $T(k)$ conveys all the informations about the pre-recombination evolution and the nature of the matter content.

Before starting with the discussion of the different scenarios for the origin of the fluctuation spectrum, we mention an important distinction between two different kinds of primeval fluctuations, namely adiabatic (curvature) and isothermal (isocurvature) fluctuations. Adiabatic perturbations correspond to fluctuations in the energy density and both matter and radiation components are equally involved in such perturbations. The name adiabatic derives from the fact that the number density of any species relative to the entropy density is constant. On the contrary, isothermal fluctuations do not correspond to perturbations in the energy density, rather they are originated by variations of the local equation of state. Such fluctuations are called isothermal since temperature fluctuations are suppressed with respect to matter fluctuations by a factor $\sim \rho_m/\rho_r$, so that during the radiation-dominated expansion any $\delta T/T$ becomes negligible. Any difference between adiabatic and isothermal fluctuations makes sense only on super-horizon scales. Viceversa, for perturbations that are well inside the horizon, causal microphysical processes give rise to a local redistribution of the energy density, due to the presence of pressure gradients in isothermal fluctuations. As a consequence, the adiabatic condition is finally attained and any distinction is no longer important. However, at sufficiently early times, presently observable scales are outside the horizon and the above distinction becomes important. As far as the origin of adiabatic fluctuations is concerned, they can either be imprinted in the initial conditions or can be generated by any mechanism which is able to push sub-horizon to super-horizon scales. This is the case for the inflationary expansion, that, indeed, is considered the classical mechanism to generate adiabatic fluctuations. On the other hand, isothermal perturbations require microphysical mechanisms to be generated, which cannot transport energy on super-horizon scales. Although suitable models have also been proposed to generate isothermal perturbations from inflation, special initial conditions are always required, while adiabatic perturbations comes out much more naturally [118, 224]. Stringent constraints about the nature of primordial fluctuations have been recently provided by COBE observations. A comparison of the temperature fluctuations predicted by a variety of isocurvature models [196] with the detected CMB temperature anisotropy seems to rule out all such models [393]. For these reasons, in the rest of this Section we will only describe the evolution of adiabatic density perturbations.

4.2.1 The evolution of baryonic fluctuations

In order to follow the evolution of fluctuations of baryonic matter, let us consider the second of eqs.(4.3), with the inclusion of a pressure term:

$$\frac{\partial \mathbf{v}}{\partial t} + (\mathbf{v}\cdot\nabla)\mathbf{v} + \frac{1}{\bar{\rho}}\nabla p + \nabla\Phi \;=\; 0\,. \tag{4.30}$$

Accordingly, the linearized equation for the evolution of the δ field in Fourier space reads

$$\frac{\partial^2 \tilde{\delta}_{\mathbf{k}}}{\partial t^2} + 2H\frac{\partial \tilde{\delta}_{\mathbf{k}}}{\partial t} + \left(\frac{v_s^2 k^2}{a^2} - 4\pi G\bar{\rho}\right)\tilde{\delta}_{\mathbf{k}} \;=\; 0\,. \tag{4.31}$$

Here

$$v_s \;=\; \left(\frac{\partial p}{\partial \rho}\right)^{1/2}_{adiabatic} \tag{4.32}$$

is the adiabatic sound speed in a medium with equation of state $p = p(\rho)$. In eq.(4.31) we can define the critical Jeans wavelength

$$\lambda_J = v_s \left(\frac{\pi}{G\bar{\rho}}\right)^{1/2}, \tag{4.33}$$

which discriminates between two different regimes for the perturbation evolution. For fluctuation modes with wavelength $\lambda > \lambda_J$, the pressure contribution can be neglected and the linear solution of eq.(4.6) is recovered. Viceversa, for $\lambda < \lambda_J$ the gravitational term becomes negligible and the solution oscillates. Thus, while fluctuations on a scale greater than the Jeans length are not pressure-supported and are able to grow by gravity, at scales below λ_J the fluctuations behave like oscillating sound waves.

If ρ_b is the average baryon density, we can define a baryon Jeans mass scale,

$$M_J = \frac{2}{3}\pi\rho_b\lambda_J^3, \tag{4.34}$$

which is the mass of the smallest baryonic fluctuation that is able to grow. Before recombination, at a redshift $z_{rec} \simeq 10^3$, matter and radiation are tightly coupled by Thomson scattering. In this regime they behave like a single fluid with

$$v_s = \frac{c}{\sqrt{3}}\left(\frac{3}{4}\frac{\rho_m}{\rho_r} + 1\right)^{-1/2}. \tag{4.35}$$

Since matter-radiation equality occurs at $z_{eq} = 4.2 \times 10^4(\Omega h^2)$, the Jeans mass just before recombination is

$$M_J \simeq 9 \times 10^{16}(\Omega_o h^2)^{-2} M_\odot, \tag{4.36}$$

of the same order of the mass of a supercluster. After recombination, however, photons are no longer coupled to matter, so that the equation of state rapidly changes and the baryonic component behaves like a monoatomic gas with

$$v_s = \left(\frac{5k_B T}{3m_p}\right)^{1/2}, \tag{4.37}$$

m_p being the proton mass. At the recombination temperature $T_{rec} \simeq 3000\,K$, it corresponds to a Jeans mass

$$M_J = 1.3 \times 10^6(\Omega_o h^2)^{-1/2} M_\odot. \tag{4.38}$$

Thus, although before recombination the Jeans mass involves scales of superclusters, after matter and radiation decouple it drops by several orders of magnitude to the value of the mass of globular clusters, and fluctuations on small scales are able to start growing again.

It is worth comparing the Jeans mass before recombination with the baryon mass contained inside the Hubble radius $M_{H,b} = (4\pi/3)\rho_b(ct^3)$. According to eq.(4.35), it is

$$\frac{M_J}{M_H} \simeq 26\left(\frac{3}{4}\frac{\rho_m}{\rho_r} + 1\right)^{-3/2}, \tag{4.39}$$

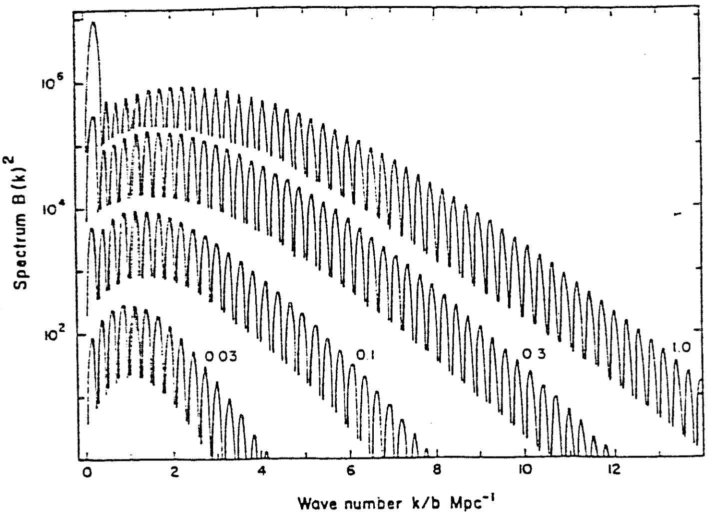

Figure 4.2: *Plot of* $B^2(k) = k^4T^2(k)$ *for adiabatic baryonic perturbations. Each curve is labeled by the corresponding value of* Ωh^2 *and the parameter* b *dividing* k *takes the value 0.065, 0.100, 0.179, 0.392 for curves from bottom to top. The spectrum amplitude is arbitrary (from [288]).*

so that, until radiation dominates, the Jeans mass exceeds the mass inside the horizon and all the subhorizon fluctuations are constrained not to grow.

A further characteristic scale, which enters in the spectrum of baryon fluctuations, is due to the collisional damping occurring just before recombination. As recombination is approached, the coupling between radiation and baryons becomes no longer perfect and the photon mean free path starts increasing. Thus, photons can diffuse more easily from overdensities carrying with them matter, to which they are however still quite tightly coupled. The final effect is to damp fluctuations below the scale which corresponds to the distance travelled by a photon in an expansion time-scale. This is known as Silk damping [356] and an accurate evaluation of the smoothing mass scale in the post-recombination baryon spectrum [126] gives

$$M_D \simeq 2\times 10^{12}(\Omega_o/\Omega_b)^{3/2}(\Omega_o h^2)^{-5/4}M_\odot\,, \tag{4.40}$$

which obviously depends on the baryon density parameter Ω_b. The Silk damping increases by several orders of magnitude the mass-scale of the smallest fluctuation, which starts growing after recombination, smaller scale perturbations being heavily suppressed.

An accurate estimate of the transmission factor for the baryon fluctuation spectrum was made by Peebles [288], and the result is shown in Figure 4.2. The severe small-scale suppression due to Silk damping is apparent. The oscillatory behaviour is due to the phases of the Jeans oscillation of the single mode at recombination. Although the simplicity of a purely baryonic model is rather attractive, nevertheless it suffers from a number of serious problems, which makes it extremely unlikely. Even without referring to the difficulty of reconciling the predictions based on primordial nucleosynthesis, $\Omega_b h^2 \lesssim 0.1$, with both dynamical estimates of the mean cosmic density and the inflationary prejudice $\Omega_o = 1$, the baryonic spectrum gives too large fluctuations at the scale of 10-20h^{-1} Mpc, with respect to what observed for the galaxy distribution. Even more, a purely baryonic model is ruled out since it predicts too high CMB temperature fluctuations with respect to current detections and upper limits [316, 357].

Peebles [290] suggested that agreement with the upper limits on the CMB anisotropy could be attained if we allow for a reionization at a redshift substantially smaller than that of standard recombination ($z_{rec} \sim 1000$). In this case, a substantial reduction of the small-scale anisotropies would be provided. In the framework of its "minimal" baryonic model, Peebles suggested an open purely baryonic Universe, in which an early formation of cosmic structures should provide the source for the ionizing radiation. Although this mechanism erases primary CMB temperature fluctuations, nevertheless it has been recognized that secondary fluctuations are generated because of peculiar motions at the time at which the optical depth attains unity (see, *e.g.*, refs.[382, 117]. The resulting anisotropies turn out to severely constraint the purely baryonic model.

4.2.2 Non-baryonic models

A fundamental property of non-baryonic dark matter is that it is not coupled to radiation, at least at the epochs relevant for the origin of the primordial fluctuation spectrum. For this reason, no dissipative Silk damping is expected. However, a non-dissipative damping of fluctuations occurs in any case, due to free-streaming of dark matter particles. In fact, until such particles are relativistic they are able to freely cross the horizon within the Hubble time, thus washing out all the fluctuations below the horizon scale. This effect stops when the temperature of the Universe drops below the mass of DM particles and they become non relativistic. The size of the horizon at this epoch fixes the smallest scale of the fluctuations surviving free-streaming damping. Thus, it is clear that a crucial parameter to establish the shape of the fluctuation spectrum in a DM model is the velocity of the constituent particles.

The importance of following the evolution of the DM spectrum lies in the fact that it determines after recombination the spectrum of fluctuations of ordinary baryonic matter, so as to provide the seeds where dissipative processes occur and galaxy formation takes place. In fact, soon after recombination the Jeans mass for the baryonic component drops to a very small value. As a consequence, baryonic fluctuations starts growing again by gravitational instability, until their amplitude matches that of the non-baryonic DM perturbations.

The HDM spectrum

In the hot dark matter (HDM) model the mass contained inside the horizon when constituent particles become non relativistic is much larger than the typical mass of a galaxy ($\sim 10^{11} M_{\odot}$), so that particles with a low mass are required. A natural candidate for HDM constituent is the massive neutrino. If a neutrino species has non vanishing mass, then its contribution to the mean matter density is

$$\Omega_\nu \simeq \left(\frac{m_\nu}{100eV}\right) h^{-2}, \tag{4.41}$$

where m_ν is expressed in eV. Although in the classical version of the Standard Model for the electroweak interaction the neutrino is considered massless, nevertheless there exists no fundamental reason which fixes $m_\nu = 0$. Viceversa, several theoretical models have been proposed to generate a non-vanishing neutrino mass [398, 395, 156]. The possibility of HDM models with massive neutrinos became very popular at the beginning of the 80s, after Lyubimov *et al.* [237] claimed the discovery of a non-vanishing mass, $m_{\nu_e} \simeq 30\,eV$, for the electron neutrino, which provides the closure density by taking $h = 0.55$ for the Hubble parameter. Although this result has been not confirmed by subsequent experiments, nevertheless the possibility of massive neutrinos received great attention due to its deep implications both in astrophysics and in elementary particle physics.

In the framework of the HDM scenario, Sciama recently suggested the possibility of decaying neutrinos of mass $m_\nu \simeq 30\,eV$ and decay time $t_d \simeq (1-3)\times 10^{23}s$ to solve a variety of ionization problems in the astrophysical and cosmological contexts (see, *e.g.*, refs.[343, 344, 330, 345]). This model also provides a series of predictions of observable quantities, which makes it quite easily testable. A strong criticism has been recently raised to this model, after the lack of detection of a UV line in the range 13.6–16 eV, which is expected to be originated by the ionization of intergalactig gas, due to the presence of photons produced by neutrino decay [97]. It is however clear that the relevance of the implications of this decaying neutrino model not only in astrophysics, but also in elementary particle physics [322, 152] surely requires a further clarification of its merits and limitations.

For a neutrino of mass m_ν, the redshift at which it becomes non-relativistic can be estimated to be $z_\nu \simeq 6\times 10^4\,(m_\nu/30\,eV)$, which corresponds to

$$M_{\nu,\mathrm{H}} \simeq 2\times 10^{15}\left(\frac{m_\nu}{30\,eV}\right) M_\odot \tag{4.42}$$

for the mass contained inside the horizon at that epoch. Numerical calculations carried out by Bond & Szalay [44] give the transmission factor

$$T(k) = 10^{-(k/k_\nu)^{1.5}} \quad ; \quad k_\nu \simeq 0.4\,\Omega_o h^2\,\mathrm{Mpc}^{-2}, \tag{4.43}$$

which suppresses all the fluctuation modes at wavelengths $\lambda < \lambda_\nu = 2\pi/k_\nu \simeq 40\,(m_\nu/30\,eV)^{-1}$ Mpc. In Figure 4.3 we show a log-log plot of $k^{3/2}|\delta(k)|$, which represents the typical mass fluctuation, $(\delta\rho/\rho)_\lambda$, at the scale $\lambda = 2\pi/k$ versus the fluctuation wavelength. The deficit of power at scales below $\sim 10\,(\Omega_o h^2)^{-1}$ Mpc, due to neutrino free-streaming is apparent. In the HDM scenario, the smallest fluctuations surviving recombination are roughly on the same scale as large galaxy clusters. Accordingly, structure formations proceeds in a "top-down" way; first large pancakes of mass $\sim 10^{15}M_{\odot}$ form, while galaxies originate later via fragmentation of structures at larger scales. Numerical simulations of structure formation in HDM dominated Universe have been done [391] and show the development of cellular structures, which are promisingly similar to those displayed by the redshift galaxy surveys. Big voids forms on scales comparable to the characteristic scale λ_ν, which are surrounded by galaxies and clusters forming at the intersection between three of such cells. Unfortunately, the agreement with the observed galaxy distribution is only apparent. In fact, since the characteristic size of the earliest forming structures is λ_ν, the variance of the matter distribution at this scale should be around one. This is quite difficult to reconcile with the much smaller correlation length displayed by the galaxy distribution, $r_o \simeq 5h^{-1}$ Mpc. In order to alleviate this problem, we can either assume that galaxy formation occurred very recently (at $z \lesssim 1$) so as to give no time for structures to become overclustered, or invoke some mechanism to reduce the galaxy clustering with respect to that of the underlying matter. It is however clear that, whatever way out we choose, additional problems arise. A too recent galaxy formation seems to be quite difficult to reconcile with the detection of high-redshift ($z \gtrsim 3$) quasars. It is however not clear to what extent quasars can be considered progenitors of all the galaxies. If this were not the case, then the criticism of galaxy formation timing for HDM models would not be so stringent (see,*e.g.*, refs.[256, 40]). Also requiring that galaxies are less clustered than matter is at variance with the expectation that dissipative galaxy formation should preferentially occur in the deep wells of the gravitational potential field, which would give an increase of their correlation with respect to the DM distribution. In addition, current upper limits on the CMB anisotropy at scales of some arcminutes are dangerously near to the HDM predictions. Hopefully, in the near future more precise observations will give the final word about the viability of the standard HDM model. It is however clear that, if a neutrino species were discovered to have a non-vanishing mass $m_\nu \simeq 30\,eV$, we are obliged to consider HDM as responsible for structure formation and try to overcome in some way all the above difficulties. To this purpose, variations of the standard HDM scenario have been proposed. As an example, Villumsen *et al.* [380] suggested that, if fluctuation evolution is driven by the presence of randomly distributed seeds (such as primeval black holes or non-topological solitons), then a considerable amount of small-scale power is added to the HDM spectrum and some of its undesirable features are avoided (see §4.3 below).

The CDM spectrum

The dark matter content of the Universe is said to be cold if particles becomes non-relativistic at sufficiently early times, so that the mass contained within the horizon at that time is much smaller than the typical galaxy mass. Thus, in the cold dark matter (CDM) scenario the free-streaming cut-off scale is to small to be of any cosmological relevance. The low velocity required for CDM particles can arise for two different reasons. Firstly, the particle mass is so large that they become non relativistic at a high temperature. This cannot be the

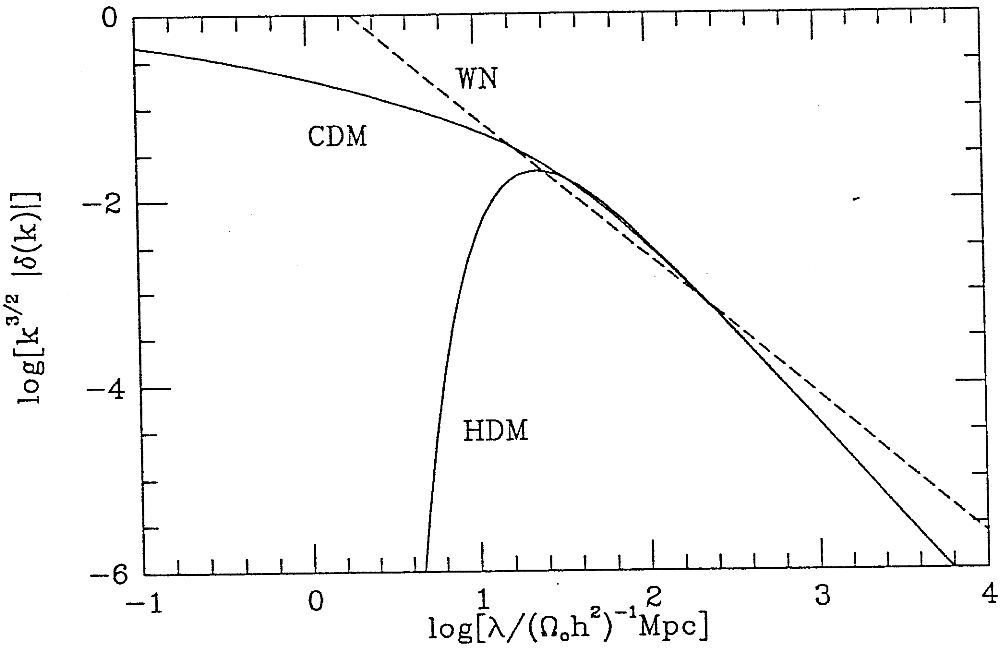

Figure 4.3: *The post-recombination spectrum for adiabatic perturbations in both HDM and CDM scenarios and primordial Zeldovich spectrum. The plotted quantity is* $k^{3/2}|\delta(k)$ *and represents the typical density fluctuation at the scale* λ, $(\delta\rho/\rho)_\lambda$. *Also plotted for reference is the white noise spectrum (dashed line).*

case for massive neutrinos, for which a mass $\gtrsim 100\,eV$ give an exceedingly high contribution to the density parameter (see eq.[4.41]). However, supersymmetric theories provide a large variety of exotic CDM candidates, such as photinos or gravitinos, with masses above $1\,GeV$. Secondly, there can be particles, like axions, that never were in thermal equilibrium, so they have a very low thermal velocity, despite their small mass ($\sim 10^{-5}eV$). See, *e.g.*, ref.[132] for a recent review of CDM candidates.

Although for CDM fluctuations neither free-streaming nor Silk damping introduce characteristic scales, a distortion of the spectrum is however generated by the Meszaros effect [261], which suppresses the growth of fluctuations of non-relativistic matter which cross the horizon before non-relativistic matter start dominating. In order to see how this happens, let us consider the equation for the evolution of non-relativistic matter fluctuations in a relativistic background:

$$\frac{d^2\delta}{dt^2} + 2H\,\frac{d\delta}{dt} - 4\pi G\bar{\rho}_m\delta = 0\,. \tag{4.44}$$

Here the relativistic background enters only in determining the cosmic expansion rate $a(t)$. By introducing the new time variable $\tau = \bar{\rho}_m/\bar{\rho}_r$ ($\tau \propto a$ since $\bar{\rho}_m \propto a^{-3}$ and $\bar{\rho}_r \propto a^{-4}$), eq.(4.44) can be rewritten as

$$\frac{d^2\delta}{d\tau^2} + \frac{2+3\tau}{2\tau(1+\tau)}\,\frac{d\delta}{d\tau} - \frac{3}{2}\,\frac{\delta}{\tau(1+\tau)} = 0\,. \tag{4.45}$$

The growing-mode solution of the above equation turns out to be $\delta \propto 1 + \frac{3}{2}\tau$. Thus, during radiation domination ($\tau \ll 1$), the fluctuation amplitude is frozen. Only when non-relativistic matter dominates ($\tau \gg 1$) the matter fluctuations start growing as $\delta \propto a$, as expected on the grounds of linear evolution. In order to evaluate the resulting distortion of the spectrum, let $\delta_k(t_i)$ be the amplitude of the fluctuation mode with wavenumber k at some initial time t_i before matter-radiation equality, and suppose that it crosses the horizon at t_H, also before equality. During this period the amplitude grows by a factor t_H/t_i. Since $t_H \propto k^{-2}$ during radiation domination, the amplitude of the perturbation after horizon crossing is frozen at the value $\delta_k(t_i)t_i^{-1}k^{-2}$ until matter starts dominating. Viceversa, fluctuations outside the horizon continue to grow according to linear theory so that no distortion of the spectrum occurs at such scales. The characteristic scale at which we expect a feature in the spectrum is that corresponding to the horizon size at t_{eq},

$$\lambda_{eq} \simeq 10\,(\Omega_o h^2)^{-1}\,\mathrm{Mpc}\,. \tag{4.46}$$

If $P(k) \propto k^n$ was the primordial spectrum, its shape after t_{eq} will be preserved at scales larger than λ_{eq}, while for $\lambda \ll \lambda_{eq}$ the freezing of the fluctuation amplitude tilts the spectral index to the value $n-4$. Precise computations of the processed spectrum in a CDM dominated Universe have been done by several groups (see, *e.g.*, refs.[289, 43]). In Figure 4.3 we plot the spectrum for adiabatic CDM fluctuations, obtained from the transmission factor

$$T(k) = [1 + (ak + (bk)^{1.5} + (ck)^2)^\nu]^{-1/\nu} \tag{4.47}$$

[$a = 6.4\,(\Omega_o h^2)^{-1}$ Mpc, $b = 3.0\,(\Omega_o h^2)^{-1}$ Mpc, $c = 1.7\,(\Omega_o h^2)^{-1}$ Mpc, $\nu = 1.13$], obtained by Bond & Efstathiou [43], assuming the presence of three species of massless neutrinos and negligible contribution from the baryonic component ($\Omega_b \ll \Omega_{CDM}$). A primordial Zeldovich spectrum is also assumed. According to eq.(4.47), as $k \to 0$, we have $T(k) \simeq 1$ and the primordial spectrum $P(k) \propto k$ is left unchanged. At small scales, $T(k) \propto k^{-2}$, so that $P(k) \propto k^{-3}$. In Figure 4.3, the presence of a characteristic scale at λ_{eq} is apparent, although the bending of the spectrum is rather gradual.

As opposed to the HDM scenario, a considerable amount of small-scale power is now present, so that the first fluctuations reaching non-linearity are at small scales. The resulting clustering proceeds in a "bottom-up" way, with structures of increasing size forming from the tidal interaction and the merging of smaller structures. It is clear that the possibility for small-scale structures not to be disrupted as the hierarchical clustering goes on depends on the ability of the baryonic component to cool down and fully virialize before being incorporated within larger DM fluctuations. Taking into account dissipative effects allows one to identify the CDM fluctuations where galaxy formation takes place. Detailed investigations of galaxy formation in the CDM scenario (see, *e.g.*, ref.[41]) have shown that the observed variety of galaxy morphology and the relative morphological segregation of the clustering can be nicely reproduced.

A series of detailed numerical simulations of structure formation in a CDM Universe have been originally realized by Davis, Efstathiou, Frenk & White (see, *e.g.*, refs.[98, 392]).

The N-body experiments show that the primordial CDM spectrum is able to account for many aspects of the observed galaxy clustering at small and intermediate scales. In Chapter 5 we will analyze in detail the statistics of the clustering developed by CDM N-body simulations. Here we only mention that, once a suitable "biassing" prescription is assigned to identify galaxies in a purely dissipationless simulation, not only the correct correlation amplitudes are reproduced, but also the density profile of galaxy halos, small-scale velocity dispersions, cluster richness and the mean number density of both galaxies and clusters. Despite the remarkable merits of CDM in reproducing the observed clustering at scales $\lesssim 10\, h^{-2}$ Mpc, serious problems are encountered when dealing with larger scales. In fact, for fluctuation wavelengths above λ_{eq}, the shape of the CDM spectrum steepens toward the Zeldovich profile, $P(k) \propto k$, with a substantial reduction of the power at such scales. As a first consequence, the resulting 2-point correlation function goes negative already at $\sim 15\,(\Omega_o h^2)^{-1}$ Mpc. This is at variance with respect to the observed 2-point function for the cluster distribution, that shows no evidence of anticorrelation up to $\sim 50h^{-1}$ Mpc. Also the amplitude of the cluster correlation is too high with respect to that provided by CDM [392], unless the observed $\xi(r)$ is substantially enhanced by contamination effects (see §2.1.4). A further problem encountered by CDM is due to the high amplitude of large-scale motions. For instance, Vittorio *et al.* [381] compared the predictions both CDM and HDM with the observed large-scale ($\sim 50h^{-1}$ Mpc) galaxy motions and concluded that both models are ruled out to a high confidence level. More recently, this model ran into even more difficulties in reproducing the large-scale ($\gtrsim 20h^{-1}$ Mpc) galaxy clustering observed from recently compiled catalogues. Using the APM sample, Maddox *et al.* [246] have shown that the angular 2-point function declines at large scales much less steeply than predicted by CDM, thus revealing an excess of power at $\gtrsim 20h^{-1}$ Mpc. A similar conclusion has also been reached by Efstathiou *et al.* [125] and Saunders *at al.* [336] from the moment analysis of the galaxy counts for the QDOT redshift sample.

It is clear that these problems could be alleviated by allowing for variations of the standard CDM model, which is based on the assumptions of $\Omega_o = 1$, Zeldovich initial spectrum and Gaussian initial fluctuations, as provided by the classical inflationary paradigma. One possibility for adding more power at large scales could be lowering Ω_o. According to eq.(4.46), this amounts to increasing the horizon size at time of matter-radiation equality, so as to push to larger scales the bending of the CDM spectrum. In this case, the agreement with the inflationary requirement for a flat Universe can still be achieved by taking a non-vanishing cosmological constant term Λ. Efstathiou *et al.* [127] have shown that taking $\Omega_{CDM} = 0.2$ and $\Lambda = 0.8$ accounts for the excess power displayed at large scales by the APM survey. It is however clear that a density parameter significantly smaller than one could eliminate many motivations to introduce non-baryonic dark matter. Further possibilities to save CDM are represented by assuming "tilted" post inflationary spectra, $P(k) \propto k^n$, with $n < 1$ [242, 85], or to abandon the random-phase prescription, which ensures the Gaussian nature of primordial fluctuations.

All such variations of the standard CDM picture introduce more parameters in the original model, at the expense of its simplicity and elegance. On the other hand, it is worth emphasizing that any comparison between models and observed clustering is based on suitable assumptions to identify galaxies out of DM fluctuations, both in analytical calculations and N-body experiments. One may ask whether changing these prescriptions substantially modifies the model predictions. For instance, Couchman & Carlberg [92] have shown that, if galaxies were weakly antibiassed with respect to the CDM distribution, then the present epoch should correspond to a more dynamically evolved stage in the simulation. The resulting increase of power at large scales significantly improves the agreement with observations. This clearly shows that, before drawing any extreme conclusion about the reliability of any model, it is appropriate to check whether any prediction strongly depends on the assumption of galaxy formation or is a robust outcome of the DM spectrum, quite independently of the relation between matter and galaxy distributions.

4.3 Do we need non-Gaussian perturbations ?

Naturalness arguments suggest that Gaussian statistics should characterize the density fluctuations at the early stages of their evolution (see §2.1.2). However, the random-phase prescription provided by classical inflation [25], joined with the dark matter models described in the previous Section, is not completely successful in accounting for the complete body of observational constraints. The idea of abandoning initial Gaussianity surely enlarges the permitted parameter space. Although the increase of degrees of freedom could make completely arbitrary any choice of initial conditions, nevertheless one's hope is that observational constraints could significantly reduce the number of allowed models.

Still keeping the advantages of inflation, non-Gaussian initial conditions could however arise in several models of stochastic and power-law inflation, or within models where the inflaton field driving the accelerated expansion is non-linearly coupled to an auxiliary scalar field (see, *e.g.*, refs.[11, 274, 29]; see also ref.[328] and references therein).

In recent years, non-Gaussian models based on the generation of global textures, cosmic strings and other topological defects during early phases of the cosmic expansion have become very popular and detailed investigations of the large-scale structure they develop have been made.

Global textures are expected to be formed during a symmetry breaking phase-transition, which leads to the formation of topological defects [218]. Phase transitions and defects are naturally expected in any particle physics theory, whose fields transform according to some representation of a non-Abelian symmetry group [61]. Non-Gaussian fluctuations are produced through the formation of texture "knots", having size of the same order of the horizon at that epoch. Subsequently, such knots collapse down to a scale ($\sim 10^{-37}$ cm) corresponding to the energy of symmetry breaking ($\sim 10^{16}\,GeV$, as expected from GUTs), accreting the surrounding DM with a spherically symmetric pattern. The resulting matter distribution is characterized by the presence of isolated non-linear clumps, which act as seeds for the formation of cosmic structures. N-body simulations of a CDM Universe with textures [280] show that, because of the large amount of power added at small scales with respect to the standard scenario, high density peaks trace the matter distribution fairly well. Although several problems of large-scale clustering are alleviated, the presence of massive clumps causes a too high velocity dispersion inside clusters.

Another kind of topological defect that arises from symmetry breaking is represented by cosmic strings ([401]; see also refs.[61, 224] and references therein). Different from texture formation, cosmic strings arise from the breaking of the Abelian $U(1)$ group. The resulting topological defect is one dimensional (a string, indeed). Expressing the metric in cylindrical coordinates, the line element for an infinite and straight cosmic string reads

$$ds^2 \;=\; dt^2 - dz^2 - dr^2 - (1-4G\mu)^2\, r^2\, d\vartheta^2 \qquad \text{for} \quad G\mu \ll 1\,. \tag{4.48}$$

Here μ is the string mass per unit length. The resulting metric reduces to the Minkowski metric of empty space after substituting $\vartheta \to (1-4G\mu)\vartheta$. In this case, the range of variation of the polar angle is $0 \le \vartheta \le 2\pi\,(1-4G\mu)$ and the resulting deficit angle, $8\pi G\mu$, causes a sort of "conical" singularity. Several interesting consequences of this conical geometry arise, such as the splitting of images for objects located behind the string, discontinuities through the string of the CMB temperature and formation of DM wakes due to the string motion. After the $U(1)$ symmetry breaks down, a string network arises, which is formed both by infinite strings and closed string loops. Once formed, this network evolves under the competing effects of string stretching, which is due to cosmic expansion and dominates on scales larger than the horizon, and of string tension, which dominates below the horizon size. If the evolution of the network were only described by string stretching, it would led to a disastrous consequences. In fact, in a comoving volume the energy density of radiation would decrease as $a^{-1}(t)$, while that associated to a string would increase as $a(t)$. As a consequence one should reach the undesirable result of a string-dominated Universe. Actually, the network evolution is not so trivial and a detailed numerical treatment is required [51]. In Figure 4.4 we show a typical simulation of a string network configuration during its evolution. The two essential aspects for the evolution of the network are: a) self-interaction of infinite strings, which produces finite loops, and b) loop oscillations, as they cross the horizon, and decay through the emission of gravitational waves. Both analytical arguments and numerical simulations suggest that at the time of matter-radiation equality, when structure formation starts, there are few long strings crossing the horizon plus a distribution of string loops. The relevance of string loops is in that they are expected to be seeds for the formation of galaxy clusters. In fact, a string loop of radius R produces a gravitational field that, at scales greater than R, is the same as that due to a point source of mass $M = \beta\mu R$, with β a suitable numerical constant, which is related to the shape of the loop. For reasonable choices of the parameters, it turns out that, for a radius

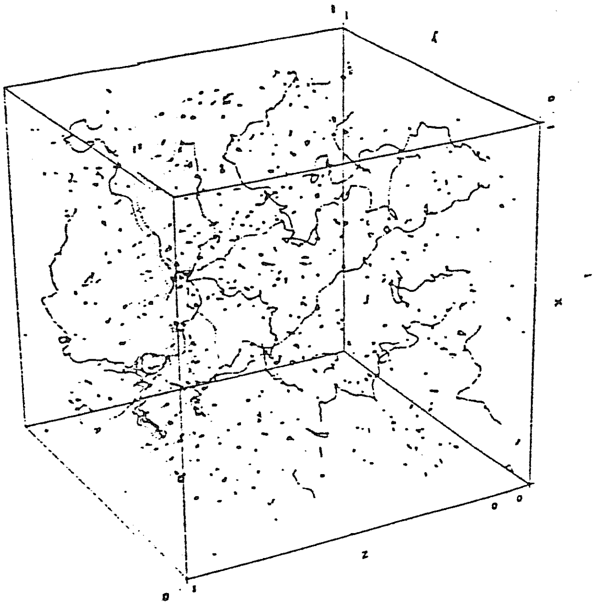

Figure 4.4: *Numerical simulation of a string network, which arises after a $U(1)$ symmetry breaking. It consists of both infinite strings crossing the box and finite string loops (after [51]).*

$R = 10^{-1}\lambda_{eq}$, it is $M \sim 10^{11}M_\odot$. Using linear theory for the growth of mass perturbations, we find that from t_{eq} to the present time, such a loop accretes a mass of $\sim 10^{15}M_\odot$, which is the typical mass of Abell clusters. In this context, the correlation properties of the loop distribution should reproduce that of clusters. Indeed, Turok [371] found that the 2-point function of string loops has a nearly power-law shape, with slope $\gamma \simeq 2$, surprisingly similar to that observed for clusters. It is however clear that a more detailed model for structure formation should also specify the dark matter content. The presence of loops as seeds for structure formation is expected to add power at small scales and, thus, could alleviate some drawbacks of HDM. Numerical simulations with cosmic strings and massive neutrinos [342] have shown that galaxy formation starts substantially earlier than in both standard CDM and HDM models, thus reconciling with observations of high-redshift QSOs. Due to the presence of accretion seeds, the final distribution contains isolated density peaks embedded in a smooth background.

The possibility of generating seeds of accretion for structure formation through a series of mechanisms, which also include primordial black holes and non-topological solitons, led Villumsen *et al.* [380] to study the general problem of seeded structure formation with N-body simulations. The general result is that galaxies again form at high redshifts and immediately after their formation they are strongly clustered. The availability in the near future of complete and extended QSO surveys at increasing redshifts will be a crucial test for these kind of models. An analytical treatment of the statistical properties of matter distribution with accretion seeds has also been recently provided by Scherrer & Bertschinger [341].

A further scenario, in which non-Gaussian fluctuations drive the formation of large-scale clustering, is provided by the explosion model. Different from the gravitational instability picture, in the explosion scenario energy perturbations of non-gravitational origin drive material away from the seeds of the explosions, sweeping primordial gas into dense, expanding shells. As these shells cool, their fragmentation could give a further generation of objects which again explode, thus amplifying the process and giving rise to large scale structure formation. At the end, clusters of galaxies are expected to be placed at the intersection of three expanding bubbles, while galaxies are arranged on spherical shells [200, 275]. The explosion scenario became very popular after the compilation of redshift surveys suggested a "bubbly" geometry of the galaxy distribution (see §1.1), with nearly spherical voids surrounded by a sheet-like galaxy distribution. Since shells enclose an appreciable amount of space, their dynamical interaction plays a fundamental role in the formation of clusters, superclusters and voids. A variety of physical mechanisms might generate such explosions, such as supermassive stars or supernovae from the earliest galaxies. However, it is at present not clear whether or not such energy sources can be sufficient to create the large voids that are observed. Holes on scales of some tens of Mpcs would require a fantastic amount of supernovae exploding coherently. Moreover, suitable initial conditions are anyway needed to generate primordial objects that act as seeds of explosions. Since both initial conditions for explosion generations and fragmentation processes for galaxy formation are poorly understood, only simplified versions of the explosion scenario have been investigated. Weinberg *et al.* [386] modelled explosions by using a random distribution of expanding shells with a power-law distribution of radii. After identifying clusters at the intersection of three shells, the statistics of their spatial distribution is quite well reproduced. Although the explosion scenario is rather successful in accounting for the presence of large-scale correlations in the cluster distribution, however it is not clear whether it turns into an acceptable galaxy distribution [326]. If galaxies were simply arranged in sheets surrounding devoid bubbles, the geometry of their distribution should be characterized by a Hausdorff dimension $D_{\rm H} \simeq 2$, which substantially agrees with what is found from the analysis of galaxy samples [249]. However, although the geometry of the galaxy distribution is rather well specified, the same is not true for their clustering.

Rather than dealing with specific non-Gaussian models, which arise from theoretical prescriptions for primeval fluctuation origin, a further possibility is to analyze the development of clustering for a wide class of non-Gaussian primordial perturbations and check whether some of these are able to reproduce the observed large-scale texture of the galaxy distribution. Moscardini *et al.* [265] and Matarrese *et al.* [252] analysed CDM N-body simulations starting with both Gaussian and non-Gaussian initial conditions. They considered several non-Gaussian models, generated through local non-linear transformations of an underlying Gaussian field. The aim of their analysis was to show whether a CDM dominated Universe can be reconciled with the observed large-scale clustering, once we take more general initial conditions than those provided by the random-phase prescription. As expected, remarkable differences with respect to the large-scale clustering produced by Gaussian initial conditions are produced, which turns out to crucially depend on the sign of the initial skewness, $\langle \delta^3 \rangle$, of the density fluctuations. Positive skewness models, which have a predominance of concentrated overdense regions, rapidly develop extremely clumped structures with a resulting small coherence length. The resulting distribution suffers even more from all the problems of the standard Gaussian CDM model. Viceversa, for negative skewness models the dynamics of the clustering is dominated by the presence of expanding devoid regions, while the merging of the surrounding shells forms large-scale filaments and knots. The resulting cellular structure resembles that arising in the explosion scenario, but with the fundamental difference that it is purely driven by gravitational instability, with large-scale coherence produced by the initial phase correlations. The rich variety of structures produced at large scales goes in the right direction to reconcile the CDM model with large-scale observational constraints. Weinberg & Cole [385] ran a variety of N-body simulations by considering a wider class of non-Gaussian models. Instead of checking whether the CDM model can be improved by adopting suitable initial conditions, these authors attempted to seek the features of large-scale clustering which are to be ascribed to the presence of initial phase-correlations. After applying a list of statistical tests, they concluded that, despite the remarkable variety of clustering realization obtainable with non-Gaussian initial conditions, the standard Gaussian model with $\Omega_o = 1$, biassed galaxy formation and power-spectrum $P(k) \propto k^{-1}$ is the most efficient in reproducing the complete body of observational data. Since the required shape of $P(k)$ closely follows that of the CDM spectrum, at least at the scales probed by such simulations, the above result seems to indicate that the problems displayed by the CDM model at scales $\gtrsim 10h^{-1}$ Mpc are not due to the standard random-phase assumption, rather they are more likely to be ascribed to the lack of large-scale power.

4.4 Biassed galaxy formation

A crucial step to test any theory about the formation and evolution of primordial inhomogeneities is to compare its predictions to the observed galaxy distribution. Differences between dark matter and galaxy distributions probably exist and their origin lies in the physical mechanisms and environmental effects occurring during the formation of cosmic structures. For this reason, it is of crucial relevance to understand which kind of processes are relevant to the formation of visible objects and whether they give rise to a segregation between luminous and dark matter. In this Section we will discuss the main motivations which require substantial differences between the clustering of DM and of observable objects. We will also describe some mechanisms of galaxy formation, which could be naturally responsible for this "bias". Finally, we point out analytical approaches to biassing, in order to show the relations between the statistics of the galaxy distribution and that of the matter density field.

4.4.1 Motivations for bias

The original motivation, which led to the introduction of the concept of biassing in the distribution of cosmic structures, is the enhanced clustering displayed by rich clusters which respect to the galaxy distribution. As discussed in Chapter 2, both galaxies and galaxy clusters are characterized by a 2-point correlation function with the same power-law shape, $\xi(r) \propto r^{-1.8}$, although holding at different scales and with a remarkably different amplitude. By comparing the value $r_{o,g} \simeq 5h^{-1}$ Mpc of the galaxy correlation length to that, $r_{o,c} \simeq 20h^{-1}$ Mpc, of rich clusters, it turns out that $\xi_c(r) \simeq 15\,\xi_g(r)$. As a consequence, the large-scale distribution of matter in the Universe can not be traced with the same efficiency both by galaxies and galaxy clusters. On the contrary, these results seem to suggest that neither galaxies nor clusters trace the actual matter distribution. The large correlation amplitude for rich Abell clusters was the main reason that lead Kaiser [213] to introduce the concept of bias. According to this model, he postulated that rich Abell clusters arise only from those peaks of the background field, that exceed a limiting density threshold value, and consequently exhibit an enhanced clustering with respect to the underlying matter. Further supports in favour of a biassed distribution of cosmic structures also come from the existing correlations between galaxy types and environment, and from luminosity and morphological dependence of galaxy clustering. On the ground of such results, it would be surprising if galaxy formation were not significantly affected by environmental effects, segregating galaxies from the underlying matter.

Another problem that would arise assuming that galaxies are fair tracers of matter lies in the difficulty to reconcile the observed density contrast between voids and the surrounding filamentary structures at scales of $\gtrsim 50h^{-1}$ Mpc with the small scale ($\lesssim 1°$) CMB isotropy. This discrepancy can be obviously alleviated by allowing for the DM distribution to be more smooth that the galaxy one, so as to be associated with smaller post-recombination fluctuations.

In the framework of the standard CDM scenario, results from N-body simulations led to the conclusion that, if $\Omega_o = 1$, the large scale distribution of galaxies cannot be reproduced, unless the galaxy formation is biassed (see ref.[98] and Chapter 5 below). In such simulations, the resulting 2-point correlation function steepens in time as steeper parts of the initial fluctuation spectrum become non-linear. If mass traces the galaxy distribution, the stage of the simulation to be considered as the present time is reached when its logarithmic slope matches that ($\gamma = 1.8$) observed for galaxies. However, this evolutionary stage corresponds to a value of the clustering length $r_o \simeq 1\,(\Omega_o h^2)^{-1}$ Mpc, too small if compared with $r_{o,g} \simeq 5\,h^{-1}$ Mpc observed for galaxies, unless $\Omega_o h \lesssim 0.2$. Thus, assuming a flat CDM dominated Universe requires an enhanced clustering of galaxies with respect to the background, such that $\xi_g(r) = (5-20)\xi_m(r)$ (for $h = 0.5$ and $h = 1$). Also in the case of a HDM dominated Universe, some biassing in the galaxy distribution should be present. In this case, the lack of small-scale power causes a high coherence length in the primeval spectrum (see §4.3). As a consequence, the requirement that the slope of the 2-point function is $\gamma = 1.8$ implies $r_o = 8\,(\Omega_o h^2)^{-1}$ Mpc for the neutrino correlation length. Here, the required bias is in the opposite sense because the resulting galaxies must be less clustered than the DM background (antibiassing).

Indications that the luminous matter should be segregated with respect to the dark matter also come form measurements of the mass-to-light ratio for cosmic structures of increasing size. Mass is in general estimated by using a relation of the type $M \simeq v^2 R/G$, where v is some observed velocity involved in a structure of size R. While at the scales ($\sim 10\,h^{-1}$ kpc) of individual galaxies a typical value of the mass-to-light ratio for the stellar content is of the order $M/L \lesssim 10$ (in units of $M_\odot/L_\odot$), data on the virial analysis of groups and clusters of galaxies suggest $M/L \simeq 200$–$500\,h$ at scales $\sim 1h^{-1}$ Mpc [41]. This indicates that luminous (baryonic) matter does not follow the DM distribution, instead it turns out to be preferentially segregated at small scales. By comparing the above M/L value for clusters to that, $M/L \simeq 1600\,h$, required to close the Universe [122], we see that the contribution to the average density coming from the DM clustered at such scales gives $\Omega_o \simeq 0.2$–0.3. This value can be reconciled with $\Omega_o = 1$ only by allowing for the rising trend of M/L to include even larger structures (superclusters), thus increasing the amount of biassing as structures at larger and larger scales are considered.

The dynamical analysis of the amount of mass clustered at scales $\sim 1h^{-1}$ Mpc is usually based on the application of the "cosmic virial theorem" [286, 287] to pairs of galaxies. This theorem, which expresses the condition for hydrostatic equilibrium of a self-gravitating system of collisionless particles, relates the quadratic velocity dispersion between pairs at a given separation r to the corresponding 2-point correlation function $\xi(r)$, which measures the mass excess at the scale r responsible for the galaxy motion. Accordingly

$$v^2(r) \,\propto\, \Omega_o r^2\,\xi(r)\,. \tag{4.49}$$

By comparing the measured $v^2(r)$ with the galaxy 2-point function according to eq.(4.49) gives a density parameter $\Omega_o \simeq 0.1$-0.3 [102, 33, 182]. If, however, galaxies cluster more than the underlying matter, the density contrast of the two distributions can be related as $\delta_g = b_g\,\delta_m$, $b_g > 1$ being the so-called galaxy biassing parameter. According to this linear biassing prescription, the galaxy 2-point function turns out to be amplified with respect to that of the background as

$$\xi_g(r) \;=\; b_g^2\,\xi_m(r)\,. \tag{4.50}$$

Here $\xi_m(r)$ represents the matter 2-point correlation function. Since pairwise galaxy velocities are related to the mass excess, and not to the galaxy number excess, the matter correlation function $\xi_m(r)$ must be used in eq.(4.49). Then, the resulting value of Ω_o turns out to be amplified by a factor b_g^2 and agreement with a flat Universe is achieved for $b_g \simeq 2$-3.

Based on a similar approach, but using the dynamical information coming from the observed rotation curves for a suitable sample of spiral galaxies, we described in §2.1.6 a further measurement of Ω_o, that we recently realized [329]. We obtained the density excess associated with dark halos of spiral galaxies by considering, rather than the motion of a companion galaxy, the motion of test bodies rotating in the disk of spiral galaxies. This is done by means of proper decomposition of the galaxy rotation curves into the contributions or dark and visible components (see, *e.g.*, ref.[295]). On scales of few tens of kpcs, we find that the mass excess around galaxies, as evaluated through the virial estimate, scales with r like the excess in number of spiral galaxies. On the assumption that the light traces the mass we estimated the density parameter in the range $\Omega_o = 0.2$-0.4. Also in this case, the requirement of a flat Universe gives $b_g \sim 2.5$ for the galaxy biassing factor. In this respect, it is interesting to observe that, according to results reported in §2.1.6, the galaxy-matter correlation length turns out to be $r_{o,gm} = (3.2 \pm 0.3)\,\Omega_o^{-1/\gamma}h^{-1}$ Mpc. If $\Omega_o = 1$, a galaxy biassing factor $b_g \simeq 2.5$ gives $r_{o,m} = b_g^{-1/\gamma} r_{o,gm} \simeq 2h^{-1}$ Mpc, which agrees remarkably with the CDM correlation length, $r_{o,\mathrm{CDM}} \simeq 1\,h^{-2}$ Mpc, coming from N-body simulations, once $h \simeq 0.5$ is taken for the Hubble parameter.

At the larger scales of some tens of Mpcs, measurements of Ω_o have been made by using all-sky redshift samples based on the IRAS point source catalogue, to check whether the acceleration of the Local Group converges within the sample depth. This kind of analysis provides Ω_o values not far from one, thus suggesting that IRAS galaxies are, at such scales, fairly good tracers of the matter distribution (see ref.[215] and references therein). This result can be interpreted by saying either that IRAS galaxies are substantially less clustered than optically selected galaxies or that the amount of biassing should depend on the scale, passing from $b_g \simeq 2$-3 at scales below a few Mpcs, where the clustering is non-linear, to $b_q \simeq 1$ at the larger scales of linearity. Although the above result is rather comfortable as far as the flatness of the Universe in concerned, it is however at variance with respect to that of similar analysis based on the distribution of galaxy clusters. The dipole estimate for the spatial distribution of Abell and ACO clusters [302, 338] shows that the acceleration of the Local Group converges at larger distances ($\sim 150h^{-1}$ Mpc) than indicated by IRAS galaxies ($\sim 40h^{-1}$ Mpc), with a larger value of the dipole amplitude at the scale of convergence. The resulting estimate of the the density parameter gives the much lower value $4.5 \lesssim b_c\Omega_o^{-0.6} \lesssim 6$ (here b_c is the clustering biassing factor). Although this result is apparently in contradiction with previous estimates, nevertheless we should bear in mind that it is based on the distribution of rich galaxy clusters, which are structures even more biassed than galaxies. By comparing the correlation amplitude for galaxies and clusters, we obtain that the biassing factor for clusters with respect to galaxies is $b_{gc} \simeq 3$. Thus, taking $b_g \simeq 2$, the global biassing factor for the cluster distribution with respect to matter is $b_c = b_{cg}\, b_g \simeq 6$, and gives an Ω_o value which is consistent with one. Note, however, that this result is based on the assumption that the relation found at $\sim 10h^{-1}$ Mpc scales between the clustering amplitudes of galaxies and clusters can be extrapolated at the much larger scales of cluster dipole convergence. Whether

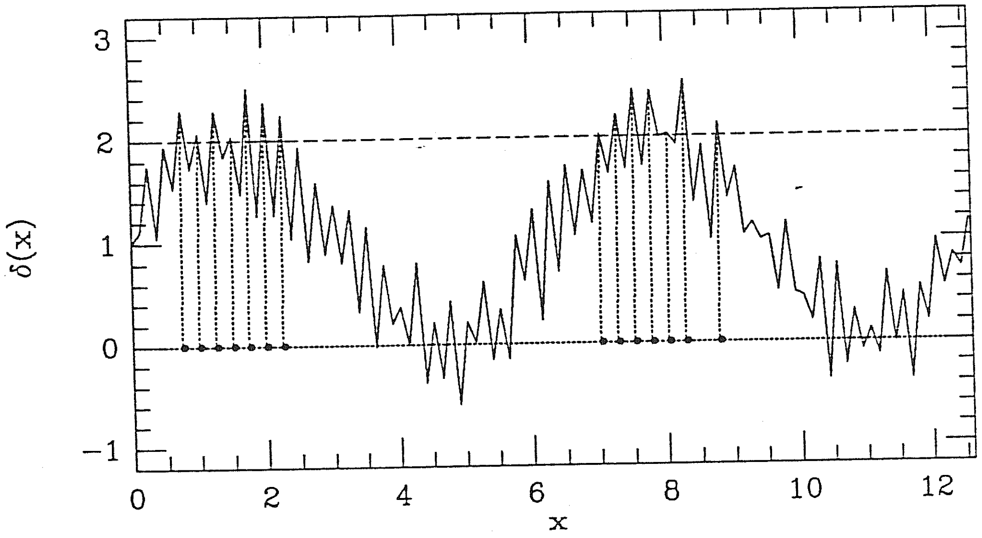

Figure 4.5: *Enhancement of the clustering of peaks higher than a fixed threshold with respect to the background peaks for a one–dimensional fluctuation field.*

or not this is a correct assumption surely requires further investigations.

4.4.2 Physical mechanisms for bias

It is clear that there is not a unique way to obtain an efficient segregation between luminous objects and DM distribution. Instead different bias mechanisms can arise in different cosmological scenarios, depending on the nature (cold or hot) of the dark matter, on the way of generating perturbations (gravitational instability or explosions) and so on (see refs.[103, 106] as reviews on biassed galaxy formation). A fundamental component to determine the resulting amount of biassing is represented by the baryon distribution at the onset of galaxy formation. In particular, it could happen that the baryonic component is segregated from the non-baryonic DM, so that galaxy formation occurs only in certain regions. Alternatively, it is also possible that the large-scale baryon distribution does trace the DM, but the efficiency with which baryons turn into luminous galaxies depends on other environmental effects, such as the local background density, or it may be the result of feedback from other galaxies. The effect may be destructive, suppressing galaxy formation, or constructive, enhancing galaxy formation in the neighborhood of other galaxies (*e.g.*, explosions).

An enhanced clustering of galaxies over the background matter can arise in a "bottom-up" scenario, if galaxies formed only from those peaks of the primordial density distribution, smoothed on the galactic scale R, that have amplitude at least ν times the *rms* value σ_R. If the power spectrum has sufficient amplitude at small wavenumbers, high peaks occur with greater probability in the crests rather than near the minima of a large scale fluctuation mode, so they display an enhanced clustering (see Figure 4.5). In particular, correlation functions arising from N–body simulation in a CDM-dominated Universe reproduce the observed ones

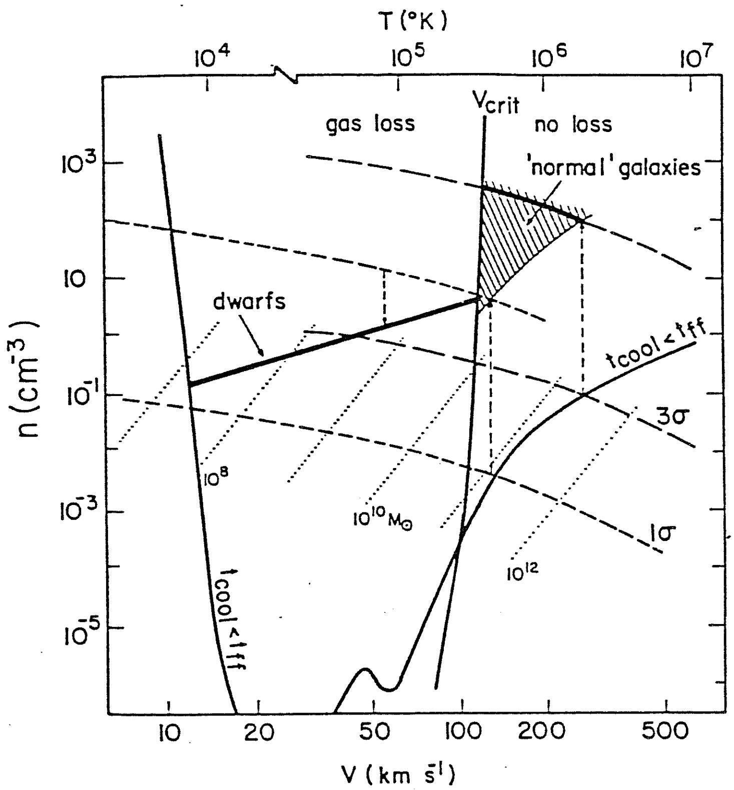

Figure 4.6: *Gas number density vs. virial velocity; the formation of dwarfs vs. "normal" galaxies in CDM halos, and the origin of biased galaxy formation (after [107]).*

if galaxies are identified with peaks at $\nu \sim 2.5$. In this picture, the crucial point is however to understand what physical mechanisms provide a sharp cutoff in the efficiency of galaxy formation for density fluctuations $\delta_R < \nu\sigma_R$.

A mechanism that has been proposed to introduce a threshold effect in the galaxy formation process is the so-called *natural bias*. In order to describe this scenario, let us observe that for a galaxy to be visible at the present time, we must ask that the baryonic matter has been able to dissipate and turn into stars. In order for dissipation to occur, the redshift of collapse clearly needs to be sufficiently large that there is time for an object to cool between its formation at redshift z_i, when the density fluctuation attains the critical value $\delta = \delta_c$ (if this epoch is identified with the end of the recollapse of a spherical fluctuation, then $\delta_c \simeq 1.69$ in the linear model), and the present epoch. More massive objects take longer to cool. Then, the requirement for a fluctuation on a given mass-scale M to have enough time from t_i (corresponding to z_i) to cool down turns into the introduction of a mass-dependent threshold $\nu(M)\sigma_M = \delta_c[1 + z_{cool}(M)]$. This situation is described in the density-temperature plot of Figure 4.6. The cooling curve, above which $t_{cool} < t_{dyn}$ (here $t_{dyn} \sim 1/\sqrt{G\rho}$ is the gravitational free-fall time, while t_{cool} is the cooling time), confines the region where the gas can contract and form stars [317, 41]. The plotted cooling curve is evaluated once a primordial gas composition is specified and under the assumption that the mean baryonic gas density is 10% of the total mass density. Each of the dotted diagonal lines indicates in the $n-T$ diagram the positions of all the structures having the same Jeans mass $M_J \simeq 100\,T^{3/2}n^{-1/2}M_\odot$. The almost vertical line V_{crit}, which has been introduced by Dekel & Silk [107], divides the permissible region for galaxy formation in two; a protogalaxy characterized by a virial velocity $> V_{crit}$ cannot expel a large fraction of its original gas content and form a normal galaxy. A protogalaxy with $V < V_{crit}$ can produce a supernova-driven wind, which would drive a substantial fraction of the protogalactic gas out, leaving behind a diffuse dwarf. The dashed curves labeled by $\nu\sigma$ ($\nu = 1,3$) refer to fluctuations with $\delta M/M$ equal to ν times the *rms* value, for a CDM spectrum. The corresponding parallel dashed curves refer to the protogalactic gas clouds, after a contraction of a factor 10 inside isothermal halos, to densities that are comparable to the halo densities such that star formation is possible. The two vertical arrows indicate the largest galaxies that can form out of 1σ and 3σ peaks, respectively. Let us observe that the major part of galaxies arising from 1σ peaks have $V < V_{crit}$, so that they would turn into dwarf galaxies. Instead, the shaded area represents the locus where normal galaxies are expected to be found. It is also evident that most of them are originated from 2σ and 3σ peaks. According to such predictions, normal galaxies, arising from exceptionally high peaks, are expected to be much more correlated than the background fluctuations and lie preferentially in rich clusters. Viceversa, dwarf galaxies form from typical (*i.e.*, 1σ) peaks, consequently they are expected to be better tracers of the matter distribution. In a scenario of this kind, morphological segregation naturally arises once different galaxy types are identified with peaks of different height of the primordial fluctuation field.

4.4.3 Properties of the biassed distribution

The possibility to devise a mechanism for interpreting the process of galaxy formation as a threshold effect on the initial density field allows us to relate the statistics of the matter distribution to that of the "biassed" field. The simplest case occurs for Gaussian density fluctuations $\delta(\mathbf{x})$ (see ref.[7] for a detailed description of the properties of Gaussian random fields). As already shown in §2.1.2, in this case the statistics are completely specified by the 2-point correlation function $\xi(r)$. According to eq.(2.71), in order to identify "physical" structures of characteristic size R out of $\delta(\mathbf{x})$, let us consider the smoothed fluctuations $\delta_{\mathrm{R}}(\mathbf{x})$, given by the convolution of $\delta(\mathbf{x})$ with a suitable window function, which suppresses fluctuation modes at wavelength $< R$. Accordingly, the correlations of the smoothed field are related to those of $\delta(\mathbf{x})$ according to

$$\mu_{\mathrm{R},n}(\mathbf{x}_1,\dots,\mathbf{x}_n) = \int\left[\prod_{i=1}^{n} W_{\mathrm{R}}(|\mathbf{x}_i-\mathbf{y}_i|)\,d\mathbf{y}_i\right]\mu_n(\mathbf{y}_1,\dots,\mathbf{y}_n)\,, \tag{4.51}$$

where $\mu_{\mathrm{R},n}$ is the "smoothed" correlation function. In Figure 4.7 we plot the power-law 2-point function before and after being smoothed by a Gaussian filter at two different scales.

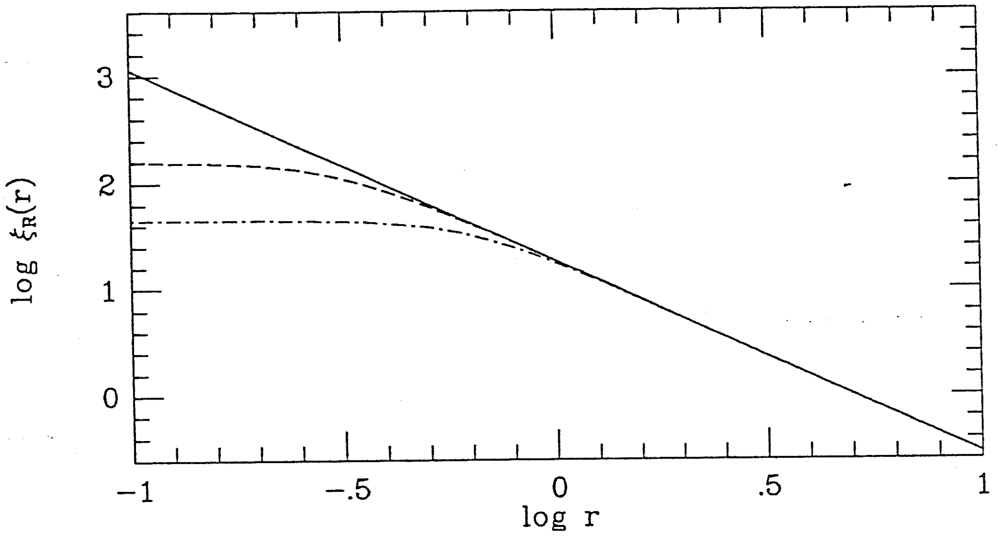

Figure 4.7: *The log-log plot of the smoothed 2-point correlation function, taking a Gaussian window and two different smoothing radii. The unsmoothed function (solid line) is assumed to have the power-law behaviour $\xi(r) \propto r^{-1.8}$. The correlation amplitude is arbitrary.*

The flattening of $\xi_R(r)$ at $r < R$ is apparent, which should simulate the cancellation of clustering details due to the structure formation process.

Following Kaiser's original prescription [213], let us introduce the biassed field

$$\rho_{\nu,R} = \theta[\delta_R(x) - \nu\sigma_R] , \tag{4.52}$$

which assigns a unity probability that a fluctuation $\delta_R(x) > \nu\sigma_R$ turns into an observable object, while structure formation is forbidden for those fluctuations lying below the critical threshold. It is interesting to note that this implementation of the natural biassing substantially reproduces the already described Press & Schechter [309] approach to the mass function (see §2.4.3). In both cases, one refers to the initial Gaussian density field in order to identify those fluctuations which turn into observable objects today. In particular, eq.(2.73) for the fraction of mass in structure having a mass above M can be equivalently rewritten as

$$\begin{aligned} \langle \rho_{\nu,R} \rangle &= \int \mathcal{D}[\delta]\,\mathcal{P}[\delta]\,\rho_{\nu,R}(x) \\ &= \frac{1}{\sqrt{2\pi}\,\sigma_R} \int_{\nu\sigma_R}^{+\infty} \exp\left(-\frac{\delta^2}{2\sigma_R^2}\right) d\delta = \frac{1}{2}\,\mathrm{erfc}\left(2^{-1/2}\nu\right) , \end{aligned} \tag{4.53}$$

so as to represent the expectation value of the biassed field, *i.e.* the fraction of volume above the threshold. It coincides with eq.(2.73) once we identify $\delta_c = \nu\sigma_R$.

The statistics of the so-called "excursion set" identified by eq.(4.52) does not coincide with those of the density peaks above $\nu\sigma_R$. However, the two distributions are expected to coincide when very high thresholds, $\nu \gg 1$, are considered. Bardeen *et al.* [24] gave a comprehensive description of the properties of peaks and the excursion set for a random Gaussian field in relation to the natural biassing scheme.

An interesting property of the biassed field $\rho_{\nu,\mathrm{R}}$ is that, due to the non-linear transformation of δ_R provided by eq.(4.52), it turns out to have a non-Gaussian statistics. In this case, non-Gaussianity is not the consequence of the non-linear dynamical evolution of $\delta_\mathrm{R}(\mathrm{x})$, but has a statistical origin. The n-point correlation functions of $\rho_{\nu,\mathrm{R}}(\mathrm{x})$ can be evaluated in terms of the n-point joint probability

$$\langle \rho_{\nu,\mathrm{R}}(\mathrm{x}_1) \ldots \rho_{\nu,\mathrm{R}}(\mathrm{x}_n) \rangle = \int \mathcal{D}[\delta]\, \mathcal{P}[\delta]\, \rho_{\nu,\mathrm{R}}(\mathrm{x}_1) \ldots \rho_{\nu,\mathrm{R}}(\mathrm{x}_n) . \tag{4.54}$$

As for the 2-point function, an analytical expression can be given in the high threshold limit $\nu \gg 1$ [213], which reads

$$\xi_{\nu,\mathrm{R}}(r) \simeq \exp\left[\left(\frac{\nu}{\sigma_\mathrm{R}}\right)^2 \xi_\mathrm{R}(r)\right] - 1 . \tag{4.55}$$

Although the correlation amplitude turns out to be increased, the first zero crossing of the "biassed" function occurs at the same scale as for the background function, so that peak selection does not introduce coherence at larger scales. In the weak correlation regime, $\xi_\mathrm{R}(r) \ll 1$, the expansion of the exponential term in eq.(4.55) gives

$$\xi_{\nu,\mathrm{R}}(r) \simeq \left(\frac{\nu}{\sigma_\mathrm{R}}\right)^2 \xi_\mathrm{R}(r) , \tag{4.56}$$

and the linear biassing prescription is recovered, with $b = \nu/\sigma_\mathrm{R}$. As the small scales of non-linearity are considered, then eq.(4.55) gives a peak correlation function which detaches from the power-law shape expected for the matter correlation function. This is at variance with the detected 2-point function, which holds as a power-law even in the $\xi > 1$ regime. Note that, at small scales, the matter distribution is expected to have non-Gaussian statistics due to the effect of non-linear gravity, so that eq.(4.55) is probably not valid in this regime.

Still keeping $\nu \gg 1$ and $\xi_\mathrm{R}(r) \ll 1$, a closed expression can be given also for the connected n-point functions. Jensen & Szalay [205] have shown that the higher-order correlations for the biassed field reproduce the Kirchwood expression of eq.(2.23). The corresponding connected 3-point function reads

$$\begin{aligned} \zeta_{\nu,\mathrm{R};123} &= \xi_{\nu,\mathrm{R}}(r_{12})\, \xi_{\nu,\mathrm{R}}(r_{23}) + \xi_{\nu,\mathrm{R}}(r_{12})\, \xi_{\nu,\mathrm{R}}(r_{13}) + \xi_{\nu,\mathrm{R}}(r_{13})\, \xi_{\nu,\mathrm{R}}(r_{23}) \\ &+ \xi_{\nu,\mathrm{R}}(r_{12})\, \xi_{\nu,\mathrm{R}}(r_{23})\, \xi_{\nu,\mathrm{R}}(r_{13}) , \end{aligned} \tag{4.57}$$

which, however, does not reproduce the hierarchical expression suggested by observational data (see Chapter 2). This could be well explained since in the weak correlation regime the cubic term in eq.(4.57) becomes negligible and it is difficult to detect any difference with the hierarchical expression. On the other hand, the galaxy 3-point function is better determined at small scales, where both the weak clustering approximation and the assumption of Gaussian fluctuations break down.

The generalization of the above biassing scheme to the non-Gaussian case has also been pursued, for both the statistics of the excursion set [251, 171] and for the peak distribution

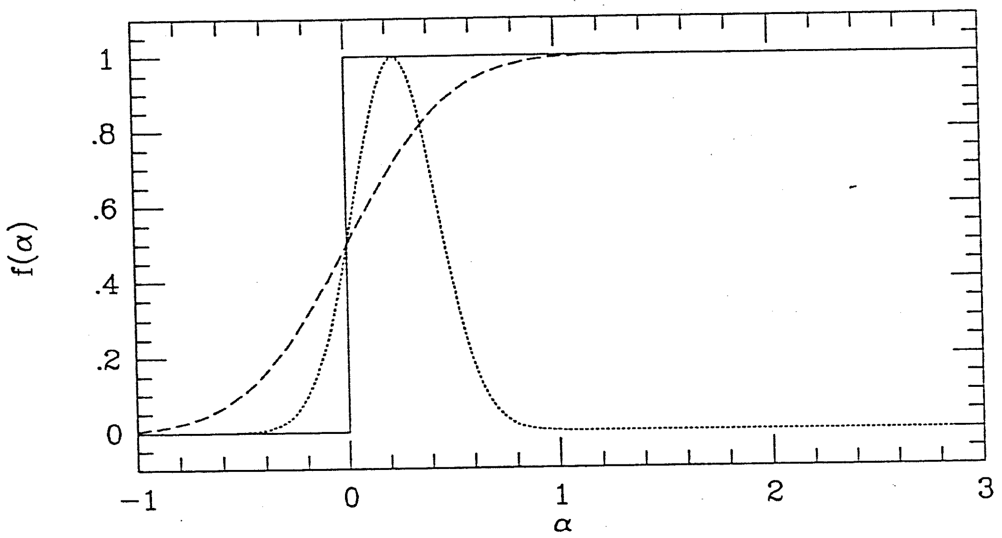

Figure 4.8: *The shapes of different threshold function. The solid line represents the usual θ-threshold of eq.(4.52), the dashed line is a smooth threshold which modulates the selection probability around the critical value $\nu\sigma_R$, and the dotted line is for a threshold which suppresses structure formation in correspondence of too high peaks.*

[76]. In this case, however, analytical expressions for measurable quantities can be given only in a limited number of cases, thus making even more difficult any comparison with observations.

The above described approach based on the natural biassing prescription surely has several merits to keep some essential features of the galaxy formation and to relate it to the observed clustering for different classes of cosmic structures. This procedure appears, however, to be too crude in several aspects: relating galaxy formation only to the height of primordial density peaks neglects other effects, such as merging within larger structures, tidal disruption, feedback from nearby forming objects, non-spherical geometry of the gravitational collapse, and so on. In this respect, selecting peaks in a yes/no fashion according to eq.(4.52) seems an exceedingly simplified representation of galaxy formation. Thus, it becomes of crucial relevance asking whether or not this model is robust, that is whether or not a slight modification of the biassing prescription leaves invariant the essential features of the biassed field. Attempts in this direction have been pursued by several authors, both by considering specific expressions for $\rho_{\nu,R}(x)$ [216, 24] or developing a general formalism to treat a wide class of biassed fields for Gaussian [361] and non-Gaussian [51] background fluctuations. In this framework, the biassed field can be expressed as

$$\rho_{\nu,R}(x) \;=\; f[\delta_R(x) - \nu\sigma_R] , \qquad (4.58)$$

where $f(\alpha)$ describes a generic non-linear transformation of $\delta_R(x)$ and generalizes eq.(4.52). By taking $0 \le f \le 1$, eq.(4.58) can be interpreted as the probability for a fluctuation to become an observable object. In Figure 4.8 we show some examples of such "threshold functions". In order to check the robustness of the results provided by the θ-threshold of eq.(4.52), we worked out some statistical properties for the other two plotted thresholds. In particular, we considered the effects of changing the criteria to select fluctuations on the mass function for groups and clusters of galaxies [52] and on the 2-point correlation function of rich clusters [48]. In both cases, we found that for suitable choices of the parameters determining the threshold profile, much better fits than those provided by the classical scheme are obtained. Far from meaning that such best-fit thresholds account for all the non-linear effects of structure formation, the results indicate that the criteria of fluctuation selection is a very critical issue; a marginal modification of the biassing scheme turns into important variations of the statistics of the biassed field. Once more, this suggests that, before drawing any conclusion about the large-scale clustering provided by a given model, a clear understanding of the physical mechanisms of galaxy formation is required.

Detailed results and applications of the generalized biassed models, as provided by eq.(4.58), have been already published in two papers, which appeared in *Astronomy & Astrophysics* (Borgani & Bonometto 1989, [51]; Borgani 1990, [48]), and in a further paper published in *The Astrophysical Journal* (Borgani & Bonometto 1990, [52]). More details can also be found in our *Magister Thesis* [49].

Chapter 5

Non linear clustering through N-body simulations

In this Chapter we analyse the statistical properties developed by cosmological N-body simulations. This allows us to study the details of the gravitational clustering in its non-linear phases. After a description of some technical aspects concerning N-body codes, we present the results of our analysis, which is based on both correlation and fractal approaches. In particular, we evaluate the 3- and 4-point correlation functions for both the background matter distribution and for biassed subsets of the entire particle configurations, which are identified as the high peaks of the initial density field. We also compare the results about higher-order correlations with the hierarchical expressions predicted by the solutions of the BBGKY equations. As far as the fractal analysis is concerned, we apply the dimension estimator already introduced in Chapter 3 in order to investigate the scaling properties associated with non-linear gravitational dynamics.

5.1 Why use N-body simulations ?

A complete description of the processes of formation and evolution of cosmic structures is very complicated and far from having reached a satisfactory level of explanation. Formation of galaxies and galaxy clusters involves both gravitational dynamics and hydrodynamical processes. As discussed in Chapter 4, a full analytical treatment of non-linear gravity has been not yet formulated, while several approximations have been devised to account for partial dynamical aspects. The situation is less clear when trying to account for dissipative hydrodynamical effects. This really represents a serious limitation to our understanding of the large-scale galaxy distribution, since the observational mapping of the Universe mostly passes through the detection of luminous structures, *i.e.* of the regions where dissipation plays a fundamental role. A complete description of the attempts devoted to describing the hydrodynamical effects involved in galaxy formation is beyond the scope of the present

Thesis. We only mention that at present the most promising approach is probably represented by numerical N-body simulations which also include hydrodynamical and radiative effects. Although only preliminary steps have been made in this direction (see, *e.g.*, refs.[77, 79]), nevertheless the emerging results are rather promising and it is to be expected that a further improvement of the "technology" will probably clarify in the next future our view of galaxy formation mechanisms.

On the other hand, in the framework of the gravitational instability picture, any non-gravitational effect is expected to be relevant only at quite small scales, where the characteristic time-scale for gravitational collapse, $t_{dyn} \sim (G\rho)^{-1/2}$, becomes comparable to the cooling time-scale t_{cool}. The determination of t_{cool} is surely less reliable than that of t_{dyn}, since it relies on the knowledge of cooling mechanisms, local chemical composition, etc. Nevertheless, it is reasonable to assume that at scales larger than that of a typical galaxy the dynamics is entirely determined by the non-dissipative gravitational interaction. At such scales, the description of the formation of large-scale structures is obtainable by solving the equations (4.3) for the evolution of the density inhomogeneities. However, the difficulty of analytically following the gravitational evolution when such equations are not linearizable (see §3.1.1) forces one to resort to numerical methods. In this context, N-body simulations furnish a fundamental contribution towards understanding in more detail the nature of non-linear gravitational dynamics. In fact, N-body codes describe the evolution of non-linear gravitational clustering by following particle trajectories under the action of the gravitational force. Initial conditions (*i.e.*, initial fluctuation and velocity fields) are fixed in a consistent way at a sufficiently early time, so that linear theory is a good approximation at all the relevant scales. Then, the final result of gravitational clustering is compared with the observational data, in order to assess the reliability of the initial condition model. It is however clear that, since small scale virialized structures probably have almost no memory of initial conditions, structures at larger scales (*e.g.*, filaments or voids) are much more useful in giving constraints about the nature of the primordial fluctuations.

A basic parameter which measures the capability of N-body codes to faithfully represent gravitational clustering is the width of their dynamical range for mass and length resolution. Mass resolution is fixed by the total number of particles employed. Since a given mass is assigned to each particle, we should require at the linear stage that fluctuations on a mass scale below that of a particle were negligible. The dynamical range for length resolution is fixed by the ratio of the size of the simulation box to the softening scale for the computation of the gravitational force. Very detailed tests are always required to measure the resolution of numerical codes, in order to be sure about the reliability of the subsequent clustering representation.

Because of the limits imposed by computational costs and computer memory, different strategies can be adopted in order to compromise between between numerical resource and extension of the dynamical range. Accordingly, three main categories of N-body simulations can be devised, which essentially differ in their prescriptions for evaluating the gravitational force between particles.

a) Direct integration of the force acting on each particle, due to the presence of all the other particles [2, 1]. Within this approach, the force softening scale is usually very small and the particle trajectories are calculated with great precision. However, the price to be payed for this accuracy is the high computational cost, which goes like N^2 (N being the number of particles). Therefore, only a rather limited number of particles ($\lesssim 10^4$) is usually employed.

b) Evaluation of the gravitational force by means of the "particle-mesh" (PM) method, in which Poisson's equation is solved by a mass assignment to a discrete grid [193]. This method is better suited when a large number of particles ($\gtrsim 10^5$) is required, although the small-scale resolution is limited by the grid spacing. For this reason, PM codes fail to describe in detail the structure of small-scale virialized clumps, although they are adequate to follow the evolution at intermediate and large scales.

c) Combination of the two above methods, in order to improve the force resolution of the PM code. The resulting "particle-particle–particle mesh" (P^3M) code corrects the small scale force acting on each particle by summing over the contributions from neighbor particles [121, 193, 120]. In this Chapter we will use the P^3M code written by Dr. R.Valdarnini to follow the development of non-linear clustering. Some more details about P^3M codes are given in the next section, while a detailed technical description can be found in refs.[193, 120].

5.2 Numerical integrations

We describe, by means of a P^3M N-body code [193, 120], the gravitational clustering evolution up to non-linear phases of a CDM model and two initially scale-free power spectra. In the following, we assume a matter-dominated expanding universe, with density parameter $\Omega = 1$.

In this Section we describe the general structure of a P^3M code. More technical details and applicative aspects are extensively treated in the Hockney & Eastwood's book [193] and in the Efstathiou *et al.* paper [120].

In the P^3M code the force acting on a particle is split between a long-range (PM) component and a short-range (PP) part. As a first step in the PM computation, the density field $\rho(\vec{x})$ is represented by a mass assignment to the grid point positions $\vec{n}$ according to

$$\rho(\vec{n}/M) = \frac{M^3}{N} \sum_{i=1}^{N} W(\vec{x}_i - \vec{n}/M) . \tag{5.1}$$

Here M is the total number of grid points, N the particle number and $\vec{x}_i$ the vector position of the i-th particle. In the following, periodic boundary conditions are chosen, while simulation box side, gravitational constant and total mass are set to unity. The key quantity in eq.(5.1) is the mass-assignment function W, whose shape should be chosen to be as smooth as possible in order to have a well behaved density field representation. In the code a triangular-shaped cloud (TSC) interpolation scheme for mass assignment is adopted, in which the mass is assigned with suitable weights to the 27 nearest neighbor grid points around each particle (see ref.[193], §5.3).

With the density field of eq.(5.1), the Poisson's equation gives for the gravitational potential

$$\Phi(\vec{n}/M) = \frac{1}{M^3}\sum_{\vec{n}'=1}^{M^3} G\left(\frac{\vec{n}-\vec{n}'}{M}\right)\rho(\vec{n}'/M), \tag{5.2}$$

where G is an approximation to the Green's function of the ∇^2 operator. The mass distribution is described with $N = 32^3$ particles, while the density field is solved over 64^3 grid points. After a suitable choice for an optimized Green's function, the potential Φ is solved by a fast Fourier transform (FFT) algorithm. Accordingly, the force at the grid points,

$$F(\vec{n}/M) = -\frac{D_{\vec{n}}\phi}{N}, \tag{5.3}$$

is evaluated (here $D_{\vec{n}}$ is the finite difference approximation to the gradient) and gives the force acting on a particle,

$$F(\vec{x}_i) = \sum_{i=1}^{M^3} W(\vec{x}_i - \vec{n}/M)\, F(\vec{n}/M), \tag{5.4}$$

as its convolution with the mass assignment function.

As for the short-range force, it is evaluated by summing all the contributions from the neighbor particles within a distance r_s, while it is set to zero for interparticle separations $> r_s$. Within r_s the force between two particles is represented by two attracting mass clouds, centered on particle positions, with linear density profile and radius $\eta/2$. For the present simulations, $r_s = 2.7/M$ and $\eta = 0.3/M$ for the smoothing scale of the interparticle force.

In a $\Omega = 1$ matter dominated Universe, the expansion factor scales as $a(t) \propto t^{2/3}$. We set $a(t_i) = 1$ at the initial time of the simulation. The simulation amounts to solving for each particle Newton's equation of motion, which in comoving coordinates reads

$$\frac{d\vec{v}_i}{dt} + 2H\vec{v}_i = \frac{\mathbf{F}_i}{a^3 m} \tag{5.5}$$

where $\mathbf{F}_i$ is the force acting on the i-th particle, which is evaluated according to the above prescriptions, and $\vec{v} = d\vec{x}_i/dt$. After introducing the new time variable $p = a^\alpha$, particle positions are displaced at each integration step according to the time-centered leapfrog scheme [120]. Particle positions at the n-th integration step are related to those at the $(n-1)$-th step and to the velocity at $n - 1/2$ according to

$$\vec{v}_{n-1/2} = \frac{\vec{x}_n - \vec{x}_{n-1}}{\Delta p}. \tag{5.6}$$

Table 5.1: *Parameters of the integration.*

	a_F	Δu	α
CDM	5.0	0.015	1.00
$n = 1$	60.0	0.006	0.33
$n = -2$	5.5	0.04	1.33

The integrations are halted at an epoch a_F, when perturbations with wavelength of the order of the box length, L, are entering the non-linear regime. In Table 5.1 we report the final epoch a_F, the integration step Δp and the exponent α for the simulations we are considering.

In the CDM case the comoving length of the cube is set to $L = 32.5h^{-1}$ Mpc at the present epoch, in such a way that the results of our integrations are directly comparable with those of ref.[98] for their model EdS1-S5 (see below). On the contrary, scale fixing is completely arbitrary in the case of scale-free spectra, because of the absence of any characteristic scale.

Initial conditions are set according to the Zeldovich algorithm (see §4.1.2 and ref.[120]). Accordingly, Eulerian particle positions and velocities are given by

$$\begin{aligned} \vec{x} &= \vec{q} - b(t)\,\psi(\vec{q})\,; \\ \vec{v} &= -\frac{db}{dt}\,\psi(\vec{q})\,. \end{aligned} \tag{5.7}$$

Here $\vec{q}$ is the lattice (Lagrangian) coordinate of the particle, $b(t)$ the growth factor of the perturbation ($b \propto a$) and $\vec{\psi}(\vec{q})$ is the gradient of the gravitational potential

$$\Phi(\vec{q}) = \sum_{\vec{k}} \frac{\delta_{\vec{k}}}{k^2}\, e^{i\vec{k}\cdot\vec{q} + \phi_{\vec{k}}}\,, \tag{5.8}$$

which gives the initial particle displacement. Because of the finite discrete number of waves representing the continuous Fourier spectrum, the final result must be averaged over several integrations with equivalent statistical conditions. Then, in eq.(5.8) the Fourier transform of the fluctuation field is related to the power spectrum P_k according to $\delta_{\vec{k}} = \sqrt{-2\ln r_1}\, P_k$, while $\phi_{\vec{k}} = 2\pi r_2$ is the random phase, which ensures the Gaussianity of the initial fluctuation field, via the Central Limit Theorem. Here r_1 and r_2 are two random numbers between 0 and 1, so that different random sequences for r_1 and r_2 amount to generating different random realizations of statistically equivalent initial fluctuation fields. Especially for spectra having a considerable amount of large-scale power, even starting with statistically equivalent intial conditions we end up with substantially different structures. For this reason, five different random phase assignment are taken for each model. While noticeable differences are expected between different random realization for the CDM and $n = -2$ spectra, no substantial effects should appear in the $n = 1$ case.

For the initial CDM spectrum we take the expression

$$P(k) = \frac{Ak}{(1 + \alpha k + \beta k^{3/2} + \gamma k^2)^2} \tag{5.9}$$

with $\alpha = 1.7(\Omega h^2)^{-1}$, $\beta = 9.0(\Omega h^2)^{-3/2}$ and $\gamma = 1.0(\Omega h^2)^{-2}$, which has been also considered by Davis *et al.* [98].

If N particles are employed, wave model along each axis having $\lambda < 2/N^{1/3}$ cannot be adequately sampled. Thus, initial perturbations at wavenumbers exceeding the Nyquist frequency $k_{Ny} = 2\pi \frac{N^{1/3}}{2}$ cannot be generated. Since for $k > k_{Ny}$ white noise dominates, the normalization of the initial $n = 1$ spectrum is $|\delta_k|^2 = 1/N$ at $k = k_{Ny}$. In the $n = -2$ and CDM integrations the normalization at the Nyquist frequency is given by $|\delta_k|^2 = 2/N$, so as to reduce the effect of initial transients in the small-scale clustering, which are more important for spectra with small power at high wavenumbers. Accordingly, the values of the expansion factor $a(t)$ in our case differ from those of ref.[98] by a factor $\sqrt{2}$. Hereafter we shall refer to the scale-free integrations with spectral indexes $n = 1$ and $n = -2$ as SF+1 and SF-2, respectively. Integrations of scale-free spectra with $n = 0, -1$ have not been performed since they represent only intermediate cases between the $n = -2$ and $n = 1$ spectra.

We plot in Figure 5.1 some particle configurations at different evolutionary stages for the initial CDM spectrum. It is apparent that, despite initial conditions are nearly homogeneous, clustering rapidly develops and gives rise to a remarkable complexity of structures, with clumps and filaments extending over scales comparable to the box-length.

According to the prescription of biassed galaxy formation (see §4.4), we follow during the integrations different species of particles, that correspond initially to various levels of density fluctuations. The initial density field $\delta_{\vec{k}}$ is smoothed with a Gaussian window $e^{-(k/k_s)^2}$, where $k_s = 200/L$. The smoothed density field is Fourier transformed and density is assigned to the grid points. Each particle is then tagged with a value of ν such that $\delta_{\vec{g}} = \nu\sigma$, where σ is the *rms* density fluctuation within the simulation cube and $\vec{g}$ is the nearest grid point to the perturbed particle position. We select five different species of particles: $\delta > -1$ which represents the background, $\nu > 0$, $\nu > 0.5$, $\nu > 1$, and $\nu > 2$. Typically, the numbers N_ν of selected particles are $N_0 \simeq 20000$, $N_{0.5} \simeq 10000$, $N_1 \simeq 5000$, and $N_2 \simeq 2000$. In the following Section we plot different quantities calculated only for subsets of particles associated with the levels $\delta > -1$, $\nu > 0.5$ and $\nu > 2$.

Following the distribution of "biassed" subsets of the whole particle distribution has been shown to be a necessary ingredient in order to compare the results of CDM N-body simulations to the observed galaxy distribution. In order to properly make this comparison, we have to decide which is the evolutionary stage to be identified with the present epoch.

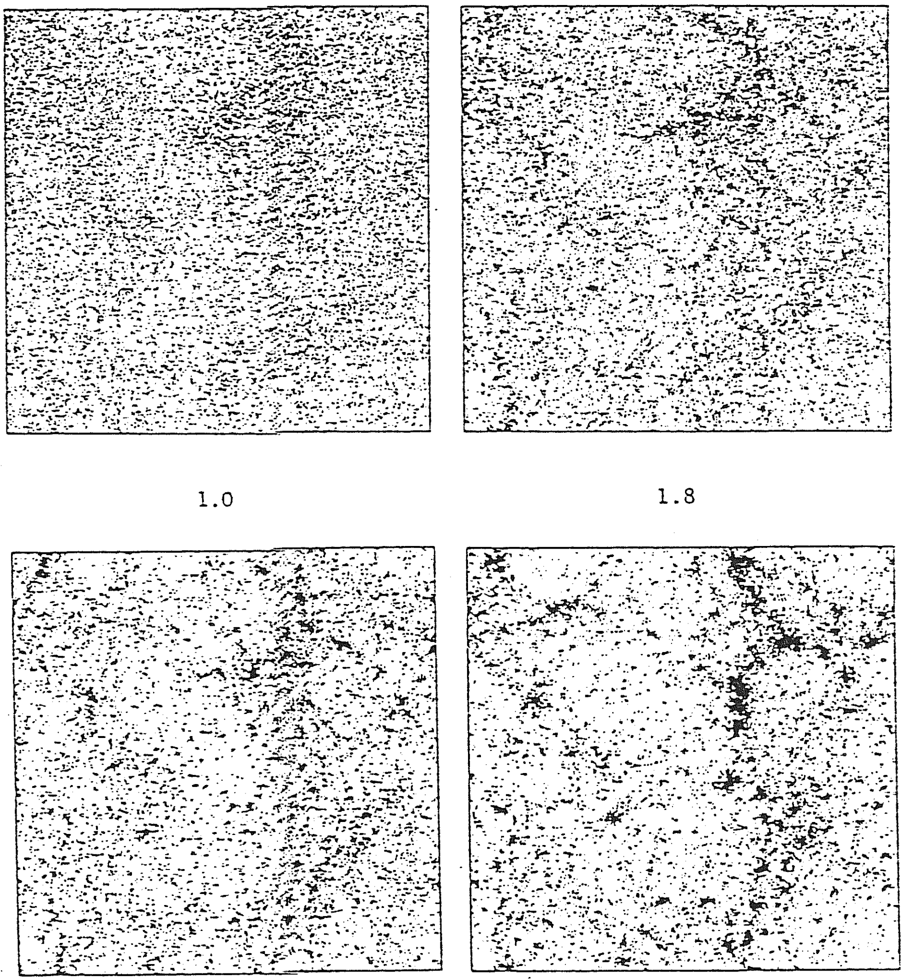

1.0 1.8 2.4 4.5

Figure 5.1: *Projections of the particle distributions in the evolving CDM N-body simulation. The box-side is normalized to have length* $32.5\,h^{-2}$ *Mpc at the present epoch. Different panels correspond to different evolutionary stages, starting from the initial condition to the most evolved configuration.*

Although different prescriptions have been proposed, one of the most often used identifies the present time with the integration step at which the logarithmic slope of the 2-point correlation function matches the observational value $\gamma \simeq 1.8$, over a comparable scale-range. Once this normalization has been chosen, the amplitude of $\xi(r)$ is also fixed. However, with such a prescription, the DM correlation length at present time turns out to be much smaller than the canonical value $r_o \simeq 5h^{-1}$ Mpc, holding for galaxies. In order to overcome this problem, Davis *et al.* [98] suggested that, in the spirit of biassed galaxy formation, the entire particle distribution in the simulations is not a faithful representation of the galaxy distribution. Instead, galaxies should be identified with only those particles which correspond to peaks of the initial fluctuations exceeding ν times the *rms* value of the smoothed density field. By taking $r_s = 2\pi/k_s \simeq 5 \times 10^{-3}$ (in units of the box length) for the smoothing length and $\nu = 2.5$, Davis *et al.* [98] found that the biassed distribution has the correct clustering length when $\gamma = 1.8$. As an extra bonus, the resulting number density of selected particles reproduces quite well the observed galaxy number density, thus supporting the reliability of the CDM model to account for the observed clustering at intermediate scales.

It is clear that introducing biassing is not required by the analysis of scale-free spectra. In this case, when the slope of $\xi(r)$ takes the correct value, the correlation length r_o can be matched to the observed one simply by suitably rescaling the box size. Nevertheless we prefer to apply biassing also for the SF+1 and SF–2 models, in order to check the effects of gravitational clustering on the statistics of peak distributions.

The integrations that we will analyze in the following have been carried out on a CRAY YMP48/432 machine.

5.3 The correlation analysis

In this Section we present the correlation analysis of the gravitational clustering as described by a P^{3}M N-body code. Other than comparing the 2-point correlation functions with previous results obtained in the literature, we apply the moment method to work out the expressions for the 3- and 4-point functions and compare them with the predictions based on the solutions of the BBGKY equations in the fully relaxed regime (see §4.1.4 and refs.[145, 183]).

5.3.1 Results of correlation analysis

In order to compare the description of gravitational clustering provided by the N-body code with those arising from previous analogous simulations, we evaluated the 2-point correlation function at different epochs, for different biassing levels and different initial spectra. The 2-point function $\xi(r)$ is shown in Figure 5.2, for different spectra (panels *a* and *b* for CDM and SF+1 models, respectively). We choose to plot for each model a single epoch [CDM: $a(t) = 2.5$; SF+1: $a(t) = 20$]. In each panel, we plot $\xi(r)$ for different particle species,

Table 5.2: *Parameters of the 2-point correlation function.*

		$a(t)$	$log(R/L)$	γ	$log(r_o/L)$
$\delta > -1$	CDM	2.5	−2.94	1.90	−1.43
		3.4	−2.85	2.00	−1.29
	$n = -2$	3.5	−2.69	1.76	−0.96
		4.8	−2.65	1.82	−0.80
	$n = 1$	20	−3.09	2.76	−1.42
		60	−2.89	2.91	−1.22
$\nu > 0.5$	CDM	2.5	−2.90	2.00	−1.27
		3.4	−2.86	2.15	−1.17
	$n = -2$	3.5	−2.72	1.92	−0.85
		4.8	−2.70	2.00	−0.74
	$n = 1$	20	−2.73	2.66	−1.40
		60	−2.77	3.10	−1.24
$\nu > 0.5$	CDM	2.5	−3.20	2.38	−1.14
		3.4	−3.10	2.46	−1.09
	$n = -2$	3.5	−2.78	2.23	−0.77
		4.8	−2.78	2.38	−0.73
	$n = 1$	20	−3.50	2.70	−1.42
		60	−2.90	2.90	−1.21

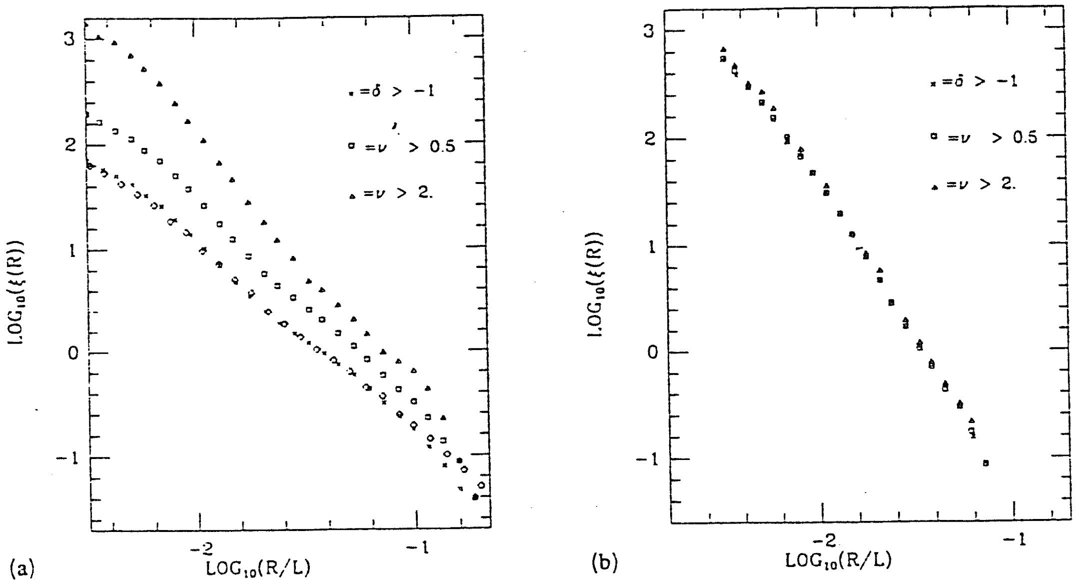

Figure 5.2: *The two-point correlation function, $\xi(r)$, versus radial distance r for a CDM model at $a(t) = 2.5$ (panel a) and for a scale-free spectrum with $n = 1$ at $a(t) = 20$ (panel b). The $\xi(r)$ for $\delta > -1$ corresponds to the whole particle population, while those for $\nu > 0.5$ and $\nu > 2.0$ are calculated from a subset of particles chosen according to their initial positions (see text). For the CDM case, open diamonds refer to the results reported in ref.[98]. Notice that, for the scale-free spectrum, differences among density thresholds are rapidly offset as non-linear evolution develops.*

corresponding to three different density thresholds (background, $\nu > 0.5$, and $\nu > 2$). The effect of introducing a biassing in the distribution of particles, in the CDM case, is that of increasing the clustering. Indeed, in the presence of a spectrum with sufficient power at large scales, high peaks occur with enhanced probability in the crests rather than in the valleys of a large-scale fluctuation mode, so that they exhibit an enhanced clustering. In Figure 5.2*a* a comparison with the CDM model of ref.[98] shows excellent agreement. From Figure 5.2*b*, it is interesting to observe that the presence of bias has no effect on the correlation amplitude for the SF+1 case, due to the very small amplitude of a $P(k) \sim k$ spectrum at small wavenumbers. This result will be confirmed in the following, from the analysis of higher-order correlation functions. The SF+1 model develops a strong clustering on small scales at late times, and the power-law model, $\xi(r) \sim r^{-\gamma}$, is no longer valid. However, as for the investigation of higher-order correlations, we are primarily interested in the application of the moment method on scales $r/L \leq 10^{-1}$, where the power-law model is a good approximation at all the considered epochs. In Table 5.2 we report the values for the parameters which specify the shape of the 2-point function, for different spectra, biassing level and evolutionary stage. In ref.[98] the present epoch is identified in the simulation when the slope of $\xi(r)$ for particles associated with $\nu > 2.5$ peaks matches the observed one. In our units, this happens at $a(t) = 2$. We have however decided to pursue the integration for the CDM model up to late epochs, $a(t) \simeq 5$. In fact, we are also interested in studying, for different spectra, correlation statistics at very evolved stages, in order to check whether gravitational dynamics gives rise to a continuously evolving clustering or if it tends toward an asymptotic relaxation regime.

5.3.2 Higher-order correlations

In order to evaluate higher-order correlations for the evolving N-body simulations, we resort to the moment method. This technique is based on the counting of the objects contained inside spherical shells centered on each object, rather than on the counting of n-plets of objects, as the direct counting approach does [352]. The major advantage of the moment method lies in its high computational speed with respect to the counting of multiplets. For this reason, it is particularly suitable for the investigation of higher order ($n > 3$) correlations, when the huge number of multiplets forces one to analyse only a small random subsample of the whole configuration. The moment method has been already used in its 2-dimensional version in the analysis of higher-order correlations from the Zwicky sample [353], and in its 3-dimensional version to investigate the spatial 3-point correlation function of galaxy clusters [209].

Let us consider the number $N_{kj}(\delta)$ of particles contained in a spherical shell from r_k down to $r_{k-1} = r_k(1-\delta)$, centered on the j-th object. The z-order moment, $\langle N^z\rangle_k \equiv N^{-1}\sum_{j=1}^{N} N^z_{kj}$, is then obtainable by averaging over all the N objects taken as centers, while the *central moments*

$$s_k^{(z)} = \langle (N_{kj} - \langle N\rangle_k)^z\rangle_j \qquad (5.10)$$

are related to the $(z+1)$-point correlation function. According to Peebles [287], for $z = 2$ we have

$$s_k^{(2)} = \langle N\rangle_k + \left(\frac{N_k}{V(r_k)}\right)^2 \int_{r_k}^{r_{k+1}} dV_1\, dV_2\, [\zeta_{012} - \xi_{01}\xi_{02} + \xi_{12}]\,, \qquad (5.11)$$

while the case $z = 3$ reads

$$\begin{aligned} s_k^{(3)} &= 3s_k^{(2)} - 2\langle N\rangle_k + \left(\frac{N_k}{V(r_k)}\right)^3 \int_{r_k}^{r_{k+1}} dV_1\, dV_2\, dV_3\, [\eta_{0123} - \\ &\quad -3\xi_{01}\zeta(r_2, r_3, r_{23}) + \zeta(r_{12}, r_{23}, r_{13}) + 2\xi_{01}\xi_{02} + \xi_{02}]\,. \end{aligned} \qquad (5.12)$$

Here N_k represents the expected number of objects in the k-th shell for a uniform (random) distribution, and $V(r_k)$ is the volume of the k-th shell. In eqs.(5.11) and (5.12), ζ and η represent as usual the connected parts of the 3- and 4-point correlation function, respectively. In Appendix A we report the calculations to evaluate the 3- and 4-point correlation functions by means of the moment method. The results are obtainable once a model for the connected function is assumed. In particular, let us take

$$\zeta_{012} = Q\,[\xi_{R,01}\xi_{R,02} + \xi_{R,01}\xi_{R,12} + \xi_{R,02}\xi_{R,12} + q\,\xi_{R,01}\xi_{R,02}\xi_{R,12}]\,. \qquad (5.13)$$

For q=0, the above expression gives the hierarchical model (1.2). The Kirkwood superposition, arising from eq.(5.13) with $q = 1$, is predicted by analytical approaches to biased models for galaxy formation (see eq.[4.57]). As for the 4-point function, we take the hierarchical expression

$$\eta_{0123} = R_a[\xi_{R,01}\xi_{R,12}\xi_{R,23} + \ldots 12\, terms] + R_b[\xi_{R,01}\xi_{R,02}\xi_{R,03} + \ldots 4\, terms]\,. \qquad (5.14)$$

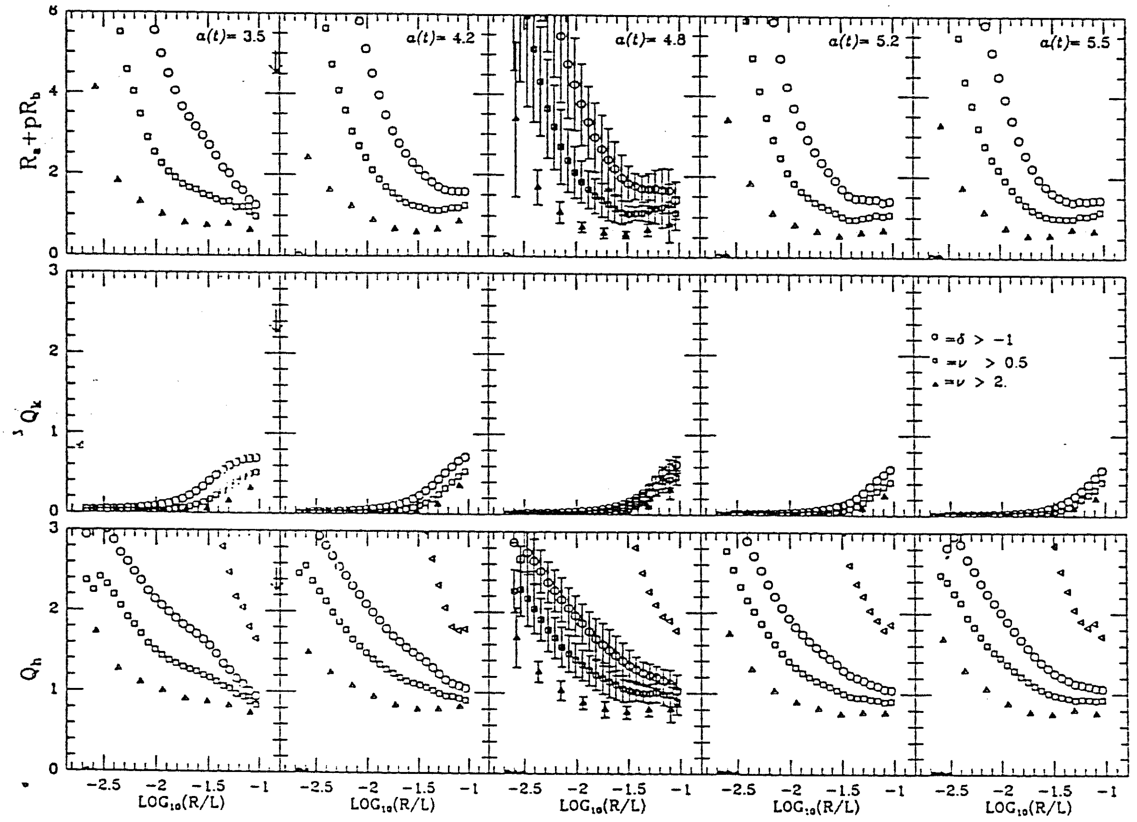

Figure 5.3: *The coefficient Q_h (hierarchical), Q_k (Kirkwood) and $R_a + pR_b$ are plotted for different expansion factors $a(t)$ and biassing levels ν in the case of the CDM model. These coefficients have been calculated by applying the moment method (see §5.3.2 and Appendix A). Open triangles refer to Fry's perturbative model [145]. Error bars represent the scatter within the ensemble; for the sake of clarity we plot them only for $a(t) = 4.8$. At later $a(t)$ the bars are not very different from the potted ones, expecially at the non-linear scales where the stability of the clustering is expected. The arrow marks the point where $\xi = 1$.*

In eqs.(5.13) and (5.14), ξ_R represents the *smoothed* 2-point correlation function

$$\xi_R(r) = \left(\frac{r_o}{r+R}\right)^\gamma, \tag{5.15}$$

which is assumed to have power-law shape with a smoothing at the scale R, in order to avoid unphysical divergences of the correlation strength at small separations. Let us observe that the introduction of the smoothing scale R is not a mathematical artifact. In fact, in N-body simulations a small-scale smoothing arises because of the limits in the numerical resolution that can be achieved at small scales. In the following, the *unsmoothed* 2-point function will be indicated by $\xi(r)$ and is assumed to have the usual power-law shape $\xi(r) = (r_o/r)^\gamma$. The values of slope γ, smoothing radius R and clustering length r_o are obtained by requiring a best fit of the expression (5.15) to the data.

The application of the moment method enables us to investigate the 3- and 4-point correlations. In particular, by substituting the values of the central moments $s_k^{(n)}$ in eqs. (A9) and (A14), we work out the coefficients Q and $R_a + pR_b$ (see eq. [A15] in Appendix A). The results of our analysis are shown in Figures 5.3, 5.4 and 5.5. We plot the Q_h (hierarchical) and Q_k (Kirkwood) coefficient for the 3-point function, as well as the combination $R_a + pR_b$ for the 4-point function, for different spectra, expansion factors and biassing levels. In some cases, we also plot the hierarchical coefficient for the 3-point function as deduced by Fry [145] in his perturbative model for the non-linear evolution of density fluctuations. In our plot, this coefficient is normalized so that agreement with Fry's model is achieved when $Q_h = 1$. Some agreement is reached only in a very narrow range around the linearity scale, where Fry's perturbative approach is expected to work.

For the CDM model (Figure 5.3), the coefficient Q_h becomes smaller at higher biassing levels, so that for $\nu > 2$ we get $Q_h \sim 1$, with a rather constant value over a wide range of scales, as non-linear evolution takes place. The coefficients corresponding to a lower biassing level also follow this trend. The coefficients Q_h both for the background and for $\nu > 2$ are in close agreement with the analogous results of ref.[98], despite the differences in the method used to investigate the 3-point function. This is a clear indication of the reliability of the moment approach, but with the advantage of a reduced computational time with respect to the multiplet counting technique.

A similar behaviour to that of Q_h is shown by the combinations $R_a + pR_b$ of the 4-point coefficients. A remarkable feature of this quantity is its dependence on r, which looks somewhat steeper than that of Q_h, in the interval of separations where the 3-point coefficient is not strictly constant. This is an indication of the validity of the recurrence relation $R_a + pR_b \sim Q_h^2$ between different order hierarchical coefficients, as suggested by many models of scale-invariant gravitational clustering. As in the case of the 3-point function, the 4-point one turns out to approach the hierarchical expression as non-linear clustering develops. It is also interesting to note the behaviour of the coefficient Q_k for the 3-point Kirkwood superposition. The very small value ($Q_k \simeq 10^{-3}$) it takes at $r \ll r_o$ indicates the non-validity

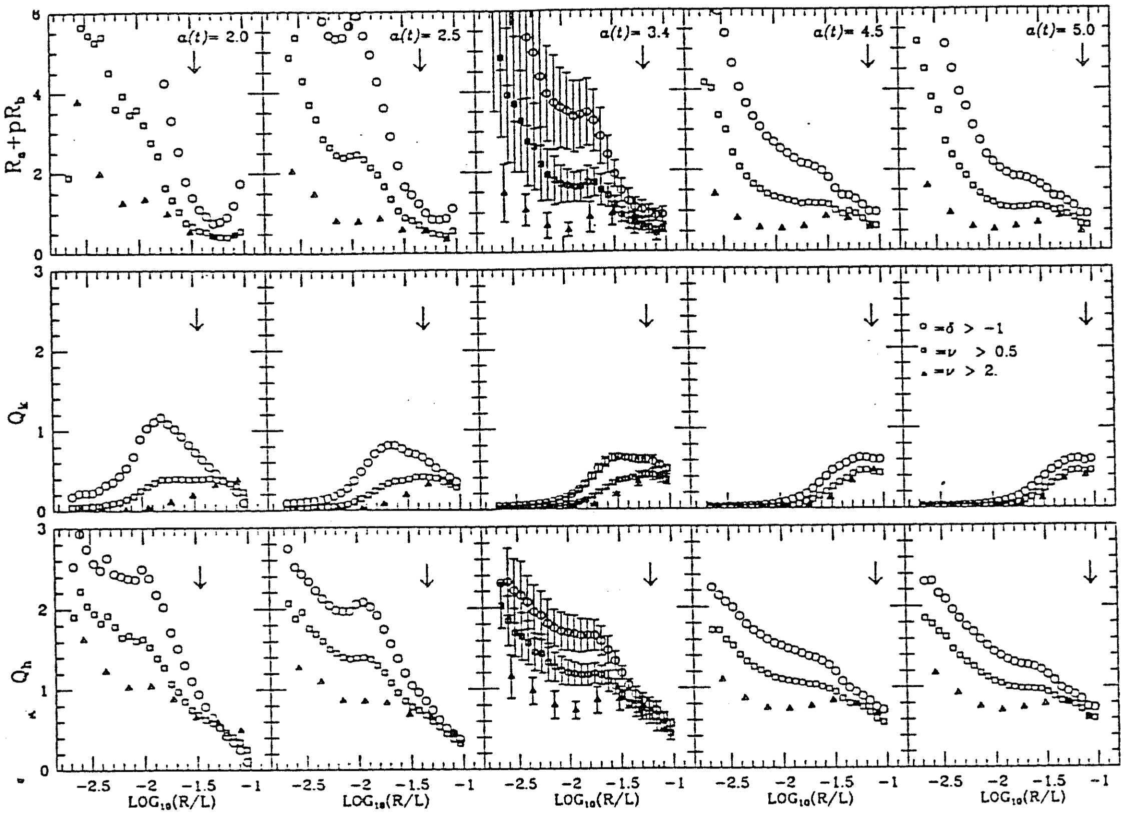

Figure 5.4: *As in Figure 5.3, but for a scale-free model with* $n = -2$.

of the Kirkwood model in the non-linear regime. Indeed, since $\xi \gg 1$, the presence of the ξ^3 term constrains Q_k to be very small. In any case there are no indications supporting the validity of this model, expecially for more evolved configurations, when any difference between different biassing levels disappears.

Figure 5.4 is the same plot as Figure 5.3 for the SF−2 spectrum. The two figures show very similar results, owing to the small differences between the initial shapes of the two spectra, at least on the scales we are considering.

Quite differently from the previous cases, in the SF+1 model a strong clustering rapidly develops on small scales. Consequently, the conditions of dynamical equilibrium are reached at such scales and the hierarchical coefficients for the 3- and 4-point functions rapidly take fairly constant values. The divergence, which occurs on linearity scales, is essentially due to the breaking in the single power-law for $\xi(r)$, occurring on such scales. From Figure 5.2*b* it can be seen that, after the breaking, the 2-point function becomes very steep and rapidly goes to zero. As a consequence, the values of Q_h, Q_k, and $R_a + pR_b$ are constrained to diverge according to eqs.(A9) and (A14). It is however to be stressed that no hierarchical expressions for the 3- and 4-point functions are to be expected corresponding to linearity scales. Also in this case, no evidence exists for the validity of the Kirkwood superposition.

The possibility of detecting correlation functions up to the fourth order enables us to test the predictions of the BBGKY hierarchy about the recurrence relations between

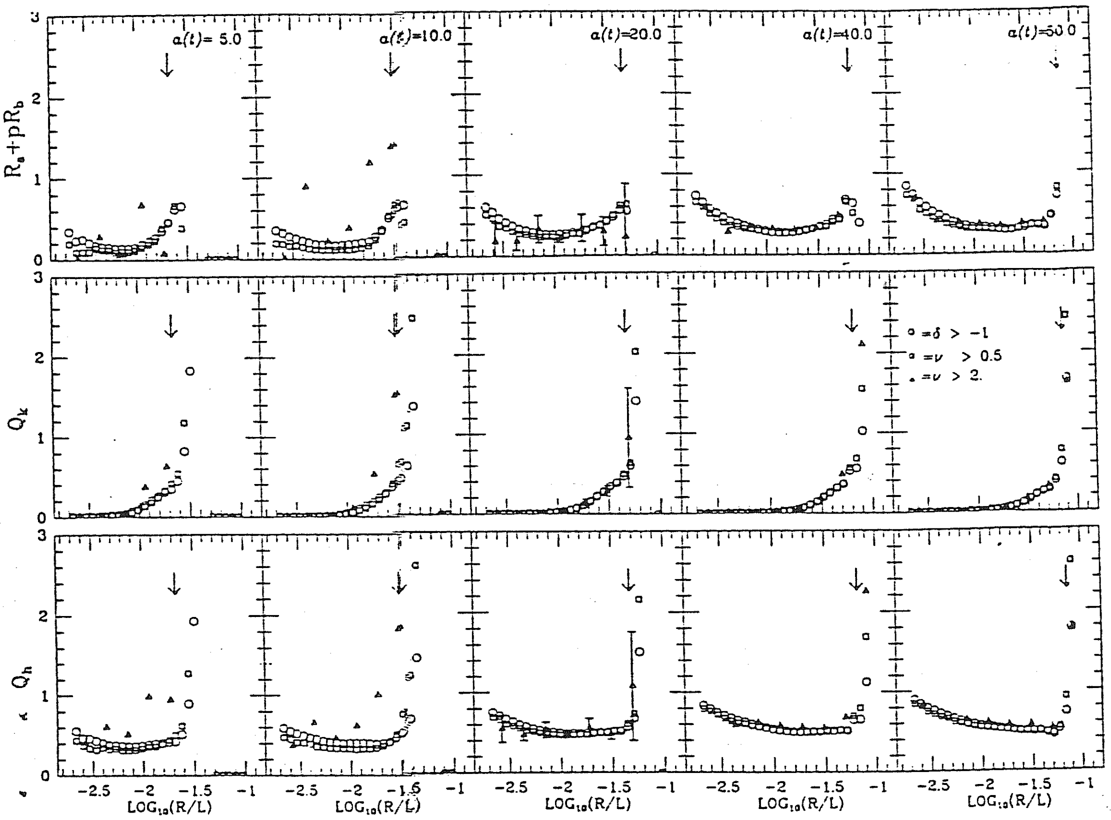

Figure 5.5: *As in Figure 5.3, but for a scale-free model with* $n = 1$.

hierarchical coefficients of different orders. Such a comparison is particularly relevant in the case of the SF+1 spectrum, which rapidly develops a very strong and stable clustering at small scales. In Figure 5.6 we plot the 3-point Q_h coefficient and the combination $R_a + pR_b$, for the whole particle distributions of the SF+1 model at $a(t) = 40$. Also plotted are the corresponding results of the solutions proposed by Fry [146],

$$R_a = R_b = \frac{2}{3} Q^2 ,$$

and by Hamilton [183]

$$R_a = Q^2 \qquad ; \qquad R_b = 0 .$$

A comparison of R_a+pR_b between the results of the numerical integrations and the predictions of the BBGKY equations shows a good agreement, with deviations when approaching linearity scales. This is an indication that these solutions must be expected to be valid only in the strongly non-linear ($\xi \gg 1$) regime (see, *e.g.*, ref.[185]). Moreover, there are also marginal indications that Hamilton's solution provides a better fit to numerical data.

5.4 Fractality of the non-linear clustering

In this Section we present a detailed fractal analysis of evolving N-body simulations. After a description of the implementation of the methods of analysis, already introduced in Chapter

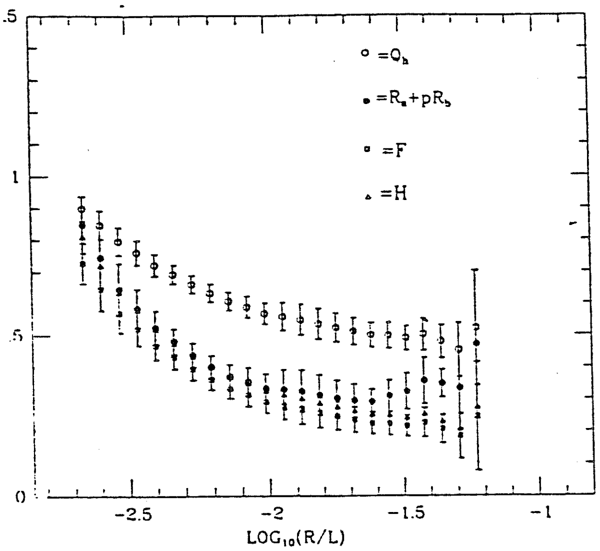

Figure 5.6: *Hierarchical coefficients Q_h (open circle), versus $log(r/L)$ at $a(t) = 40$ for the scale free model with $n = 1$. For the same integration parameters, the quantity $R_a + pR_b$ (black circles) is also shown. These quantities refer to the background distribution. Error bars represent the scatter within the ensemble. We use the solutions of the BBGKY equations proposed by Fry [146] and Hamilton [183] to calculate the coefficient $R_a + pR_b$ (open squares: Fry; black triangles: Hamilton) from Q_h. For the sake of clarity we plot error bars only for Fry's model; the uncertainties in $R_a + pR_b$ for Hamilton's model are quite similar.*

3, we discuss the results, with particular emphasis on the existing connections between non-linear gravitational dynamics and scale-invariant clustering.

5.4.1 Implementation of the multifractal analysis

In order to follow the formation and evolution of multifractal structures in the simulated universes, we apply the fractal dimension estimator described in Chapter 3. We evaluate the relative partition functions for the three initial spectra (CDM, SF–2 and SF+1 models), for each value of the expansion factor $a(t)$ and of the biassing level ν. In general, we consider spatial scales between about $10^{-2.5}L$ and $10^{-1}L$, where L is the box length. We do not consider smaller scales, where the results turn out to be affected by numerical smoothing. For the CDM case, the above scale range corresponds to scales between about 10^{-1} and $3\,h^{-2}$ Mpc at the present epoch. Thus, we are essentially exploring the regime of non-linear gravitational clustering where $\xi(r) > 1$.

The box-counting (BC) partition function $Z^B(q,r)$ is evaluated according to eq.(3.21) by dividing the simulation box in cells of varying size and counting the number of particles contained inside each of them. Cell size varies between $r = 1/640$ and $r = 1/3$ in units of the simulation box-length, while q values are taken between -8 and +8, with step $\Delta q = 0.25$.

In the case of the correlation-integral (CI) partition function $Z^C(q,r)$ of eq.(3.23), we count the number of particles, $n_i(< r)$, contained inside a sphere of radius r, centered at the

i-th particle. The values of r vary between 1/500 and 1/10 of the simulation box-length. For the generic particle i, $n_i(< r_k)$ is found by dividing the simulation cube into 10^3 small boxes. According to the "chaining cell" technique [193], each of the $n_i(< r_k)$ particles (labelled by the index j) such that $r_{ij} \equiv |\vec{x}_i - \vec{x}_j| < r_k$, is either in the cell $\vec{c}_o$, where the particle i lies, or in one of its 26 neighboring cells $\vec{c}_{\vec{n}}$. This kind of "box-assisted" method to evaluate the correlation integrals is much less time consuming, since the number of required operations goes like $N \log N$, instead of N^2 (N being the total number of particles). The values of q for which Z^C is evaluated are the same as those used for the box-counting method.

In the case of the density reconstruction (DR) method, in order to estimate the $W(\tau, p)$ partition function of eq.(3.25) we consider values of the probability p between $2/N$ and 0.1. For each particle i one has to find the radius r_i of the smallest sphere centered on i such that there are $Np \equiv m$ particles inside the sphere. Note, however, that the upper limit $p = 1$ cannot be defined for a periodic system like the simulations we are considering, for which only scales $\leq L/2$ are meaningful. The estimate of the DR partition function is particularly expensive, since for each particle i we need to sort all the other j particles according to their distances r_{ij}. In eq.(3.25) the summation is then either over a random subsample of 8000 points taken as centers or for the whole particle population if $N_\nu < 8000$. The radius $r_i(p)$, corresponding to the probability measure p for the i-th particle, is then defined as the distance r_{ij} of the j-th sorted particle to the particle i.

As far as the BC and CI methods are concerned, the scale range over which the fractal properties of the particle distributions are analyzed naturally follows from the choice of the cell size or of the sphere radius. In the case of the DR partition function, the evaluation of the local dimension is not performed in a range of physical scale, but in a range of probabilities p. Thus, in order to compare the scaling properties detected with such a method with those arising from the previous two methods, we need a criteria to associate each value of p to a characteristic scale. To this purpose, let us express the probability p in terms of the 2-point correlation function $\xi(r)$, according to

$$p = \frac{\langle N(< r)\rangle}{N} = \frac{\bar{N}(< r)}{N}\,[1 + K_1\, \xi(r)]\,. \tag{5.16}$$

Here $\langle N(< r)\rangle$ and $\bar{N}(< r)$ are the mean number of neighbors within a distance r for the real data and for a random distribution, respectively. Moreover, if $\xi(r) = (r/r_o)^{-\gamma}$, then $K_1 = 3/(3 - \gamma)$. Thus, solving eq. (5.16) in r for each value of p gives the relation between the probability range and the physical scale range. Notice, however, that since different particle distributions have different 2-point functions, the interval of scales corresponding to a fixed interval of p values is not uniquely determined for all simulations. To solve eq.(5.16), we take the values of the clustering length r_o and of the logarithmic slope γ as obtained from the correlation analysis described in the previous section (see also ref.[373]) on the same set of N-body simulations that we are now considering. Note also that, according to the definition of the DR partition function, $W(\tau = -1, p)$ provides an estimate of the average separation associated with a given probability, and that $W(\tau=-2,p)-W^2(\tau=-1,p)$ provides an estimate of the variance of the distribution of the relative separations among the particles.

The implementation of the nearest-neighbor (NN) method is based on the evaluation of the partition function $G(k,n,\tau)$, as defined by eq.(3.27), taking 16 randomly selected subsamples of the whole particle configuration. The poorest subsample always contains 500 points. The NN partition function is evaluated in correspondence of the same values of τ already selected for the DR function; the NN function has been computed up to the fourth neighbor order. For the purpose of finding the different order neighbors to each particle, the simulation cube is divided into a chaining mesh with cell size $2n^{-1/3}$ (for a random subsample with n particles). For a generic particle i, the k-th neighbor is then found by sorting all the particles belonging to the boxes, whose position vector is $\vec{c}_0$ or $\vec{c}_{\bar{n}}$, according to their distances from the i-th particle. The NN partition function is then computed, taking for ${}_k\delta_i$ the distance of the k-th sorted particle. If the number of sorted particles is smaller than k, then the cell size is doubled and the computation repeated. The set of τ values for which the NN partition function G has been evaluated is the same as that chosen for the DR method. In order to estimate the physical length scale associated to a given subsample containing n particles, we evaluate the frequency distribution of the ${}_k\delta_i$ distances for each subsample and for each neighbor order k. Then, the typical scale associated with each choice of n is given by the value of ${}_k\delta$ that corresponds to the peak of the frequency distribution. Note however that this procedure provides a rigorous scale identification only in the ideal case when the frequency distribution approaches a Dirac delta function; more generally, different scales contribute with different weights to the value of the partition function. Clearly, the scale resolution of this method is accurate only when the frequency distributions have a rather peaked shape.

For the implementation of the minimal spanning tree (MST) algorithm, we evaluate the partition function $S(m,\tau)$ of eq.(3.29) for 21 randomly selected subsamples. The minimum number of points is always 100. The maximum number of points is 15000 for the background distributions (*i.e.*, roughly half the total particle number). The selected values of τ are the same as for the previous two methods. Similarly to what has been done for the nearest neighbor method, the procedure which has been followed to estimate the range of physical scales sampled by the MST algorithm is based on finding the peak in the frequency distribution of the edge lengths inside the tree.

5.4.2 Results of the multifractal analysis

Detailed analysis of the CDM simulations

Figure 5.7 shows the partition functions $Z^B(q,r)$ for the BC method. Each panel refers to a different epoch $a(t)$ and to a different value of q; time increases from left to right and the order

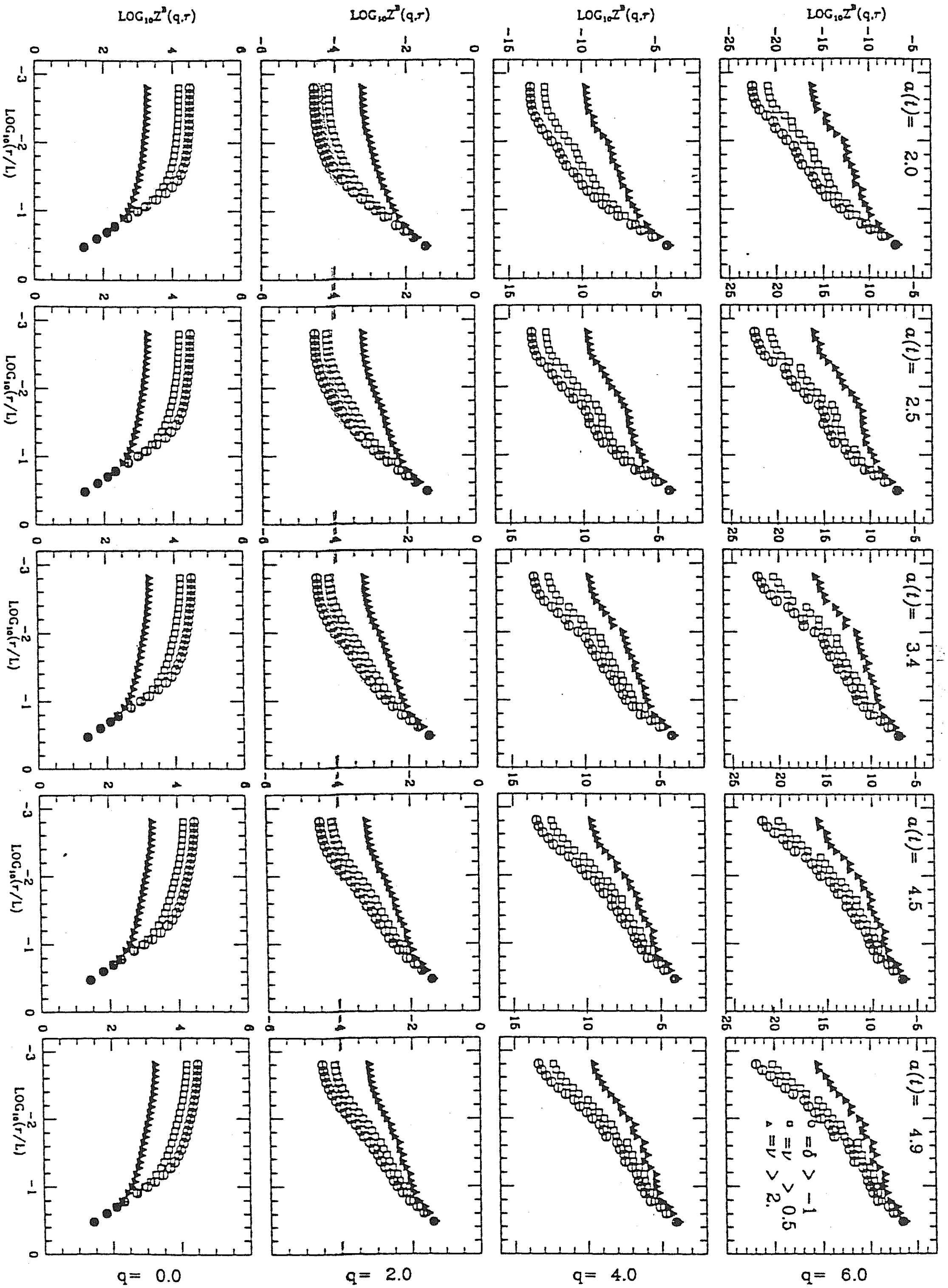

Figure 5.7: *The partition function* $Z^B(q,r)$ *versus the box size* r *for the box-counting method, as calculated from eq.(3.21), for the CDM model at various epochs. Different symbols refer to different levels of bias. Here* L *is the box length. The BC partition function is plotted for* $q = 0, 2, 4, 6$.

q of the moment increases from bottom to top. In each panel, the partition functions for the background ($\delta \geq -1$) and for two different biassing levels ($\nu \geq 0.5$ and $\nu \geq 2$, respectively) are plotted. The same scheme will also followed in all the subsequent presentations of the partition functions obtained with the different multifractal methods. In the BC case, we show the results for $q = 0,2,4,6$. At negative q's, the partition function provides information on the distribution in the underdense regions (*not* on the void distribution). However, for $q < 0$ the partition function Z^B is dominated at small scales by the contribution of boxes containing only one particle. Thus, for box sizes less than the mean interparticle distance, terms of the kind $p_{i_B}(r) = 1/N_\nu$ render Z^B quite independent of r at scales smaller than the average separation R_{und} among the particles in the underdense regions. As a result, the BC algorithm does not provide a good characterization of the distribution in the underdense regions, unless we have a very large number of particles. At positive q's, the partition function $Z^B(q,r)$ shows an approximate power-law behavior. The scaling regime becomes more and more evident as the clustering evolves. Note for example the existence of a plateau in $Z^B(q,r)$ at initial times, at scales up to about $10^{-2}L$, which is due to discreteness effects. This plateau is moved to smaller scales as the clustering piles up the particles in the fractal regime at small scales. The scaling behavior seems to be more evident at higher density thresholds and at higher q values, suggesting that high-density regions attain a fractal distribution before the lower density ones. In a sense, the scaling properties at large q's, even at the initial stages of the evolution, mimic those of the high peak distribution and anticipate the properties which will be attained by the distribution of the background particles at later evolutionary times. At large values of q, the differences between the background and the biassed distributions become less pronounced, since only the largest peaks (present at all biassing levels) are weighted by the partition function.

In order to estimate the spectrum of generalized dimensions, we have linearly least-square-fitted $\log Z^B(q,r)$ versus $\log r$ over a range of scales between $10^{-2.5}L$ and the approximate scale of linearity (about $10^{-1}L$ as defined by the usual requirement $\xi(r) \simeq 1$). Operationally, we have found that a good criterion to assess the presence of scaling behavior in the partition function is given by the requirement that the linear regression coefficient of $\log Z^B(q,r)$ versus $\log r$ be greater than $R = 0.98$ (see also ref.[377]). The spectrum of generalized dimension is summarized in Figure 5.13 where we plot the τ_q curve obtained by means of all the employed methods in the case of the CDM spectrum. The open circles refer to the results of the BC method. From Figure 5.13 one sees that the generalized dimensions D_q have a value of about one for positive q's, with some evidence of a weak but systematic decrease for increasing values of q and for increasing biassing levels. These results indicate that the generalized fractal dimensions (for positive q's) decrease from an initial value $D_q \simeq 3$ to a value of order one as the non-linear gravitational clustering evolves. During the evolution, discreteness effects are also reduced as the particles approach each other and create the small-scale fractal structure.

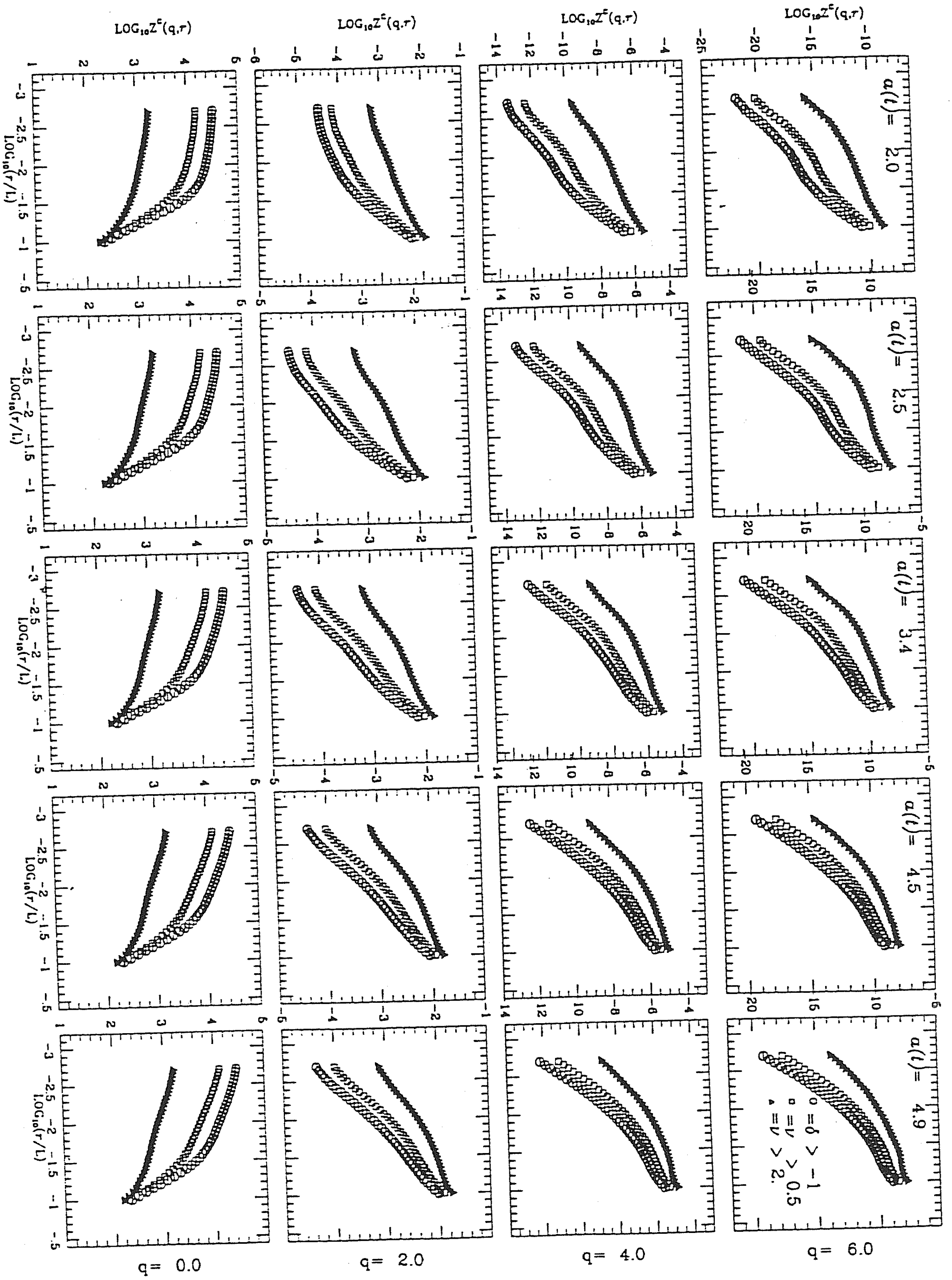

Figure 5.8: *The partition function* $Z^C(q, r)$ *versus the sphere radius* r*, (see eq.[3.23]), for the CDM case at different evolutive epochs* $a(t)$ *and biassing levels. Same details as in Figure 5.7.*

Figure 5.8 reports the results on the generalized correlation integrals $Z^C(q,r)$. We have considered the same values of q already mentioned in the box-counting case. The scaling behavior in $Z^C(q,r)$ is less clear than in $Z^B(q,r)$. Presumably, this is due to the existence of a deficit of probability at scales of the order $10^{-1.5}L$, which are the typical scales of the largest non-linear structures. The reason for that is the effect of non-linear gravitational evolution, which depletes the particle distribution on these scales and generates bound structures at smaller scales. This is particularly evident in the CI approach since the particles taken as centers of the sample spheres are expected to be found, with large probability, in the clustered regions (where most particles lie). However, the average values of the generalized dimensions D_q (for $q > 0$), obtained from a linear least-square-fit of $\log Z^C(q,r)$ versus $\log r$, are consistent with those found with the box-counting method, as summarized by the τ_q curve in Figure 5.13 (open squares). Again, the correlation method is not well suited for negative values of q.

In Figure 5.9 we show the DR partition function $W(\tau,p)$ as defined by eq.(3.25), evaluated between $p = 10^{-5}$ and $p = 10^{-1}$, for different levels of bias, epochs $a(t)$ and values of τ. We show the partition functions for $\tau = -6, -2, 2, 6$. According to eq.(5.16), the values of p we consider correspond approximately to the range of scales between $10^{-2}L$ and $10^{-1}L$. For $\tau \leq -2$ (in our case approximately corresponding to negative q's), a good scaling regime is observed in the partition function $W(\tau,p)$. Other than in Figure 5.13, where we report the τ_q curve obtained in the CDM case by using the DR partition function (open triangles), in Figure 5.16a we plot the D_τ spectrum of dimensions for different levels of biassing, at the last evolutive epoch. From these figures, we see that the generalized dimensions have a value exceeding three for $\tau \ll 0$, indicating that the scaling inside the underdense regions is characterized by the presence of minima of the density field. We note that such high values for the generalized dimensions are not generated by the fact that the DR partition function samples the large scales where homogeneity is present. Indeed, we have checked that the chosen values for the probability p correspond to physical scales that never exceed the non-linearity scale. For $\tau > -2$, on the other hand, the partition function $W(\tau,p)$ weights mainly the smallest scales which are associated with a given level of probability. In general, the scaling behavior of the DR partition function is well established and it provides indications on a dimension D_q between one and 1.5 for positive q's. The generalized dimensions tend to decrease to a value of about one as the biassing level increases. Note, in general, that some care has to be taken in the evaluation of the DR partition function, due to the existence of a numerical softening length at the lower limit of the scaling regime, which artificially increases the dimension. Since the DR partition function tends to weight also scales smaller than those sampled by the previous methods, the slightly larger values of the dimensions corresponding to positive q's found for the background could well be due to the effect of the softening length. For the highest level of biassing, on the other hand, a generalized dimension of about one is correctly reproduced; this is due to the fact that in this case there are fewer particles and a given level of probability corresponds to scales which are definitely larger than

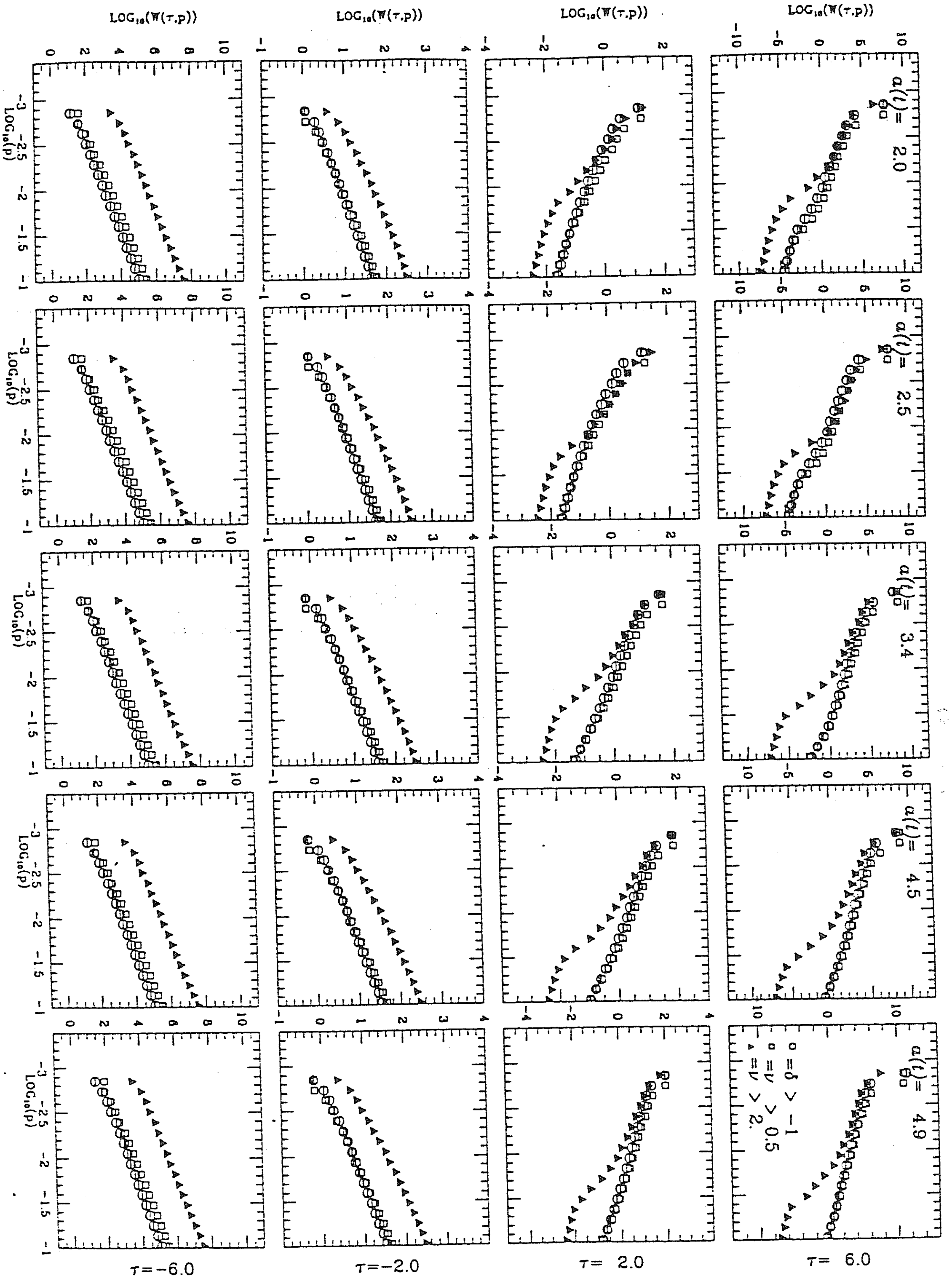

Figure 5.9: *The partition function $W(\tau, p)$ versus the probability p, as defined by eq.(3.25). Here we show $W(\tau, p)$ only for $\tau = -6, -2, 2, 6$. The expansion factors $a(t)$ and the biassing levels are the same as in the preceding figures. The length scale associated with a given p is defined through eq.(5.16).*

the softening length. The plateau observed for the biassed distribution for $p > 10^{-1.5}$ and $\tau > 0$ is associated with the break in the small-scale fractal regime and, correspondingly, with the transition toward large-scale homogeneity.

Figure 5.10 reports the partition function $G(k, \tau, n)$ for the nearest neighbor method versus the number n of particles in different random subsamples (see eq.[3.27]). We plot only the partition function for the second neighbor ($k = 2$), since operationally it turns out to be a good compromise between the need for minimizing the small-scale noise (appearing when considering the first neighbor) and the minimal set-covering requirement. We have plotted the partition functions for $\tau = -6, -4, -2, 1$. The scaling behaviour of the partition function $G(2, n, \tau)$ is extremely well defined for negative τ's, as could have been expected from the fact that this method is best suited for negative values of the exponent τ. The range of scales tested by the NN partition function may be found by considering the peak of the distribution of neighbor separations at each value of n. For small n's (*i.e.*, for large scales), this distribution is approximately Gaussian around its mean value; for larger n's (*i.e.*, at smaller scales) the distribution has a negative skewness, indicating the presence of clustering. The transition between these two regimes occurs rather abruptly at values of n corresponding to the length scales where the clustering becomes non-linear. Figure 5.11 shows two examples of frequency distributions for the second neighbor distance in the case $a(t) = 3.4$. Note that for small n's the distribution has a long tail at large distances; this implies that this method does not have a narrow-banded scale resolution. Although this should not represent a problem for strictly scale-invariant distributions, it may however affect the results when the fractality is limited to a finite range of scales, if the tail overlaps different scaling regimes. Thus, particular attention must be payed in the application of this method to observational data. In our case, however, the tail of the second neighbor distance distribution lies entirely inside the scaling regime.

The logarithmic slope of the partition function $G(2, n, \tau)$ defines a generalized dimension $D_q \gtrsim 3$ for all values of $\tau < 0$. Note, however, that at moderately negative values of τ, the generalized dimensions slowly decrease to a value $D_q \simeq 2.5$ at late evolutionary stages. For positive values of τ, the scaling behavior in the partition function $G(2, n, \tau)$ is not well established and the reliability test ($R \geq 0.98$) is not satisfied. This is consistent with the fact that the nearest-neighbor method is best suited for negative τ's. See again Figure 5.13 for a summary of the results provided by this method.

Figure 5.12 reports the results of the MST method; we show the partition function $S(n, \tau)$ versus the number n of particles in the random subsample used to build the tree. We consider values of n between $n = 100$ and the minimum between $n = 15000$ and the total number of data points (which is less than 15000 for the more biassed distributions). We show the partition functions for the same values of τ already considered for the nearest neighbor method. Again, by considering the frequency distribution of the edge links, it is possible to associate a characteristic length-scale to each value of n. By using the average

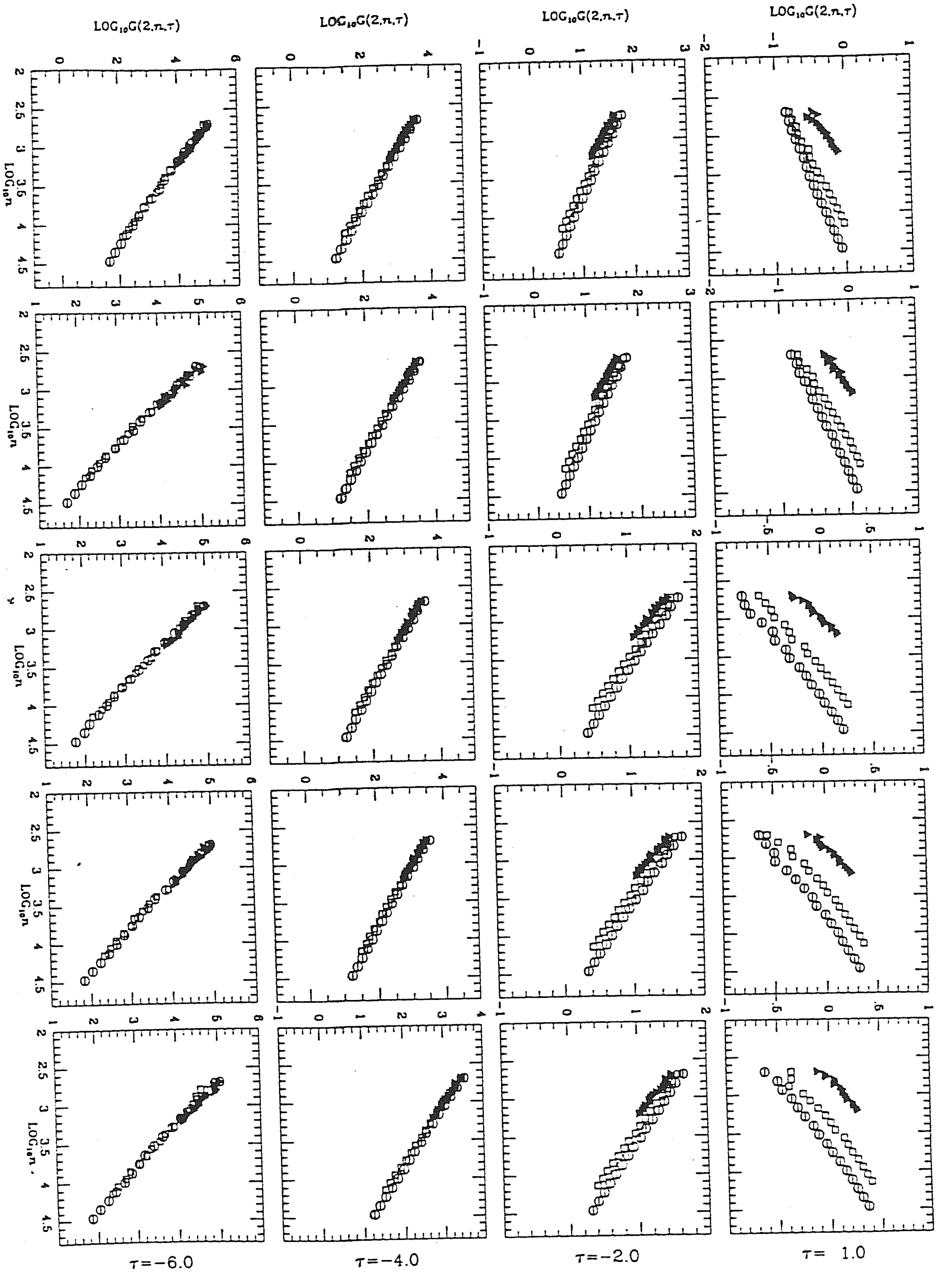

Figure 5.10: *The nearest neighbor partition function* $G(k, n, \tau)$ *versus the number* n *of points of a random subsample of the whole particle distribution (see eq.[3.27]), in the case of CDM spectrum. The values of expansion factors and biassing levels are as for the previous figures. Here we show the results only for the second neighbor* ($k = 2$).

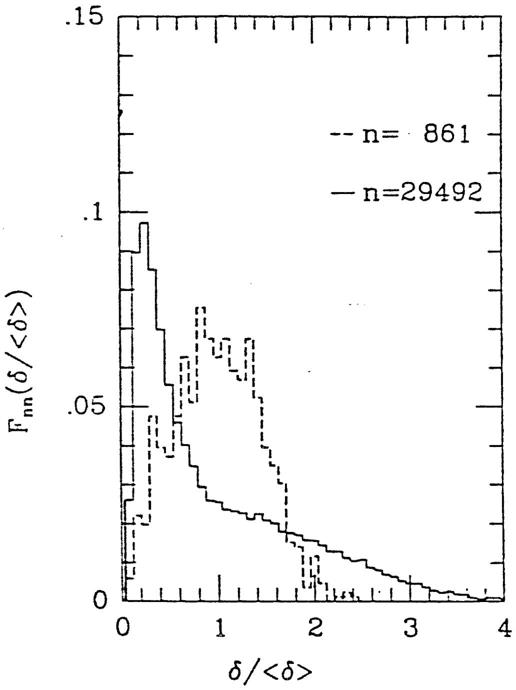

Figure 5.11: *The frequency distribution of* ${}_2\delta_i$ *as a function of* ${}_2\bar{\delta}$ *for the CDM model at* $a(t) = 3.4$ *for the background. The peak of the distribution is used to obtain the length scale associated with a given* n.

value of the edge links, the range of n values considered above corresponds to a range of scales between about $10^{-3}L$ and $10^{-2}L$. However, the distribution of the edge links has a long tail at large scales (similar to what happens for the nearest neighbor method); the MST mixes different length scales and must thus be applied with caution to limited samples with possible scale-dependent fractal properties. In fact, the large-scale tail is even stronger for the MST algorithm than for the NN method; this is due to the peculiar way in which the minimal spanning tree is built. Following the same prescription as in Chapter 3 for the analysis of synthetic samples, we cut the largest edge links for minimizing the covering as well as for avoiding spurious contributions from non-scaling parts of the distribution [377]. In general, it may also be necessary (especially for positive τ's) to cut the shorter edges for minimizing the effects of small-scale random noise. As already shown in Chapter 3, this procedure is somewhat dangerous and must be carefully checked in the case of samples with unknown scaling properties; thus, the MST method must always be supplemented by the results of other algorithms, in order to avoid incorrect inferences from its fractal dimension estimate.

The generalized dimensions provided by the linear least-square-fit of $\log S(n,\tau)$ versus $\log n$ for $\tau \ll 0$ are essentially equal to those given by the nearest neighbor method. However, for $\tau \geq -2$ the generalized dimensions are always at a value of about two. This is clearly a pitfall of the MST method which is unable to determine the correct dimension of clustered structures, as indicated by the scaling behavior of $Z^B(q,\tau)$ and $Z^C(q,\tau)$. For example, in the analysis of a pure monofractal synthetic distribution with known dimension $D = 1$, the MST

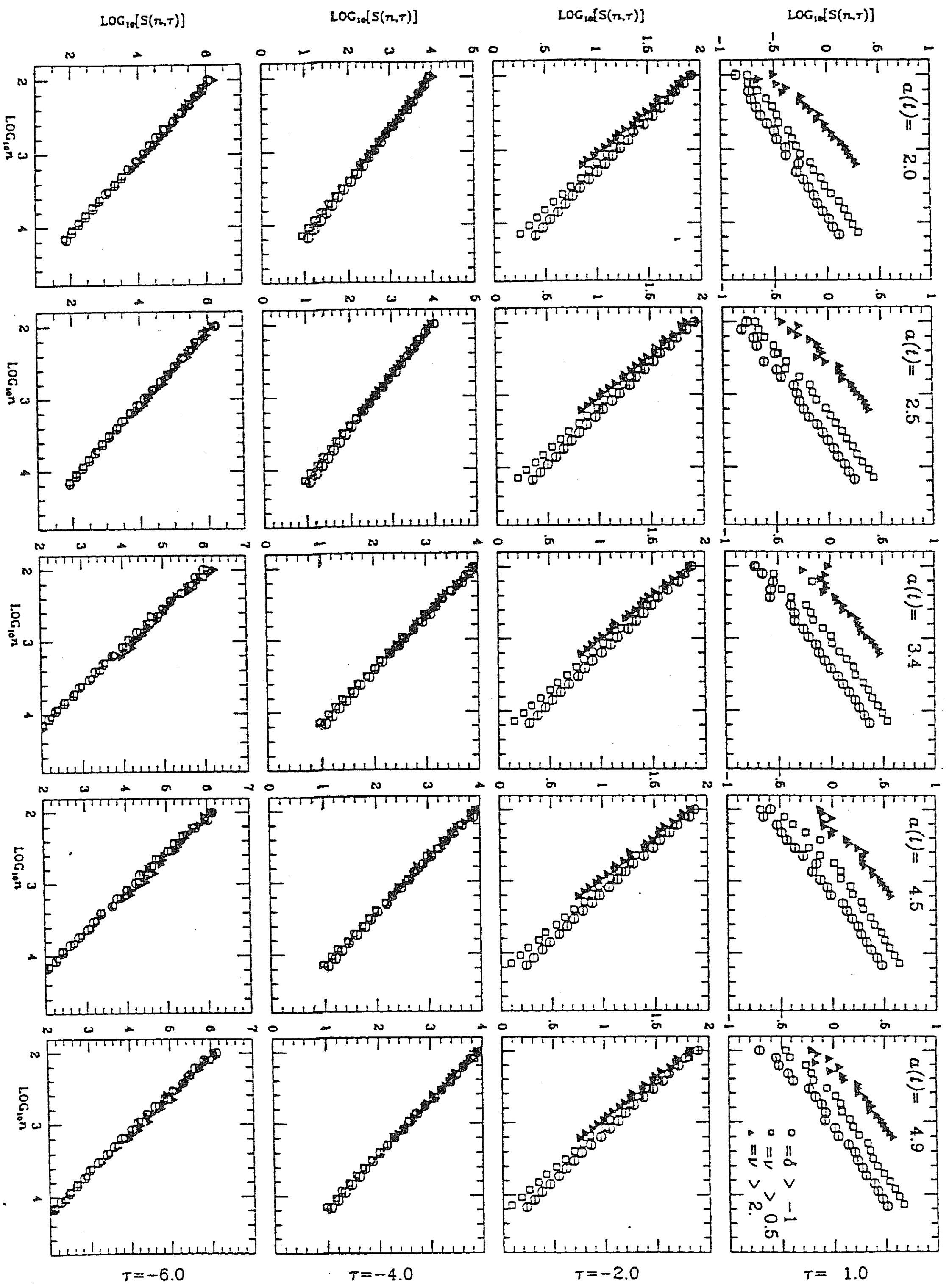

Figure 5.12: *The MST partition function $S(n, \tau)$ versus n (see eq.[3.29]), for the CDM model. The notations are the same as for the other figures. Here we show $S(n, \tau)$ for $\tau = -6, -4, -2, 1$, where n is the number of points in a random subsample extracted from the whole distribution.*

method provides $D_q \simeq 2$ for positive τ's when no edge links are cut (see Chapter 3). In the present situation, the simultaneous presence of different scaling ranges alters even more the performance of the MST.

The multifractal spectrum of CDM simulations

Putting together the results of the above analysis, one can finally draw the following picture, which is also summarized in Figure 5.13. In this figure we report the value of $\tau(q) = (q-1)D_q$ versus q for the different methods employed in the study of the CDM simulations. Analogously, Figure 5.16*a* reports D_τ versus τ as obtained from the DR partition function, which is the only algorithm working for both positive and negative τ's. For $q > 0$, the three reliable methods are represented by the BC, CI and DR algorithms. The results of the analysis indicate that, due to non-linear gravitational evolution, the generalized dimensions for positive density fluctuations very rapidly approach to one. The dimension becomes slightly lower for higher values of q and for the higher biassing levels, thus indicating a weak multifractality. The correlation dimension D_2 turns out to be between about one and 1.2 as expected from the classic correlation function studies. In general, during the gravitational evolution the dimensions of the distribution in positive density fluctuations become more and more close to one and to a "monofractal" (for positive q's) behavior. Thus, the value of about one for the generalized fractal dimensions of the galaxy distribution seems to be built by the non-linear gravitational clustering.

For negative values of q, the reliable methods are represented by the DR partition function, while some care must be used when applying the NN and MST algorithms. All these methods provide generalized dimensions exceeding three for extremely negative τ's, indicating that the particle distribution in the underdense regions contain minima of the density field, instead of singularities, as in the overdense regions. For moderately negative values of τ, the dimension is slightly less than three, due to the increasing weight of more clustered structures.

Among the generalized dimensions, a peculiar role is played by the capacity dimension D_o, owing to its independence of the statistics and to its pure geometrical meaning. For multifractal distributions, the capacity dimension D_o is known to be a decreasing function of the threshold, its variation reflecting the trend of the generalized dimensions D_q for the background. Thus, the dependence of the fractal properties on the biassing threshold should be significant in the case of D_o. However, the capacity dimension is quite difficult to compute in practice, owing to its independence of the occupation probability and its consequent high sensitivity to noise. In our case, both the BC and the CI methods do not have a clear scaling behavior for $q = 0$, due to strong discreteness effects. On the other hand, the DR, NN and MST methods indicate that $q = 0$ occurs for $\tau \simeq 3$, so that $D_o \simeq 3$ for the background. The capacity dimension slowly decreases to values between 2.5 and three as the

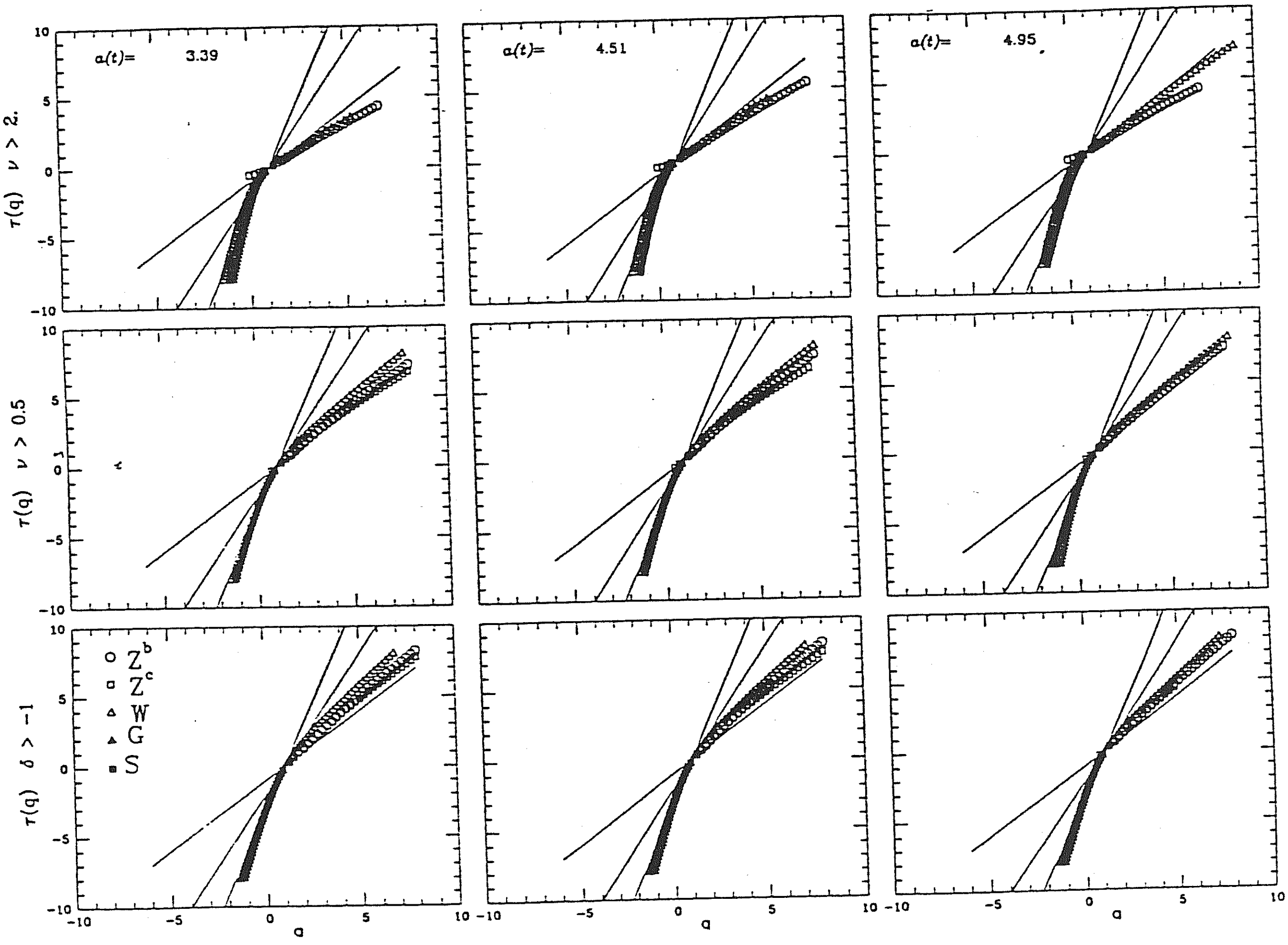

Figure 5.13: *The $\tau(q)$ spectrum for the CDM model at $a(t) =$ 3.39, 4.51, 4.95 and for different levels of bias. Here, open circles, open squares and open triangles refer to BC, CI and DR methods. Filled triangles and squares for the NN and MST methods, respectively. For the BC and CI algorithms, $\tau(q)$ at a given q is defined as the slope of the least square fit of the corresponding partition function. For the other methods one obtains q as a function of τ. We accept a scaling regime, and plot $\tau(q)$, only when the linear regression coefficient of the fit is $R >$ 0.98. The straight lines correspond to monofractal structures with dimensions $D = 1, 2, 3$.*

gravitational evolution proceeds, since particles are moved into the more clustered regions and the underdense areas are less and less sampled (this effect would presumably disappear in the limit of a huge number of particles, that adequately sample the continuous matter field). For the biassed distributions, the situation is more complex. In this case, all the methods provide values of D_o at the final evolutionary stages between about 1.5 and 2.2. In Table 5.3 we show the values of D_0, obtained from the DR algorithm, for different levels of bias, epochs $a(t)$ and initial spectra. These values are rather interesting, being in remarkable agreement with the findings of Martinez & Jones [249], who determined a value $D_o \simeq 2$ for the 14.5 CfA sample. In fact the DR method gives a value of $D_0 \simeq 1.7$ for the peak distribution of the CDM model at the present epoch.

The multifractal spectrum of the scale-free simulations

The case of an initial scale-free spectrum with spectral index $n = -2$ is characterized by the presence of large power at the largest scales; at small scales, these initial conditions have relatively less power than the CDM spectrum considered above. Thus, one expects a weaker evolution of the clustering behavior at the non-linear scales, given the fact that we used the same resolution as in the CDM spectrum. In general, the scaling properties of the partition functions for the SF–2 model are quite similar to those found in the study of the CDM evolution, apart from some interesting details connected with the weaker clustering evolution. For this reason, here we only show the final product of the multifractal analysis, namely the function $\tau(q)$ versus q as provided by the five methods discussed above.

Figure 5.14 shows $\tau(q)$ for the $n = -2$ spectrum. For negative q's, the generalized dimensions D_q are again above three, with a weak decrease for moderately negative values of q. For $q < 0$, no clear differences between the background and the biassed distributions are visible. In the case of positive q's, the dimensions found for the background turn out to be slightly larger than those found for the CDM spectrum. In particular, $D_2 \simeq 1.3$ at the end of the evolution (see also Figure 5.16*b* where we report D_τ versus τ for the $n = -2$ spectrum, as deduced from the DR partition function). The generalized dimensions of the background show a weak decrease at increasing values of q; however, they remain slightly larger than one. The results found for the biassed distributions show that the generalized dimensions definitely tend to the value $D = 1$ at increasing q's. Thus, while the largest density peaks have evolved and have reached the regime of non-linear gravitational clustering (as indicated by $D_q \simeq 1$ for $q > 0$), the background is still in a less evolved state. Again, the dimension D_o plays an important role. The results for the SF–2 model show that $D_o \simeq 3$ for the background, while it becomes of order two for the biassed distributions, analogous to what we have found for the CDM spectrum. The fractal properties of this distribution, as well as the values $D_q \simeq 1$ for the biassed distributions, seem to be well established, that is, they do not appear to be a quickly-evolving transient regime.

Table 5.3: *The generalized dimension D_0 as a function of $a(t)$ for different models and levels of bias. D_0 has been estimated using the DR method.*

		$a(t)$	D_0
$\delta > -1$	*CDM*	2.0	2.78 ± 0.02
		4.5	2.68 ± 0.02
		5.0	2.69 ± 0.02
	$n = -2$	4.2	2.73 ± 0.02
		4.8	2.72 ± 0.02
		5.5	2.72 ± 0.02
	$n = 1$	40.0	2.27± 0.03
		50.0	2.24± 0.03
		60.0	2.20± 0.03
$\nu > 0.5$	*CDM*	2.0	2.55 ± 0.04
		4.5	2.42 ± 0.03
		5.0	2.42 ± 0.03
	$n = -2$	4.2	2.50± 0.02
		4.8	2.48 ± 0.02
		5.5	2.48 ± 0.02
	$n = 1$	40.0	2.20 ± 0.04
		50.0	2.18 ± 0.04
		60.0	2.17 ± 0.04
$\nu > 2.0$	*CDM*	2.0	1.73 ± 0.08
		4.5	1.50 ± 0.06
		5.0	1.48 ± 0.05
	$n = -2$	4.2	1.56 ± 0.05
		4.8	1.55 ± 0.05
		5.5	1.54 ± 0.05
	$n = 1$	40.0	1.24 ± 0.08
		50.0	1.19 ± 0.07
		60.0	1.17 ± 0.06

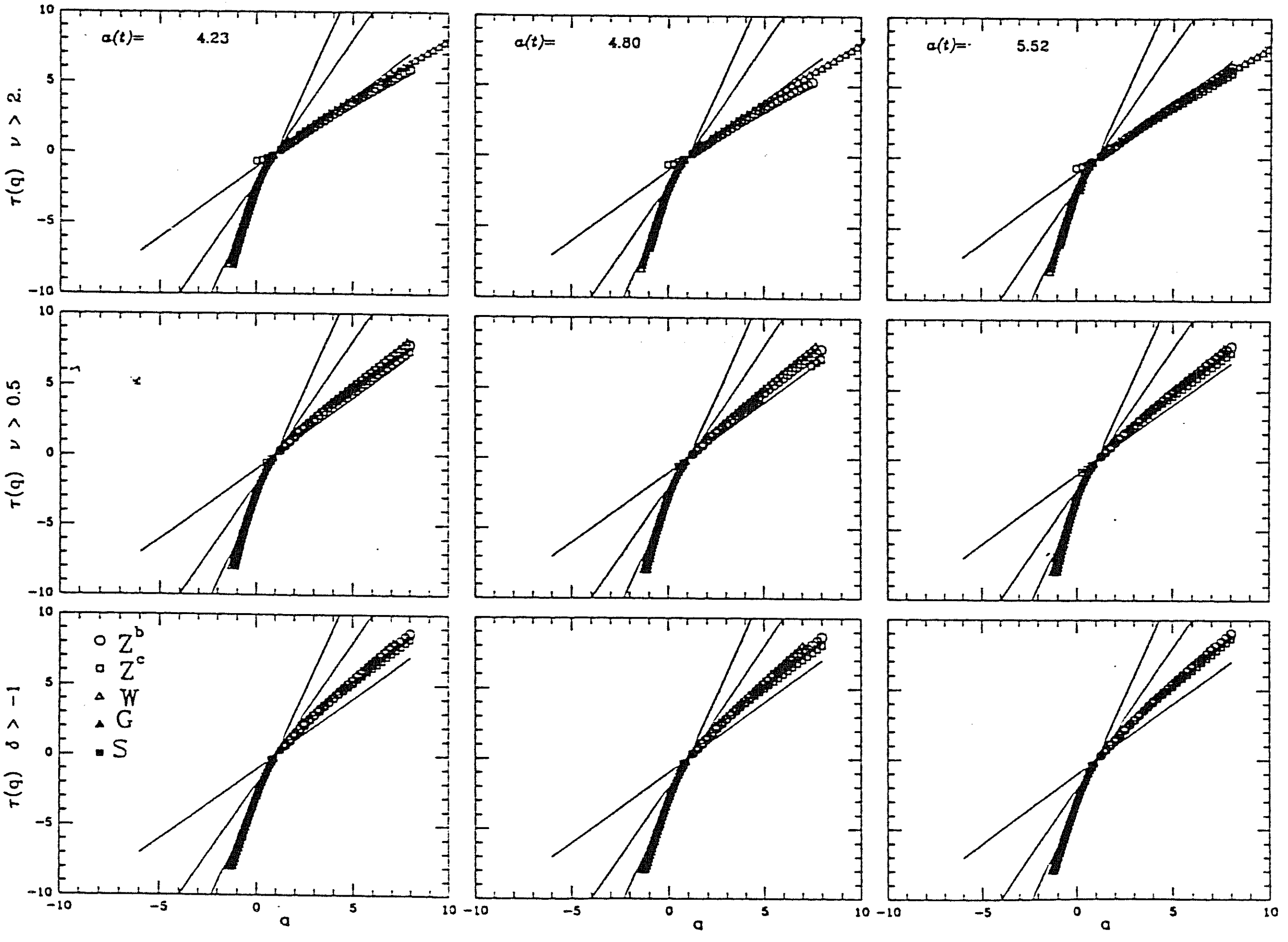

Figure 5.14: *The same as in Figure 5.13 but for a scale free spectrum with* $n = -2$.

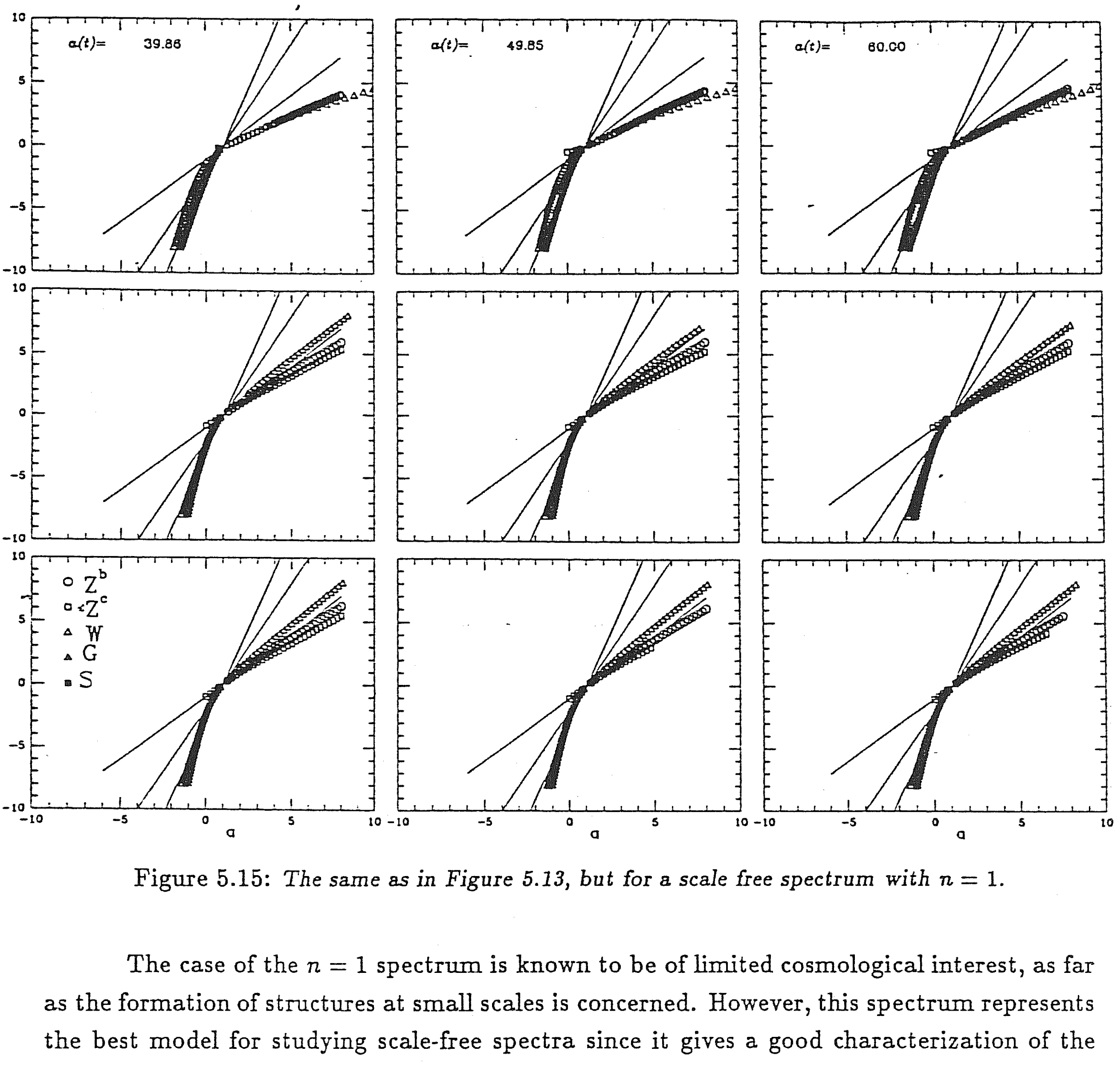

Figure 5.15: *The same as in Figure 5.13, but for a scale free spectrum with* $n = 1$.

The case of the $n = 1$ spectrum is known to be of limited cosmological interest, as far as the formation of structures at small scales is concerned. However, this spectrum represents the best model for studying scale-free spectra since it gives a good characterization of the small scale distributions at very evolved stages. This is clearly due to the presence of a large amount of power at small scales.

Figure 5.15 reports the results of the multifractal analysis for the $n = 1$ spectrum. Again, for negative values of q a dimension $D_q \gtrsim 3$ is found at all the evolutionary stages and biassing levels. In Figure 5.16c we show D_τ versus τ for the $n = 1$ spectrum, at the final stage of evolution. For positive q's, the generalized dimensions have now a value slightly *lower* than one, almost independent of evolutionary stage and biassing level. This may be understood by the very rapid evolution to the non-linear stage. All the positive density fluctuations have reached non-linear clustering and almost no differences are present between different (positive) density peaks from the point of view of clustering properties. After this rapid evolution, the clustering behavior remains essentially invariant. In this case, the D_o dimension turns out to be about two for both the background and the moderately biassed

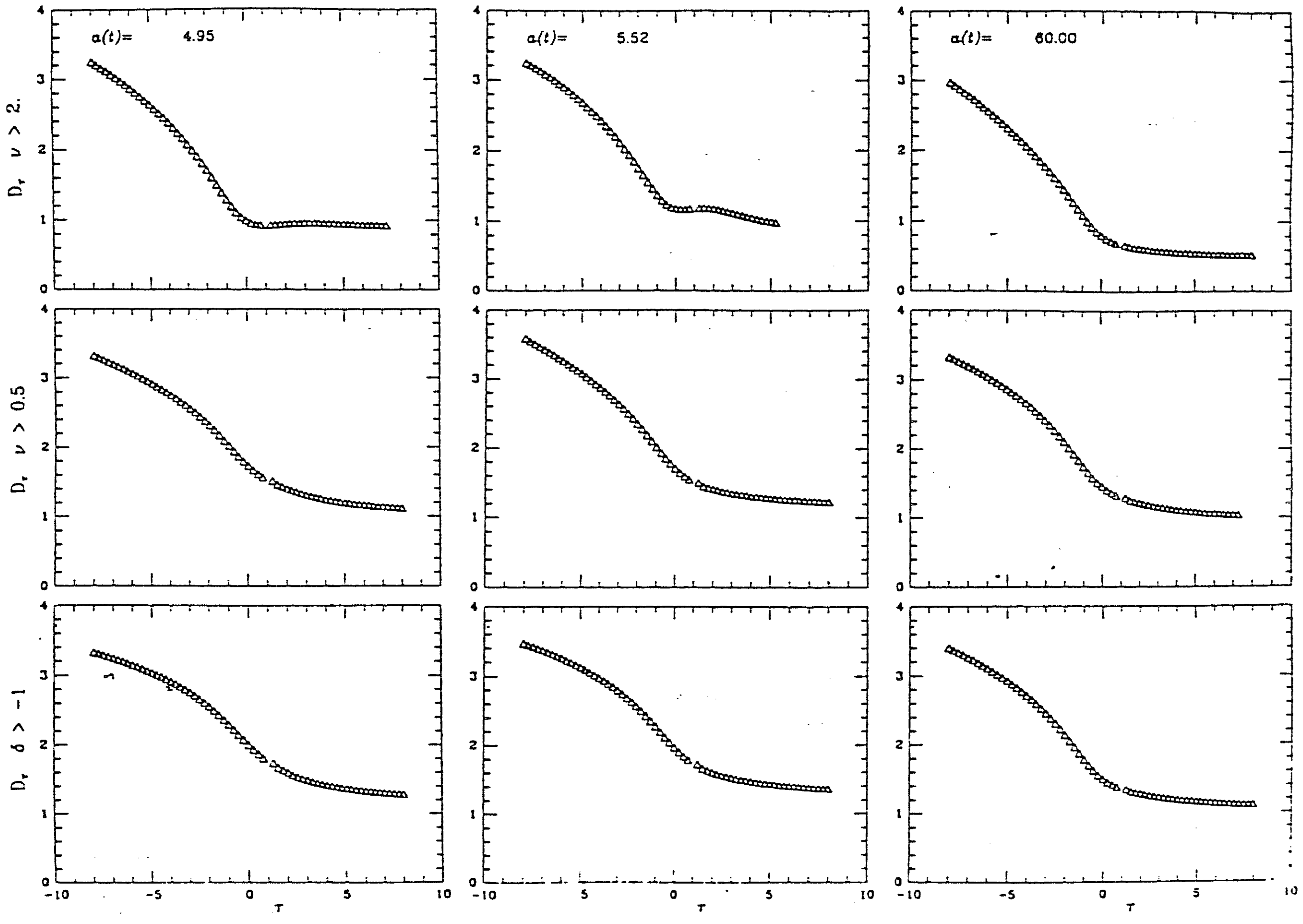

Figure 5.16: *The generalized dimensions D_τ obtained by using the DR partition function are plotted here at the final time of the integrations for the three different spectra: CDM (a), $n = -2$ (b) and $n = +1$ (c). The generalized dimensions are defined as $D_\tau = \tau/(q_\tau - 1)$, and are obtained from the values plotted in Figures 5.13,5.14,5.15.*

distributions. However, differently from the other two models, we find $D_o \simeq 1$ for the biassing level $\nu = 2$. The rapid evolution typical of this spectrum has evidently induced a stronger dependence of D_o on the biassing level. In the case of the $n = 1$ spectrum, essentially all particles have undergone non-linear gravitational clustering, and they no longer provide a good sampling of the background density field. By using a *much* larger number of particles the correct capacity dimension for the background, $D_o = 3$ should be recovered.

5.5 Outlook

In this Chapter we have carried out a series of statistical analyses of cosmological N-body simulations which have been obtained by using a P^3M code. The numerical integrations have been done for different shapes of the initial spectrum. In particular, we have considered a canonical CDM model and two scale-free models with spectral indices $n = 1$ and $n = -2$. Moreover, for each spectrum, we have selected three different particle populations, corresponding to the whole distribution and to peaks above 0.5σ and 2σ of the initial distribution.

As far as the correlation analysis is concerned, a comparison between our results on the evolution of the 2-point correlation functions with the corresponding results already obtained in the literature [98, 124] shows full agreement. Moreover, we have analysed correlation properties up to the fourth order, for various expansion factors $a(t)$ and for different levels of biassing. In particular, we have tested the hierarchical model for the 3- and 4-functions, as well as the Kirkwood expression for the 3-point correlations. Instead of the multiplet direct counting technique, in doing such an analysis we have used the so-called *moment method*, which relates the integral of correlation functions to fluctuations in the number of objects contained in spherical shells. This method has the advantage of a much greater computational speed with respect to the direct counting approach, expecially for higher-order $(n > 3)$ correlation analysis. A comparison of the deduced values for the hierarchical 3-point coefficient Q_h with past results gives good agreement and provides confirmation of the statistical significance of the moment method. Subsets of particles representing peaks of the initial density field turn out to be more clustered than the background distribution, provided the spectra has enough power on large scales (CDM and SF–2 spectra). This confirms the results of both previous numerical simulations [98] and of analytical approaches [213, 24]. On the other hand, no differences in shape and amplitude of the correlation functions among different biassing levels is found for the SF+1 spectrum, which has negligible power on large scales.

Concerning our analysis of the higher-order correlation properties, the main results we get can be summarized as follows.

a) The behaviour of the 4-point correlation function is similar to that of the 3-point one. This supports the theoretical prediction that non-linear gravitational instability gives rise to a clustering pattern described by the hierarchical expression for the n-point functions, $\xi^{(n)} \sim (\xi^{(2)})^{n-1}$. On the other hand, in all the considered cases the Kirkwood superposition does not represent a good representation of the 3-point function. For the CDM model at the present epoch $(a(t) = 2)$, we obtain, for the $\nu > 2$ peaks, $R_a + pR_b = 0.5$–0.7, to be compared with the corresponding results obtained in the literature from analyses of galaxy samples [150, 353].

b) A comparison between our deduced values for $R_a + pR_b$ and the predictions of the BBGKY hierarchy suggests quite good agreement, at least in the regime of very strong clustering, $\xi > 10^2$. In particular, for the $n = 1$ scale-free spectrum at $a(t) = 40$, we plot in Figure 5.6 the $R_a + pR_b$ coefficients obtained from the moment analysis of our simulations, with the predictions of two different solutions [145, 183] of the BBGKY equations. Both solutions give good agreement, while a departure of the theoretical model from the "observed" values occurs on the linearity scales, where the stability assumption for the clustering no longer holds.

As regards the analysis of the multifractal properties developed by N-body simulations, we have applied all the fractal dimension estimators already introduced and tested in Chapter 3. The main results of this analysis can be summarized as follows.

a) The non-linear gravitational clustering in the CDM simulations produces a scaling behavior and a fractal dimension of about one for the positive density fluctuations. On the contrary, the particle distribution in the underdense regions is arranged around minima of the density field, with corresponding dimensions $D_q \gtrsim 3$ for $q \ll 0$. This shows the multifractal character of the small-scale clustering. The generalized dimensions D_q for the CDM case show a weak dependence on the order q for positive q's, with a tendency toward the value one for increasing q's. The correlation dimension D_2 has a value of about 1.2–1.3 for the background, with a tendency to values of order one for increasing biassing thresholds. It is worth observing the flattening of the D_q curve in its $q > 0$ tail as high peaks are selected. This indicates the monofractality of the peak distribution in the overdense regions.

b) A dimension of about one for positive q's is in general produced by the non-linear gravitational evolution also in the case of the scale-free spectra. Some differences among the different spectra can however be detected. In particular, the evolution is slower in the case of the $n = -2$ model. Consequently, the dimension of the particle distribution in the background remains slightly but systematically larger than one, approaching one only for the highest peaks. Also for the $n = -2$ spectrum, a systematic decrease of the generalized dimensions with increasing biassing level is in general observed, as already mentioned in the case of the CDM spectrum. The correlation dimension D_2 for the $n = -2$ case decreases from a value of about 1.3–1.4 for the background to a stability value of about one for the highest peaks. Viceversa, for $n = 1$ the evolution is faster and the small-scale clustering is stronger; this is reflected in the lowering of the dimension slightly below one for positive q's, without significant differences between different biassing levels. For example, the correlation dimension D_2 has a value of one for this case, with no dependence on the biassing level. Thus, an $n = 1$ spectrum produces an essentially monofractal distribution for $q > 0$.

c) The above results indicate that values of the dimensions between about 0.8 and 1.3 for $q > 0$ are naturally produced by non-linear gravitational clustering and by high peak selection. Thus, the outcome of non-linear clustering tends to be a "monofractal" with approximately equal generalized dimensions D_q for positive q's, especially at late evolutionary stages and for the highest biassing levels. This is particularly evident in the case $n = 1$. In Chapter 7 we will show that the essential monofractal behavior of the particle distribution is consistent with the hierarchical behavior of the n-point correlation functions at small scales. One could then speculate that it is the gravitational evolution which forces the values of the generalized dimensions for the background matter distribution toward values of about one at small scales, while the same dimensions are recovered at larger scales for the peak distribution.

A further indication that the dimension $D \simeq 1$ is a favourite product of the non-linear gravitational evolution comes also from the observation that the density $\rho_v(r)$ in virialized isothermal galaxy halos has a dependence $\rho(r) \propto r^{-2}$, as derived from the flatness of the rotation curves for r larger than about 10 kpc (see, *e.g.*, ref.[324]). This indicates that $D_2 \simeq 1$ on these scales (see also ref.[195]). We note that, while for the $n = +1$ spectrum our results are in agreement with the prediction of Peebles' scaling argument about the stability of non-linear clustering (see ref.[284] and §4.1.4), this is not true for the $n = -2$ spectrum. In this case, the above model predicts a fractal dimension $D = 3 - \gamma = 2$ for the non-linear structures (see eq.[4.22]), remarkably different from the value $D \simeq 1$ that we find. It is difficult to assess whether or not this result is at variance with the prediction $D_2 = 2$ for $n = -2$ in the strongly non-linear regime. Efstathiou *al.* [124] have shown that the stability assumption is valid only when $\xi \gg 100$, on these scales the N-body results seem to give a quite good fit to the slope of the 2-point function according to Peebles' scaling argument. Numerical simulations of the kind employed here, however, are limited in time by an epoch a_{fin} when the fundamental mode of the cube approaches non-linearity. In the case $n = -2$, $a_{fin} \simeq 5$ and the range where one can test the BBGKY prediction is very limited. On the other hand, the evaluation of D_q with $q \gg 0$ selects regions of high density, *i.e.* where the clustering is more evolved. Furthermore, the fractal dimension for the bias is *smaller* than for the background, and the analysis of other spectra shows that the biassed particle distribution can be in a sense considered as a background population analysed at late times and, thus, at a more clustered stage. Thus, the conclusion that $D_q \simeq 1$ for gravitationally evolved systems seems to be well supported. This result is consistent with the findings of Saslaw [331, 340], who argued that the value $\gamma = 2$ (*i.e.*, $D_2 = 1$) is dynamically stable in the fully non-linear clustering regime. This is also in agreement with the Hoffman & Shaham [195] model for the density profile of virialized halos (see also §4.1.4). Based on the secondary infall paradigm, they found that nearly isothermal halos, having density profile $\rho(r) \propto r^{-\gamma}$ with $\gamma \simeq 2$, are a natural outcome of non-linear clustering, quite independently of the initial fluctuation spectrum (see eq.[4.23]).

d) The behavior of the capacity dimension D_o has been shown to be particularly interesting. This peculiar dimension is in fact insensitive to the statistics; it measures only the geometry of the system. For a rich sampling of a continuous density field without large holes where $\rho = 0$, this dimension *must* be equal to three. Recalling that the point distributions produced by the N-body simulations can be taken as Monte Carlo samplings of an underlying density field, then it immediately follows that the capacity dimension of the background must be $D_o = 3$, if a sufficient number of particles is considered. In fact, if there are no extended regions where $\rho = 0$, then on average there is at least one particle in each box and thus a sufficiently dense Monte Carlo sampling of the density field will always be space-filling. Clearly, for a small number of particles the Poisson sampling noise may be large enough to mask the $D_o \simeq 3$ behavior. A completely different situation is encountered for biassed distributions, where one introduces a threshold density and consequently weights (in a yes/no fashion) the occupancy probability. Since, as a consequence of the evolution, the distribution of peaks associated with positive density fluctuations is not space-filling, the capacity dimension D_o of the peak distribution must be definitely smaller than three. In particular, for very large values of the bias and/or for late evolutionary stages, the D_o dimension is sensitive only to the distribution of the highest density peaks, and thus one should find $D_o \rightarrow D_\infty$. Thus, the value of D_o for very large biassing thresholds should essentially be the value of D_q of the background for very large values of q. However, the convergence of D_o to D_∞ may be very slow. In fact, for the biassing levels considered here we find essentially $D_o \simeq 2$ for the "less evolved" $n = -2$ spectrum, D_o between about 1.5 and 2.2 for the CDM spectrum and $D_o \simeq D_\infty \simeq 1$ for the much evolved $n = +1$ spectrum for the highest biassing thresholds. Thus, the precise value of D_o found for galaxies and clusters could be a test on the initial spectrum and the biassing parameter. It is interesting to note that the values found for the CDM and for the $n = -2$ spectra remarkably coincide with the value of D_o found by in the analysis of the galaxy distribution in the 14.5 CfA sample [249]. This result has been sometimes considered as the consequence of a sheet-like geometry of the galaxy clustering, with objects arranged in shells surrounding big voids. However, in our analysis the value $D_o \simeq 2$ has been obtained by selecting peaks from the CDM and SF–2 simulations. Thus, a Hausdorff dimension around two does not necessarily imply the presence of a cellular structure for the large-scale galaxy distribution, as predicted by explosion or hot dark matter scenarios.

We note that the above results about the multifractal properties of cosmological N-body simulations may suggest some possible tests on the observational data. In particular, the behavior of generalized dimensions for negative q's seems to be more sensitive to the initial spectrum shape and to the biassing level. On the other hand, the rather flat profile of the D_q spectrum at $q > 0$ seems to be the natural outcome of non-linear gravitational dynamics. The stability value $D_q \simeq 1$, which arises quite independently of initial conditions, is in accordance with the predictions of several models of gravitational clustering. In this sense, the observed flatness of galaxy rotation curves , as well as the slope of the galaxy 2-point correlation function and the hierarchical behaviour of higher-order correlations, should be considered as products of the non-linear gravitational dynamics, while containing only limited information about the primordial fluctuation spectrum. Viceversa, memory of initial conditions should be preserved at larger ($\gtrsim 10h^{-1}$ Mpc) scales, where clustering is still linear.

As a general conclusion, we would like to emphasize once more the relevance of demonstrating that fractal structures are naturally formed at the small scales where non-linear gravitational dynamics takes place. From one hand, this result implies that, in order to accept a purely fractal description of the galaxy distribution at arbitrary large scales [305, 88, 87] one is forced either to reject the quasi-homogeneity of the initial conditions or to imagine that the primeval field had a large-scale coherence of non-gravitational origin. From the other hand, it represents one of the few examples of physical systems which develop scale-invariant structures from dynamical equations, where fractality is not put in "by hand". A further example of this kind is provided by the Navier-Stokes equation, which is used in hydrodynamics to describe turbulent flows. However, the limited resolution achieved in simulations of fully developed turbulence from Navier-Stokes dynamics (see, *e.g.*, ref.[354]) allows the detection of self-similar structures over a rather limited range of scales, narrower than that displayed by cosmological N-body simulations. Thus, apart from the well known cosmological relevance, N-body simulations of gravitational clustering have also a remarkable interest from the point of view of the study of complex dynamical systems.

The results presented in this Chapter are contained in two papers, that have been already published in *Montly Notices of the Royal astronomical Society* (Valdarnini & Borgani 1991, [373]) and in *The Astrophysical Journal* (Valdarnini, Borgani & Provenzale 1992, [374]).

Chapter 6

Probing the scaling of angular cluster distributions

As we have seen in previous chapters, the observed power-law shape of galaxy correlation functions naturally leads to identify the non-linear clustering as a scale invariant process. Even more, the analysis of cosmological N-body simulations has shown that small-scale fractality is the natural outcome of non-linear gravitational dynamics. The striking similarity between the clustering properties of galaxies and galaxy systems also suggests that even the cluster distribution possesses a well defined fractal behaviour, which, at scales of few tens of Mpcs, represents a sort of pantography of the galaxy clustering, as observed at scales one order of magnitude smaller.

In order to properly address this problem, in the present Chapter, we investigate both correlation and fractal properties for different samples of galaxy clusters, which are obtained by cutting the Lick catalog at different values of the galaxy surface density. This kind of cluster-finding algorithm is equivalent to the application to the Lick galaxy distribution of the biassing prescription, described in §3.3. More in detail, we will check the effect of cluster richness on the shape of the 2- and 3-point functions. A detailed multifractal analysis of the same samples allows us to verify the existence of a relation between scale-invariance and non-linear clustering in the distribution of galaxy aggregates.

6.1 Clusters as tracers of the LSS

A challenging feature of the large-scale structure of the Universe is the clumping of galaxies into clusters of varying richness and the clumping of clusters of galaxies into superclusters (see Chapters 1 and 2) and there are evidences that this clustering hierarchy continues to even larger conglomerations [17, 231]. The understanding of the processes that lead to such a clustering hierarchy is essential for the understanding of the history of the Universe. Although the clustering of galaxies could be the result of non-linear gravitational interactions, the clustering of larger units up to $\sim 100\ h^{-1}$ Mpc could not. With a typical peculiar velocity of $\sim 10^3$ km/sec a cluster could have moved only $\sim 10\ h^{-1}$ Mpc within a Hubble time. It is therefore certain that the distribution of clusters and superclusters of galaxies reflects the initial conditions of their formation. Hence, quantifying the large scale distribution of rich galaxy aggregates in a systematic and bias free way could provide a basic tool for our understanding of the structure formation processes in the early history of the Universe.

A great deal of efforts has been invested in the pursuit of this goal through conducting studies of the two- and three-dimensional distribution of galaxy systems. A detailed description of the observed clustering properties of the large scale structure has been already presented in Chapters 1 and 2. Here we only recall that galaxies, clusters of galaxies and even superclusters have been found to have the same power law 2-point correlation function, $\xi(r) \propto r^{-\gamma}$, with $\gamma \simeq 1.8$ and amplitude increasing with the scale of the objects under study (see Figure 2.3). Indeed, the correlation function of clusters of galaxies is significantly higher than that of galaxies (see, *e.g.*, ref.[236]) and a richness dependance of the clustering length has also been found [18, 307]. These observations suggest that, if the clustering hierarchy continues to even lower richness, then the mass distribution could be clustered weaker than galaxies, a suggestion that leads to the idea of biassed formation of cosmic structures [213, 24] observed structures arise from exceptionally high peaks of the underlying density field and, consequently, are more strongly clustered (see §4.4).

Current models of galaxy formation are not able, however, to account for the observed properties of rich clusters. White *et al.* [392] found that, although the abundance of Abell clusters with $R > 0$ is in good agreement with the the output of CDM N-body simulations, the cluster correlation length is only twice that of galaxies while the observations indicate that it is five times that of galaxies. Batuski *et al.* [31], using N-body simulations and comparing the abundance of Abell clusters with the highest density peaks in the simulations, find that none of the models (HDM, CDM and isothermal) can match the correlation and percolation properties of the Abell clusters.

However there are a variety of biases that can conspire to produce apparent features unrelated to physical 'reality' and therefore lead the theorist to futile research labyrinths. Such well known biases include the tendency of the human eye to select features at a very low significant level [27]. Other biases are introduced by atmospheric absorption, Galactic extinction, the subjectivity of catalogue selection procedures, projection effects, instrumental effects, etc. The recent discussion on the reality of the spatial correlation function amplitude of rich clusters illustrates the importance of the above points. As discussed in §2.1, several authors [361, 105, 272, 362] argued that the enhanced clustering of rich Abell clusters is partly real but partly also due to the contamination of the sample by foreground-background galaxies. However, recent studies of Abell cluster correlations show that contamination affect insignificantly the cluster correlations [360, 208] (see §2.1.4). The clarification of this point could be of crucial relevance since a significantly lower cluster correlation amplitude could be a way out for the CDM model that predicts a low amplitude for the fluctuation spectrum at large scales. However, it has also been shown that, in the frame of the original [82] but also general *biassed* models [48], the CDM spectrum predicts a cluster 2-point function that takes negative values at scales $\sim 18\ h^{-2}$ Mpc, while the decontaminated $\xi(r)$ for rich clusters still takes positive values up to separations $\gtrsim 50h^{-1}$ Mpc.

Despite the relevance of the 2-point function, it is however clear that it does not contain all the informations about the statistics of the cluster distribution. For this reason, different authors extended the correlation analysis of the cluster distribution to the 3-point function, [211, 366] with particular attempts to compare it with the predictions of *bias* on the 3-point function [205, 363]. In all the considered cases these authors concluded that observational data are not consistent with *bias* expectations, which predict Kirkwood type correlations (see eq.[2.23]) if a Gaussian background is assumed. They found that a good fit to the spatial 3-point function is provided by the hierarchical expression

$$\zeta(r_1, r_2, r_{12}) \;=\; Q\,[\xi(r_1)\xi(r_2) + \xi(r_1)\xi(r_{12}) + \xi(r_2)\xi(r_{12})]\,, \qquad (6.1)$$

with values of the hierarchical coefficient in the range $0.6 \lesssim Q \lesssim 1.1$.

Using large CDM N-body simulations, Gott, Gao & Park [161] selected clusters by applying the *biassing* prescription to their simulations and confirmed the hierarchical behaviour of the 3-point function, finding also consistent values of the Q coefficient. In this way, they claimed that eq.(6.1) is not in disagreement with the theoretical expectation of *biassing*, at least in the non-linear ($\xi \gg 1$) clustering regime, where the hierarchical behaviour of correlation functions is expected to hold. Jing & Valdarnini [209] recently analysed a redshift sample of Abell and ACO clusters. Using the *bootstrap* method to estimate sampling errors [28, 236], they found that quite large uncertainties affect the determination of the 3-point function. These authors showed that, within the large errorbars, the hierarchical model of eq.(6.1) is in agreement with data.

A further related aspect concerns the detection at large scales of self-similarity in the clustering pattern. As we often mentioned in this Thesis, the detection of well-defined scaling properties for the large-scale distribution of cosmic structures seems to suggest, at first glance, a fractal picture of the Universe. It is not clear, however, to which extent the self-similarity of the galaxy distribution, that is well established from the analysis of spatial samples at the small scales of non-linear clustering (see, *e.g.*, ref.[249]), does extend at larger scales where the correlation signal becomes hardly detectable above the noise. Due to the rather limited sizes of the volumes sampled by the available galaxy redshift survey, no clear evidence has been found that the galaxy distribution reaches a high degree of homogeneity at the largest scales allowed by such samples. Instead, the texture of the galaxy distribution gives rise to structures, such as filaments and voids, that involve scales comparable to that of the whole sample (see Chapter 1). Even within this picture, evidence is emerging that the galaxy distribution has at least one characteristic scale ($\simeq 4h^{-1}$ Mpc), below which a scaling regime exists, with a correlation dimension $D_2 \simeq 1$ [249]. At larger scales, it has been suggested that a second scaling regime takes place, extending up to $\sim 30\,h^{-1}$ Mpc with a larger dimension $D_2 \simeq 2.2$ [181, 128, 68]. The analysis of the multifractal properties of cosmological N-body simulations, described in the previous Chapter, clearly shows that the gravitational instability picture with quasi-homogeneous initial conditions naturally gives rise to fractality of the matter as well as of the galaxy distribution, but only up to scales where the clustering is non-linear.

In order to search for scaling of the clustering pattern at scales larger than those allowed by the galaxy distribution, it seems appropriate to use the distribution of galaxy clusters. Although their amplified clustering has been explained in the framework of *biassed* models, it was also used as a further support to the idea that the large-scale structure is described by a self-similar fractal, extending at arbitrarily large scales [88]. In this picture, the amplification of clustering of rich galaxy systems is not an intrinsic properties, but only reflects the fact that cluster catalogues sample larger volumes with a consequent increase of the correlation strength (see §4.4). If this were the case, then we should expect that the galaxy correlation function maintains the same slope also at the scales where cluster clustering is detected, thus in disagreement with the above mentioned existence of different scaling regimes for the galaxy distribution.

In order to analyze the statistics of the large-scale cluster distribution, in this Chapter we presents the results of both correlation and fractal analysis of angular cluster distributions. To this purpose, we will use different methods of analysis and error estimates, in order to assess the robustness and the reliability of our results. The cluster catalogues we use are the Plionis, Barrow & Frenk [300] samples (PBF samples, hereafter), that have been identified from the Lick map as peaks of the surface galaxy density field, that exceed fixed density threshold values. Due to this specific cluster identification algorithm, we are also able to test the effect of peak height on the scaling properties of their distribution.

6.2 Cluster catalogues

6.2.1 Description

The Plionis, Barrow & Frenk [300] cluster catalogues (PBF samples, hereafter) were identified, using an overdensity criterion, in the 'free-of-overlap' Lick galaxy counts [348, 347, 299]. For a full description of the cluster selection procedure (cluster-finding algorithm, biases, etc.) see ref.[300]. Here we will just remind that the Lick catalogue of galaxies has $m_b \lesssim 18.8$, covers declinations $\delta > -23^\circ$ (70% of the sky) and has a characteristic depth of $\sim 210\ h^{-1}$ Mpc [173]. The galaxies are binned in $10 \times 10\ arcmin^2$ cells and therefore the catalogue lists counts in cells (see also §1.2).

The cluster-finding algorithm is based on identifying peaks of the galaxy surface-density σ, that lie above a threshold κ of our choice; $\sigma \geq \kappa \times \langle\sigma\rangle$, where $\langle\sigma\rangle$ is the mean galaxy surface-density and the value of κ specifies the catalog. All the surrounding grid cells that also fulfill the selection criteria are connected so that they belong to the same cluster. A drawback in this type of algorithm is that the intrinsic richness of the clusters it picks out is a function of distance. However, since individual galaxy magnitudes are not available, this is the best one can hope to do with the Lick data. Ongoing surveys using automated measuring machines [90, 246] will eventually allow more sophisticated studies.

We use in our analysis the three cluster catalogues described in ref.[300], identified at overdensity thresholds with $\kappa = 3.6$, 2.5 and 1.8 (C36, C25 and C18 catalogues), other than a fourth catalogue with $\kappa = 3$ (C30 catalogue). Although all the samples have been analyzed for both the correlation and the fractal analysis, in the discussion of the latter we will only discuss the results for the northern C36 and C25, representing the other only intermediate cases. There is one small difference between the cluster catalogues used here and those in ref.[300], namely that we do not exclude from the lower overdensity catalogues the clusters found in higher levels. Note that to eliminate the gross effect of Galactic extinction, our catalogues contain clusters with $|b| \geq 40°$. Equal area projections of the C36, C25 and C18 catalogues are presented in Figure 6.1. A visual inspection of these distribution immediately reveals that the clusters identified with the highest density peaks are much less numerous, but remarkably more clumped than lower peaks. This is just the consequence of the coherence introduced by threshold effects.

Redshift information is available only for a subset of the C36 clusters (see ref.[340]) and for a subset of the Lick clusters that happen to be also Abell clusters. A detailed discussion of the redshift distribution of The C36 clusters have a median depth of $\sim 180\ h^{-1}$ Mpc while there is a slight tendency to pick out relatively more distant Abell clusters at lower overdensities (cf. ref.[300]).

6.2.2 Systematics

A main concern when using catalogues of extragalactic objects is whether the catalogues are homogeneously selected over the survey area. Such systematic errors are introduced by human biases, by the selection procedure and by the effects of Galactic and atmospheric extinction. The selection procedure used to identify clusters from the Lick map is free of human biases since it is based on a computer algorithm. Nevertheless the Lick catalogue itself is affected by such biases [153, 112]. Artificial large-scale density gradients are probably present with an amplitude of $\sim 20\%$ (for counter-arguments see refs.[299, 63]). These gradients, if present, could affect the homogeneity of the cluster catalogues. Whenever the galaxy surface density is enhanced, the cluster-finding algorithm will reveal poorer clusters that otherwise would have not fulfilled the selection criteria and whenever the surface density is suppressed, the algorithm will miss clusters. However, this effect should not be large since it will affect only

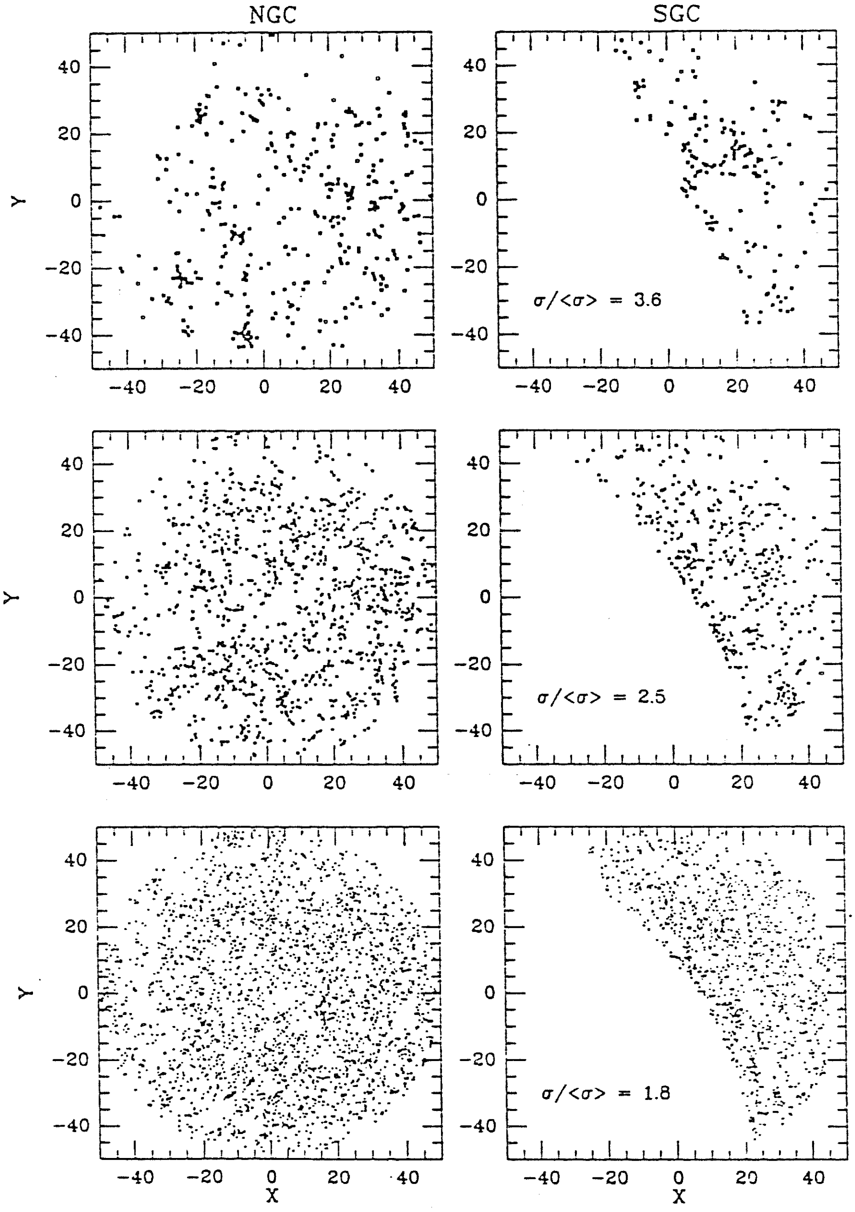

Figure 6.1: *Equal area projections of PBF clusters at different overdensity levels. The galactic North and South Pole are located at* $x = 0, y = 0$ *(after [300].*

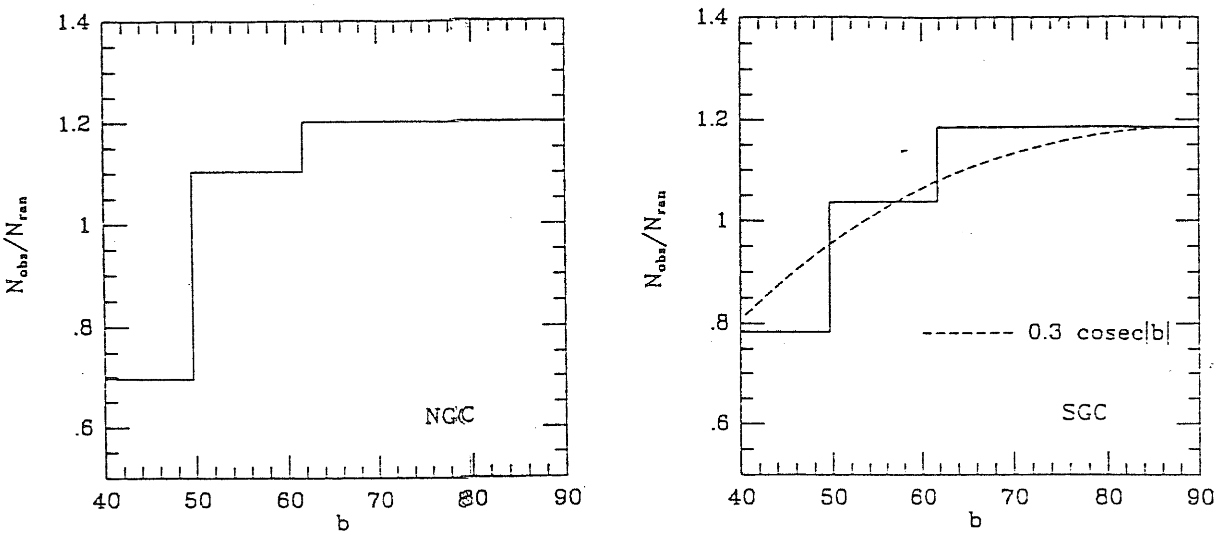

Figure 6.2: *The ratio of the observed to the expected number of C25 clusters, N_{obs}/N_{ran} as a function of the Galactic latitude $|b|$, for the northern (left panel) and southern (right panel) galactic cap. The dashed curve represents the extinction function $P(b)$.*

those clusters whose peak density lies near the limiting density threshold. We estimate that these are not more that 10% of the total number of clusters.

The next concern is whether there are any systematic density gradients due to Galactic extinction or atmospheric absorption. In order to minimize the effect of Galactic absorption we have confined our studies to $|b| \geq 40°$. In Figure 6.2 we plot the ratio of the observed to expected number of C25 clusters, N_{obs}/N_{ran}, as a function of $|b|$. For the NGC we find that a cosec$|b|$ law does not fit well the data. There is no significant extinction for $b \gtrsim 50°$ while there is an abrupt decrease of the cluster number density in $40° \lesssim b < 50°$. Therefore for the NGC we estimate correlation functions only for $b \gtrsim 50°$. For the SGC we find that the extinction function

$$P(b) = 10^{0.3(1-\mathrm{cosec}|b|)}. \tag{6.2}$$

fits nicely the data for $b \lesssim -40°$ (see Figure 6.2). An attempt to investigate the possible declination dependance of the cluster number density has shown that such an effect is not evident in our cluster catalogues.

6.3 The correlation analysis

In this Section we describe the methods we use to determine the 2- and 3-point functions for our cluster samples. In all the cases, sampling errors are estimated by using the *bootstrap* resampling method (see below). Note that, due to the rather small number of clusters contained in the samples selected at the higher density levels, we prefer to merge together the northern and southern part of the C30 and C36 catalogues for the 3-point analysis, which requires more statistics. Separate analysis for north and south are performed for C25 and C18.

6.3.1 The 2-point function

Let us consider a two-dimensional distribution of objects and let $N_i(\vartheta)$ be the number of objects contained in an angular ring $\vartheta - \Delta\vartheta/2 \leq \vartheta \leq \vartheta + \Delta\vartheta/2$, centered on the i-th object. Then, its first-order moment, $\langle N \rangle_\vartheta$, can be expressed in terms of the angular 2-point correlation function according to

$$\langle N \rangle_\vartheta \; = \; \bar{N}_\vartheta \left[1 + w(\vartheta)\right]. \tag{6.3}$$

Here $\bar{N}_\vartheta$ is the expected number of clusters in an angular shell with separation in the range $\vartheta - \Delta\vartheta/2 < \vartheta < \vartheta + \Delta\vartheta/2$. In order to evaluate $\bar{N}_\vartheta$, two slightly different prescriptions can be devised. The first possibility is to count random points in angular anuli centered on random points. This amounts to estimate the number of random-random pairs at a given separation. Since no correlation exists between data and random samples, an alternative procedure is to count random points around real data objects. In the following, we will presents the results based on the first method, although we also evaluated the random-data pairs and found no differences in the resulting correlation signal.

In order to account for boundary effects and systematic density gradients, which are usually present in real data samples, we prefer to normalize eq.(6.3) so that $\bar{N}_\vartheta$ is the average first-order moment over 20 random samples that contain the same number of points and have the same angular selection function as the real sample. For the NGC samples ($b \geq 50^\circ$) no galactic latitude dependance is introduced in the random catalogues while for the SGC samples the random points are layed down with a probability proportional to the extinction function of eq.(6.2). Postman, Geller & Huchra [307] have found that, unless the extinction is extreme, it will not significantly affect the amplitude or slope of the correlation function. We have also verified this result in our samples. In our analysis, we evaluate the first-order moments in the object distribution in 8 bins having the same amplitude $\Delta = 0.34$, and ranging from $0^\circ\!.6$ up to 9°. The first-order moment for the random sample, $\bar{N}_\vartheta$, is found by averaging over 20 realizations.

To estimate the sampling errors, we use the *bootstrap* method [236, 27]. This method is based on the generation of pseudo data sets, that are obtained by sampling N points with replacement from the true data set of N points. To be more precise, suppose that $\mathbf{X} = \{X_1, ..., X_N\}$ represents the set of N raw data. A bootstrap sample $\mathbf{Y}$ is then obtained by randomly sampling $\mathbf{X}$ N times. Since it could happen that some objects are selected more than once, other objects, that are never selected, must be randomly replaced. By repeating this operation n times, we will end up with an ensemble $\mathbf{Y}_i$ ($i = 1, ..., n$) of bootstrap samples.

If we denote with $w_i^*(\vartheta)$ the angular 2-point function estimated on the i-th bootsrap sample, then the variance over the $\mathbf{Y}_i$ ensemble is

$$\sigma_n^2 = \frac{\sum_{i=1}^n [w_i^* - \bar{w}^*]^2}{n-1}, \tag{6.4}$$

being $\bar{w}^* = \sum_{i=1}^n w_i^*/n$ the bootstrap-averaged 2-point function. Under general conditions [219], it can be shown that the variance evaluated over a given ensemble of such random resamplings converges to the true standard error, when the number of resamplings is sufficiently high, $\sigma_{true}^2 = \lim_{n\to\infty} \sigma_n^2$. Note that the bootstrap resampling procedure gives only the sampling uncertainties in the estimate of $w(\vartheta)$, while the bootstrap averaged $\bar{w}^*(\vartheta)$ must not be considered as the true correlation function. Indeed, each bootsrap resampling amounts to slightly randomize the original distribution. Therefore, we expect that the resulting $\bar{w}^*(\vartheta)$ is always smaller than $\bar{w}(\vartheta)$.

In Figure 6.3 we plot the 2-point function $w(\vartheta)$, that we obtain by inserting in eq. (6.3) the values of the first-order moments. A good representation of $w(\vartheta)$ is given, for all the considered cases, by a power-law model with slope that is always consistent with $\gamma \simeq 2$, but with an amplitude A which remarkably correlates with the height of the sample threshold. Also note that the results for the SGC systematically show a stronger correlation (~ 40%). This, however, is due to the lower mean galaxy density, $\langle\sigma\rangle$, in the SGC [299] and therefore selecting peaks over κ times the mean density of the whole sample amounts to take relatively higher peaks, which, consequently, are more strongly clustered. In Table 6.1 we report the best-fit parameters of $w(\vartheta)$ for all the considered cases.

In order to test the reliability of our detection of the 2-point function and the effect of using the rigorous bootstrap method to evaluate errors, we also estimated the error in $w(\vartheta)$ according to:

$$\sigma_w \simeq \frac{[1 + w(\vartheta)]^{1/2}}{\bar{N}_\vartheta^{1/2}} \tag{6.5}$$

(see, *e.g.*, ref.[33]), which partially accounts for the non-Poissonian nature of clustering. The reduced error bars we get when using (6.5) permits to reduce the bin size and we evaluate $w(\vartheta)$ out to separations $\vartheta \sim 45°$. The plot of Figure 6.4 shows no differences with our previous determination of $w(\vartheta)$, apart from a significant reduction of the estimated errors. This shows how misleading it can be using approximate methods to estimate errors. In Figure 6.4 we also plot $w(\vartheta)$ for the Lick galaxies (open circles) and it is evident that although the galaxy correlation function breaks at ~ 2.5° the different cluster correlation functions show the same power law out to at least 9°.

6.3.2 The 3-point function

We describe now our analysis of the 3-point cluster correlation function. Since the amount of required statistics to get stable results rapidly increase with the correlation order, for C36 and

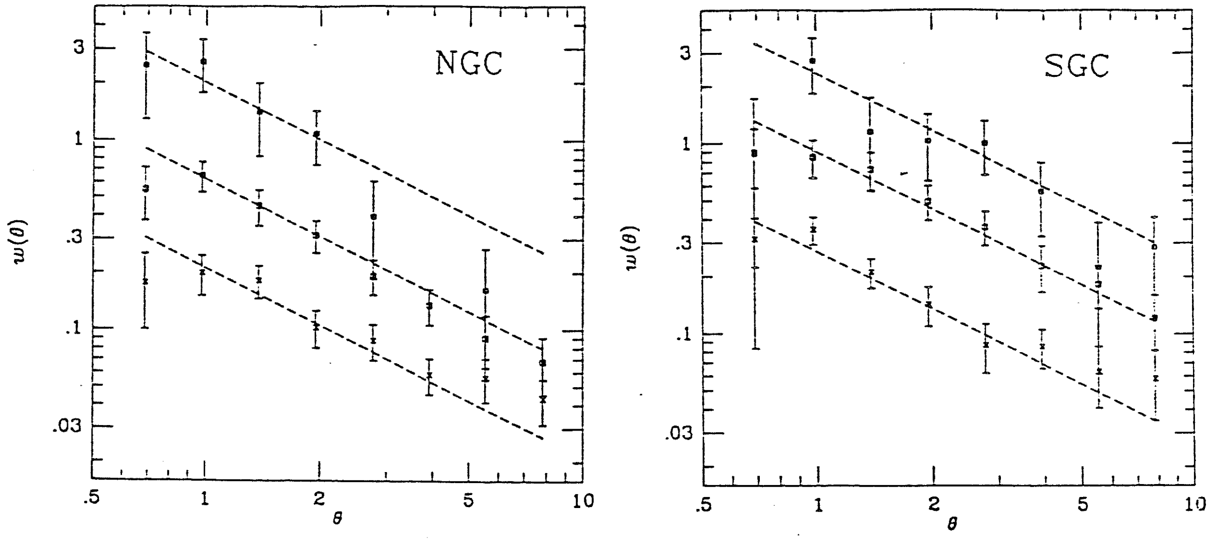

Figure 6.3: *The angular 2-point correlation functions for the NGC (left panel) and SGC (right panel) clusters. Filled squares, empty squares and crosses represent data for the C36, C25 and C18 samples, respectively. For visual clarity we do not plot our results for the C30 sample. Errorbars represent standard deviations as evaluated by the* bootstrap *method. Dashed lines represent the best-fit power laws with slope $\gamma = 2$ and amplitudes as given in Table 6.1.*

Table 6.1: *Cluster catalogues. Column 4 gives the best-fit values and relative 1σ errors for the amplitude of the angular correlation function, when $\gamma = 2$ is assumed. Column 5 & 6 give the mean values of the cluster richness, according to the two different definitions (see text) and their relative standard deviations.*

Data set		Number	A	$\langle R_1 \rangle$	$\langle R_2 \rangle$
C36	North	381	2.00 ± 0.50	5.8 ± 0.7	6.6 ± 2.0
	South	175	2.33 ± 0.75	5.9 ± 0.7	6.6 ± 2.0
C30	North	826	1.07 ± 0.09	4.7 ± 0.6	5.4 ± 1.7
	South	350	1.36 ± 0.31	4.7 ± 0.6	5.5 ± 1.8
C25	North	1531	0.62 ± 0.04	3.9 ± 0.5	4.5 ± 1.5
	South	676	0.90 ± 0.14	4.0 ± 0.5	4.5 ± 1.5
C18	North	3679	0.21 ± 0.02	2.8 ± 0.4	3.3 ± 1.3
	South	1619	0.27 ± 0.03	2.8 ± 0.4	3.3 ± 1.3

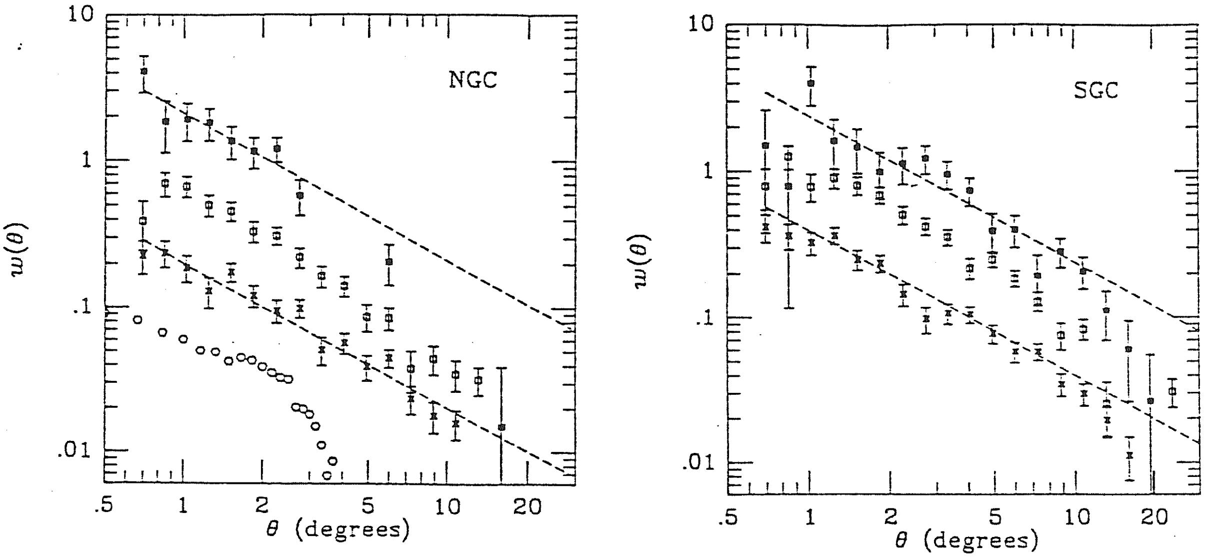

Figure 6.4: *The same plot of Figure 6.3, but with errorbars evaluated with the quasi-Poissonian estimator of eq.(6.5). The reduced errorbars permits to extend the range of angular separations where we evaluate $w(\vartheta)$. In the upper panel, also plotted is the 2-point angular correlation function for galaxies. As in Figure 6.3, we do not plot data for the C30 sample.*

C30 we merge together northern and southern samples, while separate analyses are realized for C25 and C18. We apply both the moment method, already introduced for the analysis of N-body simulations, and the direct counting method, which is based on the computation of the number of triangles of a given shape and size. This kind of comparison between different methods allows us to assess their robustness when a limited number of data is available.

The moment method

We define for the object distribution the moment of order k for the counts in angular rings, of radius ϑ, as

$$\langle N^k \rangle_\vartheta \;=\; \sum_N N^k(\vartheta)\, P_N(\vartheta)\,. \qquad (6.6)$$

Here $P_N(\vartheta)$ represents the probability of finding N objects at angular separation between $\vartheta - \Delta\vartheta/2$ and $\vartheta + \Delta\vartheta/2$ from a given cluster. Note that the determination of this quantity is of key importance since it specifies completely the clustering properties of the system through the moments of all orders. Figure 6.5 shows $P_N(\vartheta)$ for our cluster samples, at three different angular scales. At large scales, where the distribution is expected to be roughly homogeneous, $P_N(\vartheta)$ is well approximated by a broad distribution with Gaussian shape. Some skewness appears as the scale decrease and the clustering increases. At even smaller scales discreteness effects causes most clusters to have only one neighbor, and the resulting $P_N(\vartheta)$ is strongly peaked at the corresponding (small) N values. In this case, Poisson shot-noise dominates the

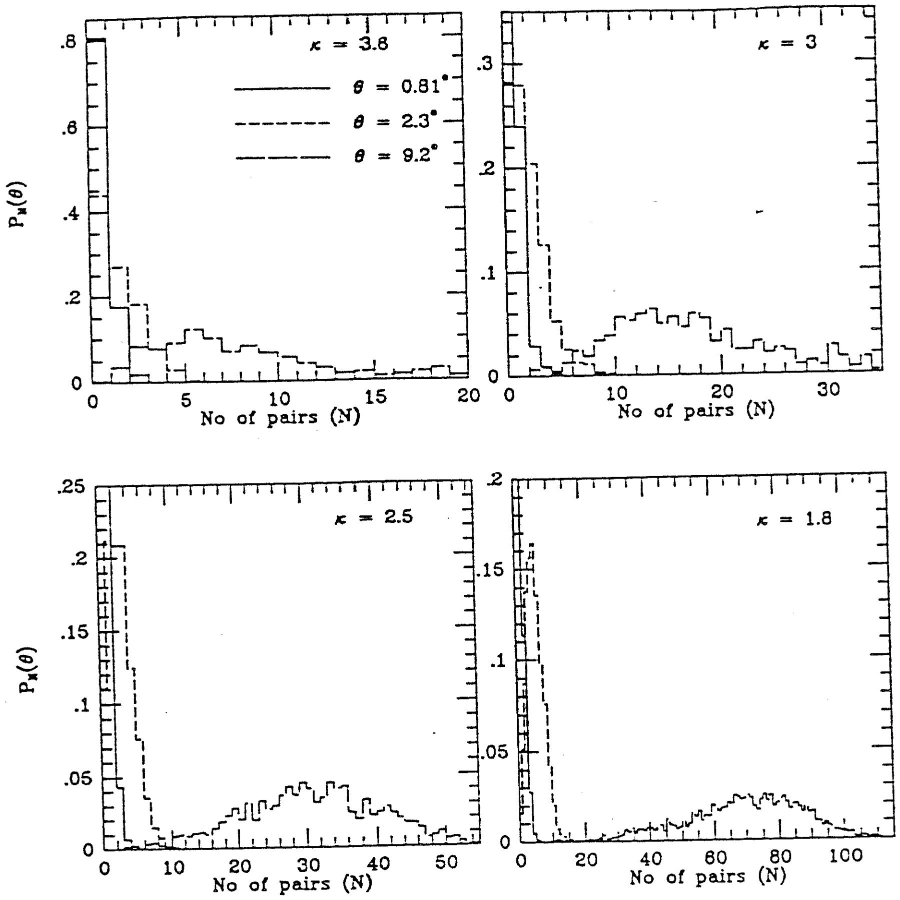

Figure 6.5: *The frequency distribution $P_N(\vartheta)$ of the number of clusters inside circular anuli of radius ϑ, for our cluster samples. In each panel, solid, short-dashed and long-dashed histograms refer to different values of the angular separation.*

statistics.

The k-th order moment of neighbor counts is related to the $(k+1)$-point correlation function according to

$$\begin{aligned} \langle N^k \rangle_\vartheta &= (\text{discreteness terms of order } m < k) + \\ &+ \; n^k \int_{\Omega_1} d\Omega_1 \dots \int_{\Omega_k} d\Omega_k [1 + w^{(k+1)}_{dis,01\dots k}] \end{aligned} \qquad (6.7)$$

(see, *e.g.*, ref.[287, 353]). Here, the quantity $w^{(k)}_{dis,01\dots k}$ represents the *disconnected* correlation function between $k+1$ points, while n is the mean density of objects in the sample. In eq. (6.7) all the integration domains are angular rings of radius ϑ and constant relative width Δ.

If the 2-point function, $w(\vartheta)$, is modeled as a simple power-law, then eq.(6.7) gives back eq.(6.3). In the case of the 3-point correlation, eq. (6.7) gives

$$\begin{aligned}\langle N^2 \rangle_\vartheta &= \langle N \rangle_\vartheta + n^2 \int_0^{2\pi} d\varphi_1 \int_0^{2\pi} d\varphi_2 \int_{(1-\Delta/2)\vartheta}^{(1+\Delta/2)\vartheta} d\vartheta_{01} \sin\vartheta_{01} \int_{(1-\Delta/2)\vartheta}^{(1+\Delta/2)\vartheta} d\vartheta_{02} \sin\vartheta_{02} \times \\ &\times \; [1 + w_{01} + w_{02} + w_{12} + z_{012}] \, . \end{aligned} \tag{6.8}$$

In this expression z_{012} is the *connected* 3-point correlation function, which in the following is assumed to have the *hierarchical* form

$$z_{012} \; = \; Q \left[w_{01}w_{02} + w_{01}w_{12} + w_{02}w_{12} \right] . \tag{6.9}$$

Notice that assuming the simple power-law expression, $w(\vartheta) = B\vartheta^{1-\gamma}$ causes some integrals in eq.(6.8) to diverge for $\gamma = 2$, value which is always very near to what we obtain. Such a divergence is essentially due to the unphysical divergence of the 2-point function when $\vartheta \to 0$. However, due to the finite size of the objects and mainly due to the smoothing over the 30 *arcmin* angular scale in the Lick map (see ref.[300]), we expect that a small-scale cutoff should be superimposed in the background field and, consequently, $w(\vartheta)$ should flatten at small separations. For this reason, it is appropriate to introduce the *smoothed* correlation function

$$w(\vartheta) \; = \; B(\vartheta^q + \vartheta_c^q)^{(1-\gamma)/q} , \tag{6.10}$$

where the parameter q specifies the smoothing model, while we take $\vartheta_c = 30$ *arcmin* for the smoothing scale. Let us observe that, as far as the 2-point function analysis is concerned, we always have $\vartheta \gg \vartheta_c$ for the separations we are dealing with, and, consequently, the pure power-law expression of $w(\vartheta)$ holds.

According to eqs.(6.8) and (6.9), we estimate the Q parameter over the whole considered range of angular separations by following a χ^2 minimization procedure. Accordingly, we define the quantity

$$\chi^2 \; = \; \sum_{i=1}^{N_{bin}} \left\{ \frac{\langle N^2 \rangle_\vartheta - \langle N \rangle_\vartheta - \bar{N}_\vartheta^2 \left[1 + (2 + K_\vartheta)\, w(\vartheta) + Q\,(1 + 2K_\vartheta)\, w^2(\vartheta) \right]}{\sigma} \right\}^2 , \tag{6.11}$$

where the sum extends over the N_{bin} angular bins. In the above expression we weight each bin by means of the error model

$$\sigma^2 \; = \; \sigma^2_{\langle N^2 - N \rangle} + \bar{N}^4 (2 + K_\vartheta)^2 \sigma_w^2 \, . \tag{6.12}$$

Since the quantities $\langle N^2 \rangle$ and $\langle N \rangle$ are not independent, we prefer to estimate from the bootstrap resamplings the quantity $\sigma^2_{\langle N^2 - N \rangle}$ instead of the variances of the second- and first-order moments. The errors in the 2-point function, σ_w^2, are estimated from the uncertainties in the amplitude B, once $\gamma = 2$ is assumed. Since the first-order moment for the random distribution is estimated after averaging over 20 realization, no significant uncertainties are associated to $\bar{N}$.

In eqs. (6.11) and (6.12) we introduced the quantity

$$K_\vartheta = (2\pi\Delta)^{-1} \int_0^{2\pi} d\varphi \int_{1-\Delta/2}^{1+\Delta/2} dy\, y \left\{[2y^2(1-\cos\varphi)]^{q/2} + (\vartheta_c/\vartheta)^q\right\}^{\frac{1-\gamma}{q}} , \qquad (6.13)$$

that turns out to be independent of ϑ only in the limit $\vartheta_c \to 0$. In this analysis we consider angular separations in the range $0.6^\circ \leq \vartheta \leq 9^\circ$. Moreover, the ϑ values are collected in 8 bins, that have the same relative amplitude $\Delta = 0.34$. In Figure 6.6 we show the dependence of K_ϑ on the angular separation in correspondence of different choices for smoothing scale ϑ_c, smoothing parameter q and 2-point function slope γ. It is apparent that, for variations of these parameters inside reasonable ranges, no drastic variations of K_ϑ are found. Moreover, due to the way in which K_ϑ appears in eq.(6.13) we also verify that such small variations leave the determination of Q essentially unaffected.

The results of this analysis are shown in Figure 6.7, where the first- and the second-order moments are plotted, and in Table 6.2, where we report the values of the hierarchical coefficient Q for all the considered cluster samples, together with the $1\,\sigma$ bootstrap errors coming from the χ^2 minimization. Note also the very small values of the minimum χ^2 that we get from eq.(6.11). This is essentially due to the large uncertainties in the determination of Q, that does not allow to put any strong constraint on the reliability of the hierarchical model. It is worth observing that, despite the fact that the signal for the moments is always detected well above the noise with remarkable power-law shapes (see Figure 6.7), very large uncertainties appear when we attempt to extract from such moments the *connected* part of the 3-point function. By comparing the results we get for different cluster samples, a marginal trend appears for the Q parameter to take smaller values as the threshold level decreases.

The direct counting method

Instead of counting the number of clusters inside spherical shells, this method is based on counting the number of triplets that define triangles with given shape and size. In order to better determine the dependence of the 3-point function on the angular separation, let us introduce the new variables $\vartheta = \vartheta_1$, $u = \vartheta_2/\vartheta_1$, $v = (\vartheta_3 - \vartheta_2)/\vartheta_1$, where $\vartheta_1 < \vartheta_2 < \vartheta_3$ are the triangle side lengths [173]. We collect ϑ and u values in bins with the same logarithmic amplitude, so that for each of them $\Delta\vartheta/\vartheta = \Delta u/u = 0.23$. On the other hand, v values are collected in linear bins of amplitude $\Delta v = 0.2$. The values for the variables u and v range in the intervals $1 \leq u \leq 10$ and $0 < v \leq 1$. As far as the ϑ variable is concerned, we consider the angular range $0\overset{\circ}{.}63 \leq \vartheta \leq 5\overset{\circ}{.}0$ for all the samples, with the exception of that with $\kappa = 3.6$. Indeed, for the northern C36 catalogue we take $\vartheta \leq 2.5^\circ$, occurring for larger separations the break in the power-law shape of $w(\vartheta)$. For the southern C36 sample we choose $0\overset{\circ}{.}79 \leq \vartheta \leq 6\overset{\circ}{.}3$, due to the relative small number of clusters. Since the computational cost increases rapidly with ϑ_3 ($\propto \vartheta_3^4$) and since the signals of z_{012} would vanish within the statistical noise for large triangles, we always limit our analysis to triangles with their longest

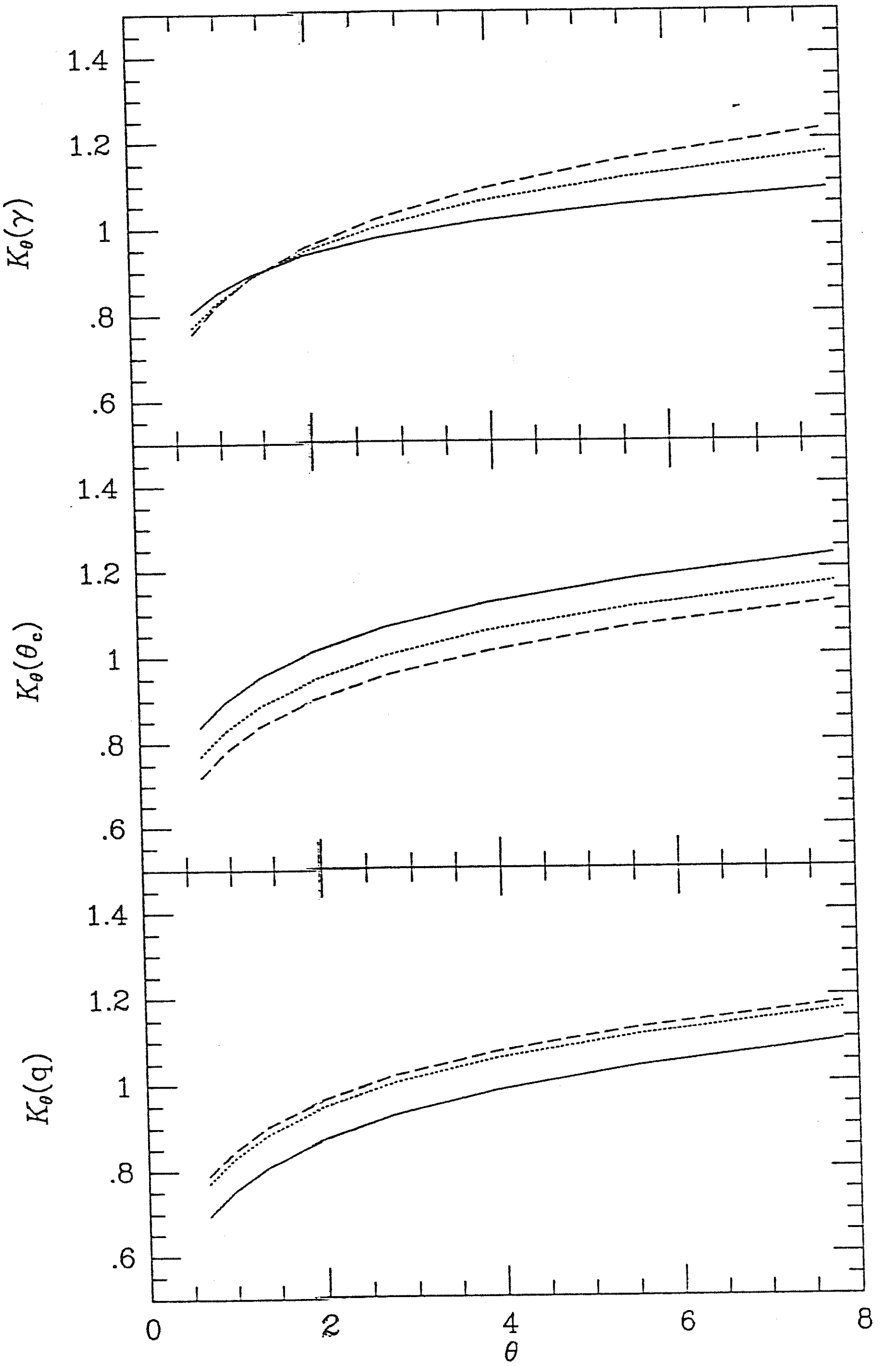

Figure 6.6: *The integral K_ϑ is plotted versus the angular scale ϑ for different choices of 2-point function slope γ, cutoff angular scale ϑ_c and smoothing parameter q (see text). Upper panel: $\vartheta_c = 30'$, $q = 2$, $\gamma = 1.8$ (solid line), $\gamma = 2$ (dotted line) and $\gamma = 2.1$ (dashed line). Central panel: $\gamma = 2$, $q = 2$, $\vartheta = 20'$ (solid line), $\vartheta = 30'$ (dotted line) and $\vartheta = 40$ (dashed line). Lower panel: $\vartheta_c = 30'$, $\gamma = 2$, $q = 1$ (solid line), $q = 2$ (dotted line) and $q = 3$ (dashed line).*

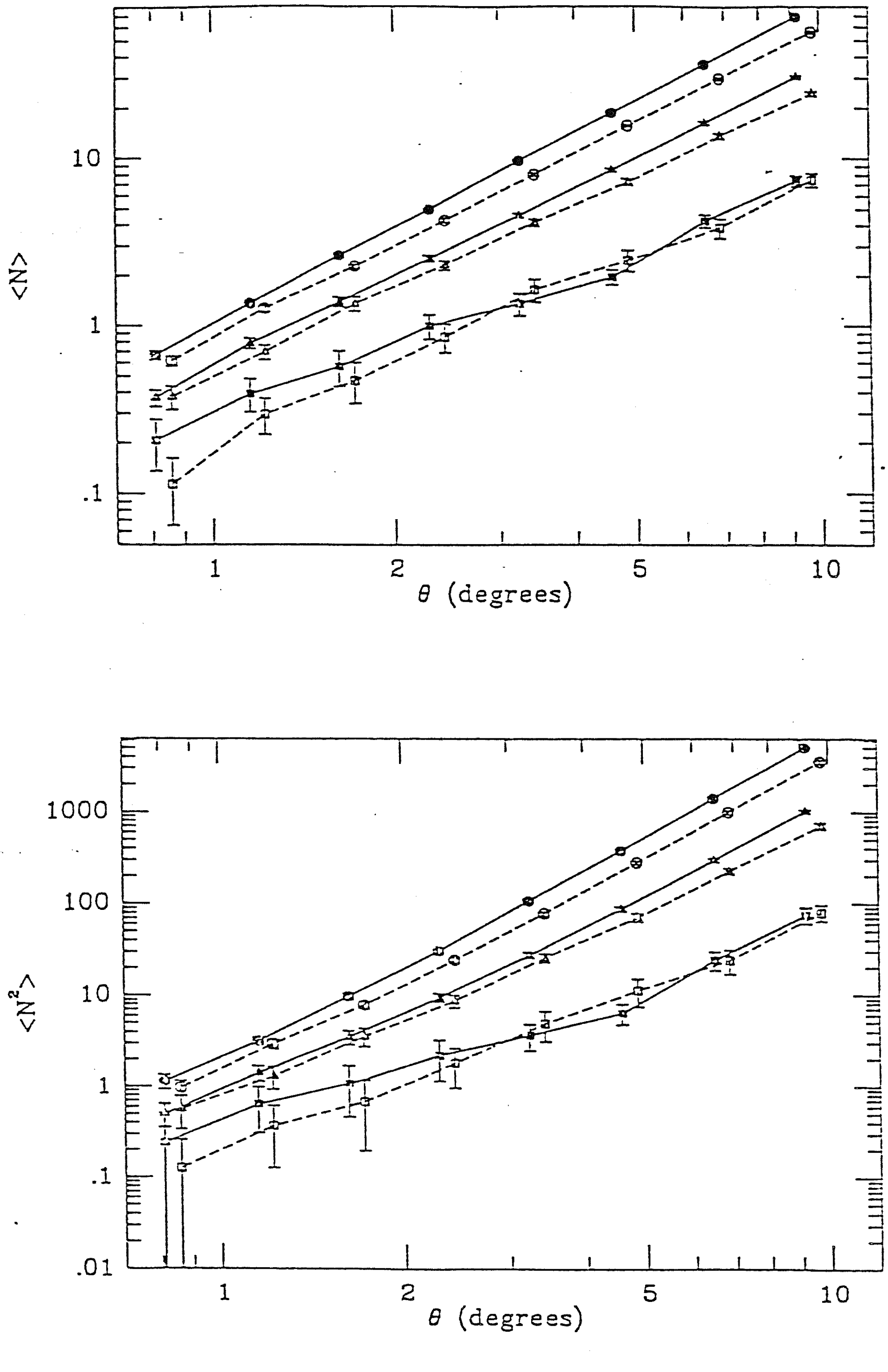

Figure 6.7: *The first- (upper panel) and the second-order moments (lower panel) are plotted as a function of the angular scale for C36 (squares), C25 (triangles) and C18 (circles) samples. Data for C30 are not plotted for sake of clarity. Filled symbols correspond to data taken from northern samples, while open symbols are for the southern ones.*

sides less than the maximum allowed value for the ϑ variable.

Let D_{ijk} be the counts of triplets in the real cluster sample and R_{ijk} the corresponding count in a random sample with mean surface density λ times that of the real sample (here i, j, k are the bin indices for the ϑ, u, v variables, respectively). Then, the 3-point function, z_{ijk}, is related to the triplet counting according to

$$z_{ijk} \;=\; \lambda^3 \frac{D_{ijk}}{R_{ijk}} - (1 + W_{ijk})\,. \tag{6.14}$$

In the above equation, the correlation functions $w(\vartheta)$ enters through the quantity

$$W_{ijk} \;=\; w_{ij} + w_{ik} + w_{jk}\,. \tag{6.15}$$

The details of our estimation are as follows. Instead of deducing R_{ijk} by averaging over many random realizations with the same number of points as the real sample, a random sample of 5000 points in North and of 4000 points in South are produced. The random sample has the same boundary and the same selection function as the observed one. We take the 2-point function and relative uncertainties as given in Table 6.1.

After counting the number D_{ijk} of triplets in the samples and assuming the hierarchical expression (6.9) to hold, we work out the values of the Q parameter by minimizing the quantity

$$\chi^2 \;=\; \sum_{ijk} \left\{ \frac{[D_{ijk} - R_{ijk}\lambda^{-3}(1 + W_{ijk})] - Q R_{ijk}\lambda^{-3}(w_{ij}w_{ik} + w_{ij}w_{jk} + w_{ik}w_{jk})}{\sigma} \right\}^2 . \tag{6.16}$$

In the above expression, σ represents the error estimates of $D_{ijk} - R_{ijk}\lambda^{-3}(1 + W_{ijk})$. Since we have used a large random sample and imposed the least-squared interpolation, the error in R_{ijk} is negligible. The error σ_D in D_{ijk} is obtained by the bootstrap method, while $\sigma_W = R_{ijk}\lambda^{-3}W_{ijk}\frac{\sigma_A}{A}$, being σ_A the error in the amplitude A of the 2-point function.

Simply assuming that these two errors are independent, we can construct the error model as

$$\sigma^2 \;=\; \sigma_D^2 + \sigma_w^2\,, \tag{6.17}$$

which is used in eq.(6.16).

The fitted values of Q for different samples are listed in Table 6.2 and shown in Figure 6.8. A comparison of these results with those obtained from the moment analysis clearly shows that, although the central values are roughly the same, the errors in Q are remarkably smaller. For both northern and southern hemispheres, a negative Q is detected for the samples of the lowest density contrast ($\kappa = 1.8$), while the trend of decreasing Q with decreasing κ is confirmed. Note also that for the lowest overdensity samples the Q parameter for the northern hemisphere is systematically lower than for the southern hemisphere. Indeed, since the southern galaxy density in the Lick map is less than the northern one [299], selecting

Table 6.2: *Values of the hierarchical coefficient Q. Column 3 (7) gives the number of bin used in the analysis of each sample. Column 4 (8) gives the best-fir value of Q. Column 5 (9) gives the fitting error for Q. Column 6 (10) gives the minimum χ^2 value for each degree of freedom.*

		Moment method				Direct counting			
Sample	N_{cl}	N_{bin}	Q	ΔQ	χ^2_{min}	N_{bin}	Q	ΔQ	χ^2_{min}
C36	460	8	0.50	0.53	0.05	104	0.85	0.08	89
C30	976	8	0.68	0.43	0.02	109	0.67	0.04	143
C25N	1159	8	−0.11	0.57	0.01	109	0.05	0.15	17.7
C25S	658	8	0.50	0.46	0.03	109	0.41	0.12	25.8
C18N	2685	8	−1.10	1.20	0.04	109	−0.84	0.18	18.4
C18S	1619	8	0.01	1.11	0.13	109	−0.43	0.18	30.4

peaks with a global threshold amounts to pick up relatively higher peaks in the south. Thus, the highest Q values in the south C18 and C25 samples reflect the increasing trend of Q with the increasing peak-height.

6.3.3 Discussion of the correlation analysis

The problem of explaining the clustering excess of clusters with respect to galaxies was the starting point that led Kaiser [213] to introduce the concept of *biassing* in the distribution of cosmic structures (see §4.4). According to this model, galaxy clusters are assumed to arise from those peaks of the underlying galaxy distribution, that exceed a fixed limiting threshold. Consequently they show an enhanced clustering strength, that turns out to depend on the height of the threshold imposed on the galaxy density field. In this framework, let us consider a generic density field $\sigma(x)$ (in the case we are dealing with, it corresponds to the two-dimensional galaxy surface-density field in the Lick map), and the fluctuations $\delta(x) = (\sigma(x) - \langle\sigma\rangle)/\langle\sigma\rangle$. If objects are identified with fluctuations above a critical value δ_c, then their distribution is described by the biassed density field

$$\rho_{\delta_c}(x) \;=\; \theta[\delta(x) - \delta_c]\,, \qquad (6.18)$$

where $\theta(y)$ is the Heaviside step-function (see also eq.[4.52]). It is important to stress that this procedure of picking up objects from a background field exactly coincides with our cluster-finding algorithm, once we take $\delta_c = \kappa - 1$. Objects that are characterized by higher δ_c values

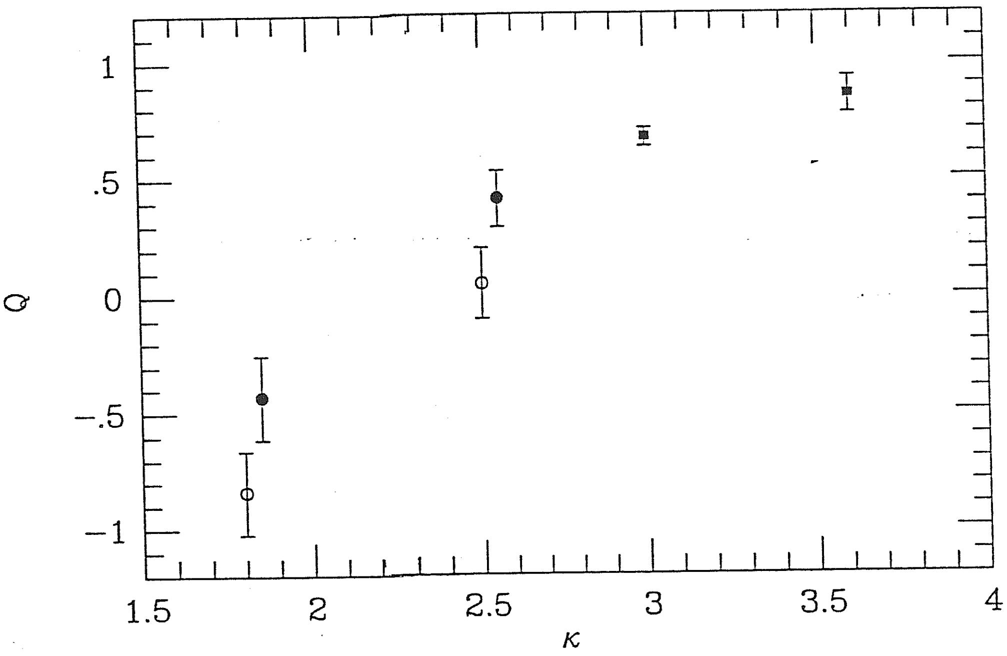

Figure 6.8: *The values of the hierarchical coefficient Q are plotted as function of the density threshold κ. For C18 and C25, the results for northern (filled circles) and southern (open circles) are separately plotted.*

turn out to be more clustered. In §4.4 we have shown that, under the assumption that the probability distribution function of $\delta(x)$ has a steeply decreasing tail, like a Gaussian, and for sufficiently high threshold values, the 2-point correlation functions for classes of objects corresponding to different choices of δ_c are proportional to each other, according to

$$w_{\delta_{c1}}(\vartheta) = \left(\frac{\delta_{c1}}{\delta_{c2}}\right)^2 w_{\delta_{c2}}(\vartheta) \qquad (6.19)$$

(see also eq.[4.56]). We find that our data nicely fit the dependence of the correlation amplitude on the threshold δ_c, implied by eq.(6.19) (see Figure 6.9). In our opinion, this interesting result confirms that the *biassing* prescription, used to identify galaxy systems, is a reliable method to relate the clustering properties of different hierarchy objects, from single galaxies up to rich clusters.

The existence of such a well defined correlation between the height of the threshold and the subsequent correlation amplitude can also be seen as an indication of an existing underlying connection between clustering and richness of galaxy systems. In their analysis of the spatial correlation function of Abell clusters, Bahcall & Soneira [18] found a well defined relation between the amplitude of the 2-point function and the Abell richness class R. Bahcall & Burgett [17] extended this analysis and observed that single galaxies, considered as systems with $R = 1$, as well as superclusters satisfy the same relation (see Figure 2.4).

For our two-dimensional samples, we define the cluster 'richness' in two possible ways:

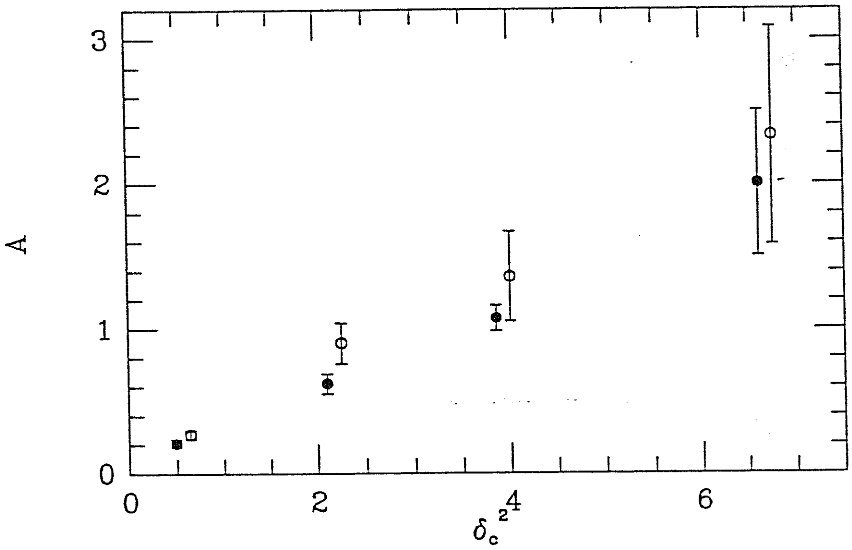

Figure 6.9: *The relation between the threshold amplitude, δ_c, imposed on the Lick galaxy field to identify clusters, and the cluster correlation amplitude A. Open and full symbols refer to SGC and NGC clusters, respectively. Errorbars of A are 1σ uncertainties from the best fit of $w(\vartheta)$ (see Table 1). An artificial small shift of the δ_c values for the SGC clusters has been imposed for clarity reasons. A comparison of the plot with eq. (6.19) shows an excellent agreement of our data with the predictions of the* biassed *models for the distribution of cosmic structures.*

(a) as the average number, over the region occupied by the cluster, of *smoothed* cluster-galaxies per 10×10 $arcmin^2$ cell [$\equiv R_1$] and (b) as the number of *smoothed* galaxies contained inside the highest density pixel of each cluster [$\equiv R_2$]. Note that our definitions of cluster richness are different from that of Abell but we are constrained to such a choice due to the nature of the Lick galaxy catalogue (galaxy counts in cells instead of galaxy positions and magnitudes). A serious problem with our definition of the individual cluster-richness is that it is distance dependent. However, we are not interested in the individual cluster-richness but in the average richness over all clusters within a specific catalogue and, unless the different catalogues trace different depths, the mean cluster-sample richness should have the same relation to the intrinsic cluster richness in all four cluster samples.

Based on our definition of cluster richness, we search for a correlation between richness and correlation amplitude. Indeed, defining a characteristic clustering angle ϑ_o, as the separation at which the 2-point function takes the value unity, we find that the relation

$$\vartheta_o \propto R^{\alpha} \tag{6.20}$$

is satisfied (correlation coefficient > 0.98) with $\alpha \simeq 2.43 \pm 0.17$ for the R_1 richness and $\alpha \simeq 2.24 \pm 0.22$ for the R_2 richness; both values consistent within the 1σ errors (see Figure 2.4). This result closely resembles that found by Bahcall & Burgett [17] about the clustering-richness dependence for Abell clusters (see Figure 2.3). However, the difference between our definitions of richness and that of Abell makes difficult a close comparison.

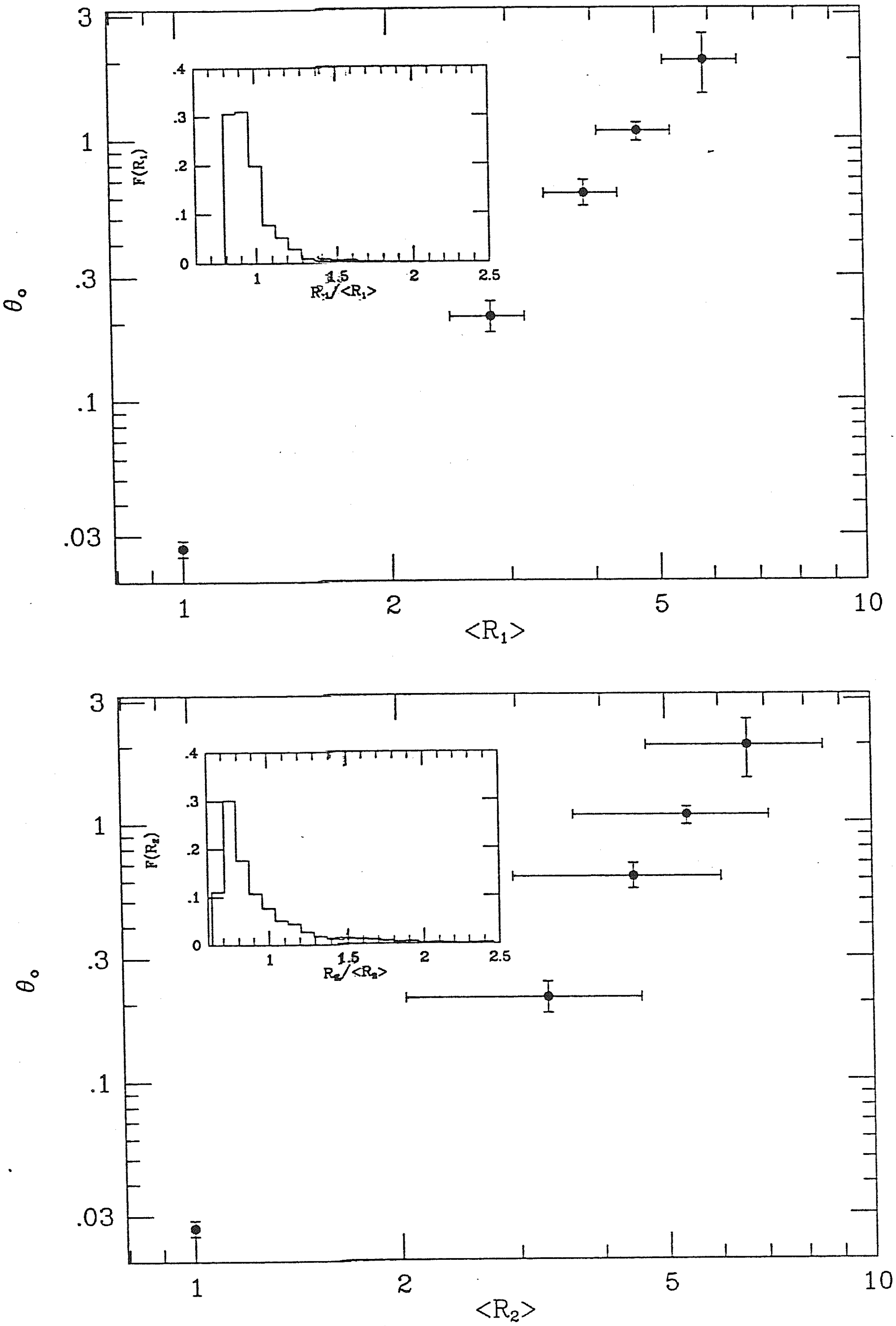

Figure 6.10: *The relation between the clustering length, ϑ_o, and the average richness, $\langle R_i \rangle$, of each northern cluster sample (see text for the two definition of richness). Errorbars of ϑ_o are $1\,\sigma$ uncertainties from the best fit of $w(\vartheta)$, and errorbars for R_i are evaluated as the standard deviations around the mean sample richness. Inside each panel, we show also the richness frequency distribution for the C36 sample.*

Let us notice, however, that the existence of a correlation between cluster richness and correlation amplitude could be due to a depth-dependent effect. Due to the fact that at lower overdensity levels more distant clusters could be selected by our cluster-finding algorithm, the corresponding correlation amplitude will be reduced at the same angular scale due to the scaling relation

$$w_s(\vartheta) = \frac{D_d}{D_s}\; w_d\left(\frac{D_s}{D_d}\vartheta\right) , \tag{6.21}$$

where D_s and D_d are the characteristic depths of the shallower and of the deeper cluster sample respectively. Fitting eq.(6.21) under the assumption of a distance dependent effect and from the fact that the median depth of C36 catalogue is $\sim 180h^{-1}$ Mpc [340], we find that the corresponding median depths of the C25 and C18 samples should be $\sim 325h^{-1}$ Mpc and $\sim 555h^{-1}$ Mpc (notice that the characteristic depth of the Lick map is only $\sim 210h^{-1}$ Mpc [173]). Although there is some evidence for a depth dependent trend for the Abell clusters found in the Lick map [300], it is of quite smaller amplitude. Furthermore this possibility seems unlikely to be the dominant one for a number of other reasons as well. First of all, for lower values of κ we would expect the break of the correlations to occur at smaller ϑ's and not at the same angular separation as that of the C36 catalogue. Secondly, as can be seen in Figure 6.10, we verify that eq.(6.20) holds with good accuracy also for single galaxies, while this feature should not be expected *a priori* if the clustering-richness dependence was entirely due to selection effects in cluster detection. Thus, it seems that the intrinsic $w(\vartheta)$-richness dependance effect, which is well established for the Abell clusters [18, 307] represents the correct explanation, although a depth-dependent effect could also contribute towards the same direction. On the other hand, if eq.(6.19) should represent the correct explanation for the clustering-richness correlation, then it indicates that the underlying galaxy-density field is consistent with a Gaussian random field at least at angular scales larger than the corresponding characteristic correlation length ($\gtrsim 1^\circ\!.2$ for the Lick galaxies; see ref.[173]). This finding is also supported by a recent study of the 2-D topology of the Lick galaxy catalogue [86], which shows that no departures from a sponge-like topology are observed at the scale probed by our correlation analysis. However, a safe detection of any departure from Gaussianity should be directly done by searching for higher-order correlation functions, which are the unique imprint of non-Gaussianity.

The problem of estimating the 3-point correlation function of galaxy clusters has been recently addressed by several authors, both considering angular samples [211, 366], three-dimensional samples [209] and numerical simulations [161]. All these analyses converge to indicate that the hierarchical model of eq.(6.9) is consistent with data. However, even though similar values of Q are worked out from such analyses, remarkably different estimates of the relative uncertainties were given, according to the different method used for the correlation and error analysis.

We decided to apply both the moment method and the direct counting technique to our angular cluster samples in order to check the consistency between such two approaches, especially in the cases where only a rather small number of objects is available. In doing such an analysis, we accounted for resampling uncertainties by means of the bootstrap technique [236]. The accuracy of the *bootstrap* method to account for sampling uncertainties has been recently pointed out by Mo, Jing & Börner [263]. Based on the correlation analysis of simulated cluster distributions, they found that using bootstrap errors compensate the underestimation of uncertainties occurring when a χ^2 minimization procedure is used to work out the Q parameter. Thus, we are confident that the errors derived from the method outlined in the previous Section represent a reliable estimation of the "true" uncertainties.

Using the moment method we obtain that, despite the observed good signal for the first- and second-order moments, the extraction from them of the *connected* part of the 3-point function, z_{012}, is a very noisy procedure. We apply a χ^2-minimization procedure to find a "best-fit" value of the coefficient Q in each sample. The resulting large errorbars we get in all cases unable us to give any significant constraint on the validity of the hierarchical model. We note however that, despite the presence of such errorbars, some marginal trend exists for the Q value to increase with the threshold κ for the cluster identification (see Table 6.2).

The situation is rather different when we apply the direct counting method. In this case the Q values are deduced by means of a χ^2 minimization over all the bins where we collect the triplets configurations. The central values of Q that we get are very similar to those obtained from the moment analysis, thus confirming the consistency of the two methods, but with much smaller errorbars. One reason for the reduced uncertainties could be the much greater number of bins ($\sim 10^2$), which therefore provides a better statistic with respect to the small number of angular bins in the moment method. Despite the remarkable noise reduction with respect to the moment method, it is interesting to observe that, even in the case of the triplet counting approach, the statistical uncertainties in our estimate of Q are systematically larger than those of other authors, which used cluster samples having size comparable to ours. In our opinion, this is mainly due to the different way in which sampling errors are estimated and shows how misleading it can be to use Poissonian errors instead of a rigorous procedure such as the bootstrap resampling method.

As shown in Figure 6.8, the improved statistics coming from the triplet counting approach enable us to strengthen our conclusions about the increasing trend of Q with the density threshold used to identify the clusters. This finding agrees with the expectation, based on the *biassing* prescription, that threshold effects introduce non-Gaussianity and consequently increase the higher-order correlations. However, a more quantitative comparison with the predictions of *biassing* is quite difficult. In fact, such a model predicts that in the linear regime the high peak distribution is characterized by the Kirkwood expression for the 3-point function

$$z_{012} = Q\,[w_{01}w_{02} + w_{01}w_{12} + w_{02}w_{12} + w_{01}w_{12}w_{02}] \qquad (6.22)$$

with $Q = 1$ in the case of a Gaussian background distribution (see eq.[4.57]) and with more complicated expressions for Q in the non-Gaussian case [251] and for more general biassing prescription [52]. However, in the linear regime ($w(\vartheta) < 1$), where eq. (6.22) is expected to hold, the cubic term becomes negligible so that it is hard to assess any difference with respect to the hierarchical model (6.9). Instead, at small scales non-linear clustering is expected to give rise to hierarchical expressions for the N-point correlation functions [145, 183].

Based on the above results, we believe that the analysis of the connected N-point functions surely represents a significant test for the global texture of the large scale structure. However, in some cases, as for the moment method, it gives very noisy results. In fact, as shown in Figure 6.7, a quite good signal exists for for the first- and second-order moment of the shell population, although the connected 3-point function is hard to detect above the noise. Moreover, the moments $\langle N \rangle$ and $\langle N^2 \rangle$ have remarkable power-law shapes, thus indicating the presence of scaling properties of the cluster distribution. In this framework, methods based on the multifractal analysis seem to be particularly suitable to test the scale-invariant nature of the clustering and, when applied to cluster samples, could give a deeper insight on the scaling properties of the cluster distribution and on their dependence on the cluster richness.

6.4 The multifractal analysis

In this Section we present a detailed multifractal analysis of suitable angular samples of galaxy clusters, that are identified as peaks of the galaxy density field in the Lick map. For sake of completeness, we also analyse the whole projected galaxy distribution. The adopted cluster identification algorithm allows us to check the existence of a possible relation between peak height and scaling properties. However, it is clear that using angular samples we should understand the effects of projection in order to correctly infer the scaling properties of the three-dimensional distribution. To this purpose, we have generated a three-dimensional multifractal structure with *a priori* known spectrum of generalized dimensions. Then, after assigning to each point a given luminosity according to a reasonable shape of the luminosity function, we projected this structure onto a sphere and generated two synthetic angular samples having different depths.

For a detailed definition of fractal concepts and for a description of methods of analysis we refer to Chapter 3. The only difference with respect to the fractal analyses previously presented is that all the introduced algorithms are now applied for distributions projected on a sphere. We briefly mention the applied methods and the strategy of analysis. After that, a comprehensive description of the main results is presented.

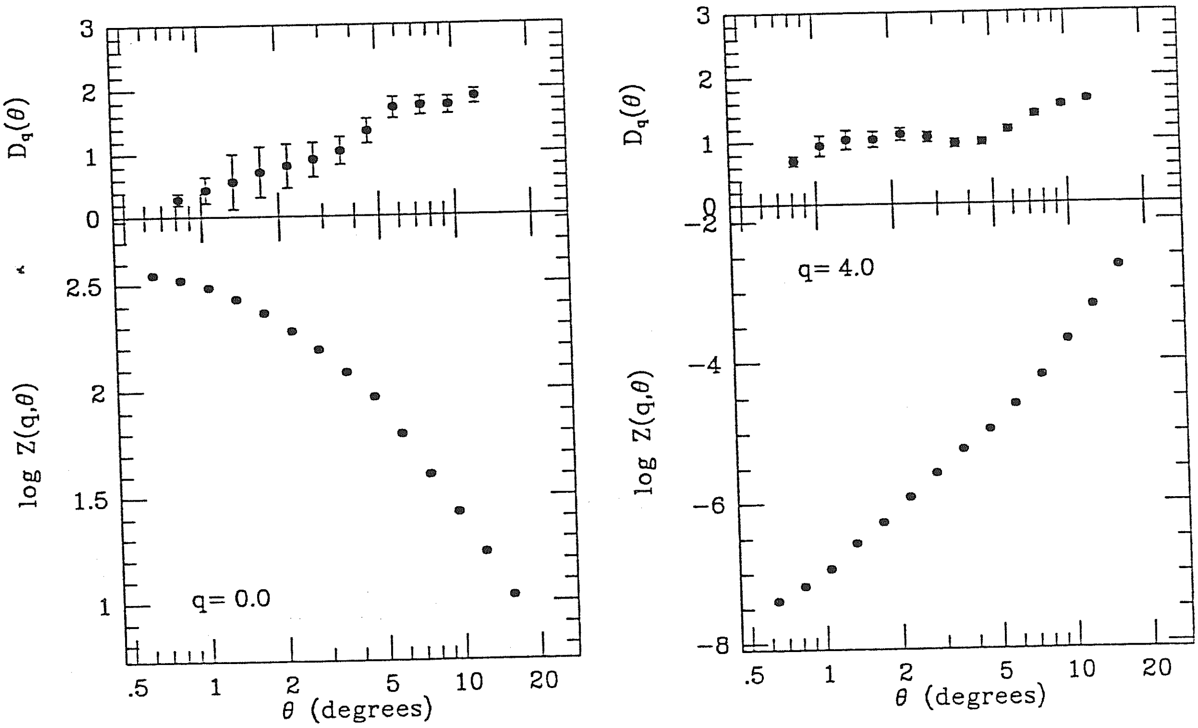

Figure 6.11: *The correlation-integral partition function* $Z^C(q,\vartheta)$ *for the C36 sample is plotted as a function of the angular scale for* $q = 0$ *(left panel) and* $q = 4$ *(right panel). Also plotted are the respective local dimensions,* $D_q(\vartheta)$*, that are obtained by a five points log-log linear regression on the partition function values. The scale ranges where such a local dimension takes a roughly constant value is the signature of scale-invariance at those scales. The errorbars in* $D_q(\vartheta)$ *corresponds to* 1σ *uncertainties in the local linear regression.*

6.4.1 The methods

The multifractal dimension estimator that we will apply for the analysis of cluster samples are the correlation integral (CI), the density reconstruction (DR) and the minimal spanning tree (MST) methods. Although the nearest-neighbor (NN) method has also been applied, the results it gives are not very reliable and heavily suffer for the limited statistics (see Chapter 3). Thus, the analysis based on this algorithm will be not discussed. In addition, we will also analyze the complete distribution of Lick galaxies, which is described by count in $10' \times 10'$ cells, so that the natural method to be employed is the box-counting (BC) algorithm. See §3.3 for a description of the advantages and limitations of these methods. We remind that the BC and CI methods, based on the evaluation of moments for cell counts and neighbor counts, respectively, are well suited for positive-order dimensions, while they suffer for discreteness effects when underdense regions are weighted in the computation of negative-order dimensions. Other methods have been introduced, which are less affected by such discreteness effects, like the DR and the MST methods. Differently from the BC and CI methods, which fixes the angular scale through the cell size or the neighbor limiting distance, the others display scale-mixing. To overcome these problems, for each value of the probability p in the estimate of the DR partition function (see eq.3.25), we evaluate the frequency distribution for the radii $\vartheta_i(p)$ $(i = 1, \ldots, N)$ of the disks containing $n = p/N$ objects. Then, the ϑ value that we associate to a given probability measure is that corresponding to the peak of the frequency distribution. In a similar fashion, for the MST method, we evaluate for each randomly selected subsample containing m objects the corresponding frequency distribution of edge lengths λ_i $(i = 1, ..., m)$. The ϑ value corresponding to each m is, therefore, individualized by the peak of the edge-length distribution.

6.4.2 Results of fractal analysis

Due to the variety of employed methods and of analyzed samples, a lot of statistical informations is obtained about the angular cluster distribution. We present the results of the fractal analysis of both cluster samples and entire Lick galaxy distribution. In order to account for the effects of considering angular samples instead of the spatial distribution of cosmic structures, we also generate a 3-dimensional fractal structure with an *a priori* known multifractal spectrum and then check the effects of projection on the sky and of luminosity selection, by generating synthetic angular samples, which correspond to two different values of the limiting apparent magnitude. This allows us to check to which extent a possible detection of scale invariance in a limited angular scaling range reflects the presence of a characteristic scale even in the spatial distribution or it is just an effect of projection.

The C36 sample

Because of the rather limited number of identified C36 clusters, particular attention must be payed to disentangle the effects of poor statistics from the real features of the clustering.

For the CI method, we plot in Figure 6.11 the corresponding partition function, as defined by eq.(3.23). The disk radii range from $\vartheta = 0\overset{\circ}{.}5$ up to $\vartheta = 20^{\circ}$. Figure 6.11*a* refers to the multifractal order $q = 0$ (corresponding to the estimate of the Hausdorff dimension), while Figure 6.11*b* is for $q = 4$. We also plot in the upper panels the local dimension $D_q(\vartheta)$, obtained by realizing a 5 point local linear regression on the partition function. The plotted error bars refer to the 1σ uncertainty in the local fit. The use of such a local dimension is particularly useful to detect scaling in the cluster distribution and the scale range where it develops. It is remarkable to note that in the case $q = 0$ the local dimension exhibits an increasing trend going from $D_o \simeq 0$ at small scales to a value $D_o \simeq 2$ at angular scales $\vartheta \gtrsim 6^{\circ}$. While the constant value $D_o \simeq 2$ indicates that the cluster distribution in the angular sample appears to be homogeneous at large ϑ values, the small number of available objects causes discreteness effects to appear at small scales. Indeed, for small radii many disks contain only one object and this number does not sensibly increase until a sufficiently large ϑ value is allowed. As a consequence, the partition function values changes only very slowly and the corresponding slope is quite small. In a sense, we can say that, due to the low number density of clusters, at such small scales we are measuring nothing but the dimension of each single point, that is indeed zero. Thus, we expect that such an effect will become more and more pronounced in the underdense regions that are mostly weighted for $q \lesssim 0$. On the contrary, the discreteness should disappear when larger q values are considered. In fact, in this case the CI partition function weights only the very clustered regions, where even the smallest disks have non negligible probability to contain more than one object. This is clearly shown in Figure 6.11*b*, where the local dimension value remarkably detaches from zero already at small angular scale. In this case, a range of ϑ values appears, over which the local dimension takes a nearly constant value $D_q \simeq 1$ (apart from small fluctuations due to the noise in the evaluation of the local slope), up to $\vartheta \sim 6^{\circ}$. Again, at larger scales the dimension approaches the value $D_4 \simeq 2$, thus indicating that also the distribution of the objects in the overdense regions turns out to be homogeneous at such scales. The appearance of a scale range where the local dimension is quite flat indicates that at such scales the cluster distribution has well defined fractal properties. This finding is even more remarkable if we observe that the scaling regime breaks at an angular scale that, at the depth of the Lick map, corresponds to a physical scale of about 20 h^{-1} Mpc, thus quite similar to the scale of transition between linear and non-linear clustering for the cluster distribution. However, this result could be spurious since the break of the scale-invariance could also be due to some systematic effects related, for example, to angular projection of the three-dimensional structure [87]. In the following we will describe the effects of projection and luminosity selection on a three-dimensional scale-invariant fractal structure with *a priori* known fractal properties and we will show that

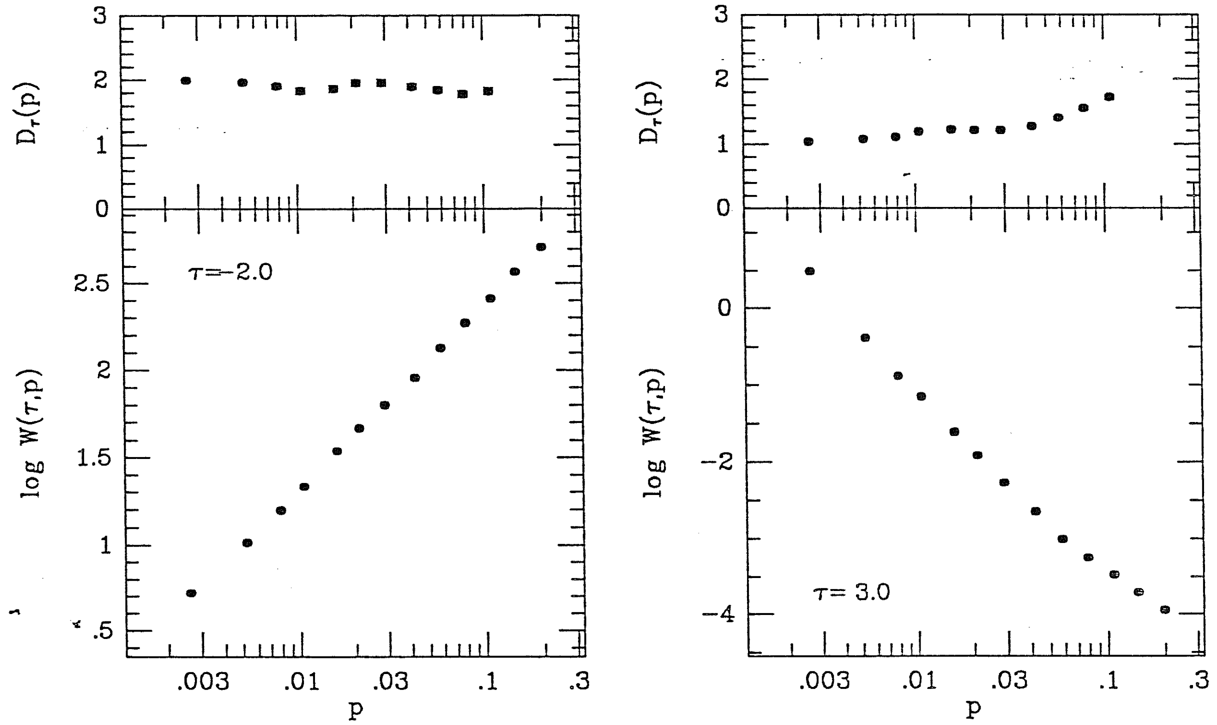

Figure 6.12: *The density-reconstruction partition function, $W(\tau,p)$, for the C36 sample is plotted as a function of the probability measure p for both $\tau=-2$ (left panel) and $\tau=3$ (right panel). The local dimension values are obtained in the same way as in Figure 6.11.*

in the case we consider no characteristic scale is introduced by such effects.

Further doubts about the reality of a fractal behaviour at small angular scales could arise due to the limited number of objects available in the C36 sample. If this were the case, we would expect that different methods, which have different sensitivities to the limited statistics, give different answers. However, the application of the density reconstruction method to the C36 cluster sample confirms the scale invariant nature of the cluster distribution at small scales. This is clearly shown in Figure 6.12, where we plot the DR partition function for $\tau=-2$ (Figure 6.12*a*) and for $\tau=3$ (Figure 6.12*b*), together with the respective local dimensions. For $\tau=-2$ we see that the local dimension has a rather flat shape with a value $D_{\tau=-2}\simeq 2$. This suggests that the distribution in the underdense regions, more weighted for negative τ's, turns out to appear essentially space-filling. On the contrary, for $\tau=3$ the local dimension shows a rather flat shape for small probabilities (corresponding to small physical scales), with a value $D_{\tau=3}\simeq 1.1$, thus remarkably similar to that coming from the correlation integral method. At larger p's the dimension again start increasing toward the homogeneity value $D_{\tau=3}\simeq 2$. A closer comparison with the results coming from the correlation integral approach can be done once we assign a range of angular scales to the range of probability scales where we estimate the DR partition function. This is done by taking for each p value the ϑ value corresponding to the peak of the radii frequency distribution. In Figure 6.13 we

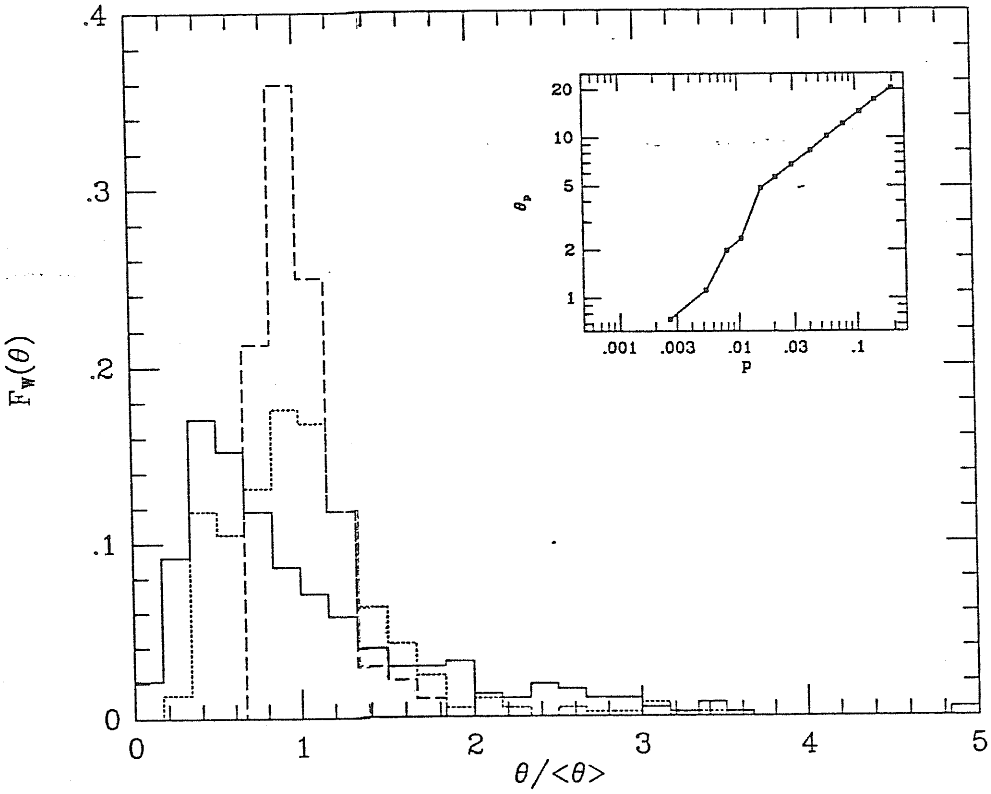

Figure 6.13: *The frequency distribution $F_W(\vartheta)$ of disk radii containing a given number $n = p/N$ of C36 clusters (here N is the total number of objects and p is the probability measure) is plotted for different p values. The solid line is for $p = 2.6 \times 10^{-3}$, the dotted line is for $p = 1.6 \times 10^{-2}$ and the dashed line is for $p = 0.2$. The box insert gives the angular scale associated to each value of p, that is estimated as the ϑ value corresponding to the peak of the corresponding frequency distribution.*

show this frequency distribution evaluated for different probabilities. A change of the shape of the frequency distribution is apparent as we go to larger and larger probabilities. In fact, while the skewed distribution at small p's indicates the presence of small-scale clustering, the roughly Gaussian profile centered at the mean disk radius, $\langle \vartheta \rangle$, for larger p's is the signature of the large-scale homogeneity. In the box insert we also plot the angular scale ϑ associated to each probability value.

Based on this plot, we show in Figure 6.14 the expanded view of the local dimensions of Figure 6.12, but as functions of the angular scale. While Figure 4*a* confirms the homogeneity of the cluster distribution in the underdense regions, in Figure 6.14*b* the break of the scale-invariance (at $\vartheta \sim 7°$) is even more apparent, a result which is in agreement with that obtained from the correlation integral method. This indicates the reliability of our method to associate a ϑ value to each p and strongly support the self-similar behaviour of the cluster distribution at small scales, followed by a transition toward homogeneity at larger scales.

We also apply the MST algorithm to investigate the scaling properties of the C36 cluster distribution. As suggested from the analysis of the synthetic samples (see §3.3), we

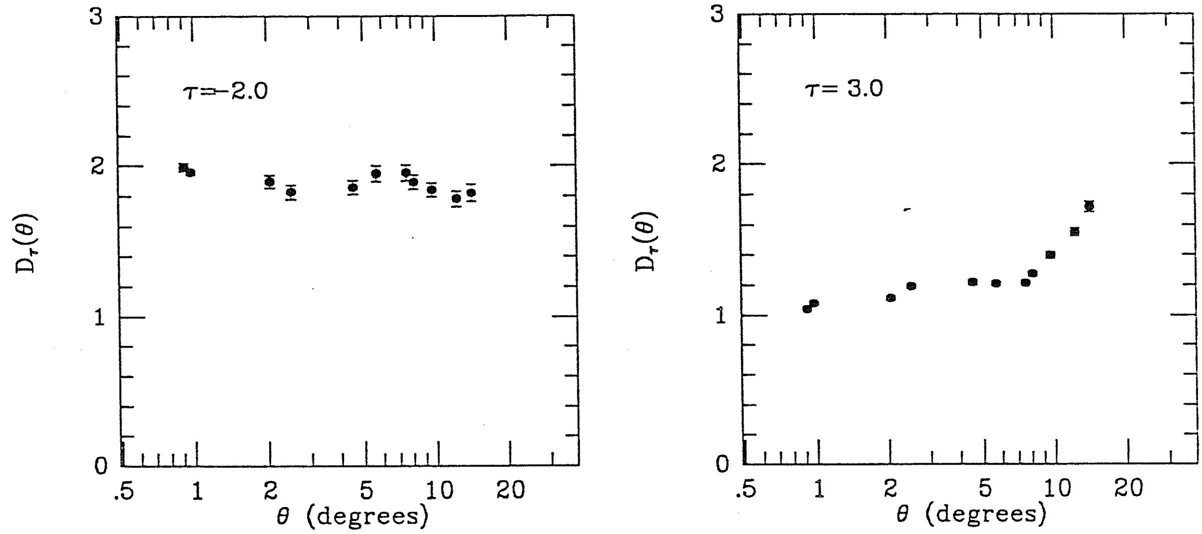

Figure 6.14: *Expanded view of the local dimensions reported in Figure 6.12, once an angular scale is associated to each p value. It is apparent that for $\tau = 3$ a well definite scaling develops up to $\vartheta \simeq 7°$, with a subsequent breaking. For $\tau = -2$ we see the homogeneity of the distribution of C36 clusters in the underdense regions.*

decided to cut the too long and too small edge links at negative and positive τ's, respectively, in order to filter out the noise, which should be even more important when only a limited number of objects is available. A further source of noise could well be due to the extraction of random subsamples, expecially when the chosen number m of points is quite small. To overcome this problem we take for each m value 10 different random subsamples when $n <$ 500. Note that this prescription will always be applied in the analysis of the C36 sample, which contains only 381 objects (see Table 6.1). The corresponding partition function is then evaluated by averaging over all the realizations. As expected, this procedure remarkably reduces the noise especially for the very poor subsamples.

The results for the MST method are shown in Figure 6.15, where we plot the MST partition function. Figure 6.15*a* shows the $\tau = -2$ case, where we cut the edge lengths that are longer that 4 times their average value $\langle\lambda\rangle$ (indeed, for $\tau < 0$ the long branches are mostly weighted, so that cutting small branches has no effect). Viceversa, in Figure 6.15*b* we plot the MST partition function for $\tau = 3$; in this case edge lengths shorter than $0.3\langle\lambda\rangle$ are cut. As for the density reconstruction method, the generalized dimensions for negative τ's shows that the distribution in the underdense regions is essentially homogeneous. However, differently from the previous methods, no clear evidence of clustering is detected for $\tau > 0$. In fact, Figure 6.15*b* shows a local dimension that never flattens at the unity value. Instead, quite large fluctuations of $D_{\tau=3}(n)$ appear that confirm the presence of convergence problem for the MST method. We believe that this is mainly due to the strong scale mixing present in the MST method (see §3.3). In fact, when we cut the small branches in order to reduce the noise, we loose information about small-scale clustering, which is indeed expected to

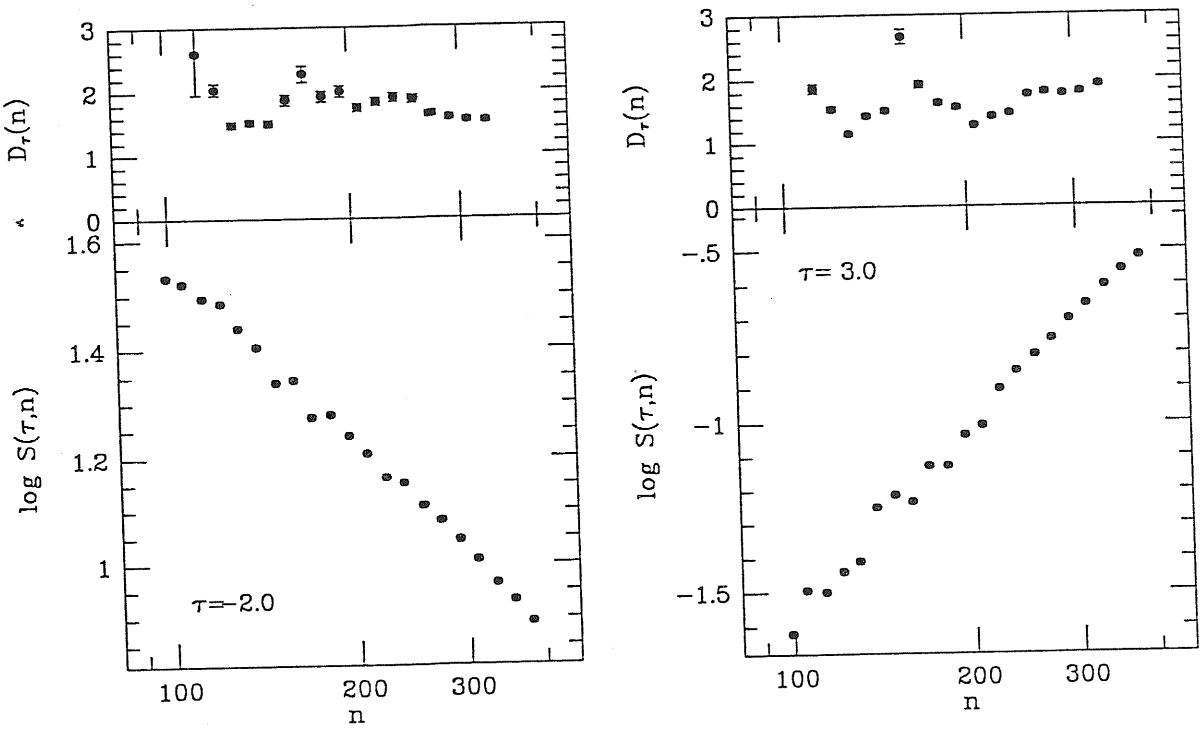

Figure 6.15: *The MST partition function, $S(\tau, m)$, and the relative local dimensions, $D_\tau(m)$, for the C36 sample are plotted as a function of the number m of objects in randomly selected subsamples, for both $\tau = -2$ (left panel) and $\tau = 3$ (right panel).*

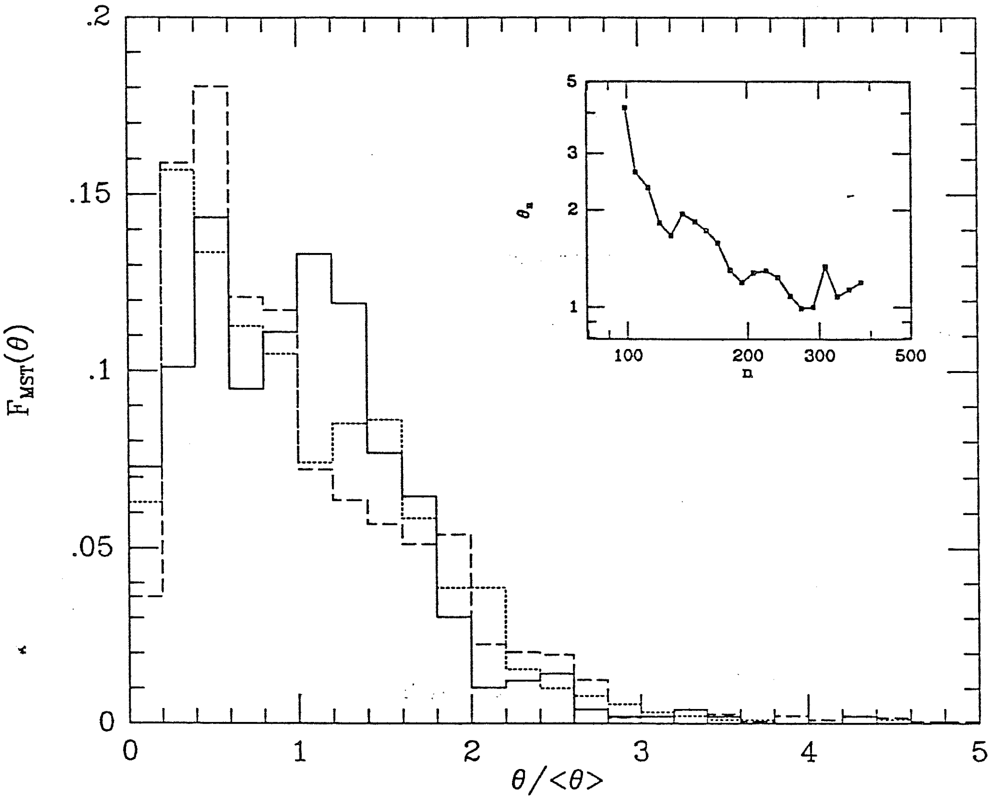

Figure 6.16: *The frequency distribution, $F_{MST}(\vartheta)$, of edge-lengths in the MST for C36 clusters. The solid line corresponds to a number of particles in the random subsample $m = 100$, the dotted line to $m = 195$ and the dashed line to $m = 272$. The box insert gives the angular scale associated to each value of m and is estimated as the ϑ value corresponding to the peak of the corresponding frequency distribution.*

be characterized by a lower dimension $D_{\tau=3} \simeq 1$. In our opinion, this represents a serious limitation of the MST method when applied to point sets that are not rigorously scale-invariant over all the scales: small-scale noise forced us to remove the shortest branches, but this cause an undersampling of the small-scale clustering. Clearly, this problem does not arise when dealing with a rigorously scale-free structure. In this case removing the small links in the tree does not modify the dimensionality since the same D_q spectrum holds at small and at large scales.

In order to assign a physical scale to each choice of the number of points in the random subsamples, we take the ϑ value corresponding to the peak of the edge-length frequency distribution. In Figure 6.16 we plot such frequency distributions for subsamples having different dilution factors. Again, for the very poor subsamples, which test larger scales, the corresponding $F_{MST}(\vartheta)$ approaches a Gaussian shape, thus indicating negligible clustering. Viceversa the more populated subsamples are characterized by skewed distributions as a consequence of the small-scale clustering. In all the cases, however, the $F_{MST}(\vartheta)$ distribution turns out to possess quite long tails both for large and short edge lengths, thus indicating that the MST algorithm mixes different physical scales. In the box-insert we show the relation between the number n of points in each subsample and the angular scale individuated by the MST. This relation appears not very smooth as a consequence of the noise present in the MST algorithm, when a small number of data points is available.

The results of the analysis of the scaling properties for the C36 sample are summarized in Figure 6.17. In Figure 6.17*a* we plot the $\tau(q)$ spectrum as deduced from the application of the various methods. It is apparent that for $q > 0$ the results of the density reconstruction method well agree with those of the correlation-integral method, while for $q < 0$ they overlap with those of the MST approach. We do not plot the results of the correlation-integral methods for $q < 0$ and of the MST for $q > 0$, where they are not expected to work. This result confirms that different methods are well suited for the multifractal analysis in different q ranges, while the DR partition function seems to be adequate for all q's. In the box-insert we also plot the $f(\alpha)$ spectrum of singularities (see eq.[3.19]), as deduced from the density reconstruction method. We see that the maximum of the $f(\alpha)$ curve indicates a value of the Hausdorff dimension $D_o \simeq 1.8$, while from the value $\alpha_{\rm min} \simeq 1$ we see that a dimension unity characterizes the cluster distribution in the very overdense regions. These results are confirmed by the D_τ spectrum of generalized dimensions (Figure 6.17*b*), as obtained from the density reconstruction method.

The C25 sample

Further informations about the scaling properties in the distributions of the cosmic structures traced by the Lick map can be obtained by considering progressively lower peaks of the galaxy density field. To this aim, we decide to extend our analysis also to the C25 sample.

In Figure 6.18, the same as Figure 6.11 for the C36 sample, we plot the CI partition function for the C25 sample, in the same range of angular scales as for the C36 clusters. Although in this case discreteness effects are less pronounced because of the higher object number density, they are however present and still cause the Hausdorff dimension to keep a very low value at small scales. Differently from the analysis of the C36 catalogue, for the $q = 4$ case there is now no evidence of a well definite scaling region where the local dimension can be considered as constant. Instead, $D_4(\vartheta) \simeq 1$ at the smallest considered scales, thus in agreement with what found for the highest peak distribution, but with a smooth transition toward the value $D_4 \simeq 2$ at larger scales ($\vartheta \gtrsim 7^\circ$), where homogeneity (at least in two dimensions) is reached.

This result is confirmed by the DR algorithm. Also in this case (see Figure 6.19) we observe that the local dimension in the $\tau = 3$ case varies from a unity value at the small scales of non-linear clustering to $D_{\tau=3} \simeq 2$ at larger scales. No remarkable differences with respect to the C36 sample are found in the case $\tau = -2$, thus confirming that the distribution of galaxy systems in the underdense regions is essentially space-filling. The weaker clustering of the C25 sample with respect to the C36 one is also reflected by the shape of the radii frequency

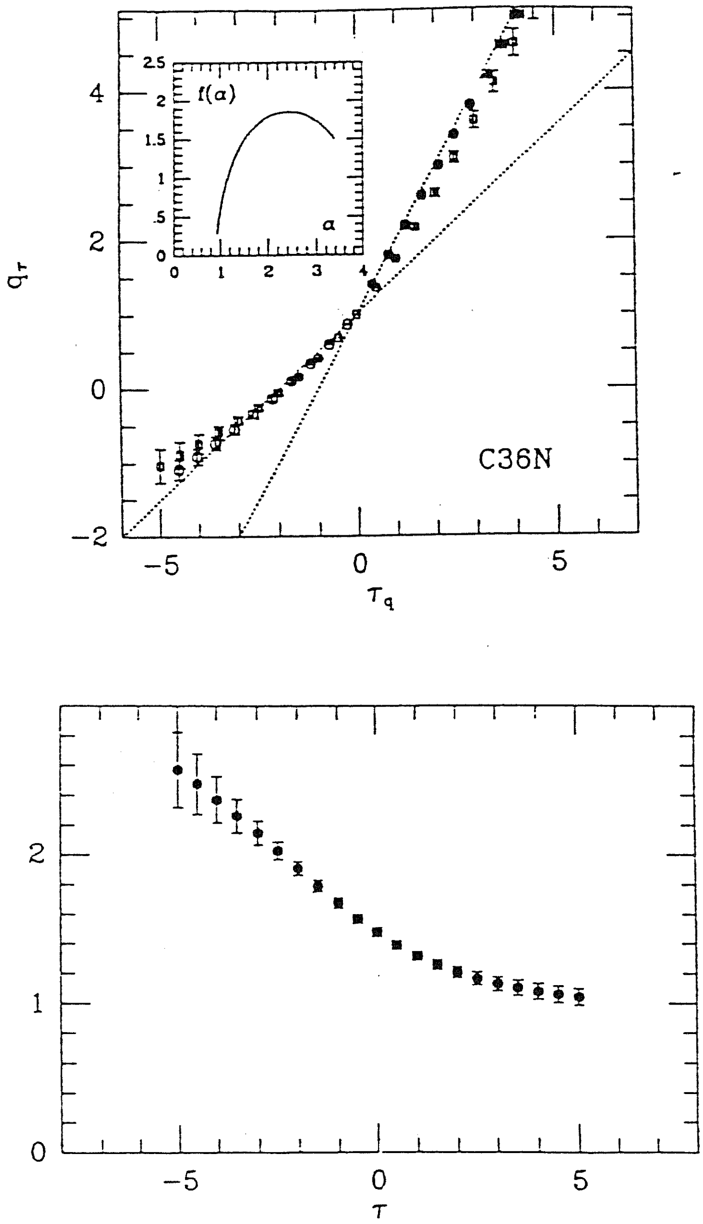

Figure 6.17: (a) *The τ_q spectrum for the distribution of C36 clusters. Filled circles for $q \geq 1$ refer to the correlation-integral method, open circles for $q \leq 0$ are for the MST method, while open squares refer to the density-reconstruction method, that holds for both positive and negative q's. These values for τ_q (or q_τ) are obtained by a log-log linear regression of the partition functions in the range of scales where the local dimension remains essentially constant. The errorbars correspond to 1σ uncertainties in the linear regression. In the box insert we report the shape of the $f(\alpha)$ spectrum of singularities given by eq.(3.19).* (b) *The D_τ spectrum of the generalized dimensions obtained from the density reconstruction method. Note that D_τ approaches a unity value for increasing τ values, corresponding to the clustering inside the more and more overdense regions.*

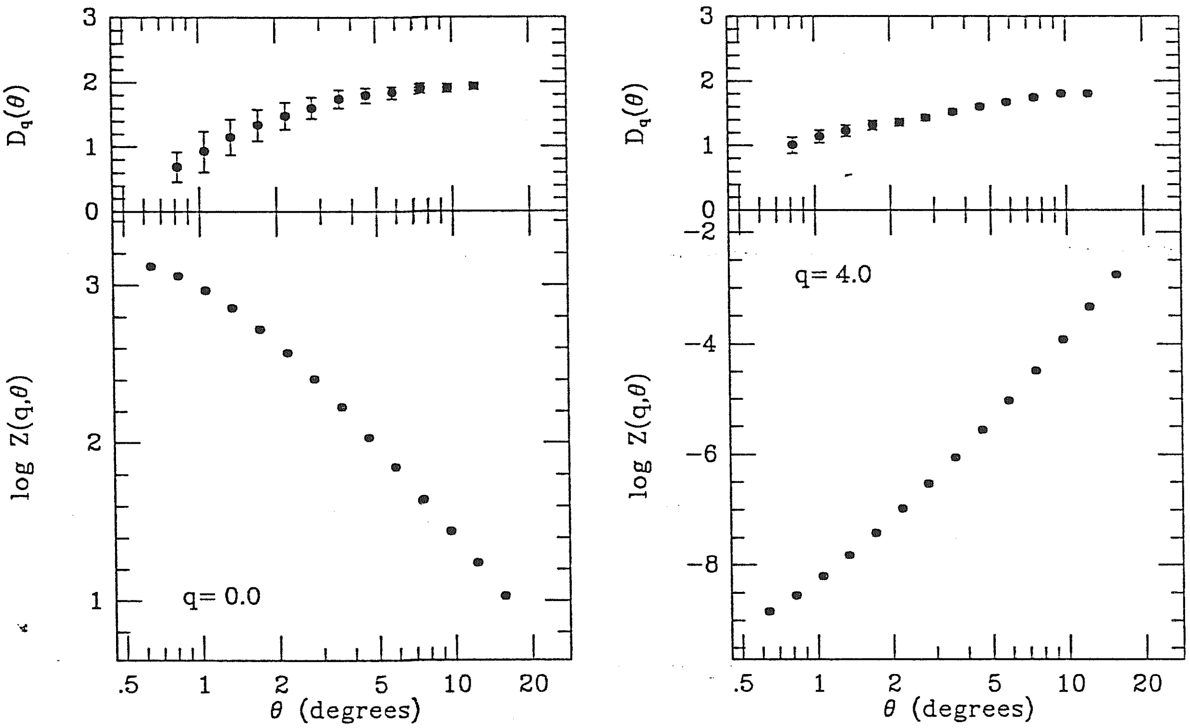

Figure 6.18: *The same as Figure 6.18, but for the C25 cluster sample. Note that no evidence of scale-invariant clustering is detected for* $q = 4$.

distribution appearing in Figure 6.20. Here, even for the smaller probability values only a small skewness appears to characterize the non-random statistics of the cluster distribution. The use of the MST method for the C25 sample shows basically the same limits as in the C36 case. Indeed, no reliable answers are obtained for $\tau > 0$, while for negative τ's the homogeneity of the cluster distribution in the underdense regions is confirmed.

We believe that the absence of any scaling regime for the distribution of C25 clusters could be due to two main reasons. Firstly, the weakening of the clustering as the peak height is lowered can cause projection effects to be more important and to increasingly disturb a safe detection of the three-dimensional clustering pattern. Secondly, lower peaks of the angular galaxy density field can be produced by spurious superposition instead of representing physical galaxy association. If such an effect is important, then the clustering of the C25 clusters could be, at least partially, the result of a serious contamination.

The galaxy distribution

In order to complete our discussion about the effect of the peak height on the scaling properties of the cluster distribution, we also performed the multifractal analysis for the whole two-dimensional galaxy distribution provided by the Lick map. Note that such a galaxy catalogue

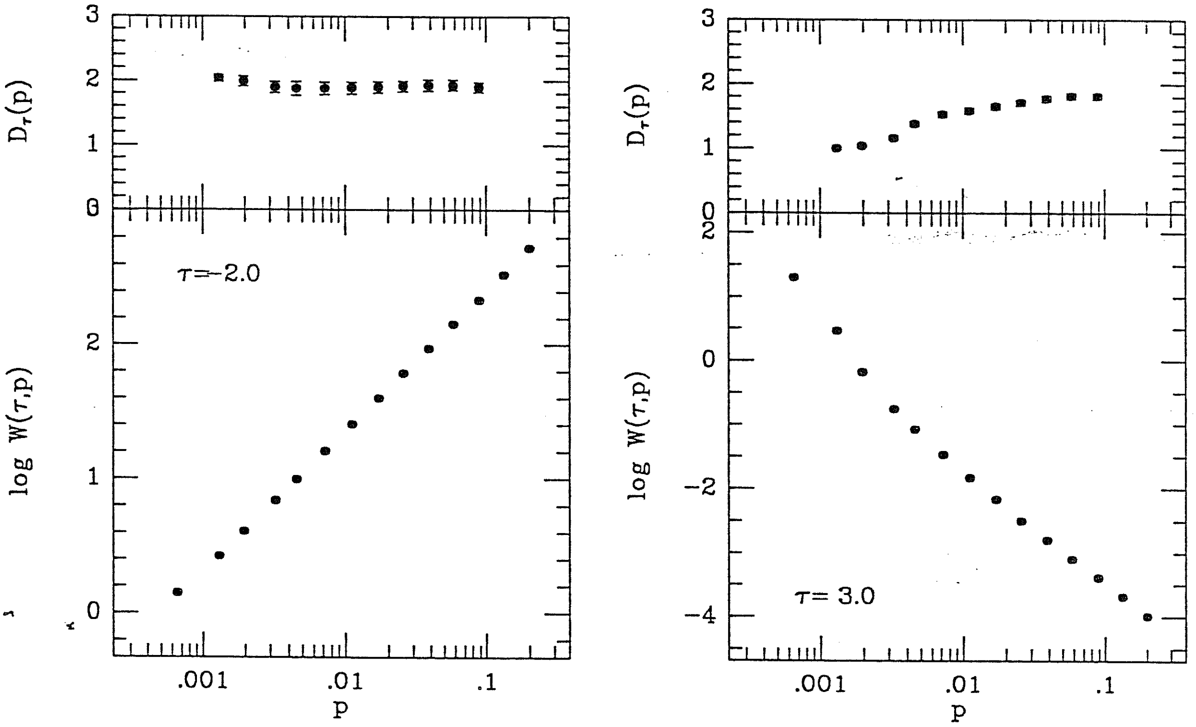

Figure 6.19: *The same as Figure 6.12, but for the C25 sample. As for the correlation-integral method, no evidence of scaling exists for* $\tau = 3$.

does not provide galaxy positions, but only counts in 10′ × 10′ cells. For this reason, we prefer to apply in this case the box-counting algorithm. In fact, the very high number of data points ($\simeq 2 \times 10^5$ non empty cells for $|b| > 50°$) is adequate for the BC approach to give reliable answers.

In Figure 6.21 we plot the BC partition function for the Lick map. From Figure 6.21*a* ($q = 0$) we see that the local dimension never significantly detaches from the value $D_o = 2$. Although this value of the Hausdorff dimension is very close to that found for the three-dimensional galaxy distribution of the 14.5 CfA sample [249], it should be taken with extreme caution. Indeed, due to its geometrical meaning, the Hausdorff dimension can never take a value greater than the dimension of the ambient space. Thus, the above estimate of D_o for the Lick map must be considered only as a lower bound of the true Hausdorff dimension of the three-dimensional galaxy distribution. It is remarkable to note that, due to the large amount of statistics, no discreteness effects are found in the considered scale range even for $q = 0$. In Figure 6.21*b* we plot the case $q = 4$. Here, only at very small scales it is possible to observe a significantly lower dimension than the homogeneity value $D = 2$, thus confirming the weakness of the projected galaxy clustering with respect to that of the density peaks. As for the C25 sample, no evidence of scaling appears; the local dimension again becomes near to one at the smallest scale, while for $\vartheta \gtrsim 2\overset{\circ}{.}5$ homogeneity is reached. These findings on the one hand confirm that a unity dimension is a preferred value to describe the strong clustering

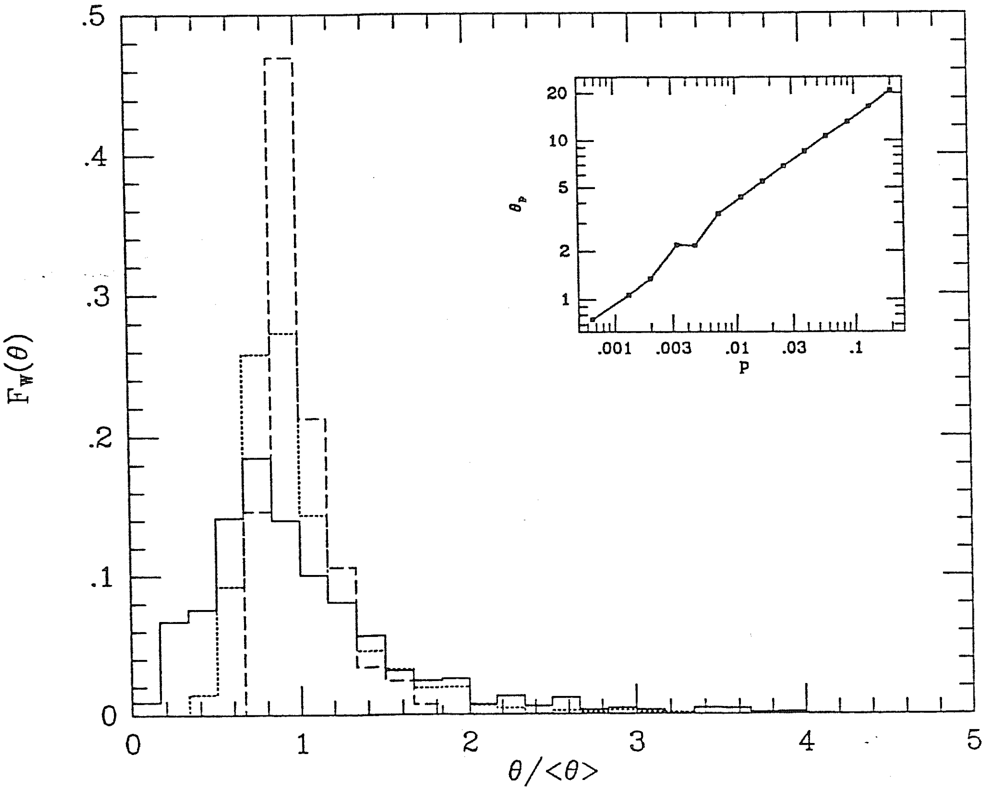

Figure 6.20: *The same of Figure 6.13, but for the C25 sample. The solid line corresponds to* $p = 6.5 \times 10^{-4}$, *the dotted line to* $p = 7.2 \times 10^{-3}$ *and the dashed line to* $p = 0.2$.

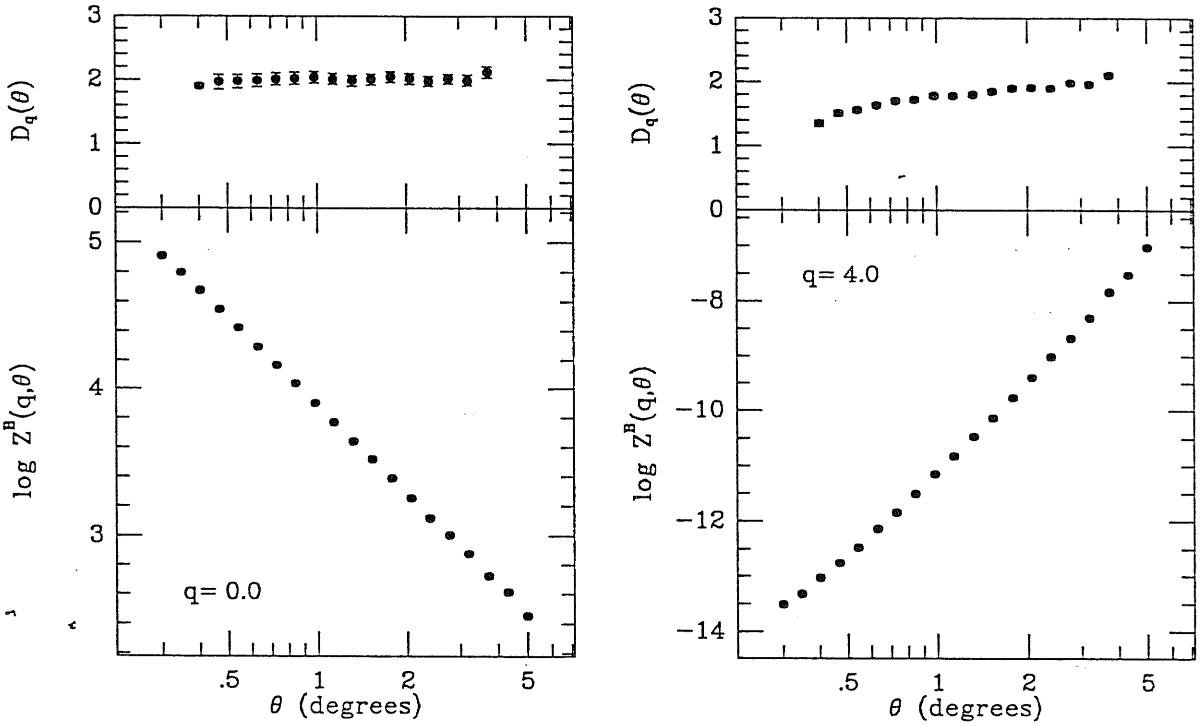

Figure 6.21: *The box-counting partition function for the distribution of Lick galaxies. The left panel is for $q = 0$ and the right panel is for $q = 4$.*

regime (*i.e.*, small scales inside overdense regions), and on the other hand indicate a nice similarity between the scale of homogeneity and the scale where the shape of the angular 2-point function breaks and starts rapidly decreasing Note that the absence of scale invariant behaviour with respect to the three-dimensional galaxy distribution indicates that projection effects seriously affect the small scale self-similarity of the clustering pattern.

Analysis of the synthetic sample

Here, we discuss in details the problem of inferring the scaling properties of the three-dimensional cluster distribution from the analysis of the angular samples, presented in the previous subsections. We expect *a priori* that projecting on the sky should cause the strength of the clustering to be partially suppressed because of the homogenization of clustered regions due to background and foreground objects.

The problem of relating two-dimensional clustering properties to the three-dimensional ones is well known in the case of the correlation analysis. In fact, a classical result is represented by the Limber equation [233] for the 2-point function (see eq.[2.32]). Assuming a power-law shape, $\xi(r) \propto r^{-\gamma}$ for the spatial function, then the angular function turns out to be also a power law, $w(\vartheta) \propto \vartheta^{-\beta}$, with the scaling exponent related to the spatial one according to $\beta = \gamma - 1$ and with amplitude depending on the depth of the angular sample, as well as on the shape of the luminosity function [287]. Accordingly, the resulting correlation dimension D_2 is not altered by the projection, at least when $w(\vartheta) > 1$. The situation becomes less clear when considering D_q for $q \neq 2$ and we expect in principle that different order dimensions are altered by different amounts.

A further cause of concern is related to the conservation of scale-invariance after projection. From the above results about the projected galaxy distribution, we have seen that, if the spatial clustering has fractal properties in a limited scale range, then projection effects can erase this scale-invariant behaviour. On the contrary, for the C36 cluster sample, that has a quite high degree of two–dimensional clustering, we have shown that a well definite scaling appears at angular scales $\vartheta \lesssim 6^\circ - 7^\circ$. Thus, the question to be addressed in this case is whether the breaking of fractality at large scales reflects a similar breaking even in the three-dimensional cluster distribution, or is it merely induced by projection, being the spatial distribution fractal at all the scales.

In order to properly answer to the above question, we generate a three-dimensional scale-invariant structure, with controlled multifractal properties, and project such a structure on a sphere in order to check the effects of projection both on the spectrum of generalized dimensions and on the scale-invariance of the resulting structure. In addition, we assign luminosities to each point by assuming a suitable shape for the luminosity function and generate magnitude limited angular samples. In this way we are able to account for the effects of luminosity selection on the scaling properties of the spatial structure.

Furthermore one should consider projection effects on structures that are self similar in a limited range. After projection the amplitude of the two–point function is suppressed by an amount that depends on the depth $\mathcal{D}$ as $w(\vartheta) \propto \mathcal{D}^{-1}$. Thus we expect that self similarity should be preserved for those structures, like the C36 clusters, that have a quite strong two-dimensional clustering, so that the power–law scaling of $w(\vartheta)$ dominates the mean count of neighbors. Viceversa, fractality is washed out when $w(\vartheta) \ll 1$, as it happens for the galaxy distribution. This can be easily tested in s synthetic catalog with large scale homogeneity. However it is clear that at a depth similar to that of the Lick map ($\simeq 210h^{-1}$ Mpc) it is difficult to disentangle the effects of small–scale fractality from that of projection. For this reason we check projection effects only for pure self-similar structures, so to verify the reliability of the characteristic scale seen in the distribution of C36 clusters.

In order to generate the three-dimensional fractal structure, we resort to the multiplicative random β-model, which has been already used in Chapter 4, to generate fractal structure with controlled dimensionality. The multifractal structure we generate is the same as that analysed in §3.3. The profile of its D_q spectrum (see Figure 3.2) resembles what observed for the galaxy distribution at small scales, with $D_o = 2$, $D_{-\infty} = 3$, $D_{+\infty} = 0.8$ and $D_2 = 1.2$. We generate the cascading with 8 iteration steps and at the end of the cascading

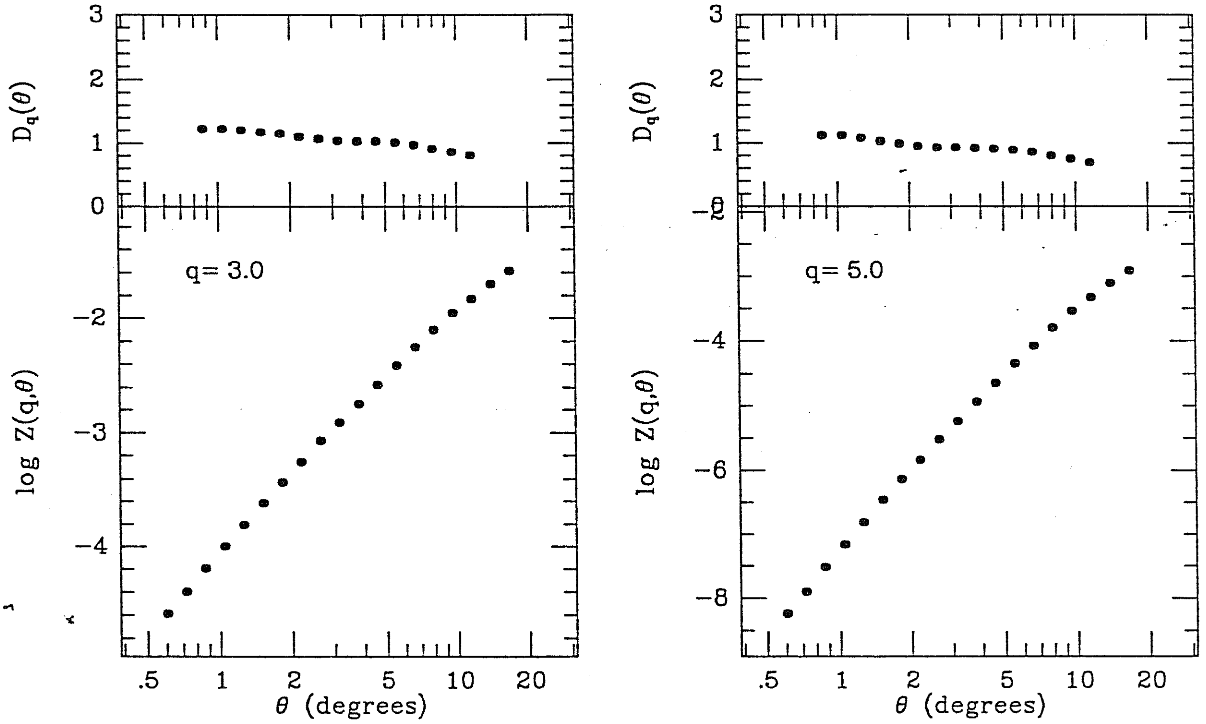

Figure 6.22: *The correlation-integral partition function for the shallower synthetic angular sample is plotted for $q = 3$ and $q = 5$. It is apparent that no significant features in the scale-invariant structure are introduced by projection and luminosity selection effects.*

process the number of non empty cells is roughly 6.5×10^4. We assign to each cell a number of particles that is proportional to the fraction of the total mass it contains, so that the total number of particles to 5×10^4. After generating the three-dimensional structure, we assign to each point a given luminosity according to the shape for the luminosity function

$$\phi(L) \propto L^{\beta} e^{-L/L_*} . \tag{6.23}$$

In the above expression we assume $L_* = 0.8 \times 10^{13} L_\odot$ and $\beta = -2$, as given in ref.[15] for the luminosity function for Abell clusters and groups of galaxies (see also §3.4.2). Although the shape of eq.(6.23) probably does not exactly fit the real luminosity function of the clusters we are dealing with, we believe that it is a reasonable approximation to seek the effects of luminosity selection on the scaling properties of a given spatial structure. Note also that, for a point distribution that is rigorously scale-invariant, the normalization of the luminosity function cannot be uniquely assigned since the mean object density depends on the sample size. Nevertheless, we *assume* that in our "fractal universe" the luminosity distribution is assigned according to eq.(6.23), while its normalization will be fixed only after fixing the physical length-scale sampled by the point distribution. After assuming $L = 64\,h^{-1}$ Mpc for the side of the simulation box we evaluate the apparent magnitude associated to each point according to eq. (6.23). Accordingly, we construct two different angular samples by projecting over the sphere of radius $L/2$, that is entirely contained in the box, all the points contained inside that sphere and with apparent magnitude below a fixed limit. Note that, because of the absence of any characteristic scale in the three-dimensional distribution we can obtain the same angular sample with a different choice for the size of the box and suitably rescaling the value of the limiting apparent magnitude. In this way, we generate two angular samples corresponding to limiting m values equal to 8 and 9, containing 1800 and 4400 objects, respectively [1]. The first of these samples has an object number density that is of the same order of that in our C36 sample. Then, the analysis of this synthetic sample enable us also to check to which extent the objects available in the observational data sets are adequate to realize safely a fractal analysis.

In Figure 6.22 we show the CI partition function for the sample limited to $m = 8$, evaluated for $q = 3$ and $q = 5$. We see that the local dimension shows no evidences of breaking of scale-invariance at large scales. Instead, its behaviour indicates that scale-invariance is essentially preserved after projection. This finding is extremely relevant for the interpretation of our results about the scaling properties for the distribution of the highest selected peaks. Indeed, it confirms that the breaking of scale-invariance for the C36 sample at the spatial scale $\simeq 20\,h^{-1}$ Mpc is real and highlights deep connections between fractality and non-linear clustering. In addition, since the angular average density of this sample is quite similar to that of the C36 catalogue, we also confirm that the limited number of available objects is enough to ensure a reliable analysis.

In Figure 6.23 we show the D_q spectrum of generalized dimensions for the two synthetic angular samples, together with the spectrum of the whole three-dimensional sample. It is apparent the effect of projection to smooth the profile of the D_q curve. This is exactly what we expect since projection tends to fill the voids, thus diminishing the dimensionality of the point distribution inside the underdensities, and also tends to smooth the density singularities, increasing the dimension inside the overclustered structures. Note also that the intersection between the three-dimensional spectrum and those of angular samples occurs at a τ value nearly corresponding to $q \simeq 2$. This means that the correlation dimension value is not affected by projection, in agreement with the expectation based on Limber's equation. At negative τ's the deeper sample has a lower dimension, while at positive τ's, the smaller dimensions occur for the shallower samples, in accordance with the fact that projection effects are more important for deeper samples.

---

[1] Due to the scale-invariance of the spatial structure, the same number of objects in a projected sample can be obtained by changing the size L of the box and suitably rescaling the limiting apparent magnitude, without changing the statistics of such an angular sample. Viceversa, in the presence of a homogeneity scale, as we go deeper and deeper the amplitude of the angular correlations decreases, according to the Limber equation.

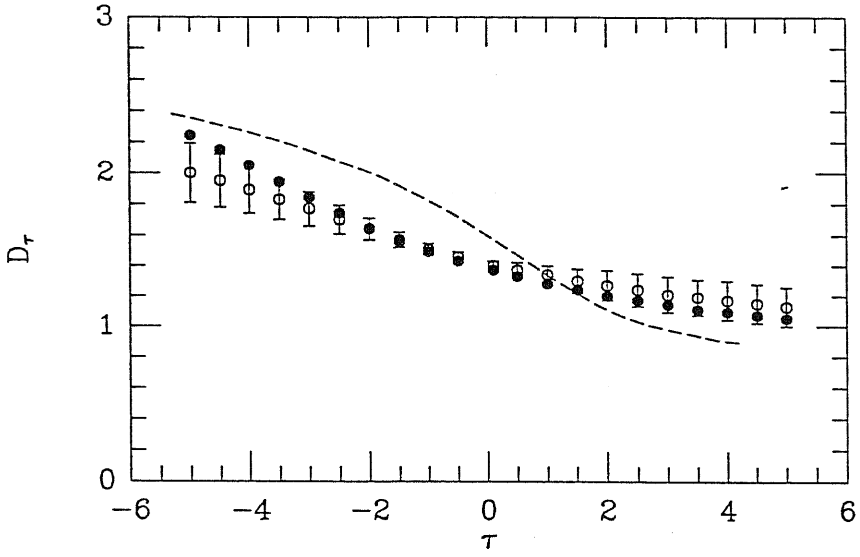

Figure 6.23: *The spectrum of generalized dimensions D_τ for the two synthetic angular samples, as deduced from the application of the density-reconstruction method. Filled circles are for the shallower sample, while open circles refer to the deeper sample. The dashed line is the spectrum before projection. It is apparent that projection reduces the multifractality and this effect increases with the sample depth. For reason of clarity, we plot the 1σ uncertainties only for one sample.*

6.5 Outlook

In this Chapter we presented a detailed statistical investigation of the clustering properties of the Plionis *at al.* [300] cluster samples, obtained from the Lick map by selecting peaks of the galaxy field at different values of the density contrast. We analyzed these angular samples by using both correlation and fractal analysis.

As far as the correlation analysis is concerned, we worked out the 2- and 3-point cluster correlation functions, by using different methods of analysis and error estimates. We considered both the quasi Poissonian error estimator (see eq.[6.5]) and the rigorous bootsrap resampling technique, in order to show how misleading it could be to adopt approximate error estimates. In the analysis of the 3-point function, we applied the moment method and the direct triplet counting. This allows us to check which method is best suited for higher-order correlation analysis, when dealing with a limited amount of statistics, as in the case of the cluster distribution. The main results of the correlation analysis that we get can be

summarized as follows.

a) The angular 2-point correlation function is well described in all the considered cases by the usual power-law, $w(\vartheta) = (\vartheta_o/\vartheta)^{1-\gamma}$ with $\gamma \simeq 2$, in the angular separation range $0.5° \lesssim \vartheta \lesssim 10°$ (see Figure 6.3). The existence of a well definite scaling in the angular cluster distribution is also confirmed by the good signals for the first- and second-order moment, which closely follow a power-law shapes (see Figure 6.7).

b) As for the detection of the 3-point function, both the moment method and the triplet counting technique give quite similar values of the hierarchical coefficient Q, but with formal uncertainties that are remarkably smaller in the case of the triplet counting. We believe that this is a consequence of the richer statistics available by counting triplets, whose number is quite high even in the presence of a rather poor sample. Instead, the application of the moment method requires counting objects inside spherical shells, and large resampling fluctuations occur when only a quite low number of clusters is available. Thus, the moment method seems to be a quite noisy procedure for high-order correlation analysis, when only a sparse object sample is available, although it is computationally cheap and has been proved to give reliable answers when dealing with dense object distributions (see Chapter 5).

c) A comparison with previous estimates of the cluster 3-point function shows a quite good agreement as far as the high-threshold clusters are concerned. However, we always find that our uncertainties in the Q values, that are based on the bootstrap resampling approach, are systematically larger than those based on the assumption of Poissonian errors [366, 161]). This clearly shows the importance of using a rigorous procedure to estimate the sampling uncertainties.

d) The detected clustering strength turns out to depend on the density threshold exactly in the same way as predicted by the biassed models discussed in §4.4 (see Figure 6.9). This result confirms the reliability of the biassing prescription to relate the clustering properties for different classes of cosmic structures. Finally, taking suitable definitions of cluster richness, we work out a well definite correlation between richness and clustering amplitude (see Figure 6.20). The fact that the richness-clustering relation includes also galaxies, considered as structure with richness $R = 1$, seems to indicate that it is not the result of selection and/or contamination effects. The richness-clustering relation also translates into an increasing trend of the 3-point hierarchical coefficient Q with the value of the cluster identification threshold (see Figure 6.8). This finding agrees with the expectation that the higher the peaks the more their statistics deviate from Gaussianity.

An even more detailed test of the scaling properties of the projected cluster distribution has been obtained using fractal analysis. This represents the first detection of multifractal properties for the cluster distribution. The amount of statistical information provided is remarkably large, thanks to the variety of applied methods and samples analyzed. The capability of fractal dimension estimator to provide detailed hints about the scaling properties of the cluster distribution allows to carefully check to which extent the scaling properties found for the galaxy clustering at scales of some Mpcs are translated at larger scales, when peaks of the galaxy density field are selected. The more interesting results that we obtained from this analysis are as follows.

a) The clusters identified as the highest selected peaks of the underlying galaxy distribution (C36 sample) are characterized by a well definite scaling of the clustering pattern at angular scales $\vartheta \lesssim 6^\circ - 7^\circ$ (see, *e.g.*, Figure 6.14). However, different dimensionalities are found in the underdense regions, where the cluster distribution looks essentially homogeneous, and a corresponding dimension $D_q \gtrsim 2$ for $q < 0$ is found, and in the overdense regions, where the presence of clustering causes the dimension to take a smaller value $D_q \simeq 1$ for $q > 0$ (see Figure 6.17). This suggests that, even at the small scales where scale-invariance develops, the large-scale cluster distribution is not described by a simple self-similar fractal structure but by a multifractal that exhibit local scaling properties. This result generalizes what found at smaller scales for the spatial distribution of CfA galaxies [249].

The above value of the angular scale at which self-similarity breaks turns out to be a remarkably robust outcome of our analysis and is confirmed by applying two independent algorithms of fractal analysis, the correlation integral method and the density reconstruction method. The presence of a characteristic scale in the cluster distribution at $\vartheta \simeq 6^\circ - 7^\circ$ is even more important if we consider that it corresponds, at the characteristic depth of the Lick map, to a spatial scale $R \simeq 20\, h^{-1}$ Mpc, thus quite similar to the rich-cluster correlation length [18, 340, 308].

The fact that a fractal dimension near to one characterizes the non-linear clustering regime confirms the independent indications coming from the multifractal analysis of cosmological N-body simulations (see Chapter 5 and ref.[374]) and of redshift galaxy surveys [250]. Note, however, that the scales involved in the clustering of galaxy clusters are much larger than those relevant to the clustering of galaxies or those where the background matter develops non-linear gravitational evolution in N-body experiment. Instead, both galaxy and underlying matter distributions are expected to reach homogeneity at the larger scales where cluster clustering develops. However, we believe that there is no contradiction between these results concerning structures of different hierarchy. In fact, it is possible to imagine scenarios, alternative to a purely fractal picture holding at all the scales, in which the distribution of density peaks has at large scales the same dimensionality as the background field at small scales, without necessarily implying the absence of large-scale homogeneity.

As an illustrative example, let us consider a point distribution that is given by the superposition of a homogeneous point distribution and of a fractal structure having a lower dimension, say $D = 1$. Since the point number density for the fractal structure depends upon the considered scale R according to $n(R) \propto R^{D-3}$, the contribution coming from the clustered structure becomes negligible as we consider larger and larger scales, where homogeneity is attained and the dimension turns out to be $D = 3$. For the same reason, at small scales the clustering is dominated by the fractal distribution and, correspondingly, we have a dimension $D = 1$. If we now select the high density peaks of such a structure we expect that they are mostly given by the peaks of the clustered (fractal) component. On the other hand, since the peak distribution of a fractal structure has the same dimensionality as the whole distribution, at large scales we will recover for the peak distribution the same dimension, $D = 1$, holding for the background at small scales. Although the above picture probably represents an oversimplification of the "true" global texture of the Universe, it illustrates nevertheless how the distributions of different hierarchy structures can be characterized by the same scaling properties, but holding at different scales. If a scenario of this kind were correct, it would show that, although the cluster distribution can be used to trace the structure of the Universe at larger scales, its statistics could significantly differ from that of the underlying matter density field.

b) For the C25 sample, we find that there is no clear evidence of scaling. Instead, while the underdense regions are still characterized by a homogeneous distribution, the local dimensions of positive multifractal order exhibit a smooth transition from a unity value at small scales to $D_q(\vartheta) \simeq 2$ at larger ($\vartheta \gtrsim 7°$) scales. The absence of any scale-invariant behaviour as we decrease the density threshold for the cluster identification could be due to two main reasons. Firstly, since these peaks correspond to less rich clusters the strength of their clustering is expected to decrease even in three dimensions. As a consequence, a possible scaling in the spatial distribution could be canceled due to more severe projection effects than in C36. Alternatively, it is also possible that, as we lower the density threshold in the angular galaxy distribution, we also select structures that have no counterparts in the spatial distribution, but are just produced by chance in the projected sample. In this case, the scaling of the C25 sample could be dis[illegible] due to contamination effects.

c) For the whole distribution of Lick galaxies, the weakness of the clustering in two dimensions causes the fractal dimension to detach from the value $D = 2$ only at very small angular scales. As for the C25 sample, no scale-invariant behaviour is detected. At the smallest scales, a dimension near to one is recovered inside the clustered regions, while the projected galaxy distribution definitely reaches homogeneity at $\vartheta \gtrsim 2.5°$, *i.e.* at the same scale where the breaking of the 2-point angular correlation function is detected [173]. The absence of scaling is at variance with respect to what observed for the spatial galaxy distribution. This discrepancy shows that projection effects can seriously disturb the scaling properties of the galaxy distribution, that is self-similar only up to the linearity scale [250].

d) Despite the interesting indications about the small-sale fractality for the C36 sample, it is appropriate to address the question about the effects of projection on the sky, that must necessarily be accounted for, when passing from the spatial clustering pattern to the projected one. For this reason, we generated two synthetic angular samples, having different depth, by projecting a three-dimensional fractal structure with controlled D_q

spectrum. A first important result of this analysis is that projection effects do not introduce any breaking of the scale-invariance up to the scales relevant to our analysis. This strongly supports the indications, based on the C36 results, that a characteristic scale exists in the distribution of rich clusters, which is very close to the cluster correlation length.

Despite the fact that scale-invariance turns out to be preserved, projection effects cause a distortion of the multifractal spectrum of generalized dimensions. Indeed, negative order dimensions decrease with respect to the three-dimensional case, since voids are filled by line-of-sight contamination. In particular, we find that the value of the Hausdorff dimension coming from the angular samples is systematically smaller than that corresponding to the spatial structure. Thus, we believe that our estimate of the Hausdorff dimension for the C36 sample, $D_o \simeq 1.8$, should be interpreted only as a lower bound. Viceversa, the positive q tail of the D_q curve increases since projection smooths out the density singularities in the point distribution. The intersection between the spatial D_q curve and the angular one occurs at $q \simeq 2$, thus in agreement with the Limber equation, that connects the 2-point correlation function of angular and spatial samples. We also find that such a smoothing of the D_q spectrum is more pronounced as we consider deeper and deeper samples.

We believe that our findings about the scale-invariant properties of the cluster distribution at the scales of non-linearity should represent a strong constraint for any cosmological model that provides the initial conditions for structure formation. Despite the relevance of analysing the angular cluster distributions, it is clear that loosing one dimension because of projection on the sky poses several limits to a complete view of the true spatial structure. The simulation of projection effects on a scale-invariant, multifractal structure ensures that the detected breaking of scale-invariance should correspond to the presence of a characteristic scale even in the three-dimensional distribution. However, the detection of homogeneity in the projected distribution says nothing about the scale at which the spatial cluster distribution attains homogeneity. In this respect, it is clear that complementary informations should be gained by considering redshift samples of galaxy clusters (Borgani, Martinez & Valdarnini, in preparation).

As a final point, it is worth observing that the detected self-similarity of cluster clustering at scales of few tens of Mpcs cannot have the same origin as the scale-invariance detected from the analysis of N-body simulations. In fact, the latter is the natural output of non-linear gravitational dynamics. This is surely not the case for the former, since at the scales of cluster clustering, the background dynamics is expected to be still in the linear or quasi-linear regime. Thus, the question that arises is whether, at scales $\sim 10h^{-1}$ Mpc, selecting the peaks of a moderately evolved Gaussian background can account for the observed fractality, that is the signature of a strongly non-Gaussian statistics, or we need something else.

The results presented in this Chapter are contained in three papers, two of which have been already published in *Montly Notices of the Royal astronomical Society* (Plionis & Borgani 1992, [301]) and in *The Astrophysical Journal* (Borgani, Jing & Plionis 1992, [54]), while the third one is in press in *The Astrophysical Journal* (Borgani, Plionis & Valdarnini [55]).

Chapter 7

Hierarchical statistics and fractal structure

Through the application of both correlation and fractal analysis, we have shown in previous chapters that a scale-invariant behaviour is always associated with non-linear clustering. The power-law shapes and hierarchical expressions of correlation functions lead to well defined small-scale multifractal properties, which are the natural output of non-linear gravitational dynamics. In order to provide a unifying description of correlation and fractal properties, in this Chapter we investigate the multifractal structure implied by a list of Non-Gaussian, hierarchical distributions already introduced in the literature. For each model we work out the multifractal spectrum of generalized dimensions, D_q, which characterizes the small-scale non-linear clustering. The resulting multifractal spectra are compared with those obtained in Chapter 5 from the analysis of N-body simulations. As an interesting result, we show that the hierarchical behaviour of n-point functions turns into monofractality inside the overdense regions, with dimension independent of the details of the hierarchical model (*i.e.*, of the sequence of Q_n coefficients). On the contrary, the D_q spectrum in the negative q tail is much more discriminating. This indicates that the fractal analysis can be more efficiently employed to constrain theoretical models than correlation analysis, which is mostly sensitive to the overdense parts of the distribution, the only problem being an adequate sampling of the "devoid" regions.

7.1 Correlations and fractal dimensions

From the power-law shape of the 2-point correlation function it turns out that galaxy clustering can be represented as a self-similar fractal process, at least at the small scales of non-linear clustering. In fact, if $N_{<r}$ is the expected number of neighbors lying within a distance r from

a given object, then

$$N_{<r} = n \int_v d^3r\,[1+\xi(r)] = nv\left[1+\left(\frac{r_c}{r}\right)^{\gamma}\right], \tag{7.1}$$

n being the average object number density and $v = 4\pi r^3/3$ (see also eq.[3.10]). In eq.(7.1) the scale-length $r_c = [3/(3-\gamma)]^{1/\gamma} r_o$ represents the distance at which the average number of neighbours is twice that expected and, thus, can be considered the scale below which the power-law shape of $\xi(r)$ dominates the scaling of $N_{<r}$. On the other hand, as we have shown in Chapter 3, for a scale-invariant structure $N_{<r} \propto r^{D_\nu}$, D_ν being the correlation dimension. Accordingly, eq.(7.1) implies that the distribution of galaxies and galaxy clusters is fractal at scales $\ll r_c$, with $D_\nu = 3-\gamma \simeq 1.2$, while at large ($\gg r_c$) scales we get $D_\nu = 3$, as expected for a homogeneous distribution.

Further pieces of information about the large scale clustering are provided by the analysis of higher-order correlation functions. Both observational data and theoretical arguments converge to indicate that the connected part of the q-point correlation function is well represented by the hierarchical expression

$$\kappa_q(\mathbf{r}_1,...,\mathbf{r}_q) = Q_q \sum_{a\neq b} \xi(|\mathbf{r}_a - \mathbf{r}_b|)^{q-1}, \tag{7.2}$$

for $q \geq 3$, while $\kappa_2(\mathbf{r}_a,\mathbf{r}_b) = \xi(|\mathbf{r}_a - \mathbf{r}_b|)$. In the above expression, the sum is over the q^{q-2} connected graphs (see Chapter 2) and the Q_q's are the q-th order hierarchical coefficients. As we have shown in previous chapters, the validity of eq.(7.2) has been tested against the galaxy distribution for $q = 3, 4$ [173, 150, 353], the distribution of dark matter inside galaxy halos [45, 53], and is also confirmed by the outputs of cosmological N-body simulations [98, 258, 124, 373] (see Chapter 5). Even at very large scales, the hierarchical expression has been found to be consistent with data on the 3-point function of galaxy clusters [366, 209, 161, 54] (see Chapter 6). From the theoretical point of view, the hierarchical behaviour of correlation functions arises from a perturbative approach to the evolution of density inhomogeneities [146], and is consistent with the solution of the BBGKY equations in the strongly non-linear, fully relaxed regime [101, 145, 183].

In order to give a phenomenological description of the galaxy clustering pattern, several authors have introduced a variety of hierarchical probability distributions, that were able to generate the sequence (7.2) of q-point functions, with hierarchical coefficients depending on the model details (see, *e.g.*, ref.[147]). Apart from the shape of the q-point functions, the assumption of hierarchical probability distribution also has precise implications on the behaviour of other observable quantities, such as the count-in-cell probabilities [72, 335, 147, 22], the void probability function [148, 131] and the mass function of cosmic structures [241, 80]. Detailed comparisons of such models with the observed galaxy distribution [148, 10, 334, 383] and with the outputs of cosmological N-body simulations [149, 333, 60] show that several aspects of the non-linear clustering can be well reproduced by any hierarchical model, while no strong preference for one particular model has been obtained as yet.

Although the hierarchical distributions have been found to be quite good in describing the clustering in the non-linear regime, some other non-Gaussian distributions have also been introduced in cosmological context. One of the most famous of such distributions is the lognormal one [84], that has been proposed as a good approximation to describe the moderately non-linear gravitational evolution of a primordial Gaussian random field, as well as the correlation properties of the very high peaks of a Gaussian density distribution.

Attempts to unify the description of galaxy clustering in terms of correlation and fractal analysis have been pursued by several authors [47, 23], showing how fractal properties arise from scale-invariant models for the q-point correlation functions. In this Chapter we explicitly analyse the multifractal properties implied by different hierarchical models and compare them with the results obtained in Chapter 5 from the analysis of N-body simulations. The multifractal analysis provides a comprehensive statistical description of the clustering pattern not only in the overdense, more clustered regions, as the correlation analysis do, but also in the underdense regions (see Chapter 3). This fact renders the comparison with N-body data particularly meaningful, since different hierarchical distributions will be shown to have largely different behaviours in their low-density tails, while their high-density profiles are only hardly distinguishable.

After reviewing the concepts of probability distribution and moment generating functions, in this Chapter we show how these quantities are connected to the multifractal structure of a point distribution. We derive the fractal structure for a list of hierarchical distributions, already introduced in the literature, and compare them with those obtained from the analysis of N-body simulations.

7.2 The statistical formalism

In this Section we introduce the moments for object counts and their generating functions. Then, we describe the connection between such quantities and the multifractal spectrum of generalized dimensions.

7.2.1 Moments of counts and generating functions

As in the case of correlation functions, introduced through their generating functionals (see §2.1), moments of increasing orders can be defined in a similar fashion by successive differentiation of suitable generating functions. To see this in more detail, let us consider the cosmic matter density field as described by a random variable ρ, and let $p(\rho)$ be its probability density function (pdf). Then, the moment of order q reads

$$m_q \equiv \langle \rho^q \rangle = \int d\rho \, p(\rho) \, \rho^q . \tag{7.3}$$

For $q = 1$, the above expression gives the average density $\bar{\rho}$, while $q = 2$ and $q = 3$ are for the variance and the skewness of the distribution, respectively. Following the expression (2.20) for the q-point joint probability of the density field, the corresponding moments can be expressed in terms of correlation functions through the relation

$$m_q = \bar{\rho}^q \int_v d^3x_1 \dots \int_v d^3x_q [1 + (\text{terms of order} < q) + \mu_q(\mathbf{x}_1, ..., \mathbf{x}_q)] . \qquad (7.4)$$

In analogy with the $\mathcal{Z}[J]$ functional generator of correlation functions, introduced in §2.1, we define the moment generating function as the Laplace transform of pdf,

$$M(t) \equiv \int d\rho \, p(\rho) e^{t\rho} = \langle e^{t\rho} \rangle , \qquad (7.5)$$

in such a way that the moments m_q are the coefficients of its McLaurin expansion

$$M(t) = \sum_{q=0}^{\infty} \frac{m_q}{q!} t^q \qquad ; \qquad m_q = \left. \frac{d^q M(t)}{dt^q} \right|_{t=0} . \qquad (7.6)$$

In a similar fashion, the cumulants or irreducible moments k_q are defined through the generating function

$$K(t) \equiv \log M(t) = \sum_{q=0}^{\infty} \frac{k_q}{q!} t^q \qquad ; \qquad k_q \equiv \left. \frac{d^q K(t)}{dt^q} \right|_{t=0} , \qquad (7.7)$$

which is analogous to the $\mathcal{W}[J]$ generator of connected correlations. In fact, the cumulant turns out to be related to the connected functions according to

$$k_q = \bar{\rho}^q \int_v d^3x_1 \dots \int_v d^3x_q \, \kappa_q(\mathbf{x}_1, ..., \mathbf{x}_q) . \qquad (7.8)$$

Suitable relations between k_q and m_q can be found by successively differentiating eq.(7.7), which resembles the analogous relations between connected and disconnected correlation functions (see eq.[2.21]). By taking the integration volume as a cubic cell of side r, the scaling of correlation functions turns into a scaling of the respective moments. As an example, by taking for the connected function κ_q the hierarchical expression of eq.(7.2), it follows from eq.(7.8) that the q-th order cumulant scales as $k_q \propto r^{(q-1)(3-\gamma)}$, where γ is the usual logarithmic slope of the 2-point function.

From eq.(7.5), we can express the probability distribution in terms of the cumulant generating function as the inverse Laplace transform

$$p(\rho) = \frac{1}{2\pi i} \int_{-i\infty}^{+i\infty} dt \, e^{-t\rho} e^{K(t)} . \qquad (7.9)$$

Note that, although $p(\rho)$ seems to depend on the whole sequence of moments k_q, there exist precise restrictions on the the shape of $K(t)$, so that moments of different orders do not contain completely independent information. As an example, note that the quantity $K'' = (M''/M) - (M'/M)^2$ represents the variance of the distribution $p(\rho)e^{t\rho}$. Thus, $K(t)$ is constrained to be a convex function ($K''(t) \geq 0$) for any real t, the limiting case $K''(t) = 0$ occurring when $p(\rho) = \delta_{\rm D}(\rho - \bar{\rho})$, that is for vanishing density fluctuations. Furthermore, since

$$K'(t) = \frac{M'(t)}{M(t)} = \frac{1}{M(t)} \int d\rho\, \rho\, p(\rho)\, e^{t\rho}, \tag{7.10}$$

the requirement of a positively defined density field implies $K'(t) > 0$ for any real t.

An asymptotic approximation to $p(\rho)$ is obtainable by introducing the quantity

$$S(x) = xt - K \qquad ; \qquad x = \frac{dK}{dt}. \tag{7.11}$$

According to the above definitions, $S(x)$ represents a sort of "effective action", with a Legendre transform relating (t, K) to (x, S). From the above requirement on the functional form of $K(t)$, it follows that $dx/dt = K''(t) > 0$, so that the inverse of $x(t)$ is uniquely defined. Moreover, since $K(t)$ is a convex function, $S(x)$ will also be convex. Substituting eq.(7.11) into eq.(7.9), we get

$$p(\rho) = \frac{1}{2\pi i} \int_{S'=-i\infty}^{S'=+i\infty} dx\, S''(x)\, \exp\left[-S'(x)\,(x - \rho) - S(x)\right]. \tag{7.12}$$

Since $S''(x) > 0$, the integral is dominated at large ρ by the stationary point of the exponential at $x = \rho$. In this regime, we can expand the exponent to the second order around $x = \rho$. This amounts to locally approximating the exponential with a Gaussian function. According to this "saddle-point" prescription, eq.(7.12) gives

$$p(\rho) \simeq \left[\frac{S''(\rho)}{2\pi}\right]^{1/2} e^{-S(\rho)}. \tag{7.13}$$

In the case of Gaussian pdf,

$$p(\rho) = \frac{1}{\sqrt{2\pi\sigma^2}} \exp[-(\rho - \bar{\rho})^2/2\sigma^2], \tag{7.14}$$

so that $K(t) = \bar{\rho}t + \frac{1}{2}\sigma^2 t^2$, and the statistics are completely specified by the average density and by the variance σ^2. In this respect, note that it is not possible to have a distribution which has only mean, variance and skewness, since the resulting t^3 term in the expansion of $K(t)$ would give $K'' < 0$ for sufficiently large t values. In the case of a Gaussian pdf, the approximation of eq.(7.13) turns out to be exact. In fact, since $p(\rho)$ is Gaussian, $K(t)$ will also be Gaussian and the effective action $S(x)$ is a quadratic function, so as to make rigorous the "saddle-point" expansion.

For a Poisson point distribution,

$$p(\rho) = \sum_{N=0}^{\infty} \frac{1}{N!} \bar{\rho}^N e^{-\bar{\rho}}\, \delta_{\rm D}(\rho - N), \tag{7.15}$$

with the corresponding cumulant generating function

$$K(t) = \bar{\rho}\,(e^t - 1), \tag{7.16}$$

that does not contain any contribution of correlation terms, according to the expectation that a Poissonian process has non vanishing correlation functions.

Although it is in general possible to introduce the moments for a given distribution, the convergence of the series, that defines the respective generating function, is not always guaranteed. The classic example is the *lognormal* density field [84], obtained by means of the exponential transformation

$$\chi(\mathrm{x}) \;=\; \exp[\rho(\mathrm{x})] \tag{7.17}$$

of the Gaussianly distributed field $\rho(\mathrm{x})$. Accordingly, the pdf of the $\chi(\mathrm{x})$ field reads

$$p(\chi) \;=\; \frac{1}{\sqrt{2\pi\sigma_\rho^2}}\exp\left[\frac{-(\log\chi-\bar{\rho})^2}{2\sigma_\rho^2}\right]\frac{1}{\chi} \tag{7.18}$$

with σ_ρ^2 the variance of the Gaussian field $\rho(\mathrm{x})$. The corresponding moments of order q are

$$m_q \;=\; \exp\left(q\bar{\rho}+q^2\sigma_\rho^2/2\right). \tag{7.19}$$

As discussed by Coles & Jones [84], the subsequent divergence of the moment series is related to the fact that the lognormal distribution is not completely determined by the knowledge of its moments.

If, instead of a continuous density field, we are dealing with a discrete point process, as it is for the galaxy distribution or for the particle distribution generated by N-body simulations, the local object count N in a volume v can be considered as given by a Poissonian sampling of the underlying continuous density field ρ. Then, according to expression (7.16) for the moment generator of a Poissonian distribution, it is easy to recognize that the discrete nature of the distribution is accounted for by changing the variable $t \to e^t - 1$ in the $M(t)$ function [287, 147]. That is,

$$M_{discr}(t) \;=\; M_{cont}(e^t-1). \tag{7.20}$$

Evaluating the moments of counts by differentiating eq.(7.20) with respect to t, it turns out that new terms appear in their expression, because of discreteness. For the moments of first orders, one finds

$$\begin{aligned}\langle N\rangle &= \bar{N}\\ \langle N^2\rangle &= \bar{N}+\bar{N}^2(1+\bar{\xi})\\ \langle N^3\rangle &= \bar{N}+3\bar{N}^2(1+\bar{\xi})+\bar{N}^3(1+3\bar{\xi}+\bar{\zeta}),\end{aligned} \tag{7.21}$$

where $\bar{N}=nv$ is the average count,

$$\bar{\xi} \;=\; \frac{1}{v^2}\int_v d^3r_1\,d^3r_2\,\xi_{12} \tag{7.22}$$

the average 2-point function inside v, and $\bar{\zeta}$ the average 3-point function, which is defined by analogy with eq.(7.22). If $\bar{N} \ll 1$, then $\langle N^n\rangle \simeq \langle N\rangle$ and the moments are dominated by discreteness (shot-noise) effects. Viceversa, for $\bar{N} \gg 1$, the terms of lowest order in $\bar{N}$ become negligible and the continuous case is recovered.

Taking into account the effects of discreteness on the pdf expression, we get

$$p(\rho) \;=\; \int_{-\infty}^{+\infty} \frac{d\phi}{2\pi}\, e^{-i\phi\rho} e^{K(e^{i\phi}-1)} . \tag{7.23}$$

Since the variable $y = e^{ik}$ takes its value on the unit circle of the complex plane centered at the origin, K turns out to be a periodic function. Accordingly, its Fourier transform, $p(\rho)$, is written as a series of Dirac δ-functions as

$$p(\rho) \;=\; \sum_{N=-\infty}^{+\infty} \delta_{\rm D}(\rho - N)\, P_{\rm N} . \tag{7.24}$$

The probability distribution vanishes except for integer ρ values, as it should for a discrete density field. According to eq.(7.23), the coefficients $P_{\rm N}$ are

$$P_{\rm N} \;=\; \oint \frac{dy}{2\pi i}\, y^{-(N+1)} e^{K(y-1)} . \tag{7.25}$$

For analytical $K(t)$, the $P_{\rm N}$'s vanish for $N < 0$, so that they are the probabilities of finding $N \geq 0$ points inside the sampling volume. For $N = 0$, eq.(7.25) gives the void probability function,

$$P_0 \;=\; e^{K(-1)} \;=\; \exp\left[\sum_{n=0}^{\infty} \frac{(-1)^n}{n!} \int_v d^3x_1 \ldots \int_v d^3x_n\, \kappa_n(\mathbf{x}_1, \ldots, \mathbf{x}_n)\right] . \tag{7.26}$$

This expression shows that the void statistics contain information about correlations of any order and, thus, P_o represents a suitable quantity to properly characterize the texture of the galaxy distribution. In a similar fashion, by further applying the Cauchy theorem to evaluate higher order residues from eq.(7.25), we get

$$P_{\rm N} \;=\; \frac{1}{N!} \frac{d^{\rm N}}{dy^{\rm N}}\, e^{K(y-1)}\Big|_{y=0} , \tag{7.27}$$

and also the count-in-cell probabilities $P_{\rm N}$ convey information about higher-order correlations. According to eq.(7.27),

$$K(y) \;=\; \sum_{N=0}^{\infty} \frac{P_{\rm N}}{N!} (1 - y)^N , \tag{7.28}$$

so that, for a discrete distribution, the cumulant generating function of the background continuous field is the generator of the count probabilities $P_{\rm N}$. The continuous limit is recovered for $\bar{N} \to \infty$, so that the density variable is given by $\rho/\bar{\rho} = N/\bar{N}$. In this case, the pdf is obtainable in the continuous limit from $P_{\rm N}$ according to $\bar{N}\, P_{\rm N} \to \bar{\rho} p(\rho)$.

Although the statistics based on the analysis of moments and count probabilities is strictly related to the correlation approach, nevertheless the relative feasibility of computing them from observational data and N-body simulations makes this method particularly suitable to get information about higher order clustering. Actually, the void probability analysis has been extensively applied in the literature to characterize the distribution of galaxies (see, *e.g.*, refs.[149, 383]) and clusters [206, 70]. While the void probability function is a measure of the geometry, rather than of the clustering, of a point distribution, the count-in-cell probabilities P_N weights in a different way regions having different densities. A detailed analysis of the P_N's as a function of the scale have been done by Alimi *et al.* [10] for the CfA1 galaxies and by Bouchet *et al.* [59] for the Strauss *et al.* sample of IRAS galaxies. The results of such investigations show remarkable scaling properties for the galaxy distribution, which confirm results based on the analysis of high-order correlation functions.

7.2.2 Relation to fractal dimensions

Following the definition of Renyi dimensions [318] given in §4.1.2, let us consider a spatial point distribution containing a total number N_t of particles, and suppose it is covered by a set of cubical boxes, all having the same volume $v = r^3$. If $V = L^3$ is the total volume occupied by the point distribution, then $B(r) = (L/r)^3$ is the total number of boxes. The scaling properties of the distribution can be characterized by the box-counting partition function

$$Z(q,r) \;\equiv\; B(r)\sum_N \left(\frac{N}{N_t}\right)^q P_N(r) \;=\; B(r)\frac{\langle N^q\rangle_r}{N_t^q}\,, \tag{7.29}$$

q being a generic real number. In eq.(7.29), $\langle N^q\rangle_r = m_q(r)$ represents the q-th order moment for the cell counting, evaluated at the scale r, and generalizes the moments previously introduced to include any real value of the order q. For $q = 0$, the partition function depends on the number of non-empty boxes and only information about the geometry, rather than on the clustering, of the distribution is provided. In this case eq.(7.29) simplifies to

$$Z(q=0,r) \;=\; B(r)\,(1-P_0)\,. \tag{7.30}$$

For integer $q \geq 2$, the scaling of the partition function can be related to the behaviour of the q-point correlation function, according to eqs.(7.21). Generalizing to moments of any positive integer order,

$$\begin{aligned}\langle N^q\rangle \;&=\; [\langle N\rangle + \dots \text{discreteness terms of order } < q] \qquad\qquad (7.31)\\ &+\; n^q\int_v d^3r_1\dots\int_v d^3r_q\,[1+(\text{disconnected terms of order } < q)+\kappa_q(\mathrm{r}_1,\dots,\mathrm{r}_q)]\,,\end{aligned}$$

where all the discreteness terms become negligible in the $\bar{N} \gg 1$ case.

According to the definition (3.13) of Renyi dimension, we expect for a fractal structure that the partition function (7.29) has a power-law dependence on the scale r, $Z(q,r) \propto r^{\tau_q}$, with the logarithmic slope τ_q that defines the spectrum of generalized dimensions as

$$D_q \;=\; \frac{\tau_q}{q-1}\,. \tag{7.32}$$

Here we recall that, while the formal definition of generalized dimension must be given in the limits of very small scales and of infinite number of points, in practical applications only a limited amount of particles is allowed, so that only finite scales can be considered. In fact, if we cover the distribution with boxes that are too small, most of them will contain just one particle and eq.(7.32) provides $\langle N^q \rangle \simeq \langle N \rangle \propto r^3$. As a consequence, the $Z(q,r)$ partition function becomes nearly independent of r and $D_q \simeq 0$. This result can be interpreted by saying that, at the scales where discreteness effects dominate, we are not measuring the dimension of the fractal structure, but the dimension of each single point that, indeed, is just zero. When only a finite number of objects is allowed, undersampling effects are more severe for the determination of negative order dimensions, which mostly weight underdense regions. For this reason, in the following we will assume that the number of particles is always sufficiently high to permit a safe determination of D_q in the relevant range of scales r and q values.

According to eq.(7.29), we see that the knowledge of the $P_{\rm N}$ probabilities, and, thus, of the generating function, completely specifies the D_q spectrum of generalized dimensions. Following the computations reported in Appendix B, it is possible to express the partition function in terms of the cumulant generating function as

$$Z(q,r) \;=\; -N_t^{-q}\,\frac{B}{N_c}\,\frac{\Gamma(q)}{2\pi i}\int_{(0,N_c)^+} dy\left[\log\left(1-\frac{y}{N_c}\right)\right]^{-q} K'(-y/N_c)\,e^{K(-y/N_c)}\,. \qquad (7.33)$$

(see also ref.[23]). Here we introduced the quantity

$$N_c \;=\; \bar{N}\,\bar{\xi} \;\propto\; r^{3-\gamma}\,, \qquad (7.34)$$

which represents the average number of particles in excess of random within each box. In eq.(7.33), the integration contour $(0,N_c)^+$ on the complex plane runs counterclockwise around the real axis from the origin to N_c (see Figure 7.1). In the next section, we will explicitly compute the integral in eq.(7.33) for a list of hierarchical density distributions.

7.3 Hierarchical distributions

A hierarchical distribution generates a sequence of q-point correlation functions, whose connected part behaves according to eq.(7.2). Accordingly, eq.(7.8) gives for the cumulants

$$k_q \;=\; \bar{\xi}^{-1}\,q^{q-2}Q_q\,N_c^q\,, \qquad (7.35)$$

so that the cumulant generating function can be written as

$$K(t) \;=\; \bar{\xi}^{-1}\sum_{q=1}^{\infty}\frac{q^{q-2}Q_q}{q!}\,(N_c t)^q\,. \qquad (7.36)$$

The above relation shows that the hierarchical generating functions depend upon the variable $N_c t$ and its shape is defined through the sequence of hierarchical coefficients Q_q.

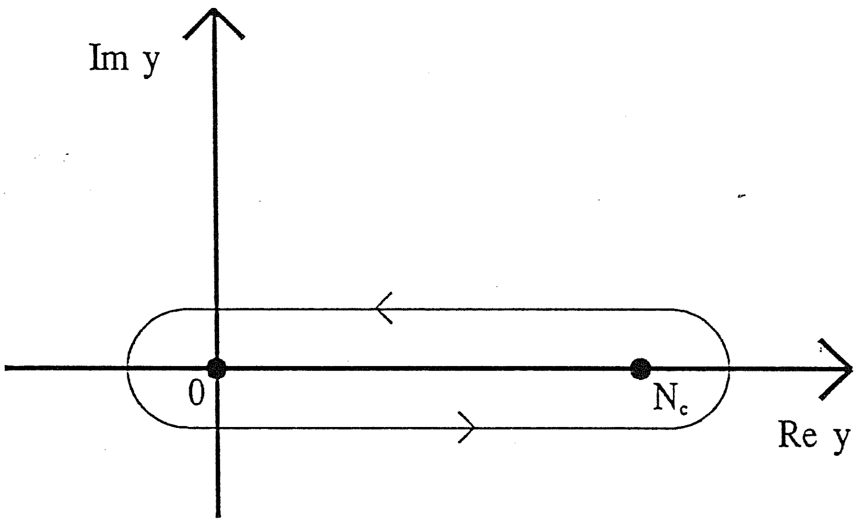

Figure 7.1: *The contour of integration which appears in the expression (7.33) for the $Z(q,r)$ partition function.*

It is remarkable to observe that, for integer $q \geq 2$, the shape of the multifractal spectrum implied at the non-linear clustering scale by any hierarchical model can be easily computed, without explicitly evaluating the integral in eq.(7.33). In fact, assuming negligible discreteness effects in eq.(7.32), we get

$$\langle N^q \rangle \;\simeq\; I_q \, q^{q-2} Q_q r^{3q-\gamma(q-1)} \tag{7.37}$$

at the small scales of non-linear clustering ($\bar{\xi} \gg 1$), where the connected part of the q-point function gives the leading contribution to the q-th order moment. In the above expression, the quantity I_q accounts for the $\mathbf{r}_i$ integrals appearing in eq.(7.32), after making the change of variable $\mathbf{r}_i \rightarrow \mathbf{r}_i/r$. In this way, I_q is a dimensionless quantity, as long as the 2-point function behaves as a power-law up to the scale r and represents only a geometrical factor. According to the scale-dependence in eq.(7.37), we have for the partition function

$$Z(q,r) \;\propto\; r^{(q-1)(3-\gamma)}\,, \tag{7.38}$$

so that the corresponding D_q spectrum reads

$$D_q \;=\; 3-\gamma\,, \qquad \forall q \in \aleph \;, \qquad q \geq 2\,. \tag{7.39}$$

Thus, hierarchical correlation functions imply monofractality of the distribution inside the overdense regions, at least at the scale of non-linear clustering, independently of the detailed shape of the density distribution function. Although positive order dimensions do not distinguish between different hierarchical patterns, we will show in the remainder of this Section that low-order dimensions can discriminate much better between different hierarchical models.

7.3.1 The negative binomial distribution

The negative binomial, or modified Bose-Einstein, distribution was originally introduced in high energy physics to account for the charged particle distributions in hadron-hadron collisions [74, 73]. Its application to the study of the large scale structure of the Universe [72, 71] reveals that it adequately accounts for some aspects of the observed galaxy distribution.

In this model, the count probabilities are

$$P_N = \frac{\Gamma(N+K)}{\Gamma(N+1)\Gamma(K)} \frac{(\bar{N}/K)^N}{(1+\bar{N}/K)^{N+K}}, \tag{7.40}$$

where the parameter K represents the number of independent sources with equal intensity and having random Gaussian emitting field. Alternatively, this parameter can also be interpreted as a measure of correlation for the system, $K = \xi^{-1}$, so that also non-integer values are allowed [131]. In this way, the P_N probabilities of eq.(7.40) generate a hierarchical sequence of cumulants, whose generating function is

$$K(t) = -\bar{\xi}^{-1}\log(1-N_c t), \tag{7.41}$$

with the corresponding hierarchical coefficients $Q_q = (q-1)!/q^{q-2}$ (see, *e.g.*, ref.[147]). In the continuous limit, eq.(7.40) gives the pdf expression

$$p(\rho) = \frac{\bar{\rho}K^K}{\Gamma(K)}\rho^{K-1}e^{-K\rho}. \tag{7.42}$$

Taking the first derivative of $K(t)$ and substituting into eq.(7.33), we obtain

$$Z(q,r) = -\frac{N_t^{1-q}}{N_c}\frac{\Gamma(q)}{2\pi i}\int_{(0,N_c)^+} dy \left[\log\left(1-\frac{y}{N_c}\right)\right]^{-q}(1+y)^{-1-\bar{\xi}^{-1}}. \tag{7.43}$$

Since for $y \sim N_c$ the last term in the integral becomes very small, we can substitute the logarithm with the first term of its McLaurin expansion and let the integration bound N_c go to infinity. Thus, in the non-linear ($\bar{\xi} \gg 1$) clustering regime, eq.(7.43) can be written as

$$Z(q,r) \simeq \left(-\frac{N_c}{N_{tot}}\right)^{q-1}\frac{\Gamma(q)}{2\pi i}\int_{(0,+\infty)^+} dy\, y^{-q}(1+y)^{-1}. \tag{7.44}$$

From the above expression, it is apparent that the only scale-dependence of the partition function comes from the term ${N_c}^{q-1}$, so that $Z(q,r) \propto r^{(q-1)(3-\gamma)}$ and the whole spectrum of generalized dimensions reads

$$D_q = 3-\gamma \quad , \qquad \forall q \in \Re. \tag{7.45}$$

This result generalizes eq.(7.39) to any order q and shows that the negative binomial model implies a monofractal particle distribution at the small scales of non-linear clustering.

7.3.2 The generalized thermodynamical model

The thermodynamical (TD) model has been introduced by Saslaw & Hamilton [335] in order to describe the gravitational clustering in an expanding Universe as a quasi-equilibrium process (see also ref.[333]). This model provides the count-in-cell probabilities

$$P_N = \frac{\bar{N}(1-b)}{N!}\,[\bar{N}(1-b)+Nb]^{N-1}\exp[-\bar{N}(1-b)-Nb]\,. \tag{7.46}$$

Here, b is the ratio of the gravitational correlation energy to the kinetic energy implied by the peculiar motions of N galaxies in the cell volume. If the gravitational interaction is negligible, then $b=0$ and eq.(7.46) gives the P_N's expected for a Poisson distribution. The reliability of the TD model has been widely tested in a series of papers by Saslaw and coworkers, versus both observational data [93, 89] and N-body simulations [203, 202]. Using the above expression for P_N to work out the second-order moment, it can be shown that the second of eqs.(7.21) is recovered by taking $(1-b)^{-2} = 1 + N_c$. Accordingly, the non-linear clustering regime ($\bar{\xi} \gg 1$) corresponds to the virialization condition $b \simeq 1$, and the probabilities (7.46) generate a hierarchical sequence of correlation functions.

According to eq.(7.46), the cumulant generating function reads

$$K(t) = \bar{\xi}^{-1}\,[1-(1-2N_c\bar{\xi})^{1/2}]\,. \tag{7.47}$$

The continuum limit of the P_N probabilities gives

$$p(\rho) = \frac{1}{\sqrt{2\pi\bar{\xi}\rho^3}}\exp\left[-\frac{(\rho^{1/2}-\rho^{-1/2})^2}{2\bar{\xi}}\right], \tag{7.48}$$

which is Gaussian with respect to the variable $y = \rho^{1/2} - \rho^{-1/2}$.

The generalized thermodynamical (GTD) model has been introduced by Fry [147] as an extension of the above model, and is characterized by the cumulant generating function

$$K(t) = \frac{1-\mu}{\mu\bar{\xi}}\left[1-\left(1-\frac{N_c t}{1-\mu}\right)^{\mu}\right] \tag{7.49}$$

where $0<\mu<1$. The corresponding sequence of hierarchical coefficients is $Q_q = (q-1-\mu)'!'/(1-\mu)^{q-1}$, with $(p-\lambda)'!' = (p-\lambda)\,(p-\lambda-1)\ldots(1-\lambda)$. For $\mu = 1/2$, eq.(7.49) reproduces the above mentioned TD model.

Since it is not possible in general to invert analytically the above expression for $K(t)$ to obtain the corresponding probability density function $p(\rho)$, we resort to the computation of the effective action $S(\rho)$. According to eq.(7.11), we obtain

$$S(\rho) = \frac{1-\mu}{\bar{\xi}}\left(\rho+\frac{1-\mu}{\mu}\,\rho^{\frac{\mu}{\mu-1}}-\frac{1}{\mu}\right), \tag{7.50}$$

so that eq.(7.13) gives the approximate expression

$$p(\rho) = \frac{1}{[2\pi\bar{\xi}\rho^{(2-\mu)/(1-\mu)}]^{1/2}}\exp\left[-\frac{1-\mu}{\bar{\xi}}\left(\rho+\frac{1-\mu}{\mu}\,\rho^{\frac{\mu}{\mu-1}}-\frac{1}{\mu}\right)\right]. \tag{7.51}$$

It is worth noting that, for the original TD model, the above expression gives back eq.(7.48), so that the "saddle-point" estimate is correct. This is not surprising, because of the Gaussian appearance of the TD probability density function shown in eq.(7.48). In Figure 7.2 we plot eq.(7.51) as a function of ρ, for two different values of $\bar{\xi}$ (corresponding to the two panels) and for different values of the μ parameter ($\mu = 0.25, 0.5$ and 0.75, going from the most narrow to the widest curves). It is apparent that lowering μ increases the skewness of $p(\rho)$, while decreasing $\bar{\xi}$ makes the distribution more Gaussian.

By differentiating eq.(7.49) and substituting into eq.(7.33) for the partition function, we obtain

$$Z(q,r) \simeq -\frac{N_t^{1-q}}{N_c}\frac{\Gamma(q)}{2\pi i}\int_{(0,N_c)^+} dy \left[\log\left(1-\frac{y}{N_c}\right)\right]^{-q}\left(1+\frac{y}{1-\mu}\right)^{\mu-1} \exp\left\{-\frac{\mu-1}{\mu\xi}\left[1-\left(1+\frac{y}{1-\mu}\right)^{\mu}\right]\right\}. \tag{7.52}$$

As in the case of the negative binomial model, for $N_c \gg 1$ the exponential term becomes so small at $y \sim N_c$ that we can expand the logarithm and deform the integration path to $(0,+\infty)^+$. Accordingly,

$$Z(q,r) \simeq \left(-\frac{N_t}{N_c}\right)^{1-q}\frac{\Gamma(q)}{2\pi i}\int_{(0,+\infty)^+} dy\, y^{-q}\left(1+\frac{y}{1-\mu}\right)^{\mu-1} \exp\left\{-\frac{\mu-1}{\mu\xi}\left[1-\left(1+\frac{y}{1-\mu}\right)^{\mu}\right]\right\}. \tag{7.53}$$

For $q > \mu$, the integral in the above expression rapidly converges at large y values, even without the exponential term. As a consequence, its contribution can be dropped without significantly affecting the result. Under this approximation, the only scale dependence of the partition function occurs through the N_c^{q-1} term. Thus, $Z(q,r) \propto r^{(q-1)(3-\gamma)}$, with a resulting spectrum of generalized dimensions

$$D_q = 3-\gamma \qquad ; \qquad q > \mu. \tag{7.54}$$

Again, this result agrees with the expectation of eq.(7.39), based only on the assumption of hierarchical behaviour of the q-point correlation functions.

For $q < \mu$, the integrand in eq.(7.53) is at most only weakly divergent at the origin, so that the path of integration can be shrunk to the positive real axis. Differently from the $q > \mu$ case, the convergence at large y is ensured now by the presence of the exponential term. Moreover, since in this case even the contribution to the integral due to small y values becomes negligible, we can consider in eq.(7.53) only the contribution for $y \gg 1-\mu$, so that

$$Z(q,r) \simeq \left(\frac{N_t}{N_c}\right)^{1-q}\frac{(1-\mu)^{1-\mu}}{\Gamma(1-q)}\int_0^{+\infty} dy\, y^{\mu-1-q}\exp\left\{-\frac{(1-\mu)^{1-\mu}}{\mu\xi}\,y^{\mu}\right\}. \tag{7.55}$$

After suitably rescaling the integration variable in the previous expression, the scale-dependence of the partition function turns out to be $Z(q,r) \propto N_c^{q-1}\xi^{1-q/\mu}$, so that the low q tail of the

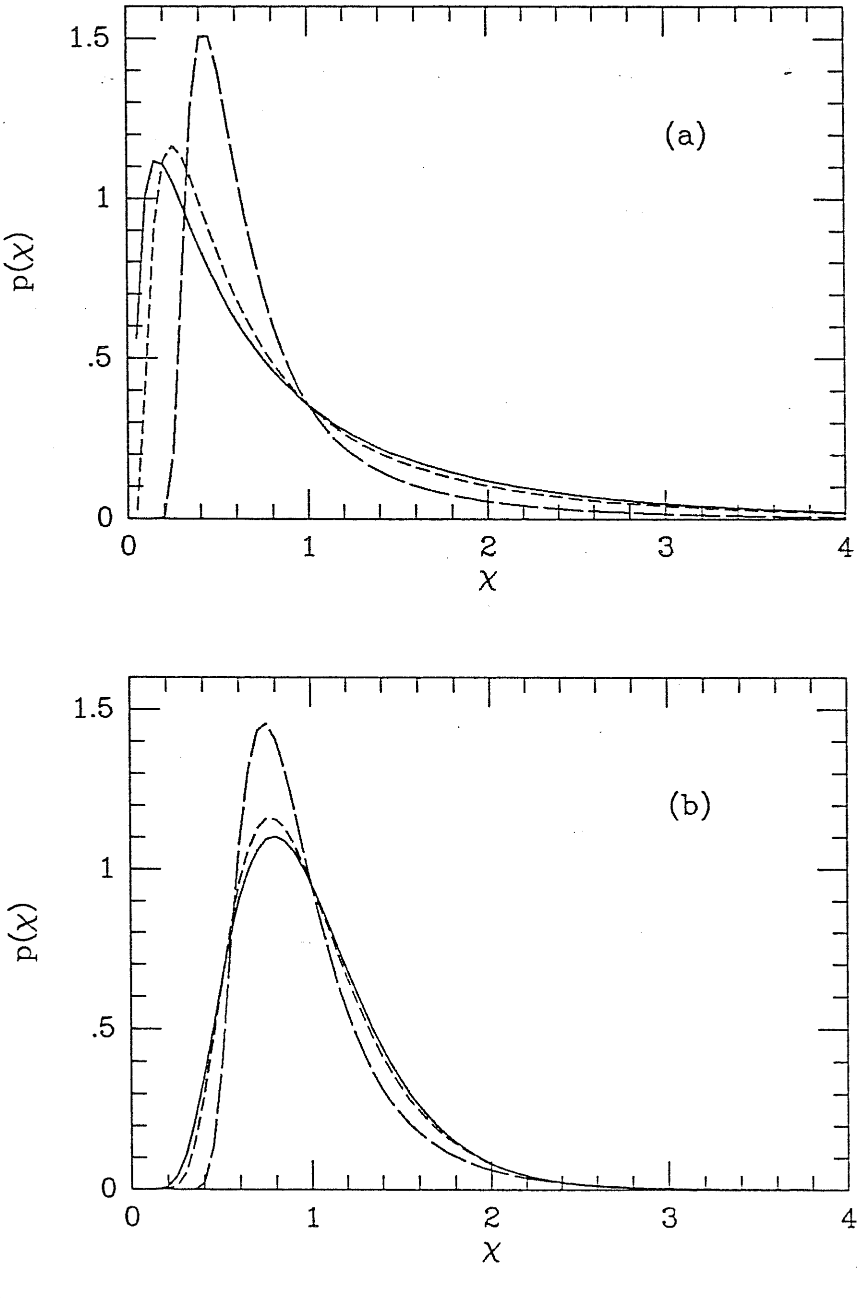

Figure 7.2: *The asymptotic approximation to the GTD probability density function, $p(\rho)$, is plotted at two different scales, corresponding to two different values of $\bar{\xi}$. (a) $R = 2r_o$; (b) $R = 4r_o$ (as usual, r_o is the clustering length). The variable $\chi = \rho/\bar{\rho}$ is normalized to the average density value. Solid, short-dashed and long-dashed curves correspond to different values of the μ parameter, $\mu = 0.25, 0.5, 0.75$, respectively. Note that in the $\mu = 0.5$ case, corresponding to the original TD model, the asymptotic approximation to $p(\rho)$ is rigorous.*

multifractal spectrum it has

$$D_q = 3+\gamma\frac{1-\mu}{\mu}\frac{q}{q-1} \quad ; \qquad q<\mu . \tag{7.56}$$

Differently from the negative binomial model, the GTD distribution implies a non-trivial spectrum of generalized dimensions at the small scales of non-linear clustering, with a manifestly multifractal behaviour. The low-q shape of the resulting D_q spectrum turns out to depend on the specific model (*i.e.*, on the value of the μ parameter). In particular, smaller μ values correspond to larger negative order dimensions, thus indicating a more relevant presence of very underdense regions. This agrees with the expectation based on the shape of $p(\rho)$ (see Figure 7.2), which gives more probability of finding extremely underdense regions as μ decreases.

The multifractal dimension spectrum, that we get for the GTD model, agrees with that obtained by Balian & Schaeffer [23], at least in the scale range where discreteness effects are negligible in the analysis of their scale-invariant model. This is not surprising, since the scale-invariant model considered by these authors is based on the assumption of a power-law behaviour of $K(t)$ as $t \to -\infty$, which is exactly the case for the GTD model (see eq.[7.49]).

According to eq.(7.56), the Hausdorff dimension is $D_o = 3$, independent of μ, thus meaning that the GTD model always implies a space-filling geometry of the clustering. Hence, although this model is adequate to describe the continuous matter density field, it is expected to fail when compared to the *biassed* distribution of galaxies, which correspond to high density peaks, so as to be manifestly non space-filling.

As far as the $f(\alpha)$ spectrum of singularities is concerned, according to eq.(3.19), we get for the crowding index

$$\alpha = \begin{cases} 3-\gamma & q\geq\mu \\ 3+\gamma\frac{\mu-1}{\mu} & q<\mu , \end{cases}$$

so that only two kind of singularities are allowed. The corresponding spectrum reads

$$f(\alpha) = \begin{cases} 3-\gamma & \alpha = 3-\gamma \\ 3 & \alpha = 3+\gamma\frac{1-\mu}{\mu} . \end{cases}$$

Thus, the distribution implied by the GTD model can be described in its overdense regions by a monofractal having dimension $3-\gamma$, while the distribution in the underdense regions is given by a random point distribution, around which the local density increases with the scale as $r^{\gamma(1-\mu)/\mu}$.

7.3.3 The hierarchical Poisson model

This model describes the galaxy clustering in terms of a Poissonian distribution of clusters, each containing a fixed number of members [147, 148]. If N_t is the total number of galaxies and N_o the number of members belonging to each cluster, then the effective number of such clusters is $N' = N_t/N_o$. If $\eta = \langle N' \rangle$ is the average cluster count, then, in order to match the first-order galaxy count of eq.(7.21) we shall take $\eta = \bar{N}/N_o$. The second-order moment for the clusters is $k_2' = \eta + \eta^2$, so that the second of eqs.(7.21) is recovered by assigning $N_o = 1 + N_c$ galaxies per cluster. The cumulants of the resulting distribution are $k_q = N_o^q\, k_q'$, which, in the $N_c \gg 1$ limit, give rise to the hierarchical sequence $k_q = \bar{\xi}^{-1} N_c^q$, with coefficients $Q_q = q^{2-q}$. The corresponding cumulant generating function is

$$K(t) \;=\; \bar{\xi}^{-1}\left(e^{N_c t} - 1\right) . \tag{7.57}$$

Note that the above expression reduces to that characteristic of a purely Poissonian distribution if $\bar{\xi}^{-1} = \bar{N}$. Following the same scheme of calculation as for the previous models, we get for the partition function

$$Z(q,r) \;\simeq\; \left(-\frac{N_t}{N_c}\right)^{1-q} \frac{\Gamma(q)}{2\pi i} \int_{(0,+\infty)^+} dy\, y^{-q} \exp\left[-y + \frac{1}{\bar{\xi}}\left(e^{-y} - 1\right)\right] . \tag{7.58}$$

Since for any q value the second exponent in the exponential term is negligible already at small y values, eq.(7.58) implies the scaling $Z(q,r) \propto r^{(q-1)(3-\gamma)}$. The resulting dimension spectrum reads

$$D_q \;=\; 3 - \gamma \qquad ; \qquad \forall q \in \Re , \tag{7.59}$$

thus showing the monofractality of the hierarchical Poisson model at the small scales of non-linear clustering.

7.3.4 The BBGKY hierarchical model

In his solution of the BBGKY equations, Fry [145] suggested that, in the strongly non-linear, fully relaxed regime, they produce q-point correlation functions of hierarchical type, with coefficients $Q_q = (4Q/q)^{q-2} q/2(q-1)$, where $Q \equiv Q_3$. Accordingly, the corresponding cumulant generating function [148] reads

$$K(t) \;=\; \bar{\xi}^{-1}\left[N_c t - \frac{N_c t}{8Q}\,\mathrm{Ein}(-4QN_c t)\right] . \tag{7.60}$$

Here, $\mathrm{Ein}(y) = \int_0^y \frac{dx}{x}(1 - e^{-x})$ is the modified exponential integral [6], that, for y larger than a few, can be approximated as $\mathrm{Ein}(y) \simeq \gamma + \log y$ ($\gamma \simeq 0.5772$ is Euler's constant, not to be confused with the slope of the 2-point function), with corrections of the order e^{-y}. The expression (7.60) for $K(t)$ is such that no arbitrarily large values of N_c are allowed. In fact, for quite large values of $4QN_c$, the requirement $K'(-1) > 0$ leads to the constraint

$$N_c \;<\; \frac{1}{4Q}\, e^{8Q-1-\gamma} . \tag{7.61}$$

It is however to be stressed that, for usual Q values around unity, quite large (~ 100) values for N_c are allowed.

After differentiating eq.(7.60) and substituting into eq.(7.33), the partition function becomes

$$Z(q,r) \;=\; -\frac{N_t^{1-q}}{N_c}\,\frac{\Gamma(q)}{2\pi i}\quad \int_{(0,N_c)^+} dy\,\left[\log\left(1-\frac{y}{N_c}\right)\right]^{-q}\left\{1-\frac{1}{8Q}\left[\mathrm{Ein}(4Qy)-1-e^{-4Qy}\right]\right\}$$
$$\exp\left\{-\frac{y}{\xi}\left[1-\frac{1}{8Q}\,\mathrm{Ein}(4Qy)\right]\right\}\,. \tag{7.62}$$

Because of the inequality (7.61), the exponent in the last term of eq.(7.62) is constrained to remain strictly negative for any allowed y value, so that the integral takes mainly contributions from small $y \ll N_c$. Hence, we can expand also in this case the logarithmic term as $\log(1-y/N_c) \simeq -y/N_c$.

For $q>0$, the integrand becomes so small at $y \sim N_c$, even without the exponential term, that we can drop it and let the integration bound N_c go to infinity, without significantly affecting the result. Under these approximations, eq.(7.62) becomes

$$Z(q,r) \;\simeq\; \left(-\frac{N_t}{N_c}\right)^{1-q}\frac{\Gamma(q)}{2\pi i}\int_{(0,+\infty)^+} dy\,y^{-q}\left\{1-\frac{1}{8Q}\left[\mathrm{Ein}(4Qy)-1-e^{-4Qy}\right]\right\}\,. \tag{7.63}$$

Also in this case, the scale dependence of the partition function reduces to $Z(q,r) \propto r^{(q-1)(3-\gamma)}$, with the corresponding generalized dimensions

$$D_q \;=\; 3-\gamma \qquad ; \qquad q>0\,. \tag{7.64}$$

If $q<0$, the contribution of the y^{-q} term at large y's is so large for $y \sim N_c$, that it is not possible to drop the exponential term in eq.(7.62). Since for sufficiently negative q's, the integrand is heavily suppressed at $y<1$, after changing the integration variable $y \to y/\xi$ and substituting the modified exponential integral with its asymptotic approximation, we get

$$Z(q,r) \;\simeq\; \left(\frac{N_t}{\bar N}\right)^{1-q}\frac{1}{\Gamma(1-q)}\quad\int_0^{\bar N} dy\,(-y)^{-q}\left\{1-\frac{1}{8Q}\left[\log 4Q\bar\xi y+\gamma-1\right]\right\}$$
$$\exp\left\{-y\left[1-\frac{1}{8Q}\left(\log 4Q\bar\xi y+\gamma\right)\right]\right\}\,. \tag{7.65}$$

Taking eq.(7.61) into account and since the exponential term is very small for $y \sim \bar N$, it is again possible to extend the integration interval to infinity, so that

$$Z(q,r) \;\simeq\; \left(\frac{N_t}{\bar N}\right)^{1-q}\frac{1}{\Gamma(1-q)}\int_0^{+\infty} dy\,y^{-q}e^{-y} \;=\; \left(\frac{N_t}{\bar N}\right)^{1-q}\,. \tag{7.66}$$

According to the above scale-dependence of the partition function, the negative q tail of the multifractal spectrum reads

$$D_q \;=\; 3 \qquad ; \qquad q<0\,. \tag{7.67}$$

Thus, the non-linear clustering arising from the BBGKY model is characterized by a D_q spectrum that is discontinuous at $q=0$.

In order to explicitly evaluate the Hausdorff dimension, we note that, for $q = 0$, the integral in eq.(7.62) takes the form

$$\int_0^a dx\, f'(x)\, e^{f(x)} \;=\; e^{f(a)} - e^{f(0)} \,,$$

so that the integral in the expression of the partition function can be easily evaluated to give

$$Z(q=0,r) \;\simeq\; \frac{N_t}{\bar{N}} \left\{ \exp\left[-\bar{N} + \frac{\bar{N}}{8Q} \left(\log 4QN_c + \gamma \right) \right] - 1 \right\} . \qquad (7.68)$$

Because of the inequality (7.61), the exponential term in the above expression becomes sufficiently small to be neglected, and

$$Z(q=0,r) \;\propto\; r^{-3} \qquad \Rightarrow \qquad D_o = 3 \,. \qquad (7.69)$$

Thus, the multifractal structure implied by the BBGKY model corresponds to a space filling distribution, whose scaling properties abruptly change when passing from underdense to overdense regions. In terms of the singularity spectrum, it turns out that, as for the GTD model, the crowding index α is a dichotomic variable,

$$\alpha \;=\; \begin{cases} 3-\gamma & q > 0 \\ 3 & q \le 0 \,, \end{cases}$$

and the $f(\alpha)$ spectrum of singularities turns out to be

$$f(\alpha) \;=\; \begin{cases} 3-\gamma & \alpha = 3-\gamma \\ 3 & \alpha = 3 \,. \end{cases}$$

This result can be interpreted by saying that the corresponding distribution is given by the superposition of a monofractal structure, having dimension $3-\gamma$ and determining the clustering inside the overdense regions, and of a Poisson distribution, that dominates the statistics inside the "devoid" regions.

7.4 Discussion of the results

Hierarchical models have been proved to be quite successful in reproducing several aspects of the non-linear clustering of galaxies at small scales, as well as of the particle distributions generated by cosmological N-body simulations. Such an agreement is even more remarkable, since some of these models do not represent purely phenomenological descriptions of the texture of the galaxy distribution, but have a theoretical origin that is rooted into general (and, maybe, plausible) assumptions about the nature of the non-linear gravitational clustering. This is the case for the TD model [335, 333] and for Fry's [145] solution to the BBGKY equations, discussed in the previous Section. Attempts to recognize the more adequate hierarchical model to reproduce the non-linear clustering (see, *e.g.*, refs.[147, 148, 59, 60]) have shown that all such models are more or less equally efficient in accounting for the clustering inside the overdense structures, while they have rather different behaviours in the low-density part of the distribution. In this respect, the study of the multifractal dimension spectrum is a very promising approach, since the D_q curve contains not only information about the more clustered regions in its positive q part, but also accounts for the distribution inside the underdense regions for $q < 0$.

In order to test the predictions of the hierarchical distributions studied in the previous Section, we plot in Figures 7.3 and 7.4 the results of the multifractal analysis of N-body simulations, as presented in Chapter 5. More in detail, Figure 7.3 shows the D_q curve characterizing the non-linear clustering developed by an initial CDM spectrum (in an Einstein-de Sitter Universe), for both the whole particle distribution (Figure 7.3*a*) and for the "biassed" galaxy distribution. Figure 7.4 is the same as Figure 7.3, but for an initial Zeldovich spectrum.

Already at first glance, the complex scaling behaviour displayed by these D_q curves at low q's definitely rules out most of the hierarchical models, that otherwise were all equally efficient in reproducing the flat D_q profile at large q's. The absence in the data of a monofractal behaviour, as predicted by the negative binomial and by the hierarchical Poisson models, is apparent. On the other hand, the smooth shape of the plotted D_q spectra indicates that even the BBGKY hierarchical model does not give a faithful description of the non-linear clustering. For these reasons, we only plot the D_q spectrum predicted by the GTD model for $\mu = 0.5$ (which corresponds to the original model proposed by Saslaw & Hamilton [335]) and $\mu = 0.75$.

We also plot the D_q spectrum for the model proposed by Jones, Coles & Martinez [212], based on approximating the $f(\alpha)$ spectrum of singularities to a parabolic function. These authors showed that this kind of singularity spectrum produces a lognormal shape for the probability of cell occupation, with a resulting spectrum of generalized dimensions

$$D_q = (D_o - \alpha_o)q + D_o . \tag{7.70}$$

Here $\alpha_o > D_o$ is the value of the crowding index corresponding to the maximum $f(\alpha)$ value, that is $f(\alpha_o) = D_o$. Although Jones *et al.* [212] have shown that eq.(7.70) is quite successful in reproducing the D_q spectrum for the CfA galaxy distribution for moderately low values of $|q|$, nevertheless it also has serious drawbacks. For instance, it gives negative generalized dimensions at positive q's, which imply a very rapid decreasing of the density around strong singularities. This behaviour is quite easy to understand in the framework of a lognormal distribution. In fact, a lognormal distribution is characterized by Kirkwood type correlation functions, as those provided by eq.(2.23) [84]. Therefore, neglecting the discreteness terms in eq.(7.32), we get

$$\langle N^q \rangle = n^q \int_v d^3r_1 \dots \int_v d^3r_q \prod_{i>j}^{\binom{q}{2}} [1 + \xi(r_{ij})] . \tag{7.71}$$

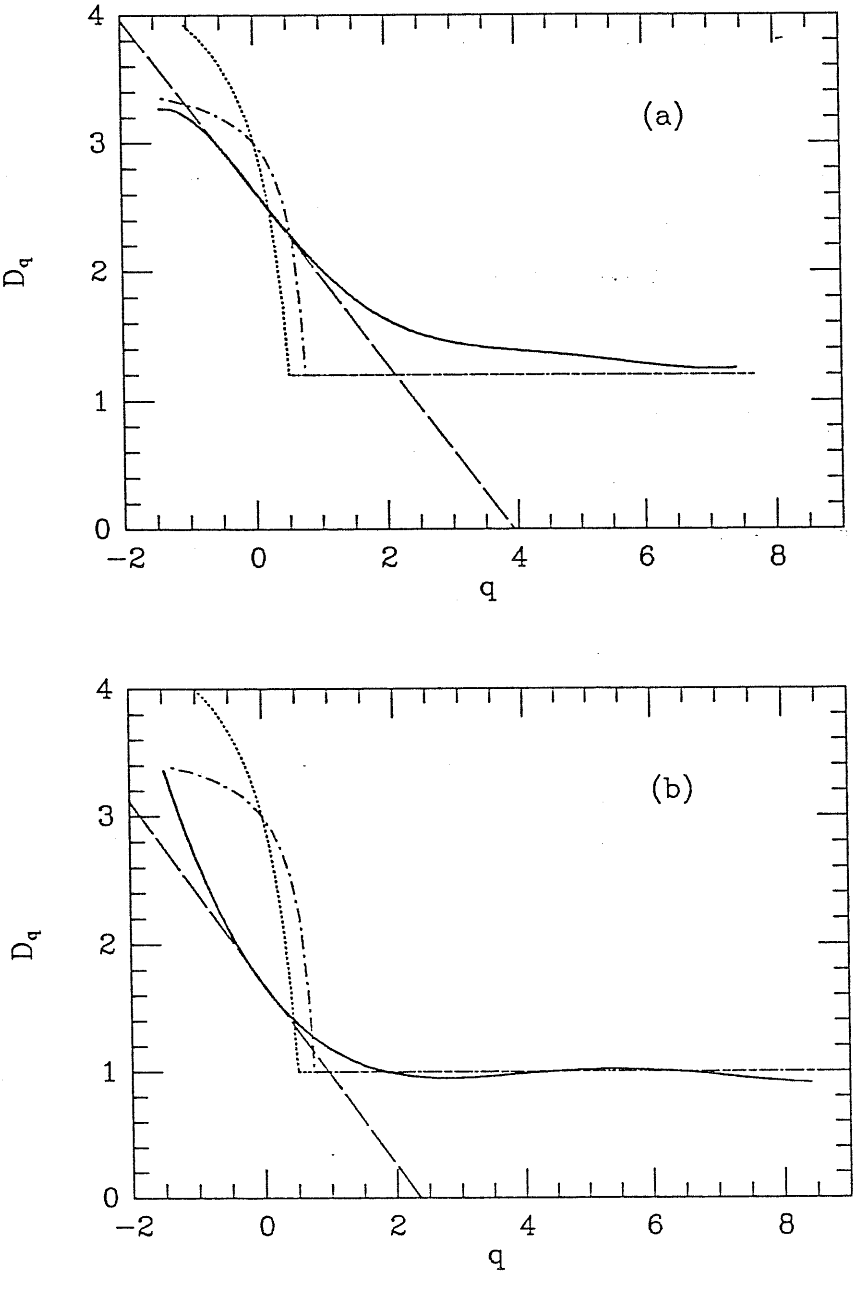

Figure 7.3: *The multifractal spectrum of the generalized dimensions as obtained from the analysis of N-body simulations, for an initial CDM spectrum (solid line). (a): background particle distribution; (b) biassed galaxy distribution. Also plotted are the model D_q spectra of the GTD model, for $\mu = 0.5$ (dash-dotted line) and $\mu = 0.75$ (dotted line), and of the "lognormal" model of ref.[212] (dashed line).*

At sufficiently small scales, the leading term in the integrand is $\xi^{q(q-1)/2} \propto r^{-\gamma q(q-1)/2}$. Thus, in the continuous limit, eq.(7.71) gives $\langle N^q \rangle \propto r^{3+(q-1)(3-\gamma q/2)}$ and the scaling of the partition function reads

$$Z(q,r) \;\propto\; r^{(q-1)(3-\gamma q/2)} \qquad \Rightarrow \qquad D_q = 3 - \frac{\gamma q}{2} . \tag{7.72}$$

The resulting dimension spectrum is a linearly decreasing function of q and becomes negative for $q > 6/\gamma$.

A first indication that we get from the plots of Figure 7.3 is that, for $q \gtrsim 1$, the GTD model nicely fits the data as well as any hierarchical model. The only exception is represented by the background distribution for the CDM model, where the D_q curve definitely flattens only at rather large q values. This is not surprising, since this is the least clustered distribution, and, consequently, is expected to be hierarchical only in its most overdense regions. The situation is different at low q values, where the GTD model gives a steepening of the D_q profile too sharp for any value of the μ parameter.

For moderately low values of $|q|$, the lognormal model [212] is much closer to the data. This agreement is less evident for the biassed distributions, where the selection of high density peaks causes a sharp variation of the scaling properties, when passing from the overdense to the underdense regions. Since for such q values the corresponding partition function mostly depends on the number of occupied cells, and not on their population, the lognormal model is adequate to account for the geometry of the distribution, rather than for the strength of the clustering. If this is the case, we should expect the lognormal model not to be able to reproduce the scaling properties of the distribution in both the very overdense and very underdense regions, where the effect of non-linear gravity is more evident. Since in the framework of the GTD model the $D_{-\infty}$ value is uniquely fixed by the μ parameter (see eq.[7.54]), the statistics of the very underdense regions should specify the hierarchical model implied by the non-linear gravitational clustering. It is however evident from the plotted data that the D_q curves have serious problems converging to $D_{-\infty}$. This is a consequence of the finite number of particles available in the N-body simulations, that does not allow an adequate sampling of the extremely underdense regions. Only in the case of the background distribution of the CDM model (Figure 7.3*a*), there is some evidence that the D_q curve tends to flatten at the smaller allowed q's. In fact, since such a distribution is not so strongly clustered as the others, not all the particles are concentrated in the overdense regions and some sampling of the devoid structures is still allowed. However, also in this case, no definite conclusions can be reached about the value of $D_{-\infty}$.

A further effect of undersampling resides in the lowering of the Hausdorff dimension for the background distributions with respect to the value $D_o = 3$, expected for a continuous density field. In fact, due to the presence of strong small-scale clustering, the sampling particles are not uniformly distributed, but are preferentially located around the density peaks. This induces a sort of biassing in the particle distribution, which modifies its geometry, with respect to that of the underlying continuous density field. Although present, this effect

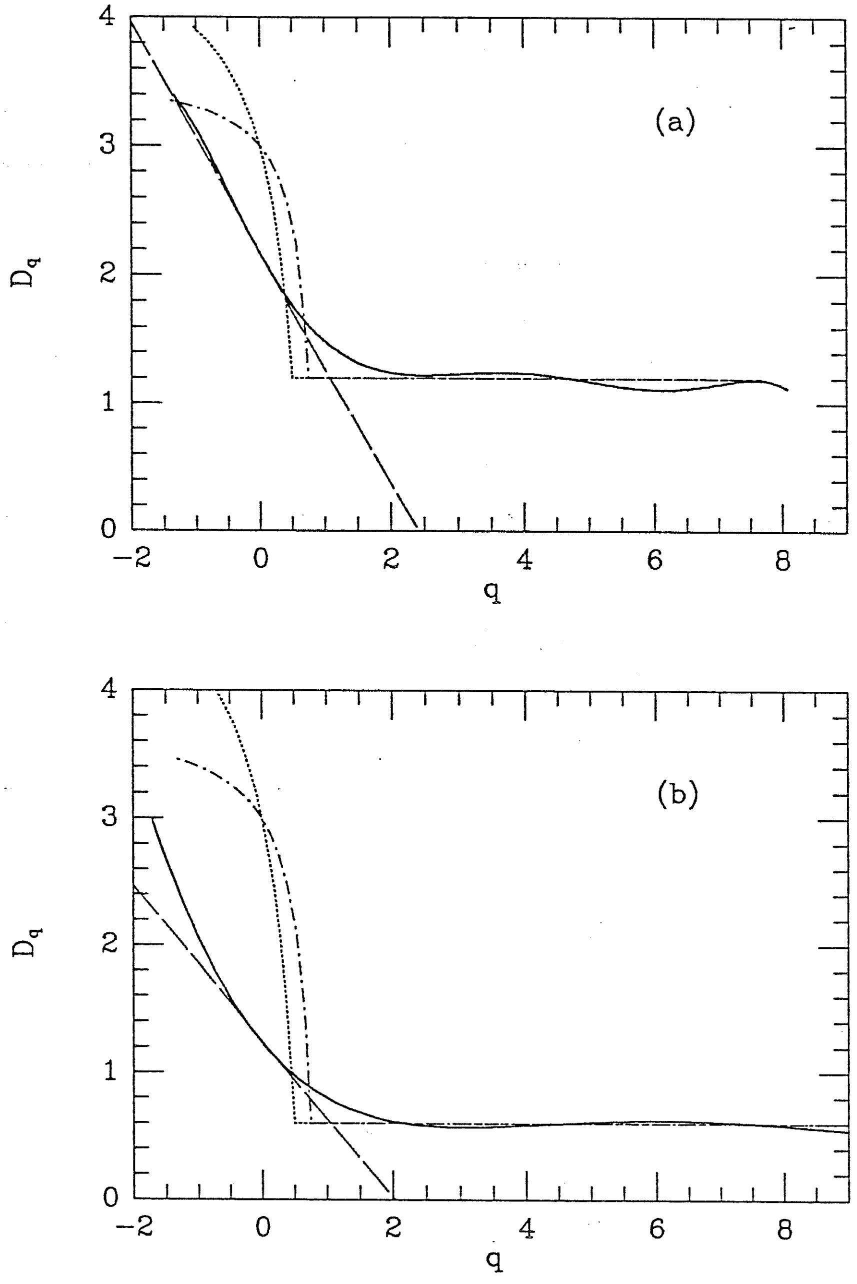

Figure 7.4: *The same as in Figure 7.3, but taking a primordial Zeldovich spectrum in the N-body simulations.*

is not so relevant for the CDM model, while it is more important in the case of the Zeldovich initial spectrum. In this case, a strong small-scale clustering rapidly develops and causes D_o to be around two (see also Table 5.3).

A general conclusion that we can draw from the above results is the extreme relevance of properly studying the clustering pattern inside the underdense regions. In fact, as already observed in ref.[147], the shape of the generating function in the non-linear ($\bar{\xi} \gg 1$) clustering regime is essentially specified by the positive order moments, that mostly weights the overdense regions. Consequently, an arbitrary variation of the distribution inside the "devoid" regions has only a small effect on the overall shape of $K(t)$. Thus, it is clear that a precise determination of D_q for $q < 0$ (*e.g.*, by using very-high resolution N-body simulations) is necessary in order to provide a unique characterization of the non-linear gravitational clustering.

As a further point, it is worth observing that the computations of the D_q spectra, that we made in §7.3, have been carried out in some limiting cases. For instance, the explicit evaluation of the partition function of eq.(7.33) has been done by introducing some approximations that, in general, are expected to be more accurate for larger and larger values of $|q|$. This could be the reason for the sharp change of the slope of the D_q spectrum for the GTD and the BBGKY models. Furthermore, all the results presented in §7.3 have been obtained with the underlying assumption that discreteness effects are negligible at the small scales of non-linear clustering, that we considered. Although this must be true for the continuous matter density field, it should not be correct when dealing with the galaxy distribution, which is traced by the high density peaks. In this case, the presence of Poissonian sampling noise can seriously affect the determination of low-order generalized dimensions. In this context, it is clear that, before drawing any conclusion about the ability of a model to reproduce the statistics of a given data set, it would be appropriate to directly compare the data to synthetic distributions, containing the same number of points and selection effects as in the real data, but with *a priori* known statistical properties.

In order to show how Poisson sampling noise can seriously affect the estimate of fractal dimensions, we plot in Figure 7.5 the Hausdorff and the correlation dimensions for different hierarchical models and taking different amounts of discreteness. The scale-dependence of the Hausdorff dimensions have been obtained through the estimate of the local slope of the partition function, given by eq.(7.30). The corresponding void probability function, $P_0 = e^{K(-1)}$, is evaluated from the expression of the cumulant generating function. The correlation dimension is simply based on the estimate of the scaling of the second-order moment (see eq.[7.32] for $q = 2$). It does not depend on the details of the hierarchical distribution, but only on the logarithmic slope, $\gamma = 1.8$ of the 2-point correlation function. Solid lines are for a point distribution having a mean interparticle distance, d, which is equal to the correlation length, r_o, as it is to good approximation for the observed galaxy distribution. Dashed lines are for a distribution with $d = 0.2r_o$, so that discreteness effects

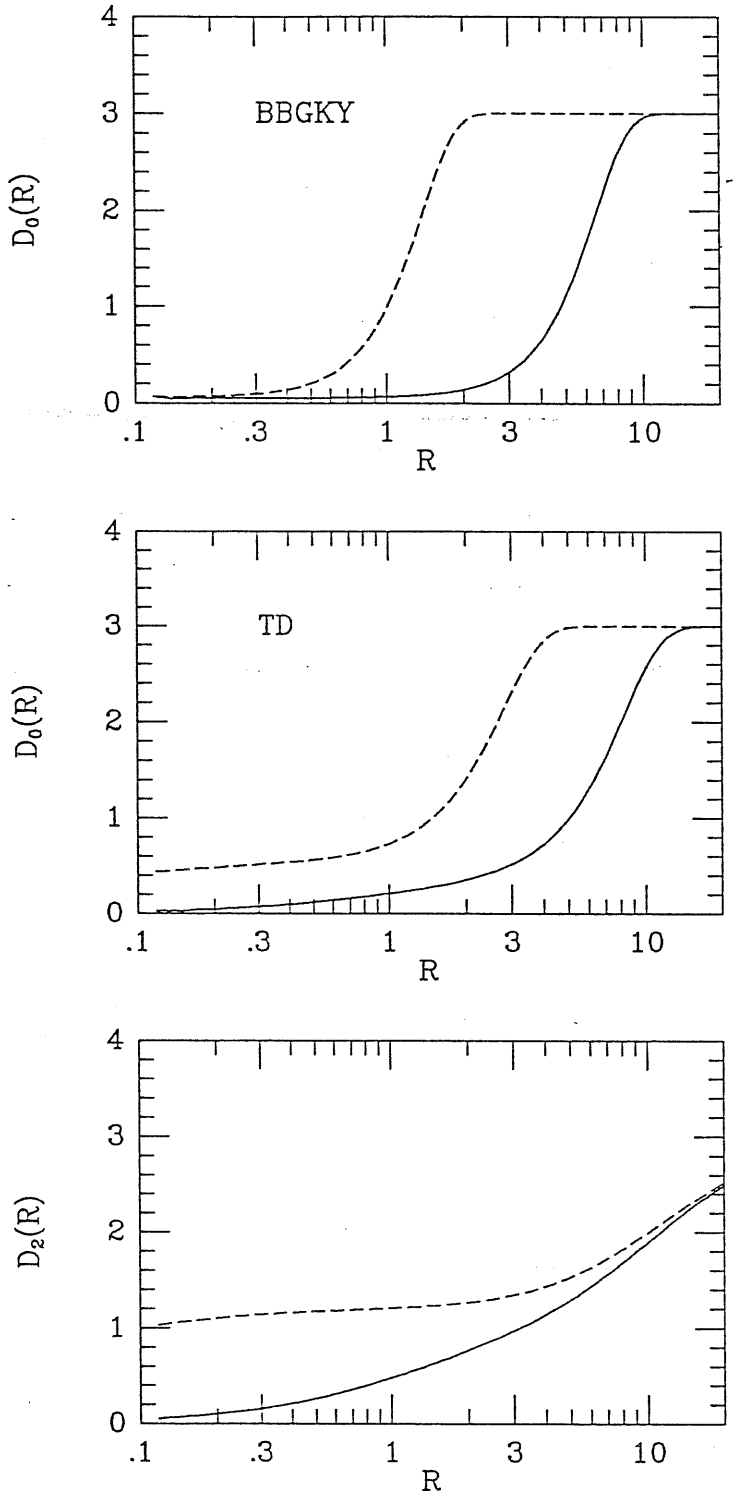

Figure 7.5: *The Hausdorff dimension, D_o, for the BBGKY (upper panel) and TD (central panel) models, and the correlation dimension, D_2, (lower panel) are plotted against the physical scale R, for two distributions having different amounts of Poissonian sampling noise. Solid lines: $d = r_o$ (d is the mean interparticle distance), as for the observed galaxy distribution; dashed lines: $d = 0.2r_o$. Units of R are chosen in such a way that $r_o = 5$.*

are less relevant. Units of the R variable are chosen in such a way that $r_o = 5$. With this normalization, a consistent comparison can be made with the galaxy clustering, taking the units of the R variable to be h^{-1} Mpc. A first important remark is that no possibility exists to detect a well defined scaling regime for a distribution having $d = r_o$, as it is for galaxies, since the local dimension never takes a nearly constant value over a sufficiently large scale range. Viceversa, a continuous trend is observed, with $D_q(R)$ ranging from zero at small scales, where Poisson sampling noise dominates, to three at large scales, where homogeneity is reached. This leads to the paradoxical conclusion that, on the ground of the detected 2-point galaxy correlation function, no conclusions can be drawn about the scale-invariance, although its power-law shape has historically been the reason to describe galaxy clustering in terms of a fractal process. Thus, the detection of scale-invariant behaviour for the galaxy distribution should suggest a stronger small-scale clustering than expected on the basis of the canonical 2-point function. A comparison between the Hausdorff dimension of the BBGKY and TD models shows that the former has a transition from small-scale shot-noise ($D_o \simeq 0$ regime) to large-scale homogeneity ($D_o \simeq 3$ regime) that is more rapid and occurs at smaller scales. As far as the correlation dimension is concerned, we note that only for the more dense (or more clustered) distribution is there a scale range where it takes a rather constant value, $D_\nu \simeq 1.2$, thus indicating the presence of fractal behaviour.

As a concluding remark, we would like to stress that the reliability of studying the D_q spectrum of generalized dimensions in order to characterize the global texture of the galaxy distribution and compare it to theoretical models. In fact, a single plot, namely the D_q curve, contains a great amount of statistical information, ranging from the scaling properties of higher order correlation functions, implied by the $q > 0$ tail, to the scale dependence of the void probability function, which is strictly related to the definition of Hausdorff dimension, to the counts in the underpopulated cells, that specify the negative-order dimensions and could be extremely useful in discriminating between different models. For these reasons, the fractal description of clustering surely represents a powerful tool in order to obtain precise hints about the nature of the non-linear gravitational dynamics and its scale-invariant properties.

Most of the results presented in this Chapter are contained in a paper that is in press in *Montly Notices of the Royal astronomical Society* (Borgani 1992, [64]).

Conclusions

In this Thesis we addressed the problem of characterizing the scale-invariant properties of the large-scale distribution of galaxies and galaxy clusters and explaining their origin in the framework of the gravitational instability picture. To this purpose, we considered cosmological N-body simulations, to probe the dynamical development of non-linear clustering at small and intermediate scales (see Chapter 5), as well as the Plionis *et al.* [300] (PBF) angular samples of galaxy clusters of different richness, in order to check the extension of the scaling properties associated with non-linear clustering at the larger scales ($\gtrsim 10h^{-1}$ Mpc) of linearity (see Chapter 6). To this purpose we applied both the classical correlation analysis and the fractal analysis.

As for the correlation analysis of N-body simulations, we attempted to investigate high-order correlations and found that the hierarchical expression, $\kappa_n \propto \xi^{n-1}$ (see eq.[2.24]), is always associated with the small-scale clustering, as predicted by several models for non-linear gravitational dynamics. The possibility of detecting for the first time correlations up to the fourth order allowed us to compare the proposed solutions of the BBGKY equations for a collisionless, self-gravitating fluid (see refs.[145, 183] and §4.1.4) to the "exact" clustering representation furnished by N-body simulations. We verified that such solutions reproduce quite well the shape and the amplitude of *simulated* higher-order correlation functions.

A similar correlation analysis for the cluster distributions showed a remarkable connection between clustering strength and richness. The 2-point function scales with cluster richness according to the prediction of *biassing* (see §4.4). The effect of superimposing a threshold on the galaxy density field to select clusters is clearly visible on the 3-point function. Its amplitude increases as higher peaks are selected, according to the expectation that non-Gaussian statistics are introduced as a threshold effect. The 3-point cluster function is also consistent with the hierarchical model, expecially as richer systems are considered.

The results based on the extensive application of fractal analysis methods (see Chapter 3) are of particular relevance. The advantage of using the fractal approach resides in the detailed information provided about the existence and the extension of scale-invariant properties. The introduction of the concept of the multifractal spectrum of generalized dimensions [277] allows one to collect in a very compact way information not only about the statistics inside the overclustered regions, as correlation functions do, but also on the scaling of the void probability function and on the distribution in the underdense parts of the distribution. This fact is remarkable since the nature of the distribution inside underdensities turns out to be much more model discriminant than the statistics of the overdense regions (see refs.[390, 148] and Chapter 7). Despite the fact that methods of fractal analysis represent powerful tools for clustering analysis, nevertheless they are based on different approximations to the formal definition of fractal dimension. Furthermore, their introduction to the study of complex dynamical systems and deterministic chaos has been motivated by their reliability when applied to well sampled fractal structures, while the presence of characteristic scales in the galaxy distribution and the limited sizes of data sets could seriously affect their performance. For these reasons, we tested in detail a list of fractal dimension estimators on several point distributions with a priori known statistical properties. Although this analysis has been made in view of applications in the cosmological context, nevertheless its results are of general interest in all physical situations where the analysis of fractal point distribution is required. After verifying the advantages and the pitfalls of each of these methods as a function of sample richness and clustering strength, we applied them to the analysis of N-body simulations and cluster distributions.

Very interesting results come from the analysis of N-body simulations. We found that a scale-invariant fractal behaviour is always associated to the non-linear gravitational clustering for the distribution of matter as well as of peaks of the initial density field. This is a robust outcome of our analysis, which comes out independently of initial conditions. As small-scale self-similarity is established, it progressively extends to larger scales, as the typical clustering length increases. A further remarkable result is that a fractal dimension near to one always characterizes the clustering inside the overdense regions, while dependence on the initial conditions only determines details of the D_q dimension spectrum. This means that both the isothermal density profile of galaxy halos, $\rho(r) \propto r^{-2}$, indicated by flat rotation curves, and the shape of the galaxy 2-point function, $\xi(r) \propto r^{-1.8}$, are natural products of non-linear gravitational dynamics, which erases any information about the initial conditions. The rather flat profile of the D_q curve for $q > 0$ also indicates that monofractal statistics characterizes the overdense structures. The connection between fractal properties and correlation functions (see Chapter 7) shows that hierarchical correlations turn into monofractality of the D_q spectrum at positive q's, consistent with our results.

From the point of view of the study of complex dynamical systems, the non-linear gravitational clustering represents one of the few known examples of dynamically generated fractal structure. In this context, it would be of interest to verify whether the detected fractality is the signature of an underlying chaotic dynamics. If this were the case, then a suitable analysis of N-body simulations should indicate an exponential divergence of the phase space trajectories of the systems during the evolution, which is the signature of the unpredictable (chaotic) character of the underlying dynamics. The evaluation of the corresponding Lyapunov exponents (see, *e.g.*, ref.[277]) should quantify the degree of chaotic behaviour of non-linear gravity. Although "exact" N-body simulations represent a necessary ingredient for this kind of investigation, analytical approaches could also be usefully employed, for instance by resorting to approximate dynamical models accounting for the essential features of non-linear gravity (*e.g.*, the adhesion approximation described in §4.1.3).

A different situation should however be expected as the larger scales ($\gtrsim 10h^{-1}$ Mpc) traced by the cluster distribution are considered, where the gravitational dynamics are still in the linear regime. The fractal analysis of the PBF cluster samples (see Chapter 6) shows that the distribution of the richest clusters displays a remarkable fractal behaviour, which however breaks down at the angular scale $\vartheta \sim 7°$. At the depth of the Lick map, this angle corresponds to a physical scale $R \sim 20h^{-1}$ Mpc, similar to the cluster correlation length. Simulations of projection effects on a self-similar point distribution indicate that the characteristic scale detected in the angular distribution is not a spurious projection effect, rather it is inherent to the spatial cluster distribution. This strongly points against a purely fractal picture of the Universe, extending out to arbitrarily large scales (see, *e.g.*, ref.[87]). The resulting dimension spectrum has $D_q \simeq 1$ for $q \gg 1$, thus confirming what was found for N-body simulations: non-linear clustering is always associated with a fractal behaviour and a dimension of nearly one characterizes the scaling inside the overdense regions. However, there is a fundamental difference between the two cases, which renders the results for clusters absolutely unexpected. In fact, while the non-linear clustering displayed by N-body particles and by galaxies at scales of few Mpc is dynamically generated, that relevant for clusters has a statistical origin, which is related to the selection of the exceptionally high peaks of the underlying density field. Therefore, it is surprising that the resulting fractal properties are very similar in the two cases, despite the largely different dynamical ranges where they develop. Fractal scaling is the imprint of non-Gaussian statistics, while the random-phase prescription provided by inflation should imply Gaussianity at the scales of linearity. Then, the question that arises is whether selecting high peaks of an underlying Gaussian background could account for the observed fractality of the cluster distribution, or do we need something else. On the one hand, the realization of a similar analysis on available redshift cluster samples could be important to definitely assess the reliability of our results (Borgani, Martinez & Valdarnini, in preparation). On the other hand, simulations of large-scale clustering should help to understand the consequence of a self-similar cluster distribution at large scales on current models for the generation of primordial fluctuations and structure formation.

As a concluding remark, we would like to point out that, despite the great amount of statistical information provided by correlation and fractal analyses, nevertheless it is difficult to expect that such methods provide an exhaustive representation of the observed large-scale structure. Several other methods, such as topology analysis, count-in-cell statistics and void probability functions, though connected to the methods we used, could be better suited to revealing certain aspects of clustering (see Chapter 2). In addition, the study of the large-scale peculiar motions should provide a more and more precise map of the cosmic matter distribution as a larger amount of data will be available in the near future. Furthermore, the increasing sensitivity of measurements of CMB temperature anisotropies at various angular scales will lead in few years to a much more precise understanding of the initial conditions for structure formation. Extended galaxy redshift surveys are now going on, while even more ambitious projects are expected. The possibility of mapping in detail the three dimensional galaxy distribution is surely a unique opportunity to test dynamical models of structure formation. For these reasons, we believe that the study of the large-scale structure of the Universe will represent in the near future an even more exciting field of investigation and the development and refinement of methods of analysis will greatly contribute to provide a much more clear statistical and dynamical picture.

Appendix

A The moment method

In this Appendix we describe the moment method used to evaluate higher order correlation functions. We applied this method in Chapter 5 to analyze the clustering properties of N-body simulations. We show how the coefficients of the 3- and 4-point functions are related to the second- and third-order moments of neighbour counts.

A.1 The 3–point function

According to eq.(5.10), the second–order *central moment*, $s_k^{(2)}$, is related to the 3-point correlation function by means of the relation

$$s_k^{(2)} \;=\; \langle N_k^2\rangle - \langle N_k\rangle^2 \;=\; \langle N_k\rangle + N_k^2\,\xi_k^2\left(\frac{J_2}{\xi_k} - K_1^2\right) + I_3\,. \qquad (A1)$$

Here

$$\xi_k \;\equiv \xi(r_k) \;=\; K_1^{-1}\,\frac{\langle N_k\rangle - N_k}{N_k}\,, \qquad (A2)$$

is the value of the *unsmoothed* 2-point function, evaluated in the k-th bin. In eq.(A1), the connected 3-point function enters through the integral

$$I_3 \;=\; n^2\int_{r_{k-1}}^{r_k} d^3r_1\int_{r_{k-1}}^{r_k} d^3r_2\,\zeta(r_1, r_2, |\mathrm{r}_1 - \mathrm{r}_2|)\,. \qquad (A3)$$

Moreover, in eq.(A1) we define the integrals

$$K_1 \;=\; \left(\frac{3}{4\pi}\right)\Delta\int_{1-\delta}^{1} d^3x\,(x+\epsilon_k)^{-\gamma} \qquad (A4)$$

and

$$J_2 \;=\; \left(\frac{3}{4\pi}\right)^2\Delta^2\int_{1-\delta}^{1} d^3x_1\int_{1-\delta}^{1} d^3x_2\,(|\mathrm{x}_1 - \mathrm{x}_2| + \epsilon_k)^{-\gamma}\,. \qquad (A5)$$

In the above expressions, we define $\Delta = [1-(1-\delta^3)]^{-1}$ and $\epsilon_k = R/r_k$.

By assuming the expression (5.13) to hold for the connected 3-point function, the integral I_3 can be written in the form

$$I_3 \;=\; N_k^2\,Q\,\xi_k^2\,(2K_2 + K_1^2 + q\,\xi_k^2\,H_2)\,. \qquad (A6)$$

In order to evaluate the integral I_3 of the 3-point function, we need the values of the further integrals

$$K_2 = \left(\frac{3}{4\pi}\right)^2 \Delta^2 \int_{1-\delta}^{1} d^3x_1 \int_{1-\delta}^{1} d^3x_2 \, (x_1 + \epsilon_k)^{-\gamma} \, (|\mathrm{x}_1 - \mathrm{x}_2| + \epsilon_k)^{-\gamma} \qquad (A7)$$

and

$$H = \left(\frac{3}{4\pi}\right)^2 \Delta^2 \int_{1-\delta}^{1} d^3x_1 \int_{1-\delta}^{1} d^3x_2 \, (x_1 + \epsilon_k)^{-\gamma} \, (x_2 + \epsilon_k)^{-\gamma} \, (|\mathrm{x}_1 - \mathrm{x}_2| + \epsilon_k)^{-\gamma} \, . \qquad (A8)$$

Then, after substituting eq.(A6) into eq.(A1), we get

$$Q = \frac{1}{C_1 + q \, C_3 \, \xi_k} \left[\frac{s_k^{(2)} - < N_k >}{(< N_k > - N_k)^2} - C_2 \, \frac{N_k}{< N_k > - N_k} + 1 \right] , \qquad (A9)$$

where we introduce the quantities

$$C_1 = 1 + \left(\frac{2K_2}{K_1^2}\right) \quad ; \quad C_2 = \frac{J_2}{K_1} \quad ; \quad C_3 = \frac{H}{K_1^2} \, . \qquad (A10)$$

Although K_1, K_2 and J_2 depend sensitively on γ, δ and ϵ_k, they appear in eq.(A10) in such a way that C_1 and C_2 turn out to be only mildly dependent (with variation of the order of 10% in all considered cases). Moreover, due to the expression ($A8$) for the H integral, the coefficient C_3, relevant to the Kirkwood model, depends on γ and ϵ_k like K_1, while it is slowly varying with δ.

The values of Q we obtain from our simulations for both *Kirkwood* ($q = 1$) and *hierarchical* ($q = 0$) models are reported in Figures 5.3, 5.4 and 5.5 (second and third rows, respectively), which describe the effects of taking different biasing levels ν and expansion factors $a(t)$.

A.2 The 4–point function

As in the previous case, the third-order central moment is related to the 4-point function, according to

$$\begin{aligned} s^{(3)} &= 3 \, s_k^{(2)} \, (1 - N_k \, \xi_k \, K_1) - \langle N_k \rangle \, (2 - 3 \, N_k \, \xi_k \, K_1) + \\ &\quad + N_k^3 \, \xi_k^2 \, (3 \, Q \, J_3 + 3 \, K_1 \, J_2 - K_1^3 \, \xi_k) + I_4 \, . \end{aligned} \qquad (A11)$$

(see eq.[5.12]. In this relation, the quantity

$$J_3 = \left(\frac{3}{4\pi}\right)^3 \Delta^3 \int_{1-\delta}^{1} d^3x_1 \int_{1-\delta}^{1} d^3x_2 \int_{1-\delta}^{1} d^3x_3 \, (|\mathrm{x}_1 - \mathrm{x}_2| + \epsilon_k)^{-\gamma} (|\mathrm{x}_2 - \mathrm{x}_3| + \epsilon_k)^{-\gamma} \, , \qquad (A12)$$

appears while, similar to eq.(A2), the connected 4-point function enters through the integral

$$I_4 = n^3 \int_{r_{k-1}}^{r_k} d^3r_1 \int_{r_{k-1}}^{r_k} d^3r_2 \int_{r_{k-1}}^{r_k} d^3r_3 \, \eta_{0123} \, . \qquad (A13)$$

A suitable combination of the coefficients R_a and R_b can be obtained by inserting eq.(A13) into eq.(A11). Indeed,

$$R_a + pR_b \;=\; D_1 \left[1 + \frac{s_k^{(3)} - 3s_k^{(2)} + 2\langle N_k \rangle}{(\rangle N_k \langle - N_k)^3} + \right.$$

$$\left. +3\,\frac{s_k^{(2)} - \langle N_k \rangle}{(\langle N_k \rangle - N_k)^2} - \frac{3N_k}{\langle N_k \rangle - N_k}\left(D_2 Q + D_3\right)\right]. \tag{A14}$$

In the above expression, we introduced the numerical coefficients

$$p \;=\; \frac{K_1^3 + K_{3b}}{K_1 K_2 + K_{3a}} \qquad ; \qquad D_1 \;=\; \frac{1}{6}\,\frac{K_1^3}{K_1 K_2 + K_{3a}}$$

$$D_2 \;=\; \frac{J_3}{K_1^2} \qquad ; \qquad D_3 \;=\; \frac{J_2}{K_1}, \tag{A15}$$

which are almost independent of the values of γ, δ and ϵ_k. The typical value of p is 0.35. In turn, eq.(A15) involves the integrals

$$K_{3a} \;=\; \left(\frac{3}{4\pi}\right)^3 \Delta^3 \int_{1-\delta}^{1} d^3x_1 \int_{1-\delta}^{1} d^3x_2 \int_{1-\delta}^{1} d^3x_3\,(x_1 + \epsilon_k)^{-\gamma} \times$$

$$\times(|\mathbf{x}_1 - \mathbf{x}_2| + \epsilon_k)^{-\gamma}\,(|\mathbf{x}_2 - \mathbf{x}_3| + \epsilon_k)^{-\gamma},$$

$$K_{3b} \;=\; \left(\frac{3}{4\pi}\right)^3 \Delta^3 \int_{1-\delta}^{1} d^3x_1 \int_{1-\delta}^{1} d^3x_2 \int_{1-\delta}^{1} d^3x_3\,(x_1 + \epsilon_k)^{-\gamma} \times$$

$$\times(|\mathbf{x}_1 - \mathbf{x}_2| + \epsilon_k)^{-\gamma}\,(|\mathbf{x}_1 - \mathbf{x}_3| + \epsilon_k)^{-\gamma}. \tag{A16}$$

We deduce the values of the combination (A14) of the hierarchical coefficients R_a and R_b after evaluating the central moments from our data. As for the 3-point analysis, the results of our computation are described in Figures 5.3, 5.4 and 5.5, for different values of the expansion factor and biasing level.

The integrals appearing in eqs.(A5), (A7), (A8), (A12) and (A16) have been evaluated on a three–dimensional grid of values ranging in the intervals $1.7 \le \gamma \le 3$, $0.05 \le \delta \le 0.55$, $-1.85 \le \log \epsilon_k \le -0.55$ and with spacings $\Delta_\gamma = 0.05$ $\Delta_\delta = 0.05$, $\Delta(\log \epsilon_k) = 0.1$. The method we used for the integration is an adaptive Monte Carlo routine with a $\sim 3\%$ required accuracy for the global value of the integral. Values of the integrals for γ, δ and ϵ_k within the integration limits have been obtained by a quadratic interpolation from the values defined on the grid points.

B. Partition function from moment generator

In this Appendix we show how the box-counting partition function, which characterizes the fractal properties of a given distribution, is related to the corresponding cumulant generating function (see Chapter 7). In particular we derive the expression (7.33) for $Z(q,r)$ starting from its definition

$$Z(q,r) \;=\; B(r)\sum_N \left(\frac{N}{N_t}\right)^q P_N(r) \qquad (B1)$$

(see eq.[7.29]). The scheme of the following calculations is similar to that described by Balian & Schaeffer [23] to work out the multifractal spectrum of their scale-invariant model.

From the integral representation of the Γ-function (see, *e.g.*, ref.[6]), we have

$$N^{q-1} \;=\; -\frac{\Gamma(q)}{2\pi i}\int_{(0,+\infty)^+} dz\, e^{-Nz}(-z)^{-q}\,. \qquad (B2)$$

Inserting this expression into eq.(B1) and taking also into account the relation (7.25) between the P_N count probabilities and the cumulant generating function, we get

$$Z(q,r) \;=\; -N_t^{-q}B(r)\frac{\Gamma(q)}{(2\pi i)^2}\int_{(0,+\infty)^+} dz \oint dt \sum_{N=1}^{\infty}\frac{N\,e^{-Nz}}{t^{N+1}}(-z)^{-q}\,e^{K(t-1)}\,. \qquad (B3)$$

After summing analytically the series appearing in the previous equation,

$$\sum_{N=1}^{\infty}\frac{N\,e^{-Nz}}{t^{N+1}} \;=\; \frac{e^{-z}}{(t-e^{-z})^2}\,,$$

the integral in eq.(B3) can be easily evaluated by applying the Cauchy theorem:

$$Z(q,r) \;=\; -N_t^{-q}B(r)\frac{\Gamma(q)}{2\pi i}\int_{(0,+\infty)^+} dz\,(-z)^{-q}\,e^{-z}\,K'(e^{-z}-1)\exp[K(e^{-z}-1)]\,. \qquad (B4)$$

Since any hierarchical generating function turns out to depend upon the variable $N_c t$, it is convenient to change the integration variable in eq.(B4) according to

$$y \;=\; N_c(1-e^{-z})\,, \qquad (B5)$$

so as to render adimensional the argument of the generating function. Accordingly, the Z partition function takes the expression

$$Z(q,r) \;=\; -N_t^{-q}\frac{B}{N_c}\frac{\Gamma(q)}{2\pi i}\int_{(0,N_c)^+} dy\left[\log\left(1-\frac{y}{N_c}\right)\right]^{-q} K'(-y/N_c)\,e^{K(-y/N_c)}\,, \qquad (B6)$$

which exactly coincides with eq.(7.33).

Bibliography

[1] Aarseth, S.J. 1984, in Methods of computational Physics, eds. J.U.Brackhill, B.J.Cohen (Academic, New York)

[2] Aarseth, S.J., Gott, J.R., & Turner, E.L. 1979, ApJ, 236, 43

[3] Abell, G.O. 1958, ApJS, 3, 211

[4] Abell, G.O. 1961, AJ, 66, 607

[5] Abell, G.O., Corwin, H.G., & Olowin, R.P. 1989, ApJS, 70, 1

[6] Abramowitz, M, & Stegun, I.A. 1972, Handbbok of Mathematical Functions, (10th ed.; New York: Dover)

[7] Adler, R.J. 1981, The Geometry of Random Fields (John Wiley: New York)

[8] Albrecht, A., & Stebbins, A. 1992, Phys. Rev. Lett., 68, 2121

[9] Albrecht, A., & Turok, N. 1989, Phys. Rev., D 40, 973

[10] Alimi, J.-M., Blanchard, A., & Schaeffer, R. 1990, ApJL, 349, L5

[11] Allen, T.J., Grinstein, B., & Wise, M.B. 1987, Phys. Lett. B, 197, 66

[12] Ashman, K.M., Salucci, P., & Persic, M. 1992, MNRAS, in press

[13] Badii, R., & Politi,A. 1984, Phys. Rev. Lett., 52, 1661

[14] Badii, R., & Politi,A. 1985, J. Stat. Phys., 40, 725

[15] Bahcall, N.A. 1979, ApJ, 232, 689

[16] Bahcall, N.A. 1988, ARAA, 26, 631

[17] Bahcall, N.A., & Burgett, W.S. 1986, ApJ, 300, L35

[18] Bahcall, N.A., & Soneira, R.M. 1983, ApJ, 270, 20

[19] Bahcall, N.A., & Soneira, R.M. 1984, ApJ, 277, 27

[20] Bahcall, N.A., & West, M.J. 1992, preprint

[21] Balian, R., & Schaeffer, R. 1988, ApJL, 335, L43

[22] Balian, R., & Schaeffer, R. 1989, A&A, 220, 1

[23] Balian, R., & Schaeffer, R. 1989, A&A, 226, 373

[24] Bardeen, J.M., Bond, J.R., Kaiser, N., & Szalay, A.S. 1986, ApJ, 304, 15

[25] Bardeen, J.M., Steinhardt, P.J., & Turner, M.S. 1983, Phys. Rev. D, 28, 679

[26] Barenblatt, G., 1980, Similarity, Self-Similarity and Intermediate Asymptotics (Plenum Press:New York)

[27] Barrow, J.D. & Bhavsar, S.P. 1987, Q.Jl.R.astr.Soc., 225, 109

[28] Barrow, J.D., Bhavsar, S.P. & Sonoda, D.H. 1984, MNRAS, 210, 19p

[29] Barrow, J.P., & Coles, P. 1990, MNRAS, 244, 188

[30] Batuski, D.J., Bahcall, N.A., Olowin, R.P., & Burns, J.O. 1989, ApJ, 341, 599

[31] Batuski, D.J., Melott, A.L. & Burns, J.O. 1987, ApJ, 322, 48

[32] Baumgart, D.J., & Fry, J.N. 1991, ApJ, 375, 25

[33] Bean, A.J., Efstathiou, G.P., Ellis, R.S., Peterson, B.A., & Shanks, T. 1983, MNRAS, 205, 605

[34] Bennet, D.P., & Bouchet, F.E. 1989, Phys. Rev. Lett., 60, 257

[35] Benzi, R., Paladin, G., Parisi, G., & Vulpiani, A. 1984, J. Phys. A, 17, 3521

[36] Benzi, R., Biferale, L., Paladin, G., Vulpiani, A., & Vergassola, M. 1991, Phys. Rew. Lett., 67, 2299

[37] Bertschinger, E., Dekel, A. 1989, ApJL, 336, L5

[38] Bertschinger, E., Dekel, A., Faber, S.M., Dressler, A., & Burstein, D. 1990, ApJ, 364, 370

[39] Birsdall, C.K., & Langdon, A.B. 1985, Plasma Physics via Computer Simulation (McGraw-Hill)

[40] Blanchard, A., Buchert, T., & Klaffl, R. 1992, preprint

[41] Blumenthal, G.R., Faber, S.M., Primack, J.R., & Rees, M.J. 1984, Nature, 311, 517

[42] Bogart, R.S., & Wagoner, R.V. 1973, ApJ, 181, 609

[43] Bond, J.R., & Efstathiou, G. 1984, ApJ, 285, L45

[44] Bond, J.R., & Szalay, A.S. 1983, ApJ, 274, 443

[45] Bonometto, S.A., Borgani, S., Persic, M., & Salucci, P. 1990, ApJ, 356, 350

[46] Bonometto, S.A., Lucchin, F., & Matarrese, S. 1987, ApJ, 323, 19

[47] Bonometto, S.A., & Scaramella, R. 1988, SISSA preprint, 92/87/A

[48] Borgani, S. 1990, A&A, 240, 223

[49] Borgani, S. 1990, Master Thesis, International School for Advanced Studies, Trieste, Academic Year 1989/90

[50] Borgani, S. 1992, MNRAS, in press, SISSA preprint, 126/92/A

[51] Borgani, S., & Bonometto, S.A. 1989, A&A, 215, 17

[52] Borgani, S., & Bonometto, S.A. 1990, ApJ, 338, 398

[53] Borgani, S., Bonometto, S.A., Persic, M., & Salucci, P., 1991, ApJ, 374, 20

[54] Borgani, S., Jing, Y.P., & Plionis, M. 1992, ApJ, 395, 000

[55] Borgani, S., Plionis, M., & Valdarnini, R. 1992, ApJ, in press, SISSA preprint, 126/92/A

[56] Borgani, S., Murante, G., Provenzale, A., & Valdarnini, R. 1992, Phys. Rev. A, submitted

[57] Börner, G., & Mo, H.J. 1990, A&A, 227, 324

[58] Börner, G., Mo, H.J., & Zhou, Y. 1989, A&A, 221, 191

[59] Bouchet, F.R., Davis, M., & Strauss, M. 1991, Proceedings of the DAEC Workshop, March 91, Observatoire de Meudon.

[60] Bouchet, F.R., Schaeffer, R., & Davis, M. 1991, ApJ, 383, 19

[61] Brandenberger, R. Physics of the Sarly Universe; Proceedings of the 36'h SUSSP, ed. J.A.Peacock, A.F.Heavens and A.T.Davis (Edinburgh: SUSSP publications)

[62] Broadhurst, T.J., Ellis, R.S., Koo, D.C., & Szalay, A.S. 1990, Nature, 343, 726

[63] Brown, E.M. & Groth, E.J. 1989, ApJ, 338, 605

[64] Buchert, T. 1992, MNRAS, 254, 729

[65] Burgers, J.M. 1948, Adv. Appl. Mech., 1, 171

[66] Burgers, J.M. 1974, The Nonlinear Diffusion Equation (Dordrecht:Reidel)

[67] Burstein, D. 1990, Rep. Progr. Phys., 53, 421

[68] Calzetti, D., Giavalisco, M., & Meiksin, A. 1992, preprint

[69] Cappi, A., & Maurogordato, S. 1992, A&A, 259, 423

[70] Cappi, A. Maurogordato, S., & Lachieze-Rey, M. 1991, A&A, 243, 28

[71] Carruthers, P. 1991, ApJ, 380, 24

[72] Carruthers, P., & Minh Duong-Van 1983, Phys. Lett., 131B, 116

[73] Carruthers, P., & Sarcevic 1989, Phys. Rev. Lett., 63, 1562

[74] Carruthers, P., & Shih, C.C. 1983, Phys. Lett., 127B, 242

[75] Castagnoli, C., & Provenzale, A. 1991, A&A, 246, 634

[76] Catelan, P., Lucchin, F., & Matarrese, S. 1988, Phys. Rev. Lett., 61, 267

[77] Cen, R.Y. 1992, ApJS, 78, 341

[78] Cen, R.Y., Gnedin, R.Y., Kofman, L.A., & Ostriker, J. P., 1992, preprint POP-458

[79] Cen, R.Y., & Ostriker, J.P. 1992, ApJ, 393, 22

[80] Colafrancesco, S., Lucchin, F., & Matarrese, S. 1989, ApJ, 345, 3

[81] Coles, P. 1988, MNRAS, 234, 509

[82] Coles, P. 1989, MNRAS, 238, 319

[83] Coles, P. 1990, Nature, 346, 446

[84] Coles, P., & Jones, B.J.T. 1991, MNRAS, 248, 1

[85] Coles, P., Moscardini, L., Plionis, M., Lucchin, F., Matarrese, S., & Messina, A. 1992, preprint

[86] Coles, P., & Plionis, M. 1991, MNRAS, 250, 75

[87] Coleman, P. H., & Pietronero, L. 1992, Phys. Rep., 213, 311

[88] Coleman, P. H., Pietronero, L., & Sanders, R. H., 1988, A&A, 200, L32

[89] Coleman, P. H., & Saslaw, W.C. 1990, ApJ, 353, 354

[90] Collins, C.A., Heydon-Dumbleton, N.H. & MacGillivary, H.T. 1989, MNRAS, 236, 7p

[91] Collins, C.A., Nichol, R.C., & Lumsden, S. L., 1992, MNRAS, 254, 295

[92] Couchman, H.M.P., & Carlberg, R.G. 1992, ApJ, 389, 453

[93] Crane, P., & Saslaw, W.C. 1986, ApJ, 301, 1

[94] da Costa, L.N., et al. 1988, ApJ, 327, 544

[95] da Costa, L.N., et al. 1989, AJ, 97, 315

[96] Dalton, G.B., Efstathiou, G., Maddox, S.J., & Sutherland, W.J. 1992, ApJ, 390, L1

[97] Davidsen, A.F., et al. 1991, Nature, 351, 128

[98] Davis, M., Efstathiou, G., Frenk, C., & White, S.D.M. 1985, ApJ, 292, 371

[99] Davis, M., & Geller, M.J. 1976, ApJ, 208, 13

[100] Davis, M., & Huchra, J. 1982, ApJ, 254, 437

[101] Davis, M., & Peebles, P.J.E. 1977, ApJS, 35, 425

[102] Davis, M., & Peebles, P.J.E. 1983, ApJ, 267, 465

[103] Dekel, A. 1987, in Observational Cosmology, ed. A.Hewitt, G.Burbidge, and L.Z.Fang, (Dordrecht: Reidel) p.145

[104] Dekel, A., & Aarseth, S.J. 1984, ApJ, 283, 1

[105] Dekel, A., Blumenthal, G.R., Primack, J.R., & Olivier, S. 1989, ApJ, 338, L5

[106] Dekel, A., & Rees, M.J. 1987, Nature, 326, 455

[107] Dekel, A., & Silk, J. 1986, ApJ, 303, 39

[108] de Lapparent, V., Geller, M.J., & Huchra, J.P. 1986, ApJ, 302, L1

[109] de Lapparent, V., Geller, M.J., & Huchra, J.P. 1988, ApJ, 332, 44

[110] de Lapparent, V., Geller, M.J., & Huchra, J.P. 1989, ApJ, 343, 1

[111] de Lapparent, V., Geller, M.J., & Huchra, J.P. 1991, ApJ, 369, 273

[112] de Lapparent, V., Kurtz, M.J., & Geller, M.J. 1986, ApJ, 304, 585

[113] Doroshkevich, A.G. 1970, Astrophisica, 6, 320

[114] Doroshkevich, A.G., & Kotok, T.V. 1990, MNRAS 246, 10

[115] Dressler, A. 1980, ApJ, 236, 351

[116] Dubuc, B., Quiniou, J.F., Roques-Carmes, C., Tricot, C., & Zucker, S.W. 1989, Phys. Rew., A39, 1500

[117] Efstathiou, G. 1988, Large-Scale Motions in the Universe, a Vatican Study Week, eds. V.C.Rubin, and G.V.Coyne (Cittá del Vaticano: Pontificia Academia Scientiarum)

[118] Efstathiou, G. 1990, Physics of the early Universe; Proceedings of the 36^th SUSSP, ed. J.A.Peacock, A.F.Heavens and A.T.Davis (Edinburgh: SUSSP publications)

[119] Efstathiou, G., Dalton, G.B., Sutherland, W.J., & Maddox, S. 1992, 257, 125

[120] Efstathiou, G., Davis, M., Frenk, C., & White, S.D.M. 1985, ApJS, 57, 241

[121] Eftathiou, G., & Eastwood, J.W. 1981, MNRAS, 194, 503

[122] Efstathiou, G., Ellis, R.S., & Peterson, B.A. 1988, MNRAS, 232, 431

[123] Efstathiou, G, Fall, S.M., & Hogan, G. 1979, MNRAS, 189, 203

[124] Efstathiou, G., Frenk, C., White, S.D.M., & Davis, M. 1988, MNRAS, 235, 715

[125] Efstathiou, G., Kaiser, N., Saunders, W., Lawrence, A., Rowan-Robinson, M., Ellis, R.S., & Frenk, C.S. 1990, MNRAS, 247, 10p

[126] Efstathiou, G., & Silk, J. 1983, Fund. Cosmic Phys., 9, 1

[127] Efstathiou, G., Sutherland, W.J., & Maddox, S.J. 1990, Nature, 348, 705

[128] Einasto, M. 1991, MNRAS, 252, 261

[129] Einasto, J., Klypin, A.A., Saar, E., & Shandarin, S.F. 1984, MNRAS, 206, 529

[130] Einasto, J., Klypin, A.A., & Saar, E. 1986, MNRAS, 219, 457

[131] Elizalde, E., & Gatzanaga, E. 1992, MNRAS, 254, 247

[132] Ellis, J. 1990, Physics of the early Universe; Proceedings of the 36^th SUSSP, ed. J.A.Peacock, A.F.Heavens and A.T.Davis (Edinburgh: SUSSP publications)

[133] Eyles, C.J., et al. 1991, ApJ, 376, 23

[134] Faber, S.M., & Jackson, R.E. 1976, ApJ, 204, 668

[135] Fall, S.M., & Tremaine, S., 1977, ApJ, 216, 682

[136] Felten, J.E. 1985, Comm. Ap. Sp. Sci., 11, 53

[137] Field, G.B., & Saslaw, W.C. 1971, ApJ, 176, 199

[138] Fournier d'Albe, E.E. 1907, Two New Worlds (London: Longmans Green)

[139] Freeman, K.C. 1970, ApJ, 160, 811

[140] Frenk, C.S., White, S.D.M., & Davis, M. 1983, ApJ, 271, 417

[141] Frisch, U., & Morf, R. 1981, Phys. Rev. , A 23, 2673

[142] Frisch, U., Sulem, P., & Nelkin, M. 1978, J. Fl. Mech., 87, 719

[143] Frisch, U., & Parisi, G. 1985, in Turbulence and Predictability in Geophysical Fluid Dynamics and Climatology, eds. R.Benzi, G.Parisi & A.Sutera (North-Holland)

[144] Fry, J.N. 1982, ApJ, 262, 425

[145] Fry, J.N. 1984, ApJ, 277, L5

[146] Fry, J.N. 1984, ApJ, 279, 499

[147] Fry, J.N. 1985, ApJ, 289, 10

[148] Fry, J.N. 1986, ApJ, 306, 358

[149] Fry, J.N., Giovanelli, R., Haynes, M.P., Melott, A., & Scherrer, R.J. 1989, ApJ, 340, 11

[150] Fry, J.N., & Peebles, P.J.E. 1978, ApJ, 221, 19

[151] Castagnoli, C., & Provenzale, A. 1991, A&A, 246, 634

[152] Gabbiani, G., Masiero, A., & Sciama, D.W.S. 1991, Phys. Lett., B259, 323

[153] Geller, M.J., de Lapparent, V. & Kurtz, M.J. 1984, ApJ, 287, L55

[154] Geller, M.J., & Huchra, J.P. 1988, Large-Scale Motions in the Universe, ed. V.C. Rubin & G.V. Coyne (Princeton: Princeton University Press), p.3

[155] Geller, M.J., & Huchra, J.P. 1989, Science, 246, 897

[156] Gell'man, M., Ramond, P., & Slansky, S. 1980, Supergravity, eds. D.Z.Freedman and P.Van Nieuwenhuizen (North Hollan, New York)

[157] Giavalisco, M., Mancinelli, B., Mancinelli, P., & Yahil, A. 1991, preprint

[158] Giovanelli, R., & Haynes, M.P. 1988, in Large-Scale Structure of the Universe, IAU Symposium No. 130, ed. J. Auduze, et al. (Dordrecht)

[159] Giovanelli, R., Haynes, M.P., & Chincarini, G.L. 1986, ApJ, 300, 77

[160] Gott, III, J.R. 1975, 201, 296

[161] Gott III, J.R., Gao, B., & Park, C. 1991, ApJ, 383, 90

[162] Gott III, J.R., Mao, S., Park, C., & Lahav, O. 1992, ApJ, 385, 26

[163] Gott III, J.R., Melott, A.L., & Dickinson, M. 1986, ApJ, 306, 341

[164] Gott III, J.R., Park, C., Juszkiezicz, R., Bies, W.E., Bennet, D.P., Bouchet, F.R., & Stebbins, A. 1990, ApJ, 352, 1

[165] Gott III, J.R., & Turner, E.L. 1977, ApJ, 216, 357

[166] Gott III, J.R., & Turner, E.L. 1979, ApJ, 232, L79

[167] Gott III, J.R., et al. 1989, ApJ, 340, 625

[168] Grassberger, P., Badii, R., & Politi, A. 1988, J. Stat. Phys., 51, 135

[169] Grassberger, P., & Procaccia, I. 1983, Phys. Rew. Lett., 50, 346

[170] Grassberger, P., & Procaccia, I. 1983, Phys. Rew., A 28, 2591

[171] Grinstein, B., & Wise, M.B. 1986, ApJ, 310, 19

[172] Groth, E.J., & Peebles, P.J.E. 1976, A&A, 53, 131

[173] Groth, E.J., & Peebles, P.J.E. 1977, ApJ, 217, 385

[174] Gunn, J.E. 1977, ApJ, 218, 592

[175] Gunn, J.E., & Gott III, J.R. 1972, ApJ, 176, 1

[176] Gurbatov, S.N., & Saichev, A.I. 1984, Izv. Vyssh. Uchebn. Zaved. Radiofiz., 27, 456

[177] Gurbatov, S.N., Saichev, A.I., & Shandarin, S.F. 1985, Sov. Phys. Dokl., 30, 921

[178] Gurbatov, S.N., Saichev, A.I., & Shandarin, S.F. 1989, MNRAS, 236, 385

[179] Guth, A. 1981, Phys. Rev., D 23, 347

[180] Guzzo, L., Collins, C.A., Nichol, R.C., & Lumsden, S. L., 1992, preprint

[181] Guzzo, L., Iovino, A., Chincarini, G., Giovanelli, R., & Haynes, M. 1991, ApJ, 382, L5

[182] Hale-Sutton, D., Fong, R., Metcalfe, N., & Shanks, T. 1989, MNRAS, 237, 569

[183] Hamilton, A.J.S. 1988, ApJ, 332, 67

[184] Hamilton, A.J.S., Gott III, J.R., & Weinberg, D. 1986, ApJ, 309, 1

[185] Hansel, D., Bouchet, F.R., Pellat, R., & Ramani, A. 1986, ApJ, 310, 23

[186] Harrison, E.R. 1970, Phys. Rev., D 1, 2726

[187] Hauser, M.G., & Peebles, P.J.E. 1973 , ApJ, 185, 757

[188] Haynes, M.P., & Giovannelli, R. 1986, ApJ, 306, L55

[189] Hawking, S.W., & Ellis, G.F.R. 1980, in The Large Scale Structure of Space–Time, (Cambridge: Cambridge University Press)

[190] Henon, M. 1976, Comm. Math. Phys., 81, 229

[191] Hentschel, H.G.E., & Procaccia, I. 1983, Physica, D8, 435

[192] Heydon-Dumbleton, N.H., Collins, C.A., & MacGillavray, H.T. 1989, MNRAS, 238, 379

[193] Hockney, R.W., & Eastwood, J.W. 1981, Computer Simulations using Particles, (Mc Graw-Hill)

[194] Hoessel, J.G, Gunn, J.E., & Thuan, T.X. 1980, ApJ, 241, 486

[195] Hoffman, Y., & Shaham, J. 1985, ApJ, 297, 16

[196] Holtzman, J.A. 1989, ApJS, 71, 1

[197] Huchra, J.P., Davis, M., Latham, D., & Tonry, J. 1983, ApJS, 52, 89

[198] Huchra, J.P., & Geller, M.J. 1982, ApJ, 257, 423

[199] Huchra, J.P., Geller, M.J., de Lapparent, V., & Corwin, H.G.Jr. 1990, ApJS, 72, 433

[200] Ikeuchi, S. 1981, Publ. Astr. Soc. Japan, 33, 211

[201] Ikeuchi, S., & Turner, E.L. 1991, MNRAS 250, 519

[202] Inagaki, S., Itoh, M, & Saslaw, W.C. 1992, ApJ, 386, 9

[203] Itoh, M, Inagaki, S., & Saslaw, W.C. 1988, ApJ, 331, 45

[204] Jaynes, E.T. 1957, Phys. Rew., 106, 620

[205] Jensen, L.G., & Szalay, A.S. 1986, ApJL, 305, L5

[206] Jing, Y.P. 1990, A&A, 233, 309

[207] Jing, Y.P., Mo, H.J., & Börner, G. 1991, A&A, 252, 449

[208] Jing, Y.P., Plionis, M., & Valdarnini, R. 1992, ApJ, 389, 499

[209] Jing, Y.P., & Valdarnini, R. 1991, A&A, 250, 1

[210] Jing, Y.P., & Valdarnini, R. 1991, ApJL, submitted

[211] Jing, Y.P. & Zhang, J.L. 1989, ApJ, 342, 639

[212] Jones, B.J.T., Coles, P., & Martinez, V.J. 1992, MNRAS, in press

[213] Kaiser, N. 1984, ApJL, 284, L9

[214] Kaiser, N. 1987, MNRAS, 227, 1

[215] Kaiser, N. 1991, Proceeding of the Texas/ESO-CERN Conference, Brighton, December 1990

[216] Kaiser, N., & Davis, M. 1985, ApJ, 297, 365

[217] Kaiser, N., & Peacok, J.A. 1991, ApJ, 379, 482

[218] Kibble, T.W.B. 1976, J. Phys., A 9, 1387

[219] Kiefer, J. & Wolfowitz, J. 1956, Ann.Math.Stat., 27, 887

[220] Kirkwood, J.C. 1935, J. Chem. Phys., 3, 300

[221] Kirshner, R.P., Oemler, A., Jr., Schechter, P.L., & Shechtman, S.A. 1981, ApJ, 248, L57

[222] Klypin, A.A., & Kopilov, A.I. 1983, Sov. Astr. Lett., 9, 41

[223] Kofman, L.A., & Linde, A.D. 1935, Nucl. Phys., B282, 555

[224] Kolb, E.W., & Turner, M.S. 1990, The Early Universe (Addison-Wesley Publ. Company)

[225] Kolmogorov, A.N. 1941, Dokl. Acad. Nauk SSSR, 30, 299

[226] Kraichnan, R.H. 1990, Phys. Rev. Lett., 65, 575

[227] Lahav, O., Edge, A.C., Fabian, A.C., & Putney, A. 1989, MNRAS, 238, 881

[228] Lake, G., & Tremaine, S. 1980, ApJ, 238, L13

[229] Landau, L.D., & Lifshitz, E.M., Fluid Mechanics (Pergamon Press)

[230] Lauberts, A., 1982, The ESO/Uppsala Survey of the ESO(B) Atlas (München:European Southern Observatory)

[231] Lebedev, V.S. & Lebedeva, I.A. 1988, Sov. Astr. Lett., 14, 7

[232] Lilje, P.B., & Efstathiou, G. 1988, MNRAS, 231, 635

[233] Limber, D.N. 1953, ApJ, 117, 134

[234] Linde, A. 1982, Phys. Lett., B 108, 389

[235] Linde, A. 1984, Rep. Prog. Phys., 47, 925

[236] Ling, E.N., Frenk, C.S. & Barrow, J.D. 1986, MNRAS, 223, 21p

[237] Lyubimov, V.A., et al. 1980, Phys. Lett., B94, 266

[238] Loveday, J., Peterson, P.A., Efstathiou, G., & Maddox, S.J. 1992, ApJ, 390, 338

[239] Lucchin, F. 1989, in Morphological Cosmology, Proceeding of the 11^{th} Crakow Cosmological School, Springer-Verlag, Ed.: P.Flin and H.W.Duerbeck

[240] Lucchin, F., & Matarrese, S., 1985, Phys. Rev., D 32, 1316

[241] Lucchin, F., & Matarrese, S. 1988, ApJ, 330, 535

[242] Lucchin, F., Matarrese, S., & Vittorio, N. 1986, ApJ, 330, L1

[243] Lugger, P.M. 1989, ApJ, 343, 572

[244] Lumsden, S.L., Nichol, R.C., Collins, C.A., & Guzzo, L. 1992, MNRAS, in press

[245] Lynden-Bell, D., et al. 1988, 326, 19

[246] Maddox, S.J., Efstathiou, G., Sutherland, W.J., & Loveday, J. 1990, MNRAS, 242, 43p

[247] Maia, M.A.G., & da Costa, L.N. 1990, ApJ, 349, 477

[248] Martinez, V.J. 1990, Vistas in Astronomy, 33, 337

[249] Martinez, V.J., & Jones, B.J.T. 1990, MNRAS, 242, 517

[250] Martinez, V.J., Jones, B.J.T., Dominguez-Tenreiro, R., & van de Weygaert, R. 1990, ApJ, 357, 50

[251] Matarrese, S., Lucchin, F., & Bonometto, S.A., 1986, ApJ, 310, L21

[252] Matarrese, S., Lucchin, F., Messina, A., & Moscardini, L. 1991, MNRAS, 253, 35

[253] Matarrese, S., Lucchin, F., Moscardini, L., & Saez, D. 1992, preprint

[254] Mandelbrot, B.B. 1982, The Fractal Geometry of the Nature (Freeman)

[255] Meiksin, A., Szapudi, I., & Szalay, A.S. 1991, preprint

[256] Melott, A.L. 1983, ApJ,, 264, 59

[257] Melott, A.L. 1990, Phys. Rep., 193, 1

[258] Melott, A.L., & Fry, J.N. 1986, ApJ, 305, 1

[259] Melott, A.L., Weinberg, D., & Gott III, J.R. 1988, ApJ, 328, 50

[260] Messina, A., Moscardini, L., Lucchin, F., & Matarrese, S., 1991, MNRAS, 245, 244

[261] Meszaros, P. 1975, A&A, 38, 5

[262] Mo, H.J. 1991, Ph.D. Thesis, Ludwig-Maximilian-Univesität München, Dept. of Physics

[263] Mo, H.J., Jing, Y.P. & Börner, G. 1992, ApJ, 392, 452

[264] Moore, B., et al. 1992, MNRAS, 256, 477

[265] Moscardini, L., Matarrese, S., Lucchin, F., & Messina, A., 1991, MNRAS, 248, 424

[266] Mukhanov, V.F., Feldman, H.A., & Brandenberger, R.H. 1992, Phys. Rep., 215, 203

[267] Nash, C., & Sen, S. 1983, Topology and Geometry for Physicists (London: Academic Press)

[268] Nichol, R.C., Collins, C.A., Guzzo, L., and Lumsden, S.L. 1992, MNRAS, 255, 21p

[269] Nilson, P. 1973, Uppsala General Catalogue of Galaxies, Nova Acta, Reg. Soc. Sci. Upsaliensis, Ser. V: A, Vol. 1

[270] Nusser, A., & Dekel, A. 1990, ApJ, 362, 14

[271] Oemler, A. 1974, ApJ, 194, 1

[272] Olivier, S., Blumenthal, G.R., Dekel, A., Primack, J.R., & Stanhill, D. 1990, ApJ, 356, 1

[273] Ore, O. 1962, Amer. Math. Soc. Colloq. Publ., 38

[274] Ortolan, A., Lucchin, F., & Matarrese, S. 1989, Phys. Rev., D 40, 290

[275] Ostriker, J.P., & Cowie, L. 1981, ApJ, 243, L127

[276] Paladin, G., & Vulpiani, A. 1984, Lett. Nuovo Cimento, 41, 82

[277] Paladin, G., & Vulpiani, A. 1987, Phys. Rep., 156, 147

[278] Park, C., Gott III, J.R., & da Costa, L.N. 1992, preprint

[279] Park, C., Gott III, J.R., Melott, A.L., & Karachentsev, I.D. 1992, ApJ, 387, 1

[280] Park, C., Spergel, D.N., & Turok, N. 1991, ApJL, 372, L53

[281] Peakock, J.A. 1990, in Particle Astrophysics: The Early Universe and Cosmic Structures, eds. J.M.Alimi et al. (Editions Frontieres)

[282] Peakok, J.A. 1991, MNRAS, 253, 1p

[283] Peakok, J.A., & Nicholson, D. 1991, MNRAS, 253, 307

[284] Peebles, P.J.E. 1974, ApJL, 189, L51

[285] Peebles, P.J.E. 1975, ApJ, 196, 647

[286] Peebles, P.J.E. 1976, Ap. Sp. Sc., 45, 3

[287] Peebles, P.J.E. 1980, The Large Scale Structure of the Universe, (Princeton: Princeton University Press)

[288] Peebles, P.J.E. 1981, ApJ, 248, 885

[289] Peebles, P.J.E. 1982, ApJ, 258, 415

[290] Peebles, P.J.E. 1987, ApJ, 315, L73

[291] Peebles, P.J.E., & Hauser, M.G. 1974, ApJS, 28, 19

[292] Peebles, P.J.E., & Groth, E.J. 1975, ApJ, 196, 1

[293] Perrin, J. 1913, Les Atoms (Paris)

[294] Persic, M., & Salucci, P. 1988, MNRAS, 234, 131

[295] Persic, M., & Salucci, P., 1990, MNRAS, 245, 577

[296] Persic, M., & Salucci, P., 1990, ApJ, 355, 44

[297] Pietronero, L. 1987, Physica, 144A, 257

[298] Pisani, A., Giuricin, G., Mardirossian, F., & Mezzetti, M. 1992, ApJ, 389, 68

[299] Plionis, M. 1988, MNRAS, 234, 401

[300] Plionis, M., Barrow, J.D., & Frenk, C. 1991, MNRAS, 249, 662

[301] Plionis, M., & Borgani, S. 1991, MNRAS, 254, 306

[302] Plionis, M., & Valdarnini, R. 1991, MNRAS, 249, 46

[303] Plionis, M., Valdarnini, R., & Coles, P. 1992, MNRAS, in press

[304] Plionis, M., Valdarnini, R., & Jing, Y.P. 1992, ApJ, in press

[305] Pokorski, S., Gauge Field Theories, (Cambridge: Cambridge University Press)

[306] Politzer, D., & Wise, M. 1984, ApJ, 285, L1

[307] Postman, M., Geller, M.J., & Huchra, J.P. 1986, AJ, 91, 1267

[308] Postman, M., Huchra, J.P., & Geller, M.J. 1992, ApJ, 384, 407

[309] Press, W.H., & Schechter, P. 1974, ApJ, 187, 425

[310] Provenzale, A. 1992, in: Applying Fractal in Astronomy, A. Heck and J. Perdang Eds. (Springer: Berlin)

[311] Provenzale, A., Galeotti, P., Murante, G., & Villone B. 1992, ApJ, in press

[312] Raychaudhury, S. 1989, Nature, 342, 251

[313] Ramella, M., Geller, M.J., & Huchra, J.P. 1989, ApJ, 344, 57

[314] Ramella, M., Geller, M.J., & Huchra, J.P. 1990, ApJ, 353, 51

[315] Ramond, P. 1981, Field Theory: a Modern Primer (New York: Wiley)

[316] Readhead, A.C.S., Lawrence, C.R., Myers, S.T., Sargent, W.L.W., Hardebeck, H.E., & Moffet, A.T. 1989, ApJ, 346, 566

[317] Rees, M.J., & Ostriker, J.P. 1977, MNRAS, 179, 541

[318] Renyi, A. 1970, Probability Theory (North Holland: Amsterdam)

[319] Rice, S.A., & Grey, P. 1965, The Statistical Mechanics of Simple Liquids (Princeton: Princeton University Press)

[320] Riordan, J. 1958, An Introduction to Combinatorial Analysis, (New York:Wiley)

[321] Rood, H.J. 1976, ApJ, 207, 16

[322] Roulet, E., & Tomassini, D. 1991, Phys. Lett., B 256, 218

[323] Rubin, V.C., Burstein, D., Ford, W.K., & Thonnard, N. 1985, ApJ, 289, 81

[324] Rubin, V.C., Ford, W.K., & Tonnard, N. 1980, ApJ, 238, 471

[325] Rudnicky, K., Dworak, T.Z., Flin, P., Baranovski, B., & Sendrakowski, A. 1973, Acta Cosmologica, 1, 7

[326] Saarinen, S., Dekel, A., & Carr, B.J. 1987, Nature, 325, 598

[327] Salopek, D.S. 1992, Phys. Rev., D 45, 1139

[328] Salopek, D.S., Bond, J.R., & Bardeen, J.M. 1989, Phys. Rev., D 40, 6

[329] Salucci, P., Persic, M., & Borgani, S. 1992, ApJ, in press, SISSA preprint, 129/92/A

[330] Salucci, P., & Sciama, D.W.S. 1990, MNRAS, 244, 9

[331] Saslaw, W.C. 1980, ApJ, 235, 299

[332] Saslaw, W.C. 1985, Gravitational Physics of Stellar and Galactic Systems, Cambridge Univ. Press

[333] Saslaw, W.C., Chitre, S.M., Itoh, M., & Inagaki, S. 1990 ApJ, 365, 419

[334] Saslaw, W.C., & Crane, P. 1991, ApJ, 380, 315

[335] Saslaw, W.C., & Hamilton, A.J.S. 1984, ApJ, 276, 13

[336] Saunders, W., Frenk, C., Rowan-Robinson, M., Efstathiou, G., Lawrence, A., Kaiser, N., Ellis, R., Crawford, J., Xia, X.-Y., & Parry, I. 1991, Nature, 349, 32

[337] Scaramella, R., Baiesi-Pillastrini, G., Chincarini, G., Vettolani, G., & Zamorani, G. 1989, Nature, 338, 562

[338] Scaramella, R., Vettolani, G., & Zamorani, G. 1991, ApJL, 376, L1

[339] Schechter, P. 1976, ApJ, 203, 297

[340] Schectman, S., ApJS, 57, 77

[341] Scherrer, R.J., & Bertschinger, E. 1991, ApJ, 381, 349

[342] Scherrer, R.J., Melott, A.L., & Bertschinger, E. 1989, Phys. Rev. Lett., 62, 379

[343] Sciama, D.W.S. 1990, ApJ, 364, 549

[344] Sciama, D.W.S. 1990, Nature, 346, 40

[345] Scott, D., Rees, M.J., & Sciama, D.W.S. 1991, A&A, 250, 295

[346] Seldner, M., & Peebles, P.J.E. 1977, ApJ, 215, 703

[347] Seldner, M., Siebers, B., Groth, E.J. & Peebles, J.E. 1977, AJ, 84, 249

[348] Shane, C.D., & Wirtanen, C.A. 1967, Publ. Lick Obs., vol. 22

[349] Shandarin, S.F., & Zel'dovich, Ya.B. 1989, Rev. Mod. Phys., 61, 185

[350] Shapley, H. 1930, Harward Obs. Bull., 874, 9

[351] Shapley, H., & Ames, A. 1932, Harward Annals, 88, Part II

[352] Sharp, N.A. 1979, A&A, 74, 308

[353] Sharp, N., Bonometto, S.A., & Lucchin, F. 1984, A&A, 130, 79

[354] She, Z.-S., Jackson, E., & Orszag, S.A. 1990, Nature, 344, 226

[355] She, Z.-S., & Orszag, S.A. 1991, Phys. Rev. Lett., 66, 1701

[356] Silk, J. 1968, ApJ, 151, 459

[357] Smoot, G.F., et al. 1992, preprint

[358] Strauss, M.A., Davis, M., Yahil, A., & Huchra, J.P. 1990, ApJ, 361, 49

[359] Struble, M.F., & Rood, H.J. 1987, ApJS, 63, 543

[360] Struble, M.F. & Rood, H.J. 1991, ApJ, 374, 395

[361] Sutherland, W. 1988, MNRAS, 234, 159

[362] Sutherland, W., & Efsthatiou, G. 1991, MNRAS, 258, 159

[363] Szalay, A.S. 1988, ApJ, 333, 21

[364] Szalay, A.S., & Schramm, D.M. 1985, Nature, 314, 718

[365] Szapudi, I., Szalay, A.S., & Boschan, P. 1992, 390, 350

[366] Tóth, G., Hollósi, J., & Szalay, A.S. 1989, ApJ, 344, 75

[367] Totsuji, H., & Kihara, T. 1969, Publ. Astron. Soc. Japan, 25, 287

[368] Tully, R.B. 1986, ApJ, 303, 25

[369] Tully, R.B., & Fisher, J.R. 1977, A&A, 54, 661

[370] Tully, R.B., Scaramella, R., Vettolani, G., & Zamorani, G. 1992, ApJ, 388, 9

[371] Turok, N. 1985, Phys. Rev. Lett., 55, 1801

[372] Turok, N. 1986, Cosmology, Astronomy and Fundamental Physics, ed. G. Setti and L. Van Hove (ESO, Garching bei München), p. 175

[373] Valdarnini, R., & Borgani, S. 1991, MNRAS, 251, 575

[374] Valdarnini, R., Borgani, S., & Provenzale, A. 1992, ApJ, 394, 422

[375] van der Kruit, P.C. 1987, A&A, 173, 59

[376] van de Weygaert, R. 1991, MNRAS, 249 159

[377] van de Weygaert, R., Jones, B.J.T., & Martinez, V.J., 1992, Phys. Lett., in press

[378] de Vaucoleurs, G., & de Vaucoleurs, G. 1964, Reference Catalogue of Bright Galaxies, (Austin: University of Texas Press)

[379] Vilenkin, A. 1985, Phys. Rep., 121, 265

[380] Villumsen, J.V., Scherrer, R.J., & Bertschinger, E. 1991, ApJ, 367, 37

[381] Vittorio, N., Juszkiewicz, R., & Davis, M. 1986, Nature, 323, 132

[382] Vishniac, E.T. 1987, ApJ, 322, 597

[383] Vogeley, M.S., Geller, M.J., & Huchra, J.P. 1991, ApJ, 382, 44

[384] Vogeley, M.S., Park, C., Geller, M.J., & Huchra, J.P. 1992, ApJL, 391, L5

[385] Weinberg, D.H., & Cole, S. 1991, preprint CfPA-TH-91-025

[386] Weinberg, D.H., Ostriker, J.P., & Dekel, A. 1989, ApJ, 336, 9

[387] Weinberg, D.H., & Gunn, J.E. 1990, MNRAS, 247, 260

[388] Weinberg, S. 1972, Gravitation and Cosmology, (New York: Wiley)

[389] West, M.J., & van den Bergh, S. 1991, ApJ, 373, 1

[390] White, S.D.M. 1979 MNRAS, 186, 145

[391] White, S.D.M., Frenk, C.S., & Davis, M. 1983, ApJ, 287, 1

[392] White, S.D.M., Frenk, C.S., Davis, M. & Efstathiou, G. 1987, ApJ, 313, 505

[393] Wright, E.L., et al. 1992, preprint

[394] Yahil, A. 1991, preprint

[395] Yanagida, T. 1979, KEK Lecture Notes, unpublished

[396] Yoshioka, S., & Ikeuchi, S. 1989, ApJ, 341, 16

[397] Zahn, C.T. 1971, IEEE Trans. Comp., C20, 68

[398] Zee, A. 1980, Phys. Lett., B 93, 389

[399] Zeldovich, Y.B. 1970, A&A, 5, 84

[400] Zeldovich, Y.B. 1972, MNRAS, 160, 1

[401] Zeldovich, Y.B. 1980, MNRAS, 192, 663

[402] Zwicky, F., Herzog, E., Karpowicz, M., & Koval, C.T. 1961-1968, Catalogue of Galaxies and Clusters of Galaxies (Pasadena, Calif.: California Institute of Technology)